UNIVERSIDADE DA BEIRA INTERIOR
Ciências

Development of layer-by-layer polymeric microneedles for cancer local delivery of therapeutics

André Ferreira Moreira

Tese para obtenção do Grau de Doutor em
Bioquímica
(3º ciclo de estudos)

Orientador: Prof. Doutor Ilídio Joaquim Sobreira Correia

Covilhã, dezembro de 2019

Dedicatory

To my family and everyone that always supported me.

Acknowledgements

First of all, I would like to thank my supervisor, Dr. Ilídio J. Correia for all the support, guidance, and knowledge that he transmitted to me since the beginning of my scientific career. The work ethics that he promotes was essential for my development as a researcher, contributing to improve my focus and technical skills as well as my ability to interpret and criticize results.

Moreover, I would like to acknowledge the Universidade da Beira Interior, in particular to the CICS-UBI, for providing the equipment and the facilities required to perform this doctoral thesis. Furthermore, I would like to acknowledge the Fundação para a Ciência e a Tecnologia (FCT) for the financial support through the individual Ph.D. fellowship (SFRH/BD/109482/2015). The funding from the projects POCI-01-0145-FEDER-007491, UID/Multi/00709/2013, CENTRO-01-0145-FEDER-028989 and POCI-01-0145-FEDER-031462 is also acknowledged.

Additionally, I am grateful for all the friendship, support, and assistance of my Ph.D. colleagues (Elisabete, Sónia, and Duarte) that walked this path with me. Further, a special thanks to all the lab colleagues and master students that I guided during this time for the joyful and companionship environment.

Finally, I would like to thank my family, especially to my parents, brother, and grandmother for the continuous support, love, care, and forgiveness during the last years. To Ana Catarina, words cannot express how grateful I am for all the love, comprehension, patience and support. Also, for her continuous encouragement that motivated me to continue moving forward during these years.

List of publications

Articles published in peer-reviewed international journals included in this Doctoral thesis

I. Thermo-and pH-responsive nano-in-micro particles for combinatorial drug delivery to cancer cells
André F. Moreira, Diana R. Dias, Elisabete C. Costa, Ilídio J. Correia
European Journal of Pharmaceutical Sciences, 2017, Vol.104, pp. 42-51
DOI: 10.1016/j.ejps.2017.03.033
I.F.= 3.532; Q2 Pharmacology & Pharmacy (71/267)
Citations: ISI Web of Knowledge – 15; Google Scholar – 17; Scopus – 15.

II. Gold-core silica shell nanoparticles application in imaging and therapy: a review
André F. Moreira, Carolina F. Rodrigues, Catarina A. Reis, Elisabete C. Costa, Ilídio J. Correia
Microporous and Mesoporous Materials, 2018, Vol. 270, pp. 168-179
DOI: 10.1016/j.micromeso.2018.05.022
I.F.= 4.182; Q1 Chemistry, Applied (46/148)
Citations: ISI Web of Knowledge – 8; Google Scholar – 10; Scopus – 9.

III. Development of poly-2-ethyl-2-oxazoline coated gold-core silica shell nanorods for cancer chemo-photothermal therapy
André F. Moreira, Carolina F. Rodrigues, Catarina A. Reis, Elisabete C. Costa, Paula Ferreira, Ilídio J. Correia
Nanomedicine, 2018, Vol. 13 (20), pp. 2611-2627
DOI: 10.2217/nnm-2018-0179
I.F.= 4.717; Q1 Biotechnology & Applied Microbiology (23/162)
Citations: ISI Web of Knowledge – 1; Google Scholar – 4; Scopus – 3.

IV. Microneedle-based delivery devices for cancer therapy: a review
André F. Moreira, Carolina F. Rodrigues, Telma A. Jacinto, Sónia P. Miguel, Elisabete C. Costa, Ilídio J. Correia
Pharmacological Research, 2019, *in press*
DOI: 10.1016/j.phrs.2019.104438
I.F.= 5.574; 1ºDecile Pharmacology & Pharmacy (18/267)
Citations: ISI Web of Knowledge – 0; Google Scholar – 0; Scopus – 0.

V. Poly (vinyl alcohol)/Chitosan Layer-by-Layer Microneedles for Cancer Chemo-Photothermal Therapy

André F. Moreira, Carolina F. Rodrigues, Telma A. Jacinto, Sónia P. Miguel, Elisabete C. Costa, Ilídio J. Correia
International Journal of Pharmaceutics, 2019, *in press*
DOI: 10.1016/j.ijpharm.2019.118907
I.F.= 4.213; Q1 Pharmacology & Pharmacy (44/267)
Citations: ISI Web of Knowledge – 0; Google Scholar – 0; Scopus – 0.

Articles published in peer-reviewed international journals that were not included in this Doctoral thesis

I. Preparation of end-capped pH-sensitive mesoporous silica nanocarriers for on-demand drug delivery
André F. Moreira, Vitor M. Gaspar, Elisabete C. Costa, Duarte De Melo-Diogo, Paulo Machado, Catarina M. Paquete, Ilídio J. Correia
European Journal of Pharmaceutics and Biopharmaceutics, 2014, Vol. 88 (3), pp. 1012-1025
DOI: 10.1016/j.ejpb.2014.09.002
I.F.= 4.708; Q1 Pharmacology & Pharmacy (28/267)
Citations: ISI Web of Knowledge – 27; Google Scholar – 34; Scopus – 30.

II. Combinatorial delivery of Crizotinib-Palbociclib-Sildenafil using TPGS-PLA micelles for improved cancer treatment
Duarte De Melo-Diogo, Vitor M. Gaspar, Elisabete C. Costa, André F. Moreira, David Markl, Eugenia Gallardo, Ilídio J. Correia
European Journal of Pharmaceutics and Biopharmaceutics, 2014, Vol. 88 (3), pp. 718-729
DOI: 10.1016/j.ejpb.2014.09.013
I.F.= 4.708; Q1 Pharmacology & Pharmacy (28/267)
Citations: ISI Web of Knowledge – 29; Google Scholar – 38; Scopus – 35.

III. Minicircle DNA Vectors for Gene Therapy: Advances and Applications
Vitor M. Gaspar, Duarte De Melo-Diogo, Elisabete C. Costa, André F. Moreira, João A. Queiroz, Chantal Pichon, Ilídio J. Correia, Fani Sousa
Expert Opinion on Biological Therapy, 2015, Vol. 15, pp. 353-379
DOI: 10.1517/14712598.2015.996544
I.F.= 3.585; Q2 Biotechnology & Applied Microbiology (44/162)
Citations: ISI Web of Knowledge – 26; Google Scholar – 41; Scopus – 28.

IV. Chitosan/Arginine-Chitosan polymer blends for assembly of nanofibrous membranes for wound regeneration
Bernardo P. Antunes, André F. Moreira, Vitor M. Gaspar, Ilídio J. Correia
Carbohydrate Polymers, 2015, Vol. 130, pp.104-112

DOI: 10.1016/j.carbpol.2015.04.072
I.F.= 6.044; 1º Decile (Top 5) Chemistry, applied (2/71)
Citations: ISI Web of Knowledge – 39; Google Scholar – 53; Scopus – 39.

V. Gas-generating TPGS-PLGA Microspheres loaded with Nanoparticles (NIMPS) for co-delivery of minicircle DNA and anti-tumoral drugs
Vitor M. Gaspar, André F. Moreira, Elisabete C. Costa, João A. Queiroz, Fani Sousa, Chantal Pichon, Ilídio J. Correia
Colloids and Surfaces B: Biointerfaces, 2015, Vol. 134, pp. 287-294
DOI: 10.1016/j.colsurfb.2015.07.004
I.F.= 3.973; Q1 Biophysics (15/72)
Citations: ISI Web of Knowledge – 27; Google Scholar – 31; Scopus – 29.

VI. Stimuli-responsive mesoporous silica nanoparticles for cancer therapy: A review
André F. Moreira, Diana R. Dias, Ilídio J. Correia
Microporous and Mesoporous Materials, 2016, Vol. 236, pp. 141-157
DOI: 10.1016/j.micromeso.2016.08.038
I.F.= 4.182; Q1 Chemistry, Applied (46/148)
Citations: ISI Web of Knowledge – 46; Google Scholar – 54; Scopus – 48.

VII. The effect of the shape of gold core–mesoporous silica shell nanoparticles on the cellular behavior and tumor spheroid penetration
Diana R. Dias, André F. Moreira, Ilídio J. Correia
Journal of Materials Chemistry B, 2016, Vol. 4 (47), pp. 7630-7640
DOI:10.1039/C6TB02668K
I.F.= 5.047; Q1 Materials Science, Biomaterials (6/32)
Citations: ISI Web of Knowledge – 10; Google Scholar – 14; Scopus – 11.

VIII. 3D tumor spheroids: an overview on the tools and techniques used for their analysis
Elisabete C. Costa, André F. Moreira, Duarte de Melo-Diogo, Vitor M. Gaspar, Marco P. Carvalho, Ilídio J. Correia
Biotechnology Advances, 2016, Vol. 34 (8), pp. 1427-1441
DOI: 10.1016/j.biotechadv.2016.11.002
I.F.= 12.831; 1º Decile (Top 5) Biotechnology and Applied Microbiology (5/162)
Citations: ISI Web of Knowledge – 66; Google Scholar – 89; Scopus – 69.

IX. Strategies to improve cancer photothermal therapy mediated by nanomaterials
Duarte de Melo-Diogo, Cleide Pais-Silva, Diana R. Dias, André F. Moreira, Ilídio J. Correia
Advanced Healthcare Materials, 2017, Vol. 6 (10)
DOI: 10.1002/adhm.201700073

I.F.= 6.270; 1º Decile Engineering, Biomedical (8/80)
Citations: ISI Web of Knowledge – 37; Google Scholar – 50; Scopus – 45.

X. Spheroids formation on non-adhesive surfaces by Liquid Overlay Technique: considerations and practical approaches
Elisabete C. Costa, Duarte Melo-Diogo, André F. Moreira, Marco P. Carvalho, Ilídio J. Correia
Biotechnology journal, 2018, Vol. 13, pp. 1700417
DOI: 10.1002/biot.201700417
I.F.= 3.543; Q1 Biochemical Research Methods (18/79)
Citations: ISI Web of Knowledge – 9; Google Scholar – 11; Scopus – 8.

XI. ClearT immersion optical clearing method for intact 3D spheroids imaging through confocal laser scanning microscopy
Elisabete C. Costa, André F. Moreira, Duarte de Melo-Diogo, Ilídio J. Correia
Optics and Laser Technology, 2018, Vol. 106, pp. 94-99
DOI: 10.1016/j.optlastec.2018.04.002
I.F.= 3.319; Q1 Optics (21/95)
Citations: ISI Web of Knowledge – 6; Google Scholar – 7; Scopus – 6.

XII. Polyethylene glycol (PEG) molecular weight influences the ClearT2 optical clearing method for spheroids imaging by confocal laser scanning microscopy
Elisabete C. Costa, André F. Moreira, Duarte de Melo-Diogo, Ilídio J. Correia
Journal of Biomedical Optics, 2018, Vol. 23 (5), pp. 1-11
DOI: 10.1117/1.JBO.23.5.055003
I.F.= 2.555; Q2 Optics (37/95)
Citations: ISI Web of Knowledge – 2; Google Scholar – 2; Scopus – 2.

XIII. 3D tumor spheroids as *in vitro* models to mimic *in vivo* human solid tumors resistance to therapeutic drugs
Ana S. Nunes, Ana S. Barros, Elisabete C. Costa, André F. Moreira, Ilídio J. Correia
Biotechnology and Bioengineering, 2019, Vol. 116 (1), pp. 206-226
DOI: 10.1002/bit.26845
I.F.= 4.260; Q1 Biotechnology & Applied Microbiology (30/162)
Citations: ISI Web of Knowledge – 2; Google Scholar – 7; Scopus – 2.

XIV. Production and characterization of electrospun Silk Fibroin based asymmetric membranes for wound dressing applications
Sónia P. Miguel, Déborah Simões, André F. Moreira, Rosa S. Sequeira, Ilídio J. Correia
International Journal of Biological Macromolecules, 2019, Vol. 121, pp. 524-535
DOI: 10.1016/j.ijbiomac.2018.10.041

I.F.= 4.784; 1ºDecile Polymer Science (8/87)
Citations: ISI Web of Knowledge – 8; Google Scholar – 4; Scopus – 7.

XV. Chitosan based-asymmetric membranes for wound healing: a review
Sónia P. Miguel, André F. Moreira, Ilídio J. Correia
International Journal of Biological Macromolecules, 2019, Vol. 127, pp. 460-475
DOI: 10.1016/j.ijbiomac.2019.01.072
I.F.= 4.784; 1ºDecile Polymer Science (8/87)
Citations: ISI Web of Knowledge – 2; Google Scholar – 9; Scopus – 6.

XVI. Development of Gold-Core Silica Shell Nanospheres Coated with Poly-2-ethyl-oxazoline and ß-cyclodextrin Aimed for Cancer Therapy
Catarina A. Reis, Carolina F. Rodrigues, André F. Moreira, Telma A. Jacinto, Paula Ferreira, Ilídio J. Correia
Materials Science & Engineering C - Materials for Biological Applications, 2019, Vol. 98, pp. 960-968
DOI: 10.1016/j.msec.2019.01.068
I.F.= 4.959; Q1 Materials Science, Biomaterials (7/32)
Citations: ISI Web of Knowledge – 0; Google Scholar – 0; Scopus – 0.

XVII. Functionalization of AuMSS nanorods towards more effective cancer therapies
Carolina F. Rodrigues*, Telma A. Jacinto*, André F. Moreira*, Elisabete C. Costa, Sónia P. Miguel, Ilídio J. Correia
*the authors contributed equally to this work
Nano Research, 2019, Vol. 12, pp. 719-732
DOI: 10.1007/s12274-019-2286-y
I.F.= 8.515; 1ºDecile Physics, Applied (13/148)
Citations: ISI Web of Knowledge – 0; Google Scholar – 1; Scopus – 0.

XVIII. An overview of electrospun membranes loaded with bioactive molecules for improving the wound healing process
Sónia P. Miguel, Rosa S. Sequeira, André F. Moreira, Cátia S. Cabral, António G. Mendonça, Paula Ferreira, Ilídio J. Correia
European Journal of Pharmaceutics and Biopharmaceutics, 2019, Vol. 139, pp. 1-22
DOI: 10.1016/j.ejpb.2019.03.010
I.F.= 4.708; Q1 Pharmacology&Pharmacy (28/267)
Citations: ISI Web of Knowledge – 0; Google Scholar – 3; Scopus – 2.

XIX. Optimization of gold core-mesoporous silica shell functionalization with TPGS and PEI for cancer therapy
Carolina F. Rodrigues, Catarina A. Reis, André F. Moreira, Paula Ferreira, Ilídio J. Correia
Microporous and Mesoporous Materials, 2019, Vol. 285, pp. 1-12
DOI: 10.1016/j.micromeso.2019.04.064
I.F.= 4.182; Q1 Chemistry, Applied (12/71)
Citations: ISI Web of Knowledge – 0; Google Scholar – 0; Scopus – 0.

XX. Production and characterization of a novel asymmetric 3D printed construct aimed for skin tissue regeneration
Sónia P. Miguel, Cátia S. Cabral, André F. Moreira, Ilídio J. Correia
Colloids and Surfaces B: Biointerfaces, 2019, Vol. 181, pp. 994-1003
DOI: 10.1016/j.colsurfb.2019.06.063
I.F.= 3.973; Q1 Biophysics (15/72)
Citations: ISI Web of Knowledge – 0; Google Scholar – 0; Scopus – 0.

XXI. Optical clearing methods: an overview of the techniques used for the imaging of 3D spheroids
Elisabete C. Costa, Daniel N. Silva, André F. Moreira, Ilídio J. Correia
Biotechnology and Bioengineering, 2019, *in press*
DOI: 10.1002/bit.27105
I.F.= 4.260; Q1 Biotechnology & Applied Microbiology (30/162)
Citations: ISI Web of Knowledge – 0; Google Scholar – 0; Scopus – 0.

XXII. Development of a Poly(vinyl alcohol)/Lysine electrospun membrane-based drug delivery system for improving the skin regeneration
Rosa S. Sequeira, Sónia P. Miguel, Cátia S. Cabral, André F. Moreira, Paula Ferreira, Ilídio J. Correia
International Journal of Pharmaceutics, 2019, Vol. 570, pp. 118640
DOI: 10.1016/j.ijpharm.2019.118640
I.F.= 4.213; Q1 Pharmacology & Pharmacy (44/267)
Citations: ISI Web of Knowledge – 0; Google Scholar – 0; Scopus – 0.

Manuscripts submitted for publication in peer-reviewed international journals not included in this Doctoral thesis

I. Telma A. Jacinto, Carolina F. Rodrigues, André F. Moreira, Sónia P. Miguel, Elisabete C. Costa, Paula Ferreira, Ilídio J. Correia, "Hyaluronic acid and Vitamin E polyethylene glycol succinate functional 1ized gold-core silica shell nanorods for cancer targeted photothermal therapy.", submitted for publication.

Book chapter in peer-reviewed scientific books not included in this Doctoral thesis

I. Chapter 6 - Multifunctional Nanocarriers for Codelivery of Nucleic Acids and Chemotherapeutics to Cancer Cells
Vítor M. Gaspar, André F. Moreira, Duarte de Melo-Diogo, Elisabete C. Costa, João A. Queiroz, Fani Sousa, Chantal Pichon, Ilídio J. Correia
Nanobiomaterials in Medical Imaging – Volume VIII, Edited by Alexandru M. Grumezescu, Published by Elsevier (2016)
DOI: 10.1016/B978-0-323-41736-5.00006-6
Citations: ISI Web of Knowledge – 0; Google Scholar – 0; Scopus – 0

Book chapters submitted for publication in peer-reviewed scientific books not included in this Doctoral thesis

I. Sónia P. Miguel*, André F. Moreira*, Déborah Simões, Ilídio J. Correia, António G. Mendonça, "3D printed scaffolds with antibacterial properties for bone tissue regeneration.", under review.

II. Carolina F. Rodrigues, Cátia G. Alves, Rita Lima-Sousa, André F. Moreira, Duarte de Melo-Diogo, Ilídio J. Correia, "Inorganic-based drug delivery systems for cancer therapy.", under review.

List of Scientific Communications

Oral presentations

I. Moreira, A.F., Fernandes, A.T., Ramos, C., Pena, F., Silva, J., "MicroMed", Sessão Intermédia 2º CEBT Ibérico, 7th of May 2014, Universidade de Coimbra, Coimbra, Portugal.

II. Moreira, A.F., Fernandes, A.T., Ramos, C., Pena, F., Silva, J., "MicroMed", Sessão Final 2º CEBT Ibérico, 8th of July 2014, Universidade de Aveiro, Aveiro, Portugal.

III. Moreira, A.F. and Correia, I.J., "Development of layer-by-layer polymeric Microneedles for specific delivery of cancer therapeutics.", Semana da Ciência e Tecnologia 2016 "3 minutos, 1 slide .... A Tua tese!", UBI, 24th of November 2015, Universidade da Beira Interior, Covilhã, Portugal.

IV. Moreira, A.F. "Development of new Drug Delivery Systems for Cancer Therapy.", Introdução a Ciências Biomédicas, UBI, 11th of October 2016, Universidade da Beira Interior, Covilhã, Portugal.

V. Moreira, A.F., Costa, E.C., Rodrigues, C. F., Reis, C.A., Dias, D.R., Correia, I.J., "Mesoporous silica-based drug delivery systems for cancer therapy" XVI Portuguese Conference on Fracture, 23rd and 24th of April 2018, TRYP Covilhã Dona Maria, Covilhã, Portugal.

VI. Costa, E. C., Carvalho, M. P., Moreira, A.F., De Melo-Diogo, D., Correia, I. J., "Agarose and Hyaluronic Acid (HA) application in 3D cell culture of breast cancer cells", XVI Portuguese Conference on Fracture, 23rd and 24th of April 2018, TRYP Covilhã Dona Maria, Covilhã, Portugal.

Poster presentations

I. Costa, E. C., Gaspar, V.M., De Melo-Diogo, D., Moreira, A.F., Marques, J. G., Coutinho, P., Correia I. J., "Evaluation of nanoparticles uptake in breast cancer co-cultures", Encontro Bienal das Divisões Técnicas da Sociedade Portuguesa de Materiais (SPM), 4th of May 2014, Covilhã, Portugal.

II. Moreira, A.F., Gaspar, V.M., Costa, E.C., De Melo-Diogo, D., Machado, P., Paquete, C.M., Correia, I.J., "Development of mesoporous silica nanoparticles for drug delivery

to cancer cells", Encontro Bienal das Divisões Técnicas da Sociedade Portuguesa de Materiais (SPM), 4th of May 2014, UBI, Covilhã, Portugal.

III. Costa, E. C., Gaspar, V.M., De Melo-Diogo, D., Moreira, A.F., Marques, J. G., Coutinho, P., Correia, I. J., "Co-cultures for nanoparticles uptake analysis", IX CICS Symposium, 30th of June and 1st of July 2014, Covilhã, Portugal.

IV. Marques, J. G., Gaspar, V.M., Markl, D., Costa, E. C., De Melo-Diogo, D., Moreira, A.F., Gallardo, E., Correia I.J., "Co-delivery of a dual drug combination in polymeric nanovehicles for improved anticancer therapy", IX CICS Symposium, 30th of June and 1st of July 2014, Covilhã, Portugal.

V. Moreira, A.F., Gaspar, V. M., Costa, E. C., De Melo-Diogo, D., Machado, P., Paquete, C.M., Correia, I. J., "Development of Mesoporous Silica Nanoparticles for Drug Delivery to Cancer Cells", IX CICS Symposium, 30th of June and 1st of July 2014, Covilhã, Portugal.

VI. De Melo-Diogo, D., Gaspar, V.M., Costa, E.C., Moreira, A.F., Oppolzer, D., Gallardo, E., Correia, I.J., "Triple drug loaded polymeric micelles for improved lung cancer therapy", Semana da Ciência, 28th of November 2014, Covilhã, Portugal.

VII. Moreira, A.F., Gaspar, V. M., Costa, E. C., De Melo-Diogo, D., Machado, P., Paquete, C.M., Correia, I. J. "pH-sensitive mesoporous silica nanoparticles for drug delivery to prostate cancer cells", Semana da Ciência, 28th of November 2014, Covilhã, Portugal.

VIII. Costa, E.C., Gaspar, V.M., De Melo-Diogo, D., Moreira, A.F., Coutinho, P., Correia, I.J., " Liquid Overlay Technique (LOT) optimizations for spheroids 3D cell culture ", Semana da Ciência, 28th of November 2014, Covilhã, Portugal.

IX. Costa, E.C., Gaspar, V.M., Melo-Diogo, D., Moreira, A.F., Coutinho, P., Correia, I.J., "Optimization of Liquid Overlay Technique (LOT) to produce 3D Breast and Cervical Co-Culture Models", VIII Jornadas Nacionais sobre Tecnologia e Saúde, 17th of April 2015, Guarda, Portugal

X. De Melo-Diogo, D., Gaspar V.M., Costa, E.C., Moreira, A.F., Oppolzer, D., Gallardo, E. Correia, I.J.,"Triple-drug co-delivery by TPGS-PLA micelles for lung cancer therapy", VIII Jornadas Nacionais sobre Tecnologia e Saúde, 17th of April 2015, Guarda, Portugal.

XI. Moreira, A.F., Gaspar, V. M., Costa, E. C., De Melo-Diogo, D., Machado, P., Paquete, C.M., Correia, I. J. " Calcium carbonate coated nanoparticles for pH-responsive drug co-delivery to prostate cancer cells ", VIII Jornadas Nacionais sobre Tecnologia e Saúde, 17th of April 2015, Guarda, Portugal.

XII. Antunes, B.P., Moreira, A.F., Gaspar, V.M., Correia I.J. "Chitosan/Arginine-Chitosan Polymer Blends For Assembly Of Nanofibrous Membranes For Wound Regeneration", X CICS Symposium, 6th and 7th of July 2015, Covilhã, Portugal.

XIII. Moreira, A.F. and Correia, I.J., "Development of layer-by-layer polymeric microneedles for cancer local delivery of therapeutics", Semana da Ciência e Tecnologia, 23rd to 29th of November 2015, Covilhã, Portugal.

XIV. Moreira, A.F., Gaspar, V.M., Costa, E.C., De Melo-Diogo, D., Machado, P., Paquete, C.M., Correia, I.J., "Calcium carbonate coated nanoparticles for pH responsive drug co-delivery to prostate cancer cells", Ciência 2016, 4th to 6th of July 2016, Centro de Congressos de Lisboa, Lisboa, Portugal.

XV. Dias, D.R., Moreira, A.F., Correia, I.J., "Synthesis and characterization of gold nanoparticles coated with mesoporous silica.", V Encontro de Estudantes de Materiais (ENEM), 29th and 30th September 2016, Covilhã, Portugal.

XVI. Moreira, A.F., Dias, D.R., Costa, E.C., Correia, I.J., "Nano-in-micro particles for stimuli responsive drug delivery to cancer cells", II International Congress in Health Sciences Research Towards innovation and entrepeneurship: Trends in Biotechnology for Biomedical Applications, 17th to 20th of May 2017, Covilhã, Portugal.

XVII. Costa, E.C., Carvalho, M.P., de Melo-Diogo, D., Moreira, A.F., Correia, I.J., "Mimicking breast cancer microenvironment with *in vitro* 3d heterotypic spheroids", II International Congress in Health Sciences Research Towards innovation and entrepeneurship: Trends in Biotechnology for Biomedical Applications, 17th to 20th of May 2017, Covilhã, Portugal.

XVIII. Moreira, A.F., Dias, D.R., Costa, E.C., Correia, I.J., "Dual-stimuli responsive nano-in-micro drug delivery systems for cancer therapy", Encontro com a Ciência e Tecnologia 2017, 3rd to 5th of July 2017, Centro de Congressos de Lisboa, Lisboa, Portugal.

XIX. Costa, E.C., Carvalho, M.P., de Melo-Diogo, D., Moreira, A.F., Correia, I.J., "Mimicking breast cancer microenvironment with *in vitro* 3D heterotypic spheroids", Encontro com a Ciência e Tecnologia 2017, 3rd to 5th of July 2017, Centro de Congressos de Lisboa, Lisboa, Portugal.

XX. Moreira, A.F., Dias, D.R., Rodrigues, C.F., Reis, C.A., Costa, E.C., Correia, I.J., "Nano-in-micro spheres for pH- and thermo-responsive drug delivery to cancer cells", Encontro com a Ciência e Tecnologia 2018, 2nd to 4th of July 2018, Centro de Congressos de Lisboa, Lisboa, Portugal.

XXI. Rodrigues, C. F., Reis, C. A., Moreira, A.F., Ferreira, P., Correia, I. J., "Optimization of gold core-mesoporous silica shell functionalization with TPGS and PEI for cancer therapy", XIII CICS-UBI Symposium, 5th and 6th of July 2018, Covilhã, Portugal.

XXII. Reis, C. A., Rodrigues, C. F., Moreira, A.F., Correia, I. J., "Optimization of the gold-core silica shell nanospheres coating with Poly-2-ethyl-2-oxazoline and Beta-cyclodextrin", XIII CICS-UBI Symposium, 5th and 6th of July 2018, Covilhã, Portugal.

XXIII. Rodrigues, C.F., Reis, C.A., Moreira, A.F., Ferreira, P., Correia, I.J., "Functionalization of Gold Core Silica Shell Nanorods with TPGS and PEI for Cancer Chemo-Phototherapy", 6th ENBENG - IEEE Portuguese Meeting in Bioengineering, 22nd and 23rd of February 2019, Instituto Superior de Engenharia de Lisboa, Lisboa, Portugal.

XXIV. Silva, D.N., Costa, E.C., Moreira, A.F., de Melo-Diogo, D., Correia, I.J., Optical clearing techniques for the imaging of 3D spheroids, 6th IEEE Portuguese Meeting on Bioengineering, 22nd and 23th of February of 2019, Instituto Superior de Engenharia de Lisboa, Lisboa, Portugal.

XXV. Jacinto, T.A., Rodrigues, C.F., Moreira, A.F., Ferreira, P., Correia, I.J., " Development of Gold Core Silica Shell Nanorods coated with HA and TPGS for the Targeted Cancer Photothermal Therapy", XIV CICS-UBI Symposium, 4th and 5th of July 2019, Covilhã, Portugal.

XXVI. Rodrigues, C.F., Reis, C.A., Moreira, A.F., Ferreira, P., Correia, I.J., " Doxorubicin loaded Gold-Core Silica Shell Nanorods Functionalized with PEI and TPGS for the combinatorial Cancer Therapy", XIV CICS-UBI Symposium, 4th and 5th of July 2019, Covilhã, Portugal.

XXVII. Daniel N. Silva, Elisabete C. Costa, André F. Moreira, Duarte de Melo-Diogo and Ilídio J. Correia, Optical clearing techniques to 3D spheroids for the imaging through CLSM, XIV Annual CICS-UBI Symposium, 4th to 5th of July of 2019, Covilhã, Portugal.

XXVIII. Rodrigues, C.F., Reis, C.A., Moreira, A.F., Ferreira, P., Correia, I.J., " Development of Gold-Core Silica Shell Nanorods coated with PEI and TPGS aimed for Cancer Chemo-Phototherapy ", Encontro com a Ciência e Tecnologia 2019, 8th to 10th of July 2019, Centro de Congressos de Lisboa, Lisboa, Portugal.

Conference Organizing Committees

Member of the organizing committee of scientific conferences

I. II International Congress in Health Sciences Research Towards innovation and entrepreneurship: Trends in Biotechnology for Biomedical Applications, 17th to 20th of May of 2017, Universidade da Beira Interior, Covilhã, Portugal.

II. XVI Portuguese Conference on Fracture, 23rd and 24th of April of 2018, Hotel TRYP Dona Maria, Covilhã, Portugal

III. XIII Annual CICS-UBI Symposium 2018, 5th and 6th of July 2018, Faculdade de Ciências da Saúde, Covilhã, Portugal.

Resumo Alargado

O cancro é uma das maiores causas da morbidade e mortalidade do ser humano em todo o mundo, constituindo o seu tratamento um dos maiores desafios para a medicina contemporânea. Na atualidade, a cirurgia, a quimioterapia e a radioterapia são as abordagens terapêuticas mais utilizadas em meio clínico, no entanto estas apresentam uma baixa eficácia terapêutica e elevada toxicidade sistémica. Esta realidade enfatiza a necessidade de desenvolver novas abordagens terapêuticas, que apresentem não só uma maior eficácia, mas que também consigam prevenir a sua interação com os tecidos saudáveis e, consequentemente, diminuam os efeitos secundários causados pelas mesmas. Nesta área, os investigadores têm explorado a conjugação de diferentes abordagens terapêuticas de forma a ultrapassar os mecanismos de resistência das células cancerígenas e, simultaneamente, maximizar o efeito anti-tumoral. Entre as diversas terapias combinatórias testadas, a conjugação de regimes de terapia fototérmica e quimioterapia tem demonstrado resultados promissores em ensaios pré-clínicos. Em particular, os investigadores têm-se focado na utilização de nanomateriais que permitam mediar o efeito fototérmico em resposta a radiação com um comprimento de onda na região do infravermelho próximo (NIR; 700-1100 nm) e, também em promover a entrega específica de agentes quimioterápicos. A utilização da radiação NIR está relacionada com o facto dos principais componentes biológicos, como a água, a hemoglobina, as proteínas, e a melanina, apresentarem uma absorção mínima ou mesmo desprezível nesta zona do espectro. De entre os diversos nanomateriais responsivos ao estímulo por radiação NIR, as nanopartículas de ouro revestidas com uma camada de sílica mesoporosa (AuMSS) têm-se destacado para aplicações médicas. Estes materiais têm a capacidade de combinar numa única plataforma as propriedades de um agente fototérmico, a entrega de fármacos e a bioimagiologia. O núcleo de ouro, principalmente as morfologias anisotrópicas devido ao fenómeno de ressonância plasmónica de superfície, pode ser otimizado para apresentar uma elevada absorção na região NIR, o que permite a produção de um efeito fototérmico localizado capaz de induzir a morte das células cancerígenas. Por outro lado, o revestimento de sílica mesoporosa adiciona uma camada biocompatível com elevada área de superfície e volume de poro que permite a encapsulação de diferentes agentes quimioterápicos. Adicionalmente, a inclusão da camada de sílica mesoporosa estabiliza e protege o núcleo de ouro impedindo que ocorra a sua degradação, quando sujeito a radiações energéticas como a luz NIR utilizada na terapia fototérmica.

Porém, apesar dos resultados promissores apresentados por estas nanopartículas, a sua translação para a clínica tem sido bastante limitada. Tal acontece como consequência da reduzida capacidade que as terapias baseadas em nanopartículas têm apresentado para se acumular no tecido tumoral. De acordo com dados recentes, menos de 0,7% da dose administrada consegue chegar com sucesso ao local alvo. Além disso, as estratégias

desenvolvidas para ultrapassar esta limitação são na sua generalidade demasiado complexas e apresentam processos de síntese difíceis de transpor para ambiente industrial. Assim sendo, recentemente, os investigadores começaram a reexplorar a utilização de sistemas de entrega de agentes terapêuticos à macroescala (p.ex. microagulhas e hidrogéis) de forma a promover uma administração controlada e localizada das terapias no tecido tumoral. Em particular, a utilização de sistemas de microagulhas tem mostrado resultados promissores que suportam a sua aplicação na terapia anti-tumoral. Os sistemas baseados em microagulhas podem ser fabricados utilizando diversos materiais (metais, polímeros e cerâmicas) bem como apresentar uma grande variedade de morfologias e organizações. De facto, estes sistemas podem ser utilizados apenas para aumentar a permeação de agentes terapêuticos no tecido alvo, ou para promover a entrega desses mesmos agentes, quando encapsulados na sua estrutura, em regiões mais profundas do tecido tumoral de uma forma controlada. Na terapia anticancerígena, a aplicação das microagulhas tem sido explorada com o intuito de ativar respostas imunológicas anticancerígenas (antigénios, material genético e adjuvantes imunológicos) ou para entregar agentes com atividade anticancerígena (fármacos e nanopartículas). Desta forma, a aplicação local de sistemas de microagulhas tem potencial para aumentar a distribuição e a quantidade de agentes terapêuticos que se acumulam nas regiões mais profundas do tecido tumoral e, simultaneamente, reduzir a interação destes com os tecidos saudáveis adjacentes. Tendo em consideração as vantagens da entrega localizada das terapêuticas anticancerígenas, o principal objetivo do plano de trabalhos desenvolvido nesta tese foi o desenvolvimento de um sistema de microagulhas com uma organização camada sobre camada (*Layer-by-Layer*, LbL) para mediar a entrega de nanobastões com um núcleo de ouro e revestimento de sílica mesoporosa, bem como o de agentes quimioterapêuticos. Para tal, procurou-se i) explorar um método de produção de AuMSS na forma de bastão que apresente a capacidade de realizar simultaneamente funções de imagiologia e terapia; ii) desenvolver um microssistema que consiga incorporar estas nanoplataformas e permitir o controlo da sua libertação em resposta a variações no pH e temperatura; e iii) produzir um sistema de microagulhas para entrega combinada das nanoplataformas desenvolvidas e fármacos quimioterápicos.

No primeiro estudo apresentado nesta tese, foi avaliada a capacidade terapêutica de nanobastões de AuMSS funcionalizados com poli-2-etil-2-oxazolinas e carregados com doxorrubicina. Os nanobastões de ouro foram produzidos utilizando um método denominado de "*seed mediated growth*" sendo posteriormente revestidos com uma camada de sílica utilizando o método modificado de Stöber. Seguidamente, a superfície desta nanopartícula foi modificada com poli(2-etil-2-oxazolinas) previamente modificadas com um silano, através de um processo de condensação. A funcionalização dos nanobastões permitiu neutralizar a carga de superfície das nanopartículas de -30 mV para -15 mV. Além disso, também se verificou uma melhoria na biocompatibilidade dos nanosistemas, nomeadamente a nível da redução da hemólise para valores negligenciáveis quando utilizadas concentrações de 200 $\mu g.mL^{-1}$. Além disso, a funcionalização dos nanobastões não afetou negativamente a sua capacidade fototérmica,

podendo induzir um aumento na temperatura de cerca de 40ºC quando irradiados com luz NIR durante 5 min. Adicionalmente, os ensaios *in vitro* em linhas celulares do cancro do colo do útero revelaram que a combinação do efeito fototérmico e quimioterapêutico mediada pelos nanobastões carregados com doxorrubicina permitiu a erradicação das células tumorais.

No segundo estudo apresentado nesta tese, foi explorada uma abordagem de encapsulação de ácido salicílico e nanobastões de AuMSS carregados com doxorrubicina em micropartículas de poli(ácido láctico-*co*-ácido glicólico) (PLGA) para a quimioterapia combinatória do cancro. Para tal, micropartículas de PLGA contendo os nanobastões e o fármaco foram produzidas utilizando um método de dupla emulsão (*water-in-oil-in-water*). Os resultados obtidos demonstraram que as micropartículas podiam atuar como agentes de entrega de fármacos e nanopartículas. Além disso, a libertação do seu conteúdo revelou ser dependente do pH (ativada por pH acídico) e da irradiação por luz NIR (produção de calor). Nos estudos *in vitro*, as micropartículas mostraram ser biocompatíveis e internalizadas pelas células cancerígenas do colo do útero. Adicionalmente, em estudos realizados esferóides (modelos de cultura celular 3D), a terapia combinatória mediada pelas micropartículas provocou uma diminuição do tamanho dos esferóides em 50%, bem como a indução de morte em mais de 60% das células cancerígenas presentes nestes agregados celulares após 48 h de incubação.

No terceiro estudo apresentado nesta tese, foi avaliado o potencial terapêutico de uma terapia combinatória administrada por microagulhas com uma organização de camada sobre camada. Inicialmente, um sistema de microagulhas (4x4 pontas) de polivinilpirrolidona foi produzido através da técnica de micromoldagem. Posteriormente, esta camada base do sistema de microagulhas foi revestida utilizando a técnica de *electrospray*, introduzindo desta forma, uma camada de quitosano contendo doxorrubicina e uma camada de álcool polivinílico contendo nanobastões de AuMSS. Os resultados obtidos mostraram que as microagulhas apresentavam uma ponta biselada com uma largura de 425 μm, altura de 1420 μm e uma distância entre pontas de 1740 μm. Adicionalmente, as microagulhas demonstraram ser mecanicamente resistentes para suportar a aplicação no tecido tumoral e libertarem o seu conteúdo forma sequencial e responsiva a pH acídico e à irradiação com luz NIR. Nos estudos *in vitro*, a terapia combinatória mediada pelas microagulhas mostrou ser mais eficaz contra as células cancerígenas do colo do útero do que as terapias individuais. De facto, observou-se uma redução na viabilidade das células cancerígenas para ≈55 e ≈80% quando apenas a quimioterapia ou a terapia fototérmica foram utilizadas. Por outro lado, a combinação das duas terapias no sistema de microagulhas levou à erradicação das células cancerígenas (menos de 5% de células viáveis).

Em suma, os dados obtidos nestes estudos demonstram a aplicabilidade dos sistemas produzidos para promoverem a entrega localizada de terapêuticas no tecido tumoral. Para além da administração local de terapias utilizando sistemas de microagulhas, o potencial terapêutico das AuMSS (terapia fototérmica) pode ser melhorado através de terapias combinatórias,

nomeadamente a quimioterapia através da co-encapsulação de fármacos. Adicionalmente, a organização de camada sobre camada dos sistemas de microagulhas representa uma abordagem simples para a produção de estruturas complexas e hierarquicamente organizadas, que podem encapsular diversos agentes terapêuticos, libertá-los de forma controlada e por ordens específicas de forma a maximizar o efeito anticancerígeno. Neste sentido, o sucesso na administração destas terapias depende de diversos fatores como o espaço temporal em que ocorre a combinação das diferentes terapias, as concentrações administradas e a sequência de libertação. No futuro, estudos pré-clínicos mais aprofundados em modelos animais serão essenciais para determinar o potencial destes sistemas para aplicação no tratamento de diferentes tipos de cancro que afetam o ser humano.

Palavras-chave

Cancro, agentes de entrega, nanopartículas de ouro com revestimento de sílica mesoporosa, microagulhas, fototermia, quimioterapia, terapia combinatória.

Abstract

Cancer is one of the leading causes of morbidity and mortality of the worldwide population. The treatments currently applied in the clinic, such as surgery, chemotherapy, and radiotherapy, present low therapeutic efficacies and induce systemic toxicity. This reality highlights the need to develop new anticancer approaches that can improve not only the therapeutic efficacy but also reduce/avoid the interactions with healthy tissues and consequently the side effects. Furthermore, the researchers have also been exploring the combinatorial therapeutic approaches to overcome the cancer cells resistance mechanisms and maximize the antitumoral effect. Among the various combinatorial therapies, the simultaneous administration of photothermal (PTT) and chemotherapy regimens has shown promising results in preclinical trials. Particularly, researchers have been focused on the utilization of nanomaterials that can mediate a PTT effect in response to near-infrared light (NIR; 700-1100 nm) and that promote a tumor-specific delivery of chemotherapeutic agents. The use of NIR light to mediate the PTT effect is fundamental since the major biological components have minimal absorption in this region of the spectrum. Among the various NIR-responsive nanomaterials, gold-core mesoporous silica shell (AuMSS) nanoparticles are promising candidates for medical applications. These materials can combine on a single platform the properties of a PTT, drug carrier, and bioimaging agent. The gold nucleus, mainly the anisotropic morphologies, due to the surface plasmon resonance phenomenon can be optimized to present a high absorption in the NIR region, which allows the production of a localized PTT effect capable of inducing cancer cell death. On the other side, the mesoporous silica coating provides a large surface area and pore volume that allows the encapsulation of different chemotherapeutic agents. Additionally, the mesoporous silica layer stabilizes and protects the gold core from degradation upon irradiation with energetic radiations (*i.e.* photodegradation) such as the NIR light.

However, despite the promising results presented by these nanomedicines, their translation into the clinic has been quite limited. Such has been attributed to the nanostructures' reduced accumulation in human tumors (*i.e.* latest data indicates that less than 0.7% of the administered nanoparticle dose can successfully reach the tumor site), high complexity, and difficulty to synthesize large batches. Thus, in the last years has been observed a paradigm shift and researchers started to re-explore the use of macroscale delivery systems (*e.g.* microneedles and hydrogels) to promote a controlled and localized delivery of therapeutics to tumor tissue. Particularly, the use of microneedle systems has shown promising results that support their application in anti-tumor therapy. Microneedles-based devices can be manufactured using a variety of materials (metals, polymers, and ceramics) as well as with different morphologies and organizations. These systems can be used to increase the permeation of therapeutic agents

in the target tissue or to promote the delivery of such agents when encapsulated in their structure to deeper regions of the tumor tissue in a controlled manner. In general, in cancer therapy applications, the microneedles have been explored to activate anticancer immune responses from the host (antigens, genetic material, and immune adjuvants) or to deliver agents with anticancer activity (drugs and nanoparticles). Thus, the local application of microneedle systems has the potential to increase the distribution and quantity of therapeutic agents that accumulate in the deepest regions of the tumor region while simultaneously reducing their interaction with adjacent healthy tissues. Considering the advantages of the localized delivery of anticancer therapies, the main objective of this thesis' work plan was the development of a layer-by-layer (LbL) microneedle system to mediate the simultaneous delivery of AuMSS nanorods and chemotherapeutic agents. Such was pursued by (i) exploring a production method of AuMSS nanorods with imaging and therapy properties; ii) optimizing a nano-in-micro system that can incorporate these nanoplatforms and allow to control the release rate in response to variations in pH and temperature; and iii) developing a microneedle system that can improve the therapeutics penetration in the tumor and promote the local and combined administration of AuMSS nanorods PTT agents and chemotherapeutic drugs.

In the first study presented in this thesis, the therapeutic capacity of poly-2-ethyl-2-oxazolines (PEOZ) functionalized AuMSS nanorods loaded with doxorubicin (Dox) was evaluated. Gold nanorods were produced using a method called "seed-mediated growth" and then were coated with a mesoporous silica layer using the Stöber's modified method. Thereafter, a PEOZ polymer previously modified with a silane was used to functionalize the AuMSS nanorods' surface via a condensation process. The PEOZ grafting on the AuMSS nanorods induced the neutralization of nanodevices' surface charge, from -30 mV to -15 mV. Further, there was also an improvement in the AuMSS nanorods' biocompatibility, particularly reducing the blood hemolysis to negligible values at a nanoparticle concentration of 200 $\mu g.mL^{-1}$. Additionally, the nanorods' functionalization did not impact their PTT capacity mediating a temperature increase of about 40ºC when irradiated with NIR light for 5 min. On the other side, the *in vitro* assays performed with cervical cancer cell lines revealed that the combined treatment mediated by the PEOZ coated AuMSS nanorods result in a synergistic effect, allowing the complete eradication of cervical cancer cells.

In the second study, a nano-in-micro approach was explored for allowing the intra-tumoral administration of salicylic acid (SA) and Dox-loaded AuMSS nanorods. For this purpose, poly(lactic-*co*-glycolic acid) (PLGA) microparticles containing the nanorods and Dox were produced using a water-in-oil-in-water method. The obtained results showed that the microparticles could act as a drug and nanoparticle delivery agent. Moreover, the PLGA microparticles presented a pH (activated by acidic pH) and NIR light irradiation (heat production) dependent drug release profile. Further, in *in vitro* studies, the microparticles shown to be biocompatible and internalized by cervical cancer cells. Additionally, assays

performed on 3D cell culture models (tumor spheroids) demonstrated that the microparticle-mediated combinatorial therapy caused a reduction of 50% in the spheroids' size as well as induced the death of more than 60% of the cancer cells present in the spheroids within 48 h of incubation.

In the third study presented in this thesis, the therapeutic potential of the combinatory therapy mediated by microneedle device with a layer by layer organization was evaluated. Initially, a polyvinylpyrrolidone (PVP) microneedle (4x4 tips) system was produced using the micromoulding technique. Subsequently, this base layer of the microneedle system was coated using the electrospraying technique, thereby introducing a Dox-containing chitosan (Ch) layer and an AuMSS nanorods-enriched polyvinyl alcohol (PVA) layer. The results showed that the produced microneedles had a bevel-like tip with a width of 425 μm, a height of 1420 μm and a distance between tips of 1740 μm. Additionally, the microneedles were mechanically resistant to withstand the application on the tumor tissue (agarose tumor-mimicking gels) and release their charge sequentially and in response to acidic pH and NIR light irradiation. In *in vitro* studies, the microneedles-mediated combinatorial therapy was more effective against cervical cancer cells than the individual therapies. In fact, when only the chemotherapy or PTT were administered, a reduction in the cancer cells viability to ≈55 and ≈80%, respectively, was observed, whereas the microneedles combinatorial therapy led to the eradication of the cancer cells (less than 5% of viable cells).

In summary, the data obtained from these studies demonstrate the applicability of localized delivery systems in cancer therapy. Apart from the microneedles' advantages, the therapeutic potential of the AuMSS nanorods (PTT) can be enhanced through the combinatory therapies, including chemotherapy through the co-encapsulation of drugs. Additionally, the LbL organization of the microneedle systems represents a simple approach to the development complex and hierarchically organized structures that can encapsulate various therapeutic agents as well as release them in a controlled and orderly manner to maximize the anticancer effect. In the future, preclinical studies in animal models must be performed to determine the potential of these delivery systems for being applied in cancer therapy.

Keywords

Cancer, delivery agents, gold-core mesoporous silica shell nanoparticles, microneedles, photothermal therapy, chemotherapy, combinatorial therapy.

Thesis Overview

This Doctoral thesis is organized in 6 chapters.

The first chapter presents the general and specific aims established for the work plan of this doctoral thesis.

The second chapter encloses the introductory section providing a summary of the different applications of microneedles in cancer therapy and an overview of the AuMSS nanomaterials potential for bioimaging and therapy.

The third, fourth, and fifth chapters present the results of the research works developed during this doctoral thesis:

- Research Work 1: Development of poly-2-ethyl-2-oxazoline coated gold-core silica shell nanorods for cancer chemo-photothermal therapy (Chapter 3);
- Research Work 2: Thermo- and pH-Responsive Nano-in-Micro Particles for Combinatorial Drug Delivery to Cancer Cells (Chapter 4);
- Research Work 3: Microneedles Mediated Chemotherapy and Photothermal Therapy for the Treatment of Cancer (Chapter 5).

Finally, the sixth chapter contains the concluding remarks highlighting the advances obtained during this doctoral thesis and discussing the future directions of this research area.

Index

List of Figures

Chapter 2

Chapter 3

Chapter 4

Chapter 5

List of Tables

Chapter 2

Abbreviations

1-MT	1-methyl-DL-tryptophan
AA	Ascorbic acid
ALA	5-aminolevulinic acid
ANOVA	One-way analysis of variance
APCs	Antigen-presenting cells
aPD1	Anti-programmed cell death protein 1 antibody
APTES	(3-Aminopropyl)triethoxysilane
A.R.	Aspect ratio
AuMSS	Gold-core mesoporous silica shell
AuMSS/Dox	Doxorubicin loaded AuMSS nanorods
AuMSS_TPEOZ	TPEOZ modified AuMSS
AuMSS_TPEOZ/Dox	Doxorubicin loaded TPEOZ modified AuMSS nanorods
Ch	Chitosan
CLSM	Confocal laser scanning microscopy
CT	Computed tomography
CTAB	Hexadecyltrimethylammonium bromide
Cy5.5	Cyanine5.5
DCM	Dichloromethane
DLS	Dynamic light scattering
DMEM-F12	Dulbecco's Modified Eagle Medium: nutrient mixture F-12
DMEM-HG	Dulbecco's Modified Eagle medium-high glucose
DMSO	Dimethyl sulfoxide
DOTA	Tetraazacyclododecane tetraacetic acid
Dox	Doxorubicin
Dox@MicroN	LbL polyvinylpyrrolidone microneedle system loaded with doxorubicin and AuMSS nanorods
DSPE	1,2-distearoyl-sn-glycero-3-phosphoethanolamine
E.E.	Encapsulation efficiency
FDA	Food and drugs administration
FibH	Primary normal human dermal fibroblast
FITC	Fluorescein-5-isothiocyanate
FTIR	Fourier transformed infrared spectroscopy
HA	Hyaluronic acid
HeLa	Human negroid cervix epithelioid carcinoma
ICG	Indocyanine green

IFN-γ	Interferon gamma
IL-12	Interleukin 12
K^-	Negative control
K^+	Positive control
LbL	Layer-by-layer
MCF-7	Michigan cancer foundation-7
micro/AuMSS/Dox	PLGA microparticles loaded with Dox enriched AuMSS nanorods
MicroN	LbL polyvinylpyrrolidone microneedle system loaded with AuMSS nanorods
mPEG-SH	Thiol-terminated methoxy polyethylene glycol
MRI	Magnetic resonance imaging
NIMPS	PLGA microparticles loaded with salicylic acid and Dox enriched AuMSS nanorods
NIR	Near-infrared
OVA	Ovalbumin
PAI	Photoacoustic imaging
PBS	Phosphate-buffered saline
PDMS	Polydimethylsiloxane
pDNA	Plasmide deoxyribonucleic acid
PDT	Photodynamic therapy
PEG	Poly(ethylene glycol)
PEOZ	Poly-2-ethyl-2-oxazoline
PLGA	Poly (lactic-*co*-glycolic acid)
PNIPAM	Poly (Nisopropylacrylamide)
PPIX	Protoporphyrin IX
PTT	Photothermal therapy
PVA	Polyvinyl alcohol
PVP	Polyvinylpyrrolidone
PVP_Ch/Dox_PVA	LbL polyvinylpyrrolidone microneedle system loaded with doxorubicin
PVP_Ch_PVA	LbL polyvinylpyrrolidone microneedle system
R848	Resiquimod
RBCs	Red blood cells
RGD	Arginine-Glycine-Aspartic acid
SA	Salicylic acid
SEM	Scanning electron microscopy
SERS	Surface enhanced raman spectroscopy
siRNA	Small interfering ribonucleic acid
STAT3	Signal transducers and activators of transcription protein 3
TEM	Transmission electron microscopy

TEOS	Tetraethylorthosilicate
TESPIC	3-(triethoxysilyl)propyl isocyanate
TGA	Thermogravimetric analysis
THF	Tetrahydrofuran
TLR 7/8	Human toll-like receptor 7 and 8
TNF-α	Tumor necrosis factor alpha
TPEOZ	Silane derivative of PEOZ
TPGS	D-α-tocopherol polyethylene glycol succinate
UV	Ultraviolet
W/O/W	Water-in-oil-in-water
WGA-Alexa Fluor® 594	Wheat germ agglutinin conjugate Alexa 594®
XRD	X-ray diffraction

Chapter 1

Global Aims

Global Aims

AuMSS nanoparticles' intrinsic characteristics enable their application as cancer theragnostic agents. However, the systemic administration of nanomedicines leads to unfavorable biodistribution profiles and therapeutic efficiencies that are too complex to modulate, thereby hindering the successful translation of these therapies into the clinic. Therefore, the main objective of this doctoral thesis was to develop a LbL microneedle system for the local administration of AuMSS nanoparticles and chemotherapeutics, in order to improve their accumulation in the tumor while simultaneously bypassing all the obstacles associated with the systemic circulation.

The specific aims of this thesis were:

- Produce a multifunctional nanomedicine with imaging and therapeutic capacities;
- Design a LbL polymeric microneedle system for the combinatorial cancer therapy;
- Evaluate the combinatorial chemo-PTT on cervical cancer cell models.

Chapter 2

Introduction (Part A)

Microneedle-based delivery devices for cancer therapy

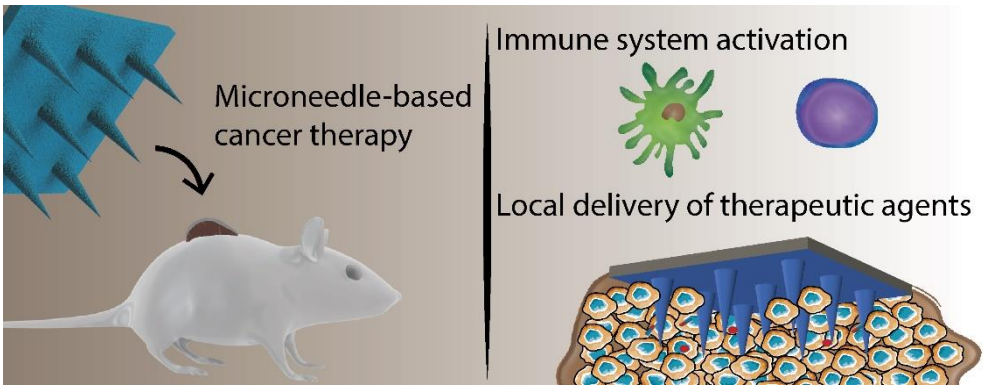

This chapter part is based on the publication:

Moreira, A.F., Rodrigues, C. F., Jacinto, T. A., Miguel. S.P., Costa, E. C., & Correia, I. J. (2019). Microneedle-based delivery devices for cancer therapy: a review. Pharmacological Research, *in press*, DOI: 10.1016/j.phrs.2019.104438.

2.1. Introduction

Despite all the efforts, cancer remains as one of the leading health problems affecting the world population. In fact, recent data clearly show that the cancer incidence has been increasing in the last decades [1, 2]. On the other side, both the conventional (*e.g.* chemotherapy and radiotherapy) and novel (*e.g.* nanomedicines) anticancer therapeutics present sub-optimal efficacies [3-5]. Further, the clinical translation of highly promising nanoparticle-based anticancer therapies has been severely hindered by their low capacity to accumulate within the tumor tissue (*i.e.* less than 0.7% of the administered dose reach the tumor site) [6, 7]. Moreover, the nanomedicines' high complexity also difficult the synthesis procedures scale-up and the reproducibility of the therapeutics outcome [5]. Therefore, in the recent years, researchers started to re-explore macroscale delivery devices (*e.g.* microneedle systems and hydrogels) that can mediate a local and controlled delivery of the therapeutic agents at the tumor region [8-10].

Particularly, microneedle devices have been showing promising results that support its application as anti-tumoral therapies. The concept of microneedle-based drug delivery systems was firstly described at more than three decades ago and their practical clinical application started to be highly pursued within the past 15 years [11]. Since then, microneedles have been fabricated using a myriad of materials including metals, polymers, glass, and ceramics as well as in a wide variety of shapes and arrangements, in order to meet the desired clinical requirements [12-14]. Further, during the last decade, extensive preclinical evaluation studies have been performed by the scientific community for validating the microneedles' application as drug delivery systems in the biomedical field. To date, microneedles have been used in the pre-clinical and clinical investigation to i) enhance the passive transdermal delivery, ii) evaluate the vaccines' antigenicity, iii) evaluate altered protein pharmacokinetics and pharmacodynamics, iv) determine pain and other perceptions associated with microneedle delivery and lately v) transport anticancer therapeutics [15-20].

In cancer therapy, the application of microneedle devices has been explored to trigger anticancer immunologic responses (*e.g.* antigens, immune adjuvants, genetic material) or to deliver anticancer compounds (*e.g.* drugs and nanoparticles) [21-25]. In that way, the local application of microneedle-based systems can increase the distribution and the amount of drug that reaches the deeper regions of the tumors, while minimizes the therapeutics leakage to adjacent tissues and the side effects [18, 26, 27]. Further, the microneedles also facilitate the combination of different drugs in one single therapy as well as allows their temporally controlled release, which can be used in the drug development phase for screening the best therapeutic combinations and in the clinic to enhance the anti-tumoral effect [28-30]. Therefore, this review provides an overview of the different microneedle formulations described in the literature for cancer therapy, emphasizing those produced with polymers. The

microneedles general properties, type of therapeutic approaches, and their main advantages are also highlighted in the following sections.

2.2. General properties of microneedles

Microneedle devices are composed of micron-size needles that can be organized in single structures or arranged in small arrays to mediate the localized delivery of therapeutic molecules [31, 32]. These micro-projections generally present dimensions around 50 to 250 μm in wide and lengths that can range from few micrometers to those as long as 1500 μm [32, 33]. In general, the microneedles application aims to create a transport pathway for the delivery of therapeutic molecules, bypassing the external barriers that limit the therapeutics penetration in the target tissue. Further, the microneedles devices are compatible with the delivery of both small and macromolecular therapeutics such as small drugs (*e.g.* Dox), proteins (*e.g.* ovalbumin (OVA)), genetic materials (*e.g.* pDNA and siRNA), or even nanomedicines [33-35]. Additionally, the microneedles are highly versatile and are regarded as less painful, damaging, and safer to use, when compared to conventional needles [13]. Moreover, the microneedles can be produced using several different materials (*e.g.* stainless steel, titanium, glass, and polymers) and fabrication methods [36-39]. Such results in a wide variety of microneedle designs that in general are categorized as solid microneedles, drug-coated microneedles, dissolving microneedles, and hollow microneedles [13, 31, 40]. As shown in Figure 2.1, these microneedle designs enable the delivery of therapeutics by different mechanisms, which can be explored for the temporally control of the therapeutics action.

Solid microneedles are usually applied for tissue pretreatment in order to increase the therapeutic agents' delivery to the target tissue [41, 42]. In this approach, the microneedles insertion and subsequent removal originates micron-scale pores in the tissue, allowing the posterior application of a drug formulation, in the form of a drug solution or hydrogels, that will diffuse through the pores to deeper regions of the tissue [41, 43]. On the other side, the microneedles can present a layered organization where the base layer confers mechanical support for insertion in the target tissue and the remaining layers contain the therapeutic molecules [44, 45]. In this way, after the microneedles' application, the dissolution of the different microneedle layers will allow the diffusion of the therapeutic molecules to the tissue [46, 47]. Alternatively, the microneedles can present the therapeutic agent homogeneously dispersed in the microneedles' polymeric matrix [48]. Therefore, the release of the encapsulated payload will occur in a process mediated by the microneedles' degradation (*e.g.* polymer enzymatic breakdown, hydrolysis, or dissolution) [49-51]. Further, microneedles can be engineered to contain a drug deposit and hollow tips with empty channels that allow the passage of the drug solution to the target tissue [13, 52]. In this way, the selection and optimization of the microneedles design and materials allow the controlled and localized delivery of therapeutic molecules directly to the target tissue and the ability to easily explore

different drug formulations for achieving an enhanced therapeutic effect. In the following sections, the application of polymer-based microneedles aimed for treating cancer will be described, highlighting the microneedle device production method, therapeutic approach, and efficacy.

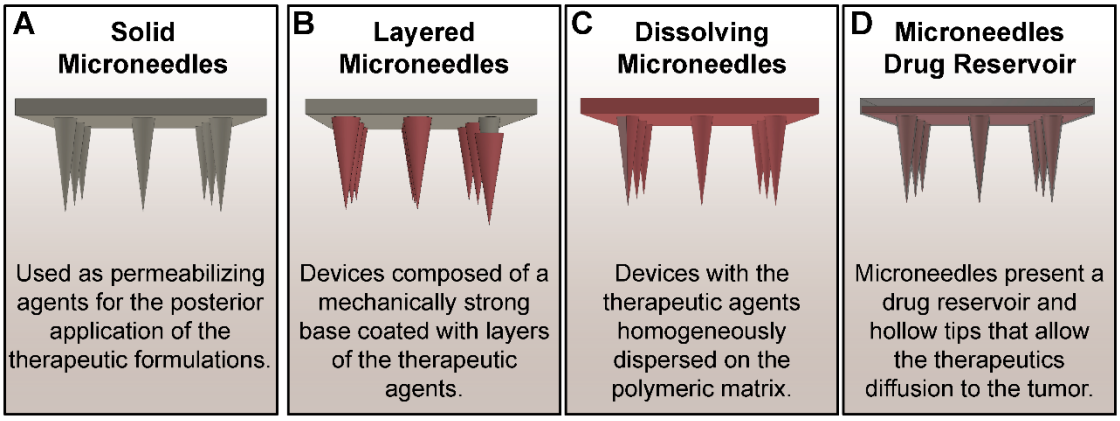

Figure 2.1 - Representation of the main microneedle designs explored for drug delivery applications, (A) Solid microneedles, (B) Layered microneedles, (C) Dissolving microneedles, and (D) Microneedles drug reservoir.

2.3. Microneedles anticancer vaccines

Cancer vaccination (immune and gene-based therapies) has been receiving a great attention by the scientific community in the last years, since it has been revealing promising anticancer results (Table 2.1) [53, 54]. In this field, the utilization of microneedles can be advantageous due to its capacity to overcome the skin's stratum corneum layer and deliver its payload upon contact with the interstitial fluid, usually at a depth of superior to 200 μm [55, 56]. In fact, when compared to the conventional hypodermic needles, the microneedle-based delivery systems avoid the pain and discomfort of the hypodermic needle insertion in the skin as well as the creation of hazardous wastes [31, 34]. Further, the microneedles contain the vaccine (immune or gene-based) in a dried solid form, which increases its thermostability and facilitates the application on the target area [35, 57].

2.3.1. Immune therapies

Cancer immune-based vaccinations purpose to trigger a systemic immune response by the host in order to eradicate the tumor tissue (Figure 2.2) [58]. Such approaches usually explore the vaccine delivery to the skin, the largest immunological organ of the body, which is densely populated by antigen-presenting cells (APCs), *i.e.* macrophages, Langerhans, and dendritic cells [59]. These APCs, when activated, can stimulate the T ($CD4^+$ and $CD8^+$) and B cells and consequently induce a systemic antitumoral immune response [60, 61].

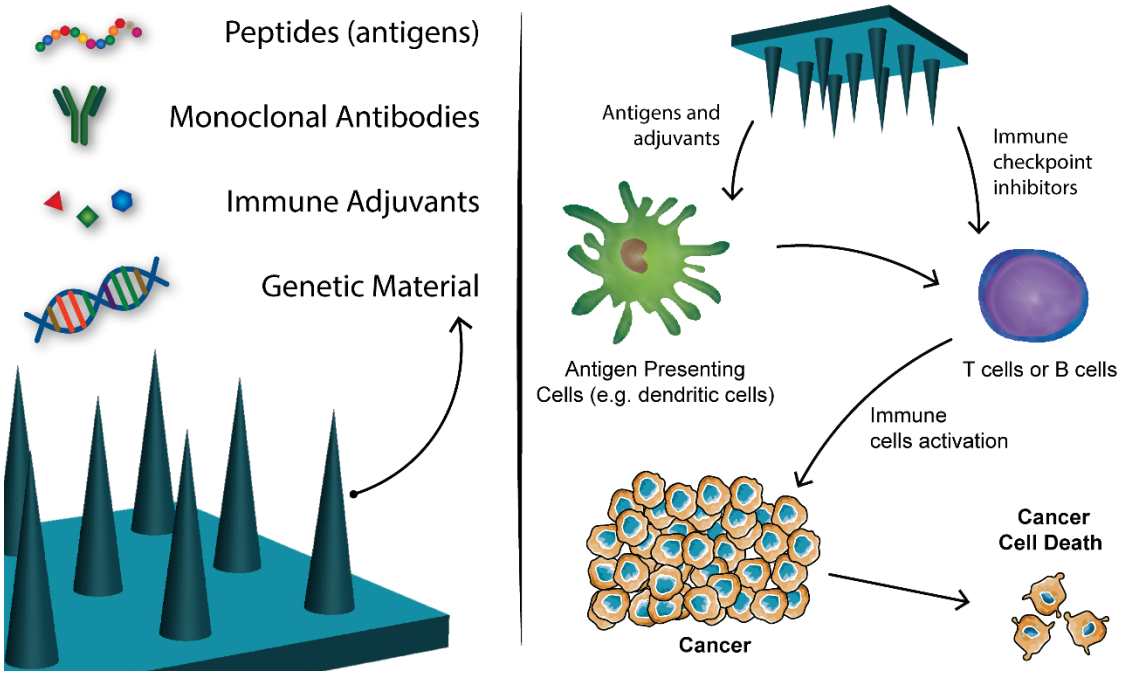

Figure 2.2 - Representation of the microneedles' application as anticancer vaccines. The loading of peptides, monoclonal antibodies, immune adjuvants, or even genetic material on the microneedle devices aims to induce the activation of the immune cells triggering an antitumoral response by the host.

For that purpose, researchers have been exploring the application of microneedle patches, containing immunostimulatory adjuvants and/or antigens, as anticancer therapeutic approaches. Zaric *et al*. described the application of methylvinylether and maleic anhydride microneedles enriched with OVA-loaded PLGA nanoparticles for triggering the antigen-specific immune response against OVA expressing B16 melanoma tumors [62]. In this approach, the authors prepared OVA loaded PLGA nanoparticles via water-in-oil double emulsion technique and then added the nanoparticles to a solution of methylvinylether and maleic anhydride that was poured on silicone templates to create the microneedles (19 by 19 array). These authors observed, in the *ex vivo* assays, that the microneedles could penetrate the murine skin, reaching the dermal layer and the local dendritic cells. Further, they also observed that the transfected dendritic cells could migrate to the proximal lymph nodes and trigger the activation of $CD8^+$ T cells and the production of cytokines such as IFN-γ. Moreover, this immune system activation, mediated by the nanoparticles release from the microneedles, prevented the development of OVA expressing B16 melanoma tumors for 13 days. In a similar way, Kim and colleagues developed a microneedle patch composed of Pluronic F127 and polyethylene glycol for the simultaneous delivery of resiquimod (R848) and tumor antigens [63]. The R848 is a ligand of the human toll-like receptor 7 and 8 (TLR 7/8) expressed by immune cells, like macrophages, dendritic and B cells. The R848 interaction with TLR 7/8 can trigger the production of IL-12, IFN-γ, and TNF-α and therefore stimulate the antigen-specific humoral and Th1 immune responses [64, 65]. Further, this device also mediated the simultaneous delivery of OVA to direct the immune response towards E.G7-OVA (lymphoma cells expressing OVA) tumor-xenografts. The microneedle array with 49 pyramid-shaped needles was prepared by

depositing a mixture of Pluronic F127/R848 and poly(ethylene glycol) (PEG)/OVA and drying it at room temperature under vacuum in a polydimethylsiloxane (PDMS) mold. Then, it was also noticed that the microneedles could penetrate the superficial layers of the mouse skin and allow the diffusion of its payload to the adjacent cells. Moreover, the authors reported that upon dissolution, the microneedles form nanomicelles that could mediate the delivery of R848 and OVA to RAW264.7 cells and, consequently, stimulate the production of cytokines as well as induce the macrophages maturation. On the other side, the *in vivo* assays showed that the microneedles loaded with R848 and OVA could not only activate the skin APCs but also migrate to lymph nodes. In fact, when comparing to the mice treated using hypodermic syringes, the authors reported that the microneedles could mediate the generation of higher levels of antigen-specific antibodies (37x increase for hypodermic needles and 46 x increase for microneedles) and cytotoxic T cells. This improvement in the immune response hindered the E.G7-OVA tumor growth (tumor weight: ≈2.5 g in control group and ≈0.4 g in the microneedles treated group) (Figure 2.3). Additionally, extended necrotic areas were noticed in the tumor tissues treated with the microneedles.

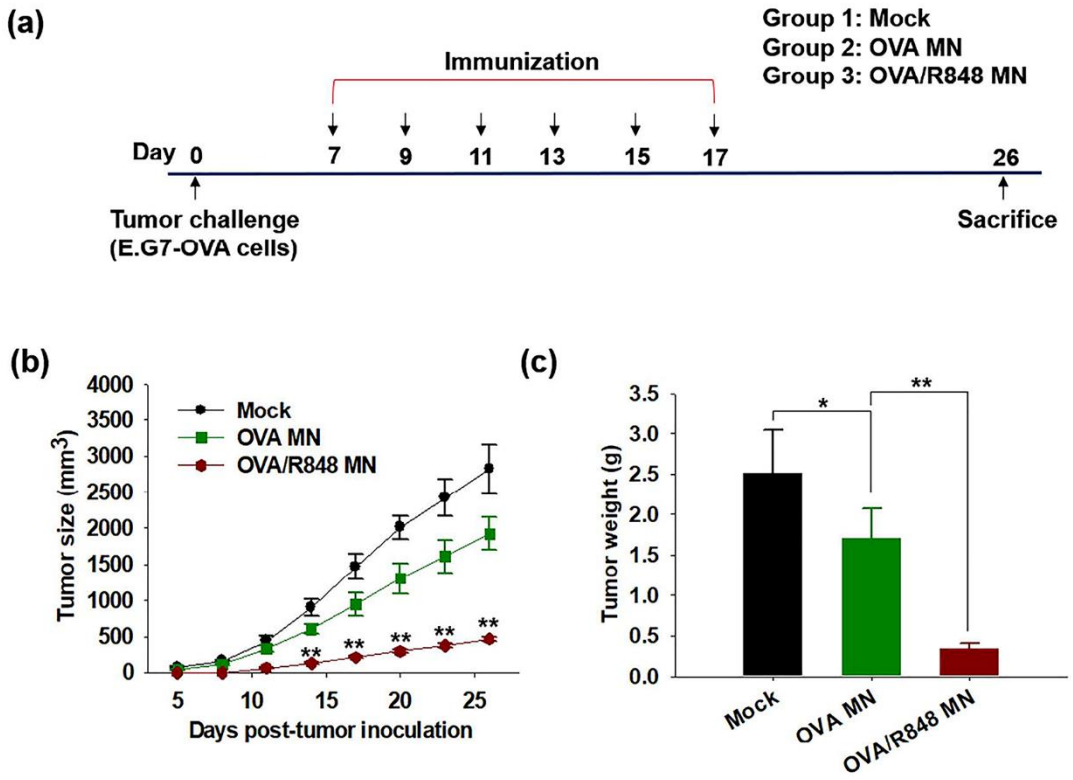

Figure 2.3 - Evaluation of the OVA and R848 loaded microneedles antitumoral efficacy on E.G7-OVA tumor bearing mice. (A) Timescale of the cancer cells inoculation and therapeutic vaccinations. (B) Analysis of the tumor size progression for 28 days. (C) Tumor weight measurements at day 28. Reprinted with permission from ACS Nano, Vol. 12 (10), Kim, *et al.*, Enhanced Cancer Vaccination by In Situ Nanomicelle-Generating Dissolving Microneedles, 9702-9713. Copyright (2018) American Chemical Society.

On the other side, microneedles can be engineered to deliver antibody based immune therapies aimed to revert/by-pass the tumor cells' immune suppressive signals. Ye and coworkers produced a Hyaluronic Acid (HA)-based microneedle array for mediating the delivery of anti-PD1 antibody (aPD1) and 1-methyl-DL-tryptophan (1-MT) to B16F10 melanoma tumors [66]. The aPD1 targets the PD-1 receptors expressed by T cells and therefore can avoid the cancer cells inhibitory signaling that prevent the T cells activation [67]. The 1-MT is an inhibitor of the immunosuppressive enzyme indoleamine 2,3-dioxygenase favoring the occurrence of an enhanced immune response [68]. The conical shaped microneedle arrays (15 by 15) were produced using silicone molds. For that purpose, the authors chemically grafted the 1-MT to the HA chains, which subsequently were used to create micelles loaded with the aPD1. Then, the micelles were deposited on the silicone molds, dried, coated with additional 1-MT modified HA, and dried at room temperature under vacuum to obtain the microneedles. The authors observed that the 1-MT and aPD1 release occurred in response to the HAase-triggered degradation of the microneedles and micelles [66]. Further, the microneedles presented a fracture force of 0.41 N, which allowed them to penetrate the mice's dorsum skin and, consequently, deliver its payload at a depth of 200 μm. Additionally, the microneedles administration on mice bearing B16F10 melanoma cells increased the retention of 1-MT and aPD1 at the tumor tissue. In fact, the accumulation of 1-MT on melanoma was 3-fold higher at day 1 and 5-fold higher at day 2 and 3 on the group treated with the microneedles than in that treated with free 1-MT. Moreover, the simultaneous delivery of aPD1 and 1-MT by the microneedles impaired the tumor progression (tumor area inferior to 50 mm^2, whereas in the control group the area was superior to 300 mm^2) and increased the mice survival rate. Alternatively, Wang and colleagues explored the development of HA microneedles for the delivery of aPD1 and glucose oxidase loaded dextran nanoparticles for the treatment of skin cancer [69]. In this approach, the aPD1 and glucose oxidase loaded dextran nanoparticles were deposited on silicone molds that were subsequently filled with acrylate modified HA and N,N'-methylenebisacrylamine allowing the microneedles formation (15 by 15 array) upon exposition to UV light. The glucose oxidase can mediate the generation of gluconic acid from the glucose present in the medium and consequently promote the nanoparticles dissociation and the aPD1 release [70]. The authors showed that the produced microneedles presented a failure force of 0.38 N/needle, which allowed its penetration into the mouse skin up to 200 μm in depth. Additionally, *in vivo* assays where B16F10 mouse model of melanoma was used revealed that the administration of aPD1 could efficiently stimulate the $CD8^+$ T cells infiltration into the tumor tissue (% of $CD8^+$ T cells increased from 30% to 43% when comparing the groups treated with free aPD1 and microneedles). Such improvement resulted in a significant tumor inhibition/regression as well as an increase in the mice survival rate, 40% of mice survived for 40 days after microneedles treatment, whereas the mice treated with free aPD1 only survived for 30 days.

2.3.2. Gene therapies

Apart from the application of microneedles for mediating the immune system activation through the delivery of antigens, adjuvants, or even antibodies, these macroscale delivery devices have been also explored for the administration of antitumoral gene therapies. Ali and colleagues developed a PVP microneedle patch loaded with E6/E7 pDNA RALA nanoparticles for the treatment of cervical cancer [71]. The microneedles were produced using a micromoulding process, by depositing a PVP solution containing E6/E7 pDNA/RALA nanoparticles on a negative mold. Additionally, the authors observed that upon manual application 90% of needle length could be inserted on the porcine skin and that after 15 min the microneedles tips were already completely dissolved within the skin layers. Further, the authors demonstrated that after microneedles administration the concentration of antibodies was 2 times higher than that of the control and the T cells were more responsive to HPV-16 oncogenic antigen expressing cells (TC-1) (IFN-γ levels in control ≈250 $pg.mL^{-1}$ and ≈530 $pg.mL^{-1}$ for microneedle immunized group). This enhanced immune response prevented the establishment of cervical tumors on 4 of the 9 mice treated with microneedles. Moreover, the authors also reported that the microneedles administration on mice bearing cervical tumors induced the regression of the tumor area, 246 mm^2 microneedle treated mice and 503.13 mm^2 for mice vaccinated with RALA-E6/E7 nanoparticles. Alternatively, Pan and coworkers utilized dextran/HA/PVP microneedle patches for the delivery of polyethyleneimine/STAT3 siRNA complexes to skin melanoma tumors (Figure 2.4) [72]. STAT3 is a protein overexpressed in several tumors (*e.g.* melanoma, breast, and prostate) that can prompt the cancer cells proliferation, angiogenesis, survival, and immune evasion [73]. These microneedles were produced by blending polyethyleneimine/STAT3 siRNA complexes with a dextran/HA/PVP solution, followed by the casting in PDMS molds of pyramidal-shaped needles (12 by 12 arrays). The authors reported that almost 100% of microneedles tips penetrate the rat skin when forces superior to 20 N are applied, microneedles have failure force 86 N, which allows the delivery of the polyethyleneimine/STAT3 siRNA complexes at a depth of 330 μm [73].

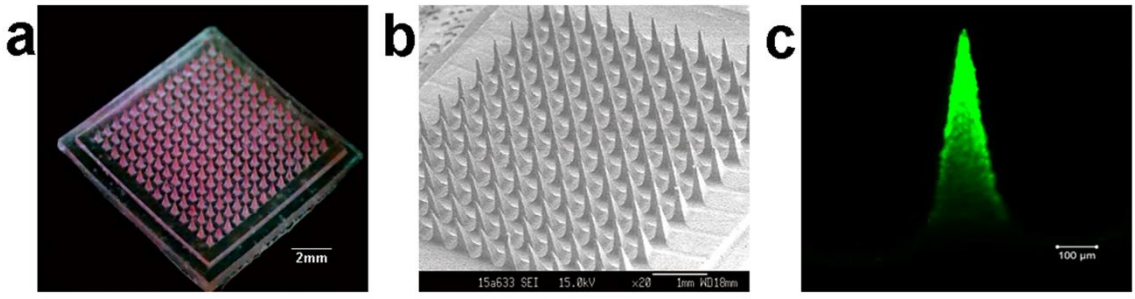

Figure 2.4 - Morphological characterization of the microneedle devices loaded with polyethyleneimine/STAT3 siRNA complexes. (A) Macroscopic photographs of the microneedles. (B) Scanning electron microscope images of the microneedle patches. (C) Analysis of the complexes loading on the microneedles through confocal laser scanning microscope.

Further, the authors also observed that the topical administration of STAT3 siRNA mediated by the microneedles could reduce the STAT3 mRNA expression in 30% as well as induce the necrosis of 40% of the tumor cells. Such effect inhibited the growth of the melanoma tumor, registering a tumor weight 5 times lower than the control.

Table 2.1 - Overview of the microneedles devices as cancer vaccines for cancer therapy.

Microneedle Material	Production Method	Therapeutic agent	Needles Size	Model	Type of study	Results	ref.
Dextran, PVP, and HA	Micromoulding 12x12 arrays	STAT3 siRNA/ polyethylenimine complexes	Height: 650 µm; Base width: 300 µm	B16F10 tumor-bearing C57Bl/6 mice	*In vivo*	Decreased the tumor growth, tumor weight 5 times inferior to control	[68]
PVA	Micromoulding 19x19 arrays	RALA/E6 and E7 pDNA	Height: 600 µm; Base width: 300 µm;	TC-1 tumor-bearing C57 BL/6 mice	*In vivo*	Microneedles administration increased the antigen specific IgG and decreased the tumor growth	[18]
Pluronic F127/PEG	Micromoulding 7x7 arrays	OVA and R848	Height: 350 µm	HCT116 tumor-bearing C57BL/6 mice	*In vivo*	Decreased the tumor growth and induced extended areas of necrotic cells	[59]
PVP	Micromoulding 19x19 arrays	RALA-E6/E7 DNA nanoparticle	Height: 600 µm; Base width:300 µm	TC-1 tumor-bearing C57BL/6 mice	*In vivo*	Increased mice survival and decreases the tumor growth	[67]
HA	Micromoulding 9x9 arrays	aPD1 and glucose oxidase	Height: 600 µm; Base width: 300 µm	B16F10 tumor-bearing C57BL/6 mice	*In vivo*	Increased mice survival and impaired the tumor growth	[65]
HA	Micromoulding 15x15 arrays	1-MT and aPD1	Height: 800 µm; Base width: 300 µm	B16F10 tumor-bearing C57BL/6 mice	*In vivo*	Increased the infiltration of effector T cells to the tumor tissue. Impaired the tumor growth,	[51]
Methylvinylether and maleic anhydride	Micromoulding 19x19 arrays	OVA loaded PLGA nanoparticle	Height: 600 µm;	B16.OVA melanoma-bearing mice	*In vivo*	Triggered the activation of effector T cells and prevented the establishment of OVA expressing B16 melanoma tumors.	[58]
PLGA, poly(ß-amino ester), poly(4-styrene sulfonate) and protamine sulfate	Micromoulding 19x19 arrays	pDNA and PLGA nanoparticle	Height: 650 µm; Base width: 250 µm	C57BL/6 mice	Proof-of-concept	Long-term release of pDNA	[70]
AdminPen	Array with 43 microneedles	Particle loaded with whole cell lysate of ID8 ovarian cancer cells	Height: 1100 nm	ID8 tumor bearing C57BL/6 mice	*In vivo*	Decreased tumor growth and increased amount of effector T cells	[71]

2.4. Local administration of anticancer therapeutic agents

In recent years, the microneedles arisen as an alternative to the chemotherapeutics systemic administration (Figure 2.5 and Table 2.2). This local administration of the therapeutic agents decreases the non-specific interactions with healthy tissues and consequently the side-effects [4]. Further, when comparing to the intra-tumoral administration of liquid drug formulations, the microneedles provide a better spatial and temporal control over the therapeutics release to the tumor tissue, which can limit the drug leakage to the adjacent healthy tissues [76].

Zhao and colleagues developed an HA based microneedle patch loaded with 5-aminolevulinic acid (ALA) for the photodynamic therapy (PDT) of subcutaneous tumors [77]. The ALA can be converted into protoporphyrin IX (PPIX) in cell mitochondria, acting as a photosensitizer by mediating the production of highly reactive oxygen species upon light irradiation. The microneedles were produced by depositing a HA solution containing ALA on PDMS molds of pyramidal-shaped tips (5 by 5 arrays). The authors observed that the microneedles could penetrate the rat skin up to 218±58 μm of depth and the drug content could reach the 600 μm in 2 min. Further, the authors also demonstrated that the PDT effect mediated by the microneedles could induce a decrease on the tumor volume.

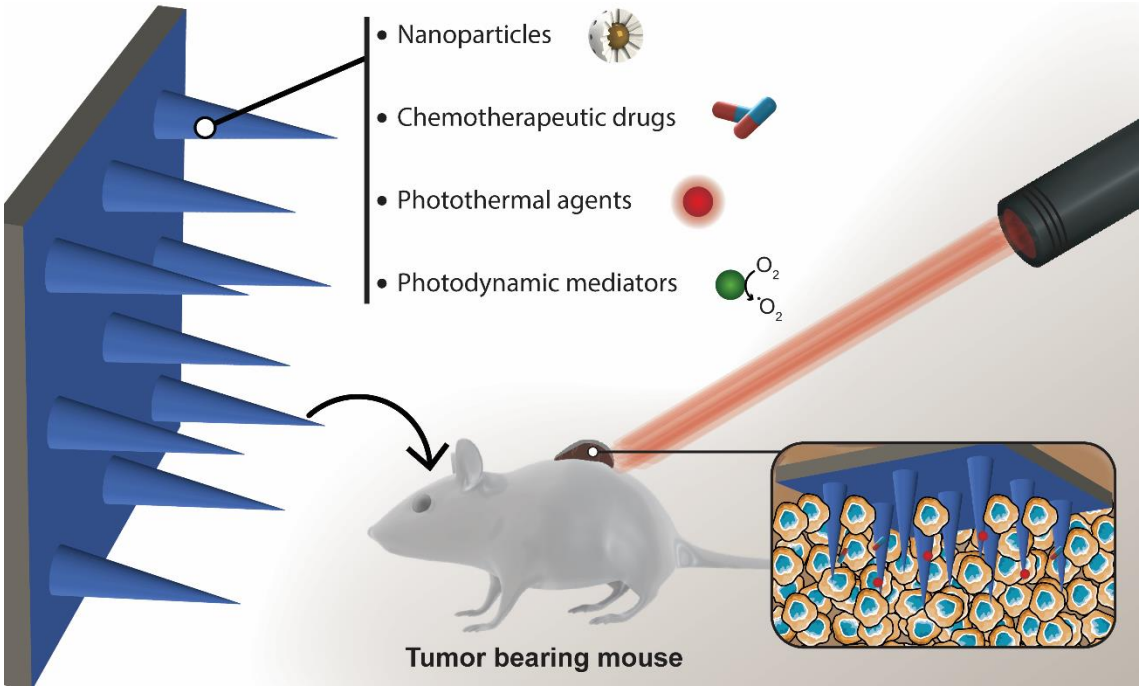

Figure 2.5 - Representation of the microneedles' application as delivery devices for cancer therapy. The microneedles allow the delivery of conventional anticancer drugs, PTT and PDT agents as well as nanomedicines.

In fact, mice treated with microneedles and subjected to the light irradiation (635 nm, 450 mW, for 10 min) presented a reduction of the initial volume of the tumor to 44% in just 7 days, whereas the group treated with free ALA and light the tumor volume increased in 455% (Figure 2.6). Such data demonstrated that the microneedles-mediated local administration can improve the drug bioavailability, avoiding the non-specific interactions and degradation during blood circulation.

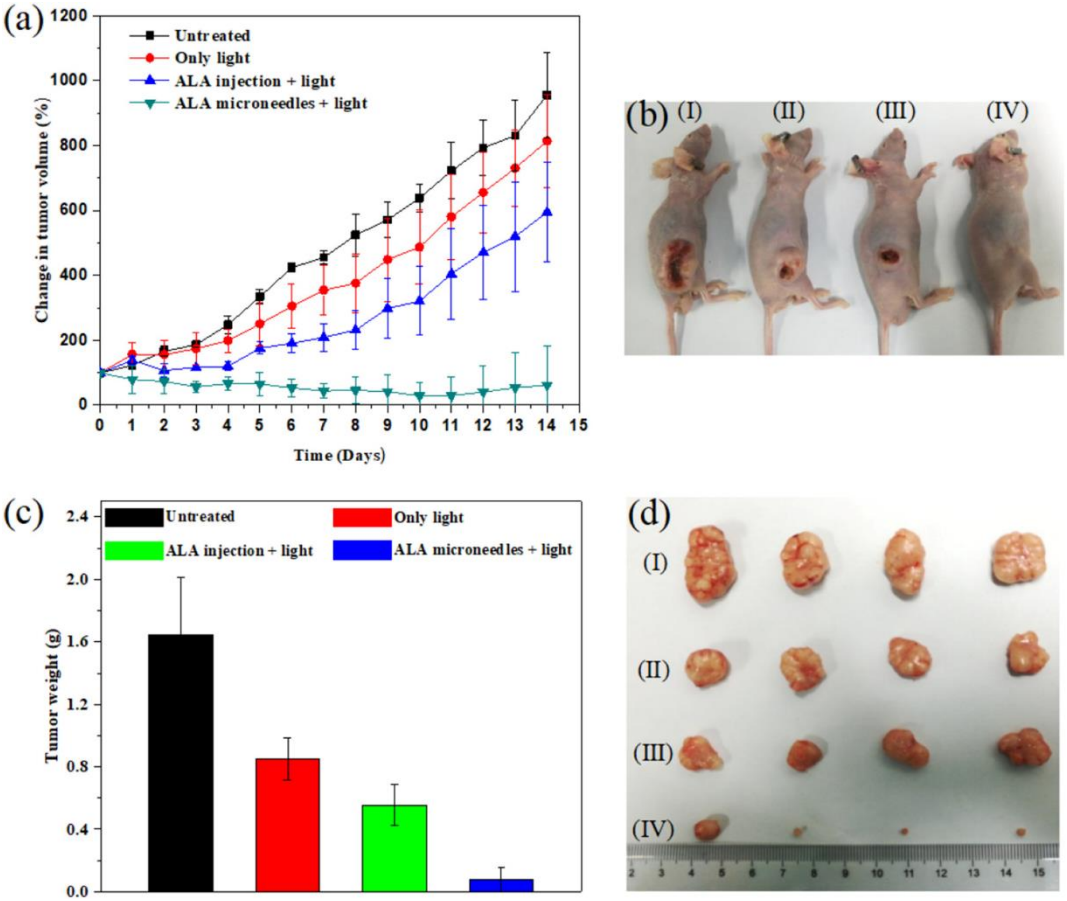

Figure 2.6 - Evaluation of the ALA loaded HA-based microneedle patches antitumoral efficacy. (A) Analysis of the tumor growth and (B) photographs of the tumor bearing mice. (C) Analysis of the tumor weight after 14 days and (D) photographs of the excised tumors. Reprinted from Journal of Controlled Release, vol. 286, Zhao, Xiao, *et al.*, Tip-loaded fast-dissolving microneedle patches for PDT of subcutaneous tumor, 201-209. Copyright (2018), with permission from Elsevier.

Microneedles can also mediate the simultaneous delivery of different therapeutic agents such as drug-drug and drug-nanoparticle combinations for improving the efficacy of anticancer treatments. Bhatnagar and coworkers developed a PVP/PVA microneedle patch for the combinatorial delivery of Dox and docetaxel to breast cancer tumors [29]. Dox and docetaxel are two chemotherapeutics commonly used to treat this type of cancer. Dox is a non-selective class I anthracycline that can induce the cell death by intercalating with the DNA and suppressing the macromolecules biosynthesis [78]. The docetaxel interferes with the normal function of microtubule growth affecting the cytoskeleton flexibility and cell mitosis [79].

In this approach, the drugs were incorporated on the microneedles tips by dissolving them on the PVP solution [79]. Then, this solution was deposited on a PDMS mold of pyramidal-shaped needles and coated with a PVP/PVA mixture to further increase the patch mechanical strength. The authors observed that this methodology allowed the production of microneedles with a compression strength superior to 5 N, which endured the insertion on the mice skin being detected the drug delivery until a depth of 140 μm. Further, the authors described that the microneedles patch was completely dissolved in 33 min, with 90% of the docetaxel being released in the first 15 min. Additionally, the *in vivo* studies performed on 4T1 breast tumors bearing mice revealed that the combinatorial delivery of Dox and docetaxel was more efficient than the single treatment approaches leading to an impaired tumor growth. Moreover, when compared to the free drug administration, the increased mice survival rate and the long-term maintenance of the mice weight demonstrated that the microneedles-mediated chemotherapeutic administration also mitigate the drugs non-specific toxicity. In a similar approach, Pei *et al*. applied PVP microneedles for mediating the delivery of Dox and indocyanine green (ICG) to the synergistic chemo- and PTT-therapy of osteosarcoma tumors [80]. ICG is a dye that can induce cancer cells death through the production of heat and/or singlet oxygen upon irradiation with NIR light [81]. For this purpose, the authors encapsulated the ICG on mesoporous silica nanoparticles and blended them with a solution, composed of Dox and PVP, that was casted on PDMS molds of pyramidal needles (10 by 10 arrays) [81]. The microneedle patches presented a compressive strength of 0.37 N and achieved a complete penetration of skin stratum corneum when a force of 0.03 N was applied. Moreover, the authors observed *in vitro* that upon NIR light irradiation (808 nm, 0.34 $W.cm^{-2}$, 1 min), the microneedles could mediate an increase in the temperature to values superior to 50ºC. In fact, the microneedles application on subcutaneous tumors and subsequent NIR light irradiation (808 nm, 0.34 $W.cm^{-2}$, 2 min) induced an increase in the temperature of the tumor tissue up to 48ºC. Additionally, the authors also reported that the combination of the PTT effect with the Dox action provoked a decrease in the tumor volume to 50% and induced the necrosis of ≈80% of the tumor cells. Hao and colleagues also explored the combinatorial application of nanoparticles and drugs, *i.e*. gold nanorods and Dox, for the chemo- and PTT-therapy of human epidermoid cancer therapy [82]. The gold nanorods are one type of NIR responsive nanomaterials, due to the surface plasmon resonance phenomenon, that can be used for mediating a PTT effect [83]. In this strategy, the gold nanorods, Dox, and HA were blended and casted on a PDMS template of 20 by 20 microneedle patches [82]. The authors demonstrated that upon NIR light irradiation (808 nm, 1 $W.cm^{-2}$, 5 min), these patches could induce an increase in the temperature up to 65ºC. Additionally, this temperature increase could also expedite the Dox release to the adjacent tissue. In the *in vitro* assays, the authors observed that the microneedles (loaded with the drug) were able to induce a similar cytotoxic effect to that attained through free drug administration. Nevertheless, in the *in vivo* assays, the authors demonstrated that the microneedles local administration and controlled release of both gold nanorods and Dox renders a superior antitumoral efficacy. In fact, the combinatorial treatment

mediated by the microneedles resulted in the complete remission of the A431 tumors, contrasting with the slightly inhibited tumor growth on the stand-alone therapies (*i.e.* free drug, microneedles mediated chemotherapy, or microneedles mediated PTT effect). Similarly, Dong and coworkers developed a gold-nanocage and Dox loaded HA microneedles for the transdermal PTT and chemo-therapy of skin tumors [84]. For this purpose, PDMS molds were filled with a solution containing Dox and gold nanocages. Then, the samples were dried, and a solution of HA was added to the previous PDMS molds, originating microneedles patches (10 by 10 arrays) with pyramidal needles enriched with Dox and gold nanocages. The authors observed that the inclusion of the gold nanocages improved the microneedles mechanical strength, the young modulus increased from 68.9 to 224.9 MPa, which is crucial for facilitating the microneedles penetration of the skin's stratum corneum and accomplish a 220 μm penetration depth. Further, these authors also demonstrated that the local administration of the microneedles on subcutaneous melanoma tumors could induce a temperature increase up to 55ºC when irradiated with a NIR light (808 nm, 1 $W.cm^{-2}$, 1 min). This localized delivery of Dox and gold nanocages to melanoma tumors peaked at 24 h and the authors observed that the therapeutics still remained in the tumor tissue after 72 h. Moreover, despite the authors did not report any significant difference on the antitumoral effect mediated by the microneedles and the intra-tumoral administration of free Dox and gold nanocages (both treated tumors presented a size 83% smaller that the non-treated group), the microneedles successfully reduced the therapeutics non-specific toxicity, being observed a reduction on the mice weight in the free therapeutics treated group (Figure 2.7).

Alternatively, some authors also have been exploring the application of microneedle devices for the high-throughput screening of the tumors' drug sensitivity. These approaches aim to simultaneously test a range of therapeutics on a *in vivo* tumor as well as evaluate the patient individual responsiveness to a specific therapeutic agent or therapeutic combinations. For this purpose, Jonas and colleagues developed a microscale needle containing several drug reservoirs, each with a unique single agent or drug combination, that can be implanted inside the tumor for the short-term evaluation of the tumor drug sensitivity (Figure 2.8) [30]. This cylindrical device with 820 μm of diameter and 4 mm in length, presented up to 16 drug reservoirs in its surface and could be implanted into the tumors through a biopsy needle. Then, the drugs can diffuse into different tumor regions of 200-300 μm, the drug diffusion can be controlled (*i.e.* delayed or favored) by modulating the reservoir size, incorporation of polymer matrixes, and utilization of expansive hydrogels. The authors observed that this device could restrict the drug release from each reservoir to individual tumor regions and the therapeutics combination could be achieved by encapsulating the different compounds into the same reservoir. Further, the authors also reported that this control over the therapeutics release could match the intra-tumoral drug concentration achieved by the systemic administration of the therapeutics, i.e. tumor zones with drug levels of 8 to 13 $mg.kg^{-1}$ or 3 to 7 $mg.kg^{-1}$, which strengthens the translation of the results obtained with this device to the clinic.

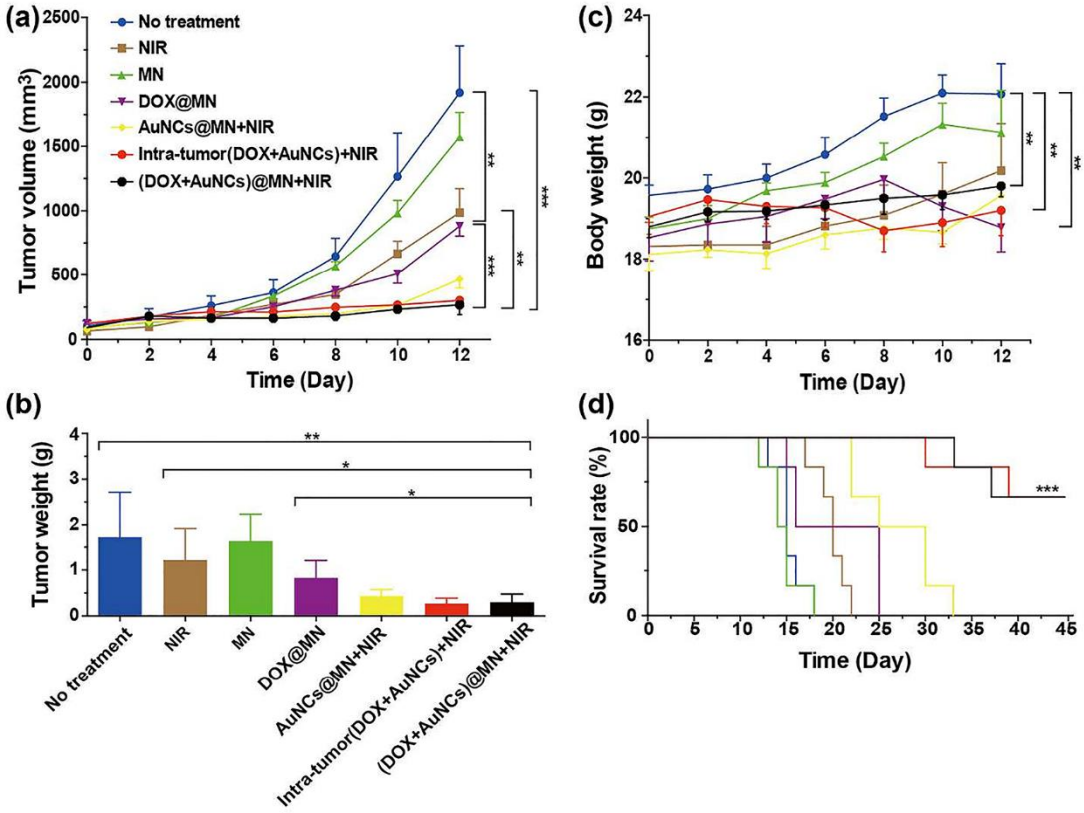

Figure 2.7 - Evaluation of the *in vivo* antitumoral capacity of gold nanocages and Dox loaded HA microneedles. (A) Analysis of the tumor volume progression during the 12 days. (B) Tumor weight measurements at day 12. (C) Body weight analysis and (D) Survival rates of the C57 mice. Reprinted with permission from ACS Applied Materials and Interfaces, Vol. 10 (11), Dong, *et al.*, Au Nanocage-Strengthened Dissolving Microneedles for Chemo-Photothermal Combined Therapy of Superficial Skin Tumors, 9247-9256. Copyright (2018) American Chemical Society.

Furthermore, the authors evaluated the device capacity to act as a predictor of the systemic efficacy in three human cancer mouse models (A375 melanoma, BT474 breast, and PC-3 prostate) demonstrating that the Dox could induce the highest apoptotic index (55%) on A375 cells followed by BT474 and PC-3 cells (18% and 8%, respectively). These data were coherent with those obtained from the mice treated through intravenous administration, apoptotic index of 34.9% and 8.7% for A375 and PC-3 cells respectively. In this way, the authors also demonstrated that this microneedle device can be used to determine the most effective drug formulation towards a specific tumor. For example, the authors reported that for the microneedle device treated groups the paclitaxel presented the highest apoptotic index (54%) against triple-negative breast cancer tumors, followed by Dox (36%), cisplatin (25%), gemcitabine (12%), and lapatinib (4%).

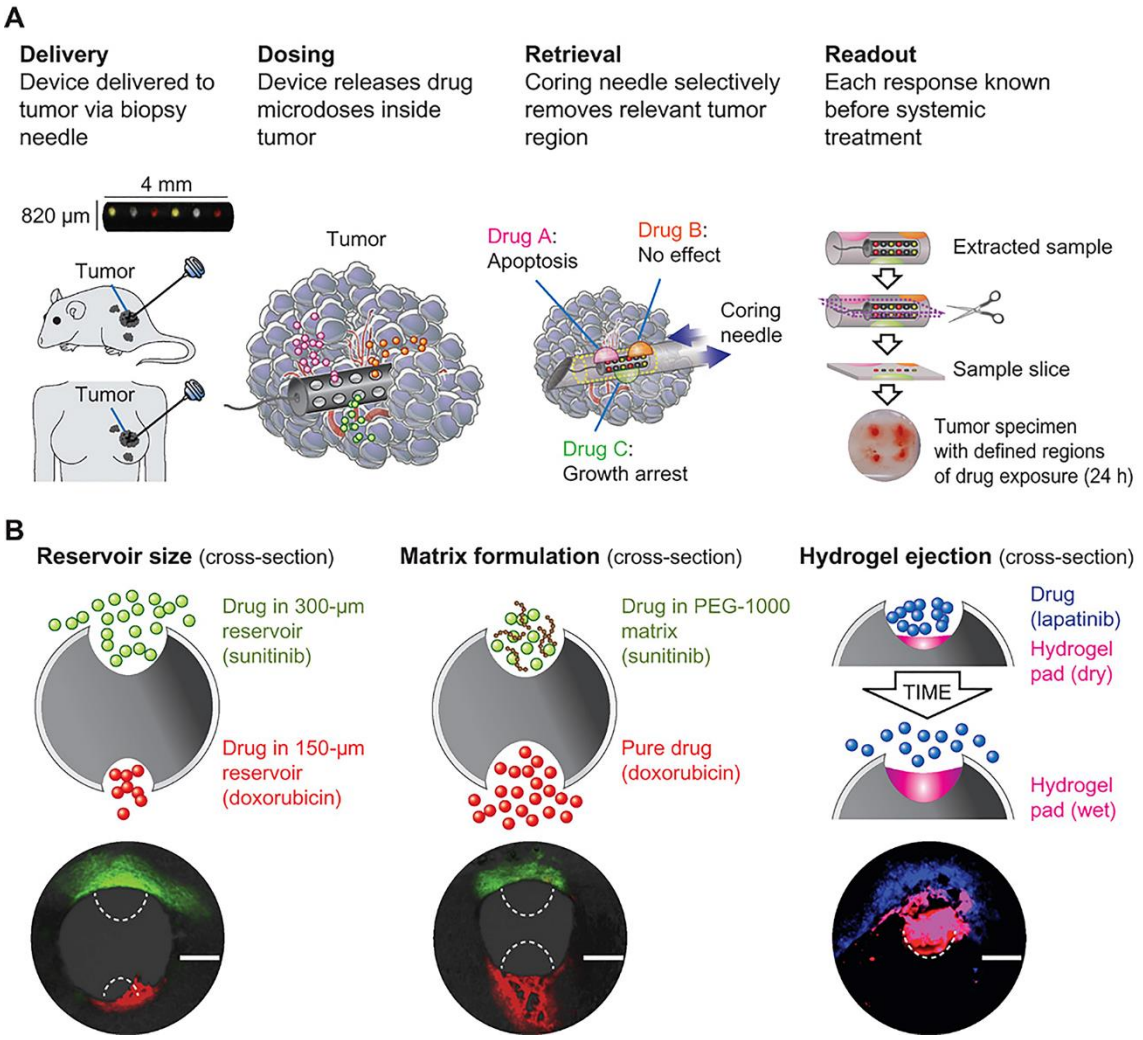

Figure 2.8 - Representation of the microneedle device application as drug screening device. The device can be implanted directly on the tumor tissue, allowing the drugs diffusion from the reservoirs to confined regions in the tumor. This behavior allows to evaluate the tumor-specific response to a determined drug. (B) Effect of the different reservoir characteristics on the drug release profile. The drug release kinetics can be controlled by the reservoir size, drug-polymer matrix formulation, or by the utilization of expansive hydrogels. From Science Translational Medicine, Vol. 7, Jonas, *et al.*, An implantable microdevice to perform high-throughput *in vivo* drug sensitivity testing in tumors, 284ra57. Reprinted with permission from AAAS.

Moreover, the microneedle device also allowed the authors to determine the best drug combinations, for example on BT474 tumors, the combination of Dox with sunitinib leads to an increase of the apoptotic response from ≈3% to ≈5.5%, this apoptotic response was further improved when the Dox was combined with lapatinib (13.45%). In a subsequent study, Davidson and colleagues also utilized the previous microneedle device to demonstrate that pancreatic cancer cells can use extracellular proteins (*e.g.* albumin) as a source of amino acids, which can translate to a preferential uptake of albumin based nanocarriers and improve the tumor delivery of therapeutics [81].

Table 2.2 - Overview of the microneedles' application as drug delivery devices for cancer therapy. N.A. – non applicable.

Microneedle Material	Production Method	Therapeutic agent	Needles Size	Model	Type of study	Results	ref.
PVA and PVP	Micromoulding 6x6 arrays	Dox and docetaxel	Height: 597.2±31.5 µm; Base width: 245.8±16.1 µm	4T1 tumor-bearing athymic nude mice	*In vivo*	Increased mice survival and impaired tumor growth	[24]
Sodium hyaluronate	Micromoulding 5x5 arrays	ALA	Height: 907±20 µm; Base width: 309±16 µm	KB tumor-bearing BALB/c nude mice	*In vivo*	Reduction of the tumor volume in 56%	[73]
PVA	Micromoulding 10x10 arrays	Dox	Height: 451.02±8.07 µm; Base width: 161.45±8.49 µm	N.A.	Proof-of-concept	Increased Dox delivery across the skin	[82]
PVP	Micromoulding 10x10 arrays	Dox and ICG-loaded mesoporous silica nanoparticles	Height: 600 µm; Base width: 200 µm	MG-63 tumor-bearing BALB/c nude mice	*In vivo*	Reduction of the tumor volume in 50 % and 80% of tumor cells necrosis	[76]
HA	Micromoulding 20x20 arrays	Gold nanorods and Dox	Height: 480 µm; Base width: 300 µm	A431 tumor-bearing BALB/C nude mice	*In vivo*	Complete eradication of the tumor	[78]
Cellulose	Micromoulding 9x9 arrays	Lipid-coated cispatin nanoparticles	Height: 800 µm; Base width: 400 µm;	HNSCC cell lines FaDu, CAL 27, SCC 15 and Female BALB/c nude mice	*In vivo*	Stalled tumor progression and increased skin safety	[22]
HA	Micromoulding 10x10 arrays	Gold nanocubes and Dox	Height: 450 µm; Base width: 200 µm;	B16F10 tumor-bearing C57 mice	*In vivo*	Increased mice survival and impaired tumor growth	[80]
Zein	Micromoulding 6x6 arrays	Tamoxifen and gemcitabine	Height: 965±23 µm; Base width: 363±15 µm	N.A.	Proof-of-concept	Increased skin permeability to the drugs	[20]
Stainless steel	Wet etching 57 tips	ALA	Height: 700 µm;	A-20 tumor-bearing BALB/c mice	*In vivo*	Reduction of the tumor volume in 70%	[83]
PVA, PVP and polycaprolactone	Micromoulding 9x9 arrays	Dox and LaB_6 nanomaterials	Height: 600 µm; Base width: 300 µm;	4T1 tumor-bearing SCID mice	*In vivo*	Complete eradication of the tumor and increased mice survival	[23]
Stainless steel	Wet etching 57 tips	Dox loaded PLGA nanoparticles	Height: 700 µm; Base width: 200 µm;	HeLa cancer cells	*In vitro*	Increased Dox penetration on cervical cancer tissue phantom models and enhanced cell death	[84]

Polycaprolactone	Micromoulding 15x15 arrays	Silica coated LaB_6 nanoparticles loaded with Dox	Height: 600 µm; Base width: 200 µm;	Sprague-Dawley rats	Proof-of-concept	NIR-dependent Dox release in the mice skin	[85]
Silicon	Lithography – plasma etching	ALA	Height: 270 µm; Base width: 240 µm;	BALB/c nude mice	Proof-of-concept	Increased the drug penetration in 2-fold	[86]

2.5. Future directions for microneedles research

Despite all the efforts, the systemic anticancer therapeutic approaches still present several disadvantages such as the excessive complexity to be adequately applied in the clinic and undesired interactions with healthy tissues. Therefore, the development of macroscale delivery systems that can be locally implanted on the tumor tissue and by-pass all the hurdles of the systemic delivery have been showing promising results for cancer therapy. As an emerging delivery device, the microneedles can be used to efficiently deliver both small and macromolecules, such as chemotherapeutics, proteins, and genetic material, or even nanoparticle-based anticancer therapies. Moreover, the microneedles can be fabricated using diverse materials and through different methods allowing a great diversity on the device design and therapeutics release. As highlighted in this chapter, microneedle-based devices have the potential to deliver simultaneously combinations of drugs and PDT agents, nanoparticles and drugs, genetic material and antibodies, and others. Nevertheless, despite the great potential of microneedles for improving the efficacy of the commonly applied anticancer therapies, several comprehensive studies are still necessary to fully characterize the behavior of these microscale drug delivery devices on human therapeutic applications. Moreover, the successful application of these therapies is dependent on several important parameters, such as the timing of combining these different strategies, therapeutics concentration, exposure time, and release sequence. In this field, the combination of microneedles with LbL production techniques can be a highly promising and straightforward approach to allow the production of complex and hierarchically organized structures. Further, these microneedle devices carry the potential for improving not only the efficacy of anticancer therapies but also improve the transdermal drug delivery in the context of other health disorders.

Chapter 2

Introduction (Part B)

Gold-core silica shell nanoparticles application in imaging and therapy

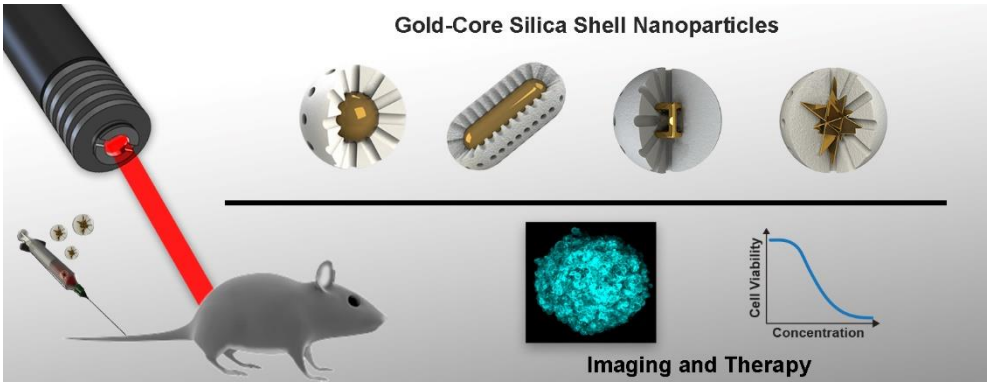

This chapter part is based on the publication:

Moreira, A.F., Rodrigues, C. F., Reis, C. A., Costa, E. C., & Correia, I. J. (2018). Gold-core silica shell nanoparticles application in imaging and therapy: A review. Microporous and Mesoporous Materials, 270, 168-179.

2.6. Gold-core mesoporous silica shell nanoparticles

Gold is one of the least reactive known metals and presents resistance against oxidation and corrosion [91]. Further, gold nanoparticles present unique optical properties, due to the surface plasmon resonance phenomenon (*i.e.* the light scattering or absorption in response to the free electrons synchronized oscillation when the particle is exposed to light at their resonance wavelength). The production of gold nanoparticles with different shapes (*e.g.* rods, cubes, triangles, cages, stars or others) has allowed the tuning of the particles' resonance wavelength to the NIR region, a radiation range where the human body presents almost no absorption (reviewed in detail by [92-95]). This control over gold nanoparticles surface plasmon resonance has been exploited to apply them as bioimaging and/or PTT agents [96-101].

Despite the wide scope of applications of gold nanostructures, they also display some limitations that can impair their utilization in biological systems. Gold nanoparticles can interact with compounds containing thiol or disulfide groups through the formation of relatively strong gold-thiolate bonds [102]. This well-known gold binding affinity or the establishment of non-specific interactions triggers the biomolecules adsorption on the nanoparticles' surface [103, 104]. Particularly, the adsorption of proteins can induce changes on the nanoparticles' surface properties and thus on their interaction with the human body (*e.g.* nanoparticles uptake, blood circulation time and biocompatibility) [105, 106]. Moreover, gold nanoparticles during bioimaging or therapeutic applications can be exposed to high-energy laser pulses and a portion of the incident radiation is converted into heat [107]. In turn, the generated heat can lead to the gold nanoparticle reshaping (*i.e.* melting) and consequently loss of their optical properties [108, 109]. Therefore, the post-synthesis modification of gold nanoparticles is highly desirable for surpassing these limitations as well as potentiate gold-based nanoparticles application in nanomedicine [110-112]. From the wide number of materials used in the literature (*e.g.* dextran, poly(isobutylene-*alt*-maleic anhydride)-graft-dodecyl and PEG), silica arises as one of the main coating alternatives for gold nanoparticles [113, 114]. Nanoparticles produced with this material have been reported as stable colloidal suspensions, chemically inert, biocompatible and ease to modify with different functional groups [115, 116]. Further, silica derivatives such as mesoporous silica possess a large surface area and pores that can act as reservoirs for bioactive molecules aimed for therapeutic purposes [116, 117]. Such features allow the encapsulation of poorly soluble compounds and simultaneously confer them protection from premature degradation and clearance from the human body [118, 119]. In addition, the inclusion of the silica shell also enhances the colloidal stability of gold nanoparticles when they are in contact with biological fluids or irradiated with a specific radiation [120, 121]. Silica is also optically transparent to the NIR radiation, often used in PTT, which indicates that the silica shell does not compromise the therapeutic capacity of gold-

based PTT agents [122, 123]. Therefore, the multifunctional potential of gold core-silica coated nanoparticles provides an ideal platform for theranostic modalities combining therapeutic, targeting, and imaging functions (please see Figure 2.9).

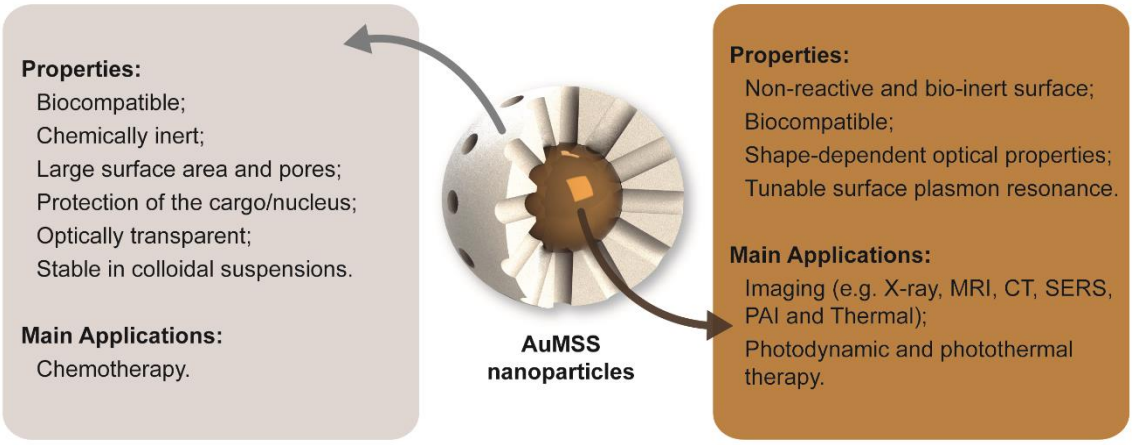

Figure 2.9 - General properties and main applications of the AuMSS materials.

2.7. Synthesis overview

During the past years, a huge effort has been performed to allow the fabrication of gold core-silica shell nanoparticles in a scalable, controlled and reproducible manner [124-126]. Generally, the production of these nanoparticles can be achieved through two main steps (please see Figure 2.10), i) the production of the gold core with the desired size and shape and ii) the synthesis of the silica shell [125, 127, 128]. The gold cores can be synthesized using different synthetic routes to yield gold nanoparticles with distinct sizes and shapes, as extensively reviewed in [129-132]. Briefly, gold cores are usually prepared by inducing the reduction of gold salts and consequent gold nucleation and growth in the presence of a stabilizing agent, such as trisodium citrate and cetyltrimethylammonium bromide, to prevent the particles aggregation [130]. The sphere is one of the most stable shapes and can be obtained when the gold core synthesis is performed under thermodynamically controlled conditions [133]. Alternatively, to obtain non-spherical gold-cores the synthesis process must be fine-tuned to favor an anisotropic growth of the gold core by using surfactants that block some of the growing directions (*e.g.* cetyltrimethylammonium bromide) [134, 135], halides [136, 137] or weak/mild reduction agents [138, 139]. Up to date, the rod-like shape remains as one of the most explored gold nanostructures. In general, gold nanorods are produced by using a seed mediated growth methodology [128, 140], where small spherical gold spheres (*i.e.* seeds) are synthesized by nucleation and then they are added to a solution denominated of "growth solution", which is composed of a gold salt (*e.g.* chloroauric acid), silver nitrate and high concentrations of cetyltrimethylammonium bromide to induce the rod-shaped growth [140].

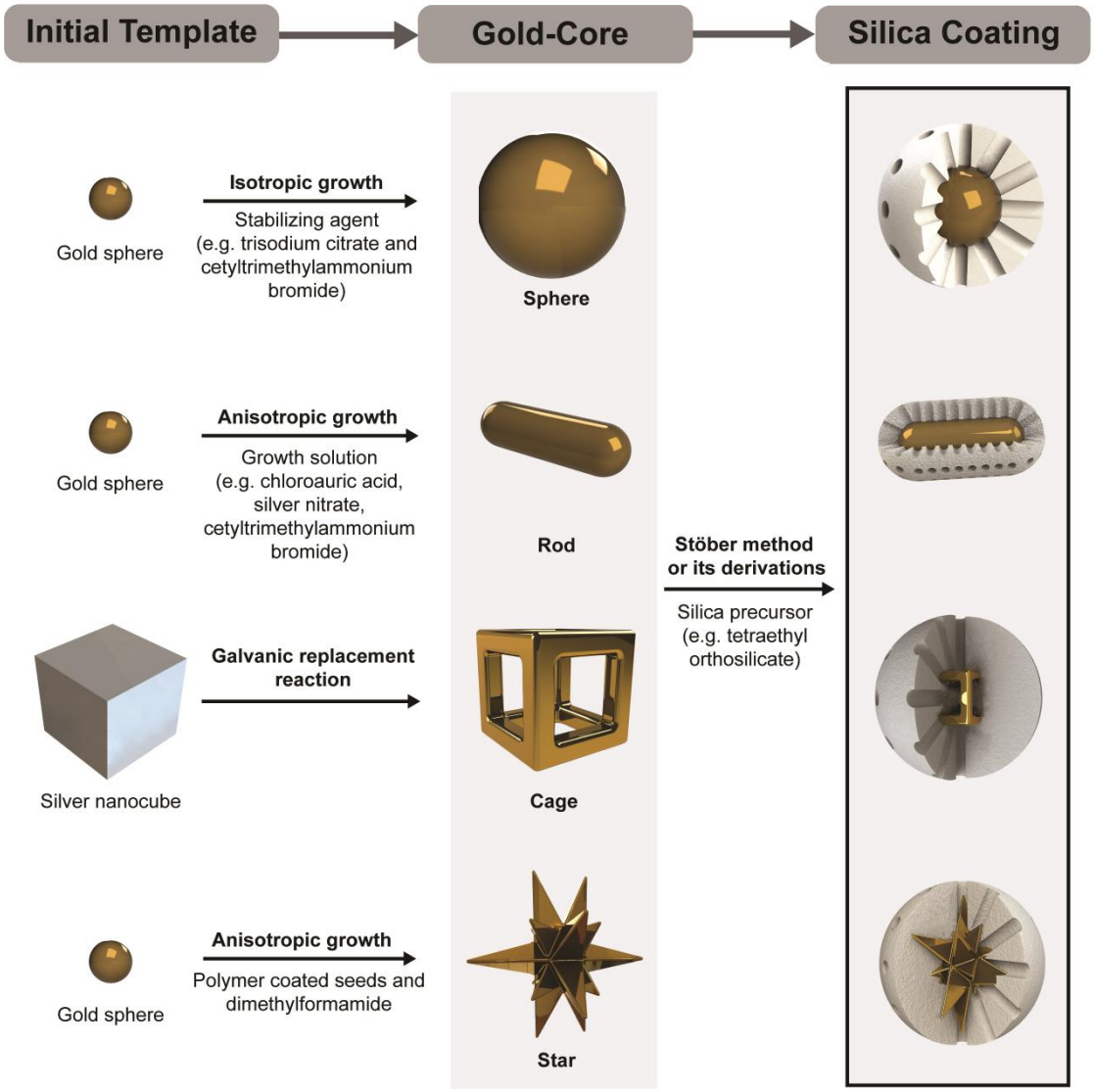

Figure 2.10 - Representation of AuMSS production process. The production of the gold-core is achieved by promoting an isotropic or anisotropic growth or using sacrificial templates. Afterwards, the gold-core with the desired shape is coated with a silica layer by using the Stöber method or its derivations.

Gold nanostars and nanocages have also been used for biomedical applications. Gold nanostars are also produced by using a seed mediated growth method, however, the particle growth occurs in the surface of PVP coated gold seeds in the presence of dimethylformamide [141]. Otherwise, gold nanocages are prepared by using sacrificial silver nanocubes which are exchanged by gold through a galvanic replacement process [142].

Subsequently, the silica coating of the gold cores is accomplished by using the classic Stöber method or its derivations [125, 126]. During the synthesis procedure, the silica precursor (*e.g.* tetraethyl orthosilicate (TEOS)) molecules will start to condensate around the gold core originating the silica shell. The thickness of this silica shell can be tailored by fine-tuning the reaction time and reagent concentrations [125]. In these systems, the optical and electronic

properties can be adjusted by varying the shape and size of the gold core as well as the thickness of the silica shell [143, 144]. On the other side, the silica coating allows the stabilization of the gold nanostructures as well as the encapsulation of drugs, dye molecules, or other imaging agents either via physical adsorption or covalent attachment [68, 69]. Further, silica presents an increased surface area that can be functionalized with antibodies, targeting moieties or even stealth agents [119, 146]. Therefore, AuMSS nanoparticles with different core shapes (*i.e.* spheres, rods, stars and cages) have been employed, in different reports in the literature, for therapeutic and bioimaging applications (please see Table 2.3) [147-149]. AuMSS nanoparticles have been explored to mediate single or combinatorial therapeutic approaches based on drug delivery, PTT and PDT [101, 150-153]. The possibility to combine different therapeutic functions into one nanoparticle presents several benefits, since it improves the therapeutic efficacy, due to possible synergic interactions, and minimizes the side-effects originated by the administration of multiple doses [154, 155]. Further, the gold-core allows to perform bioimaging techniques such as computed tomography (CT), magnetic resonance imaging (MRI), photoacoustic imaging (PAI) and surface enhanced raman spectroscopy (SERS) [156, 157].

2.8. Biomedical Applications

2.8.1. Nanospheres

The majority of the nanoparticles produced up to now present spherical shape. The spherical gold core-silica shell nanoparticles size and relatively simple synthesis make them appealing for applications in the clinic [158]. Up to now, these spherical gold core-silica shell nanoparticles have been mainly applied as imaging agents [147, 159]. The gold core has the capacity to improve the image contrast in structural imaging modalities, such as CT and MRI. In fact, the mass attenuation of gold, at energies superior to 80 kV, is higher than that of the iodinated contrast agents usually applied in the clinic, which can result in images with a superior resolution [160-162]. Kobayashi and colleagues prepared a colloid solution of gold core-silica shell nanoparticles with a gold nucleus of 17 nm and total particle size of 136 nm to be used as a CT contrast agent [163]. In their work, the authors showed that the AuMSS nanoparticles attenuation capacity was almost seven times larger than Iopamiron®, a commercial iodine-based X-ray contrast agent. Further, the contrast of different mice tissues (*e.g.* liver, spleen, and kidneys) was also monitored along time. The authors noticed that the liver and spleen contrast increased (76.7 and 96.5 HU to 115.0 and 120.2 HU, respectively) 5 min after the particles injection and remained constant for 2 days allowing the obtainment of clear images of the liver and spleen throughout the study [163]. Schooneveld *et al.* also developed spherical AuMSS nanoparticles with 88 nm size (*i.e.* gold core with 66 nm coated with an 11 nm silica shell), further modified with paramagnetic Gd–DTPA–DSA (gadolinium diethylene triamine pentaaceticacid di(stearylamide)), fluorescent Cy5.5-PEG-DSPE

(Cyanine5.5 conjugated 1,2-distearoyl-*sn*-glycero-3-phosphoethanolamine-N-mPEG-2000) and PEG-DSPE amphiphiles to be used as contrast agents in different techniques such as MRI, CT, fluorescence imaging and positron emission tomography [164]. The addition of this PEGylated lipid layer on the surface of the AuMSS nanoparticles improved the long-term stability of the nanoparticles (*i.e.* particles were stable in aqueous suspension for at least 3 months). Further, the *in vitro* studies performed in J774A.1 macrophage cell line revealed that it was possible to monitor the nanoparticles cellular internalization by using MRI, CT, and confocal microscopy. Moreover, when intravenously administered in wild-type C57Bl mice the nanoparticles enhanced the CT and MRI signals in 50% and 24%, respectively, even using particle doses in the nanomolar ranges, 0.15 $nmol.kg^{-1}$ [164]. In a similar approach, Kircher and colleagues produced a 60 nm gold core covered with trans-1,2-bis(4-pyridyl)-ethylene, a Raman molecular tag, and a 30 nm silica layer further functionalized with DOTA-Gd^{3+} that allowed the detection and imaging of glioblastoma cells through MRI, CT, and SERS imaging on glioblastoma bearing mice [165]. Further, 30 min after intravenous injection, the authors observed that the nanoparticles increased the MRI image contrast no noise ratio from 1.4 to 8.7 and the PAI signal in 60%, remaining these values stable for 24 h [165].

Another prominent application of spherical AuMSS nanoparticles is therapy. The mesoporous silica coating provides pores that can act as reservoirs for the encapsulation of therapeutic molecules in a more efficient way than bare gold nanospheres [146]. In our group, Dias and colleagues demonstrated that Dox can be loaded onto the mesopores of the silica shell and delivered successfully to cancer cells [158]. The *in vitro* studies performed in 2D and 3D cell cultures showed that these spherical nanoparticles with 109 nm size (20 nm gold core and 45 nm silica shell) were efficiently uptaken by cancer cells and could penetrate into deeper regions of Human negroid cervix epithelioid carcinoma (HeLa) spheroids. Further, after 48 h of incubation, the Dox loaded AuMSS (AuMSS/Dox) nanoparticles were able to reduce the cancer cells viability to 20% when a 100 $\mu g.mL^{-1}$ dose was used [158]. On the other side, Ramasamy utilized AuMSS nanoparticles loaded with cinnamaldehyde, an antimicrobial compound, for the treatment of bacterial biofilms [166]. During the nanoparticles production, cinnamaldehyde was chemically linked to gold nanoparticles through an imine linkage and covered with the silica shell, which stabilizes and protects the cinnamaldehyde from premature degradation, leading to a final particle size of 326 nm. The antibiofilm capacity of this nanosystem was then evaluated using different pathogenic strains of *Escherichia coli*, *Pseudomona aeruginosa*, methicillin-sensitive *Staphylococcus aureus* and methicillin-resistant *Staphylococcus aureus*. The authors observed in confocal microscopy imaging and bacterial density measurements that the nanoparticles were able to potentiate the cinnamaldehyde effect by inhibiting the biofilm formation for each of the four bacteria strains [166]. Nevertheless, the use of spherical AuMSS nanoparticles in PTT and PDT therapeutic based applications is hindered by their absorbance peak, which is localized in the visible region of the spectra, at around 520 nm [167]. Therefore, different particle shapes (rod, stars and cages) presenting an absorbance peak in the NIR region

(*i.e.* so-called "biological window") have been gaining an increased relevance when therapeutic applications are aimed.

2.8.2. Nanorods

The rod-like shaped nanoparticles are the most explored AuMSS particles when therapeutic applications are intended. This increased interest on the AuMSS nanorods is based on their tunable optical properties and effective light-heat conversion [94, 106]. The AuMSS nanorods present two distinct absorption peaks that correspond to the transverse and longitudinal resonances [94]. The transverse resonance leads to an absorption peak at 520 nm, whereas the longitudinal resonance can be easily tuned to present high absorption in the NIR region, through the simple manipulation of the rod aspect ratio (A.R.), *i.e.* rod length/width coefficient [168]. These important characteristics favor the AuMSS nanorods application in imaging (PAI and X-ray) and therapy (*e.g.* chemotherapy, PTT, PDT or their combination) [169-171]. The PAI imaging takes advantage from the ultrasounds generated by the temperature increase and consequent rapid pressure differences created by NIR laser irradiation of AuMSS nanorods [172]. Cheng *et al.* demonstrated that AuMSS nanorods present an increased stability when compared to bare and PEGylated gold nanorods, for being applied in PAI imaging [107]. The extra protection provided by the silica shell (*i.e.* thickness 6 nm or 20 nm) resulted in the stabilization of the PAI signal during 300 pulses. In contrast, the signal of PEGylated gold nanorods decreased 40% in the first 100 pulses. Further, they also observed that the inclusion of the 20 nm silica shell increases the amplitude of the PAI signal generated by the gold nanorods, which can lead to clear and better images [107].

Apart from imaging, the AuMSS nanorods capacity to absorb radiation in the NIR region have also been explored to mediate therapeutic applications, mainly in cancer PTT [173, 174]. Liu *et al.* developed a tLyp-1 peptide-functionalized, ICG-loaded AuMSS nanorods for the breast cancer PTT treatment and ICG-mediated imaging [175]. The nanorods had an A.R. of 3.5 (length 47 nm and width 14 nm) with a 17-32 nm silica shell and presented a strong absorption peak in the NIR region, at 754 nm. Further, the nanoparticles mediated an increase in the temperature up to 55°C and a decrease in MDA-MB-231 cells viability to values inferior to 20%, when irradiated with a NIR laser (785 nm, 3 $W.cm^{-2}$ for 2 min). Similarly, Lee *et al.* developed an RVG29 (29 residue peptide derived from rabies virus glycoprotein) functionalized AuMSS nanorods for the PTT treatment of brain gliomas [176]. The produced AuMSS nanorods had an A.R. of 2.4 (length 180 nm, width 75 nm, and 14 nm shell thickness) and presented high absorption in the NIR region. The RVG29 functionalization of the AuMSS nanorods proved to be capable of increasing the nanoparticles accumulation in the brain region of glioma-bearing mice. Further, the nanoparticles NIR laser irradiation (808 nm, 5 min, and 1.5 $W.cm^{-2}$) increased the local tumor temperature to values around the 50°C, thus suppressing the growth of the xenografted tumor and allowed the real-time monitoring via MRI during the 7 days, the total duration of the study [176].

However, the AuMSS-mediated PTT effect is hindered by light scattering and absorption phenomena that occur when the NIR light travels deeper into the tissues [167, 177]. Therefore, depending on tumor location, some cells will inevitably receive suboptimal laser exposure and survive [167, 177]. With that in mind, several studies have been combining the AuMSS-mediated PTT with chemotherapy or PDT to improve the therapeutic outcome [152, 178]. Shen and colleagues produced AuMSS/Dox nanorods functionalized with RGD moieties for the targeted chemo- and PTT combinatorial therapy (please see Figure 2.11) [179].

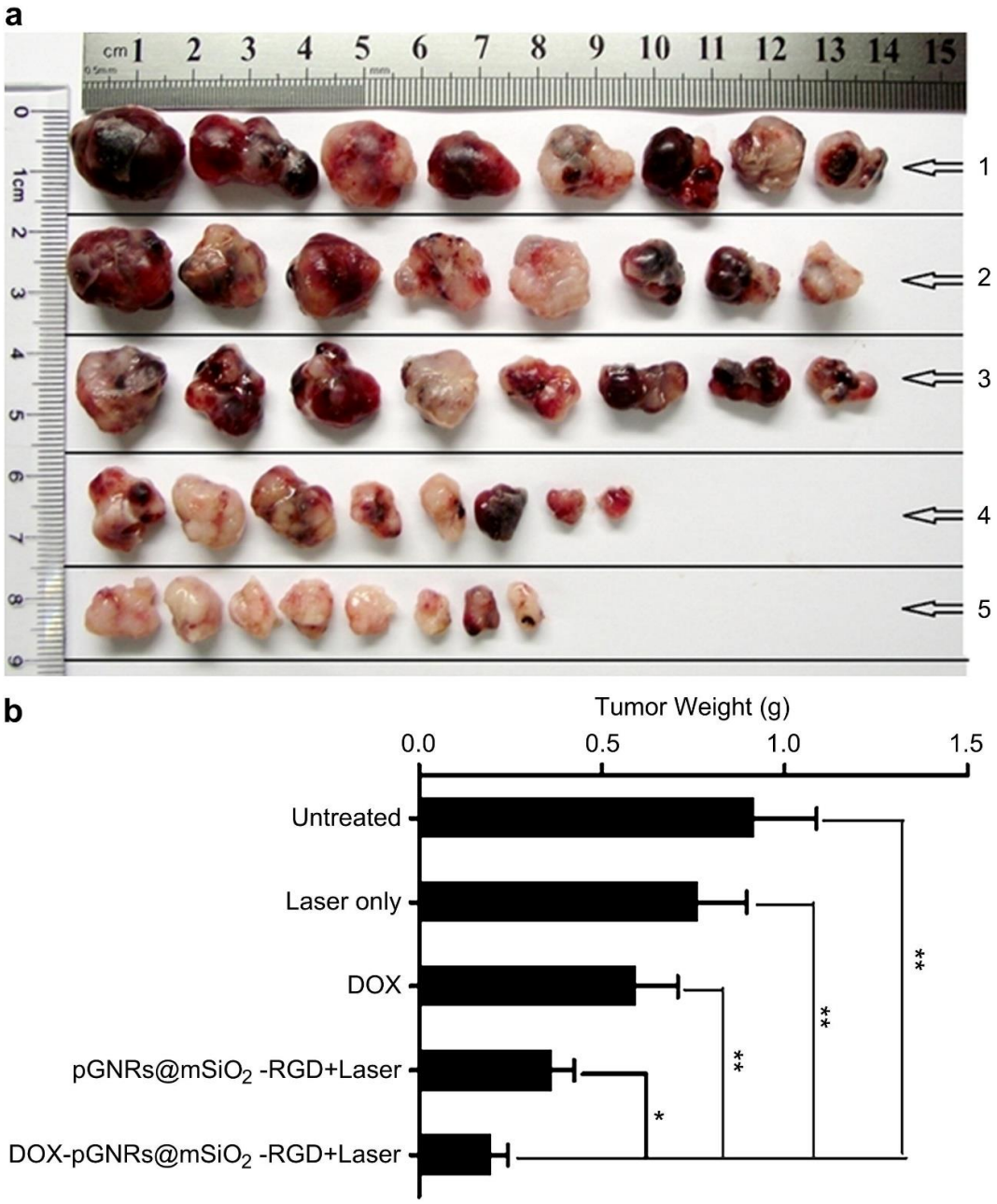

Figure 2.11 - Photographs (a) and weight (b) of A549 tumors excised from mice after being treated with NIR laser, chemotherapy (Dox), AuMSS nanorods mediated PTT and AuMSS nanorods combinatorial PTT and chemotherapy. Reproduced from [179] with permission from Elsevier.

The particles presented an A.R. 3.9 (length 52 nm, width 13 nm, and 25 nm shell thickness), strong absorption in the NIR wavelength region (absorption peak at 840 nm) and a drug release that could be induced by the NIR laser irradiation and consequent heat generation. Additionally, the nanoparticles intravenous administration in A549 tumor bearing mice shown that the nanoparticles could mediate an increase in the tumor temperature up to 65.9°C after NIR laser irradiation (808 nm, 30 seconds and 3 $W.cm^{-2}$). Moreover, the anti-tumoral efficiency of the nanorods was enhanced when chemo and thermal therapies were combined, being registered a tumor weight inhibition rate of 66.5% and 45.2% for the combinatorial therapy and single PTT, respectively. Recently, Zhou *et al*. developed HA and RGD peptide functionalized AuMSS nanorods loaded with Dox for the combinatorial therapy of ovarian cancer [174]. The nanorods (length 50 nm, width 10 nm, and shell thickness of 15 nm) irradiation with NIR laser (808 nm, 2 $W.cm^{-2}$ and 4 min) resulted in an improved therapeutic effect towards ovarian SKOV-3 cancer cells (10%, 29% and 46.5% cell viability for combinatorial, chemotherapy and PTT, respectively) [174]. With a different approach, Moreira and colleagues encapsulated AuMSS nanorods loaded with Dox within PLGA based microparticles containing SA for the chemotherapy and PTT combinatorial therapy of cervical cancer [4]. The authors observed that the heat generated by the nanorods irradiation with a NIR laser (808 nm, 1.7 $W.cm^{-2}$ and 5 min) could trigger the drug release and enhance the particles cytotoxicity, *i.e*. the cell viability within HeLa spheroids was reduced to 25%, when spheroids were irradiated with NIR laser, whereas in the non-irradiated group 50% of the cells remained viable. On the other side, Seo *et al*. explored the combination of the PTT and PDT by using AuMSS nanorods (length 32 nm, width 11 nm, and shell thickness 20 nm) loaded with methylene blue [180]. Upon NIR laser irradiation (780 nm, 1 $W.cm^{-2}$), the authors observed a synergistic effect between the heat generated by the nanorods and the reactive oxygen species created by the irradiation of the methylene blue molecules leading to a decrease in the cell viability to 11%. Moreover, these nanoparticles also allowed the detection of both agglomerated and single cancer cells through SERS imaging. In an integrative study, Luo and colleagues developed cisplatin and AlPcS4 loaded AuMSS nanorods functionalized with ß-cyclodextrins, adamantine conjugated PEG and lactobionic acid for the simultaneous PTT, PDT, and chemotherapy of hepatic cancer [181]. The intravenous administration of AuMSS nanorods (length 40 nm, width 10 nm, and shell thickness 14 mn) triple therapy in HepG2 tumor-bearing mice increased the tumors local temperature to 53°C and ceased the tumor progression upon irradiation with NIR laser (808 nm and 606 nm, 1 $W.cm^{-2}$ for 5 min). In sharp contrast, the tumor continued to progress when only PTT/chemotherapy (4-fold volume increase) or PDT/chemotherapy (4.9-fold volume increase) were used.

2.8.3. Nanocages

Gold-based nanocages have a hollow structure with porous walls and are usually synthesized through a galvanic replacement reaction between silver nanocube templates and the gold precursor [182, 183]. In these structures, the surface plasmon resonance peak can be adjusted to the NIR region of the spectra by fine-tuning the gold precursor amount [184]. Additionally, the silica coating thickness can also influence the plasmon resonance peak. Khlebtsov and colleagues observed that an increase in the thickness of the silica shell (12-127 nm) result in a shift of the plasmon resonance peak to longer wavelengths from 775 to 817 nm [185]. Additionally, the structural organization of AuMSS nanocages allows the drug encapsulation both in the hollow space of the gold nanocage as well as in the outer mesopores of the silica shell [150, 186]. Khlebtsov *et al*. explored the application of Yb-2,4-dimethoxyhematoporphyrin loaded AuMSS nanocages for the PDT and PTT of cervical cancer [187]. The nanocages presented an average size of 140 nm with a shell thickness of 45 nm and a pronounced absorption peak in the NIR region at 790 nm and after being irradiated for 5 min (808 nm and 1 $W.cm^{-2}$), the particles mediated a temperature increase up to 75°C. Additionally, the irradiation of the particles with a 625 nm laser (50 $mW.cm^{-2}$ and 15 min) resulted in the reduction of the HeLa cells viability to 25% via a PDT mediated effect. In a different study, Khlebtsov and colleagues also demonstrated the applicability of these Yb,4-dimethoxyhematoporphyrin loaded AuMSS nanocages as an antibacterial agent capable of reducing the bacteria cell viability through PTT and PTD approaches [188]. Otherwise, Yang and colleagues produced poly(Nisopropylacrylamide) (PNIPAM) coated AuMSS nanocages to attain a stimuli-responsive Dox release towards cervical cancer cells [150]. When irradiated with NIR laser (808 nm, 1 $W.cm^{-2}$ and 10 min) these nanoparticles (size 126 nm and 33 nm shell thickness) mediated an increase in the temperature from 25°C to 41°C, which prompted the drug release due to the conformational changes in PNIPAM. Further, the heat generated also contributed for the improvement of the therapeutic efficiency, *i.e*. HeLa cell viability was reduced to 85.5%, 80.6% and 19.9% when chemotherapy, PTT and chemo-PTT combination were used, respectively.

Hu *et al*. verified the application of Tat peptide-capped AuMSS nanocages loaded with Dox in SERS imaging and chemo-PTT [189]. The nanocages (size 129 nm and 45 nm shell thickness) administration to breast cancer cells in conjugation with NIR laser irradiation (808 nm and 123.8 $mW.cm^{-2}$) decreased the cell viability to 21.1% and simultaneously allowed the real-time imaging of the Michigan Cancer Foundation-7 (MCF-7) cells (please see Figure 2.12).

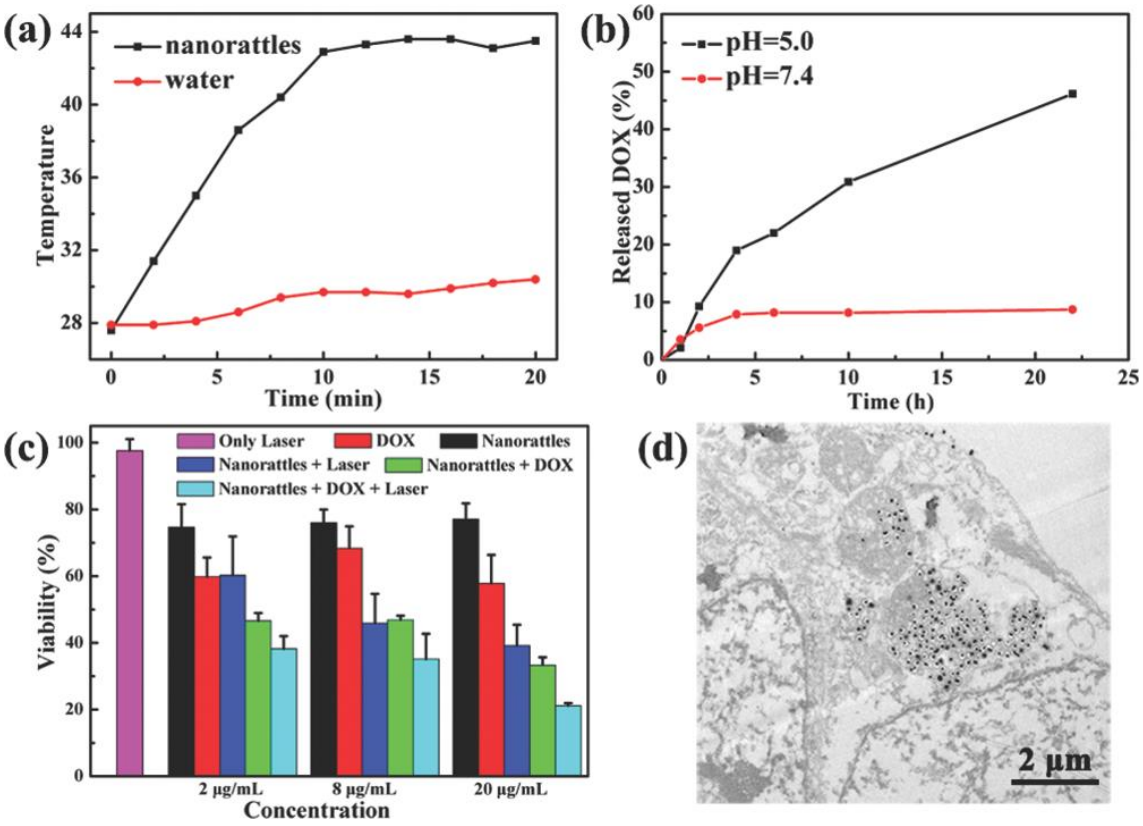

Figure 2.12 - AuMSS nanocages PTT curves (a), Dox release profile (b), MCF-7 cells viability (c) and TEM images of the AuMSS nanocages uptake (d). Reproduced from [189] with permission from John Wiley and Sons.

2.8.4. Nanostars

The gold nanostar cores are highly anisotropic nanoparticles composed of a small spherical core and a variable number of tips [153]. The optical properties displayed by these nanoparticles are strongly related to the size and number of tips and, usually, present a high absorption in the NIR region due to nucleus and tips plasmons hybridization interactions [190]. Atta and colleagues observed that the growth of the silica shell from 12.2 nm up to 29 nm modify the UV-vis spectra of the aminothiophenol doped nanostars [191]. The increase in the silica shell thickness promotes a red-shift and an increase in the intensity of the absorption peak and additionally, amplifies the obtained SERS signal [191]. In turn, Harmsem *et al*. demonstrated the applicability of the PEGylated AuMSS nanostars (size 75 nm) doped with IR-780 in the SERS based imaging of breast cancer, sarcoma, pancreatic ductal adenocarcinoma, and prostate cancer in mice [192]. The authors observed that the high sensitivity and signal specificity of the IR-780 doped AuMSS nanostars allowed the detection of primary tumors as well as premalignant lesions smaller than 100 μm. In addition, these nanostars also identified small malignant cell remains that would lead to the cancer recurrence, even after the authors performing resection surgeries (please see Figure 2.13).

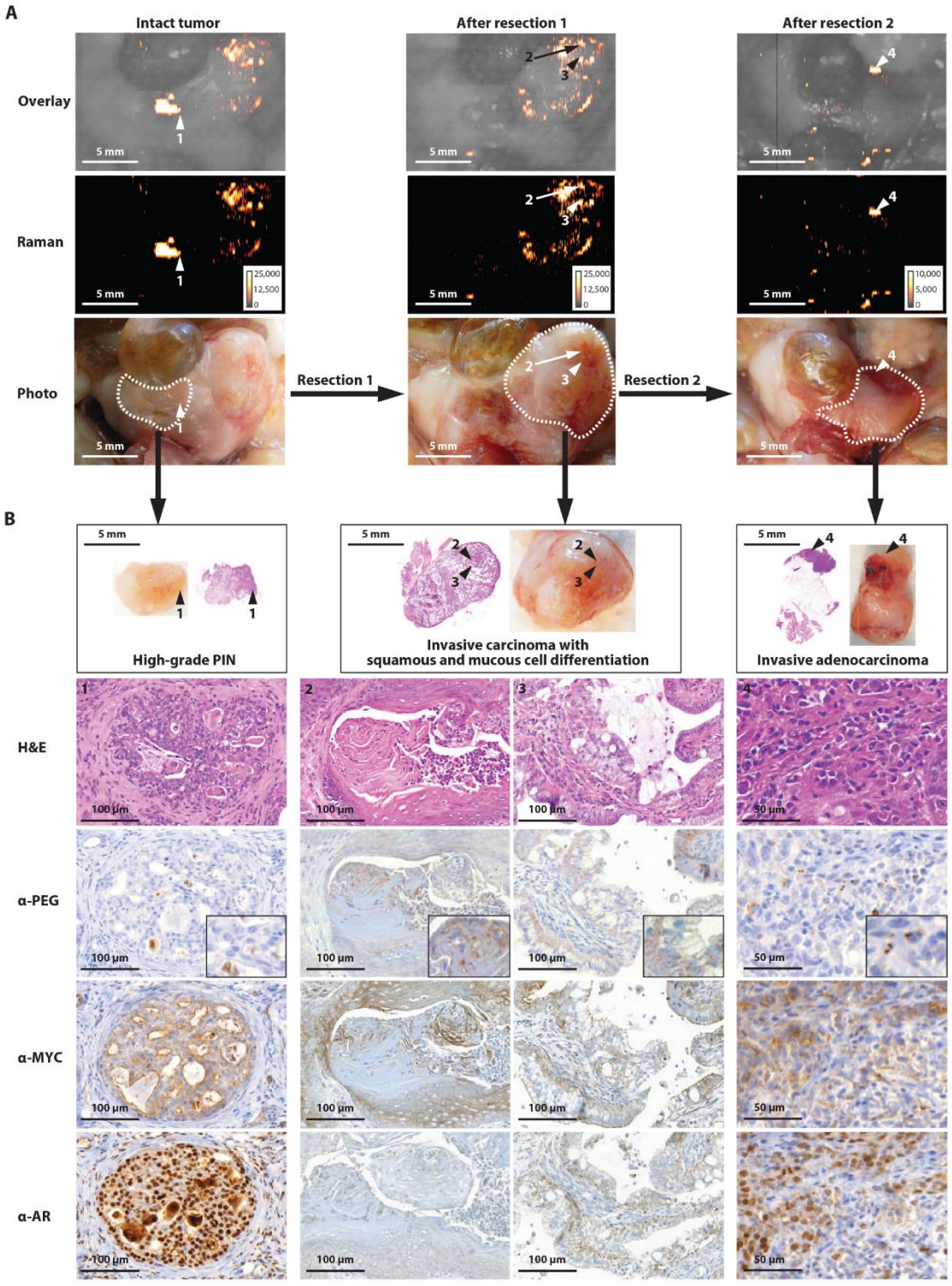

Figure 2.13 - AuMSS nanostars imaging of different stages and grades of prostate cancer in Hi-Myc mouse model. Photographs and SERS images of sequential resections of the prostatic tumors (A). Histological staining for tumor marker MYC, androgen receptor (α-AR) and PEG. Reproduced from [192] with permission from The American Association for the Advancement of Science.

Further, Fales *et al.* reported the application of methylene blue loaded AuMSS nanostars doped with 3,30-diethylthiatricarbocyanine iodide for simultaneous SERS imaging and PDT of breast cancer [193]. The authors observed that the nanostars irradiation (785 nm, 10 sec) resulted in a strong SERS signal, whereas the irradiation at 633 nm, 900 $mW.cm^{-2}$ for 1 h prompted the reactive oxygen species production. This particle behavior led to the death of BT549 breast cancer cells within the spot irradiated with the laser. In another study, Li and colleagues produced PEGylated gold-silica shell nanostars loaded with perflurohexane for multimodal imaging and PTT of glioma xenograft models [194]. When irradiated with NIR laser (808 nm, 1.2$W.cm^{-2}$ for 10 min), the nanostars mediated an increase in the tumor temperature to 70°C resulting in an apoptosis rate of 84% and allowed the tumors imaging via ultrasounds, CT, PAI and thermography. An *et al.* evaluated the application of folic acid-PEG-phospholipid coated AuMSS nanostars loaded with Dox in the cervical cancer therapy and imaging [195]. The authors observed that the nanostars (size 50 nm and 60 nm shell thickness) allowed both PAI and CT imaging of the tumors, mediated a raise in the tumor temperature up to 65°C under NIR laser irradiation and presented heat-responsive drug release profile. Further, the conjugation of the chemo and PTT therapies induced the tumor necrosis and eradication, being observed only one relapse in five mice at day 12. In contrast, Dox and PTT stand-alone treatments presented a low efficacy being only capable to reduce the tumor growth rate or to inhibit the tumor growth until day 8, respectively.

2.9. AuMSS nanoparticles biocompatibility

The application of AuMSS nanoparticles in the clinic is closely connected to the complete understanding of the nanoparticles-host interactions that occur upon administration. Therefore, several extensive *in vitro* and *in vivo* toxicological evaluations must be performed using different AuMSS systems and cell or animal models, before they can be tested in clinical trials. Zeng and colleagues observed that the cytotoxicity of AuMSS nanospheres is size and dose dependent [196]. They verified that AuMSS nanospheres with 50, 100 and 200 nm silica layers did not induce any significant cytotoxicity in concentrations inferior to 200 $pmol.L^{-1}$, whereas when the concentration was increased to 400 $pmol.L^{-1}$, the spheres with 200 nm silica layer decreased the HepG2 cell viability in 10%. In another work, Dias and colleagues compared the cytotoxicity of spherical and rod-like AuMSS nanoparticles [158]. The administration of both spherical and rod-like nanoparticles to HeLa cells and normal human dermal fibroblasts (FibH) revealed that both systems were biocompatible up to 100 $\mu g.mL^{-1}$. Moreover, the authors observed that the rod-like nanoparticles exerted a positive effect on the cell migration capacity, presenting a gap with smaller width than the cells treated with the spherical AuMSS in the *in vitro* wound closure assays. Apart from the acute toxicity of the AuMSS nanoparticles, the systemic toxicity and distribution greatly impact the biological performance of the nanoparticles. Thakor *et al.* studied the systemic biodistribution and acute effects of PEGylated AuMSS nanospheres (size 120 nm) administered via intravenous administration in mice [197].

Their initial results demonstrated that the particles did not affect the physical appearance, behavior, or social interactions in any of the mice studied as well as did not induce any acute effects on basal cardiovascular function or did affect any of the hematological and biochemical parameters recorded. Furthermore, the authors found out that the PEGylated AuMSS nanospheres accumulate mainly on liver and spleen, which induced a mild inflammatory response in the liver through reactive oxygen species formation at 24 h post-administration, but not detected 1 week after injection. In turn, Gao *et al*. evaluated the biocompatibility and biodistribution of folic acid functionalized AuMSS nanorods in rabbits [198]. In their study, particles concentration up to 40 ppm did not elicit any significant cytotoxic effect on HepG2 cells. Further, the folic acid functionalized AuMSS displayed a preferential accumulation in the tumor tissues and started to be cleared from the body after 24 h through the kidneys. Moreover, no serious signs of toxicity in vital organs were observed by the authors even when high doses (10.5 $mg.kg^{-1}$) were administered. Despite, to rationally apply AuMSS nanoparticles in the clinic it is still necessary to perform additional studies, such as the characterization of the AuMSS particle shape and administration route influence on the particles' performance, to better understand the AuMSS particles behavior in biological environments.

Table 2.3 - Overview of the different AuMSS nanoparticle shapes application in bioimaging and therapy (N.D. – non disclosed, N.A. – not applicable, A.R. – aspect ratio, L – length, W - width).

Morphology	Size (nm)			Absorption Peak (nm)	Surface Modification/Cargo	Type of study	Test model	Application	Ref.
	Core	Shell	Particle						
Spheres	45	N.D.	N.D.	N.D.	N.A.	*In vitro*	HepG2 cells	N.A.	[196]
	15	10, 23, 58 and 83	N.D.	520	N.A.	Proof-of-concept	N.A.	N.A.	[199]
	15	29-88	N.D.	520-530	N.A.	Proof-of-concept	N.A.	N.A.	[200]
	50	20 and 80	N.D.	540	N.A.	Proof-of-concept	N.A.	N.A.	[201]
	15	10, 50 and 80	N.D.	N.D.	N.A.	Proof-of-concept	N.A.	N.A.	[202]
	32	N.D.	120	552	N.A.	Proof-of-concept	N.A.	N.A.	[121]
	20	45	109	550	Dox	*In vitro*	Hela and FibH cells	Therapy	[158]
	N.D.	N.D.	326	530	Cinnamaldehyde	*In vitro*	*Candida elegans*	Therapy	[166]
	66	11	88	660-710	PEGylated lipid	*In vitro*/*In vivo*	J774A.1 cells/C57BL mice	Imaging	[164]
	64	N.D.	139	490	PEG	*In vitro*	A431, HT29, U87MG and MDA-435S cells	Imaging	[203]
	17	N.D.	136	N.D.	N.A.	*In vivo*	ICR mouse	Imaging	[163]
	60	30	120	N.D.	DOTA- Gd^{3+} coating	*In vivo*	$eGFP^{+}$ U87MG orthotopic tumor-bearing mice	Imaging	[165]
Rods	L:52; W:13; A.R.:3.9	25	143	840	PEGylated RGD and Dox	*In vitro*/*In vivo*	A549 cells/A549 cells bearing Balb/c mice	Therapy	[179]
	A.R.:3.9	6 and 20	N.D.	800	PEG	Proof-of-concept	N.A.	Therapy and Imaging	[107]
	L:47;	17-32	N.D.	754	tLyp-1 peptide and ICG	*In vitro*	MDA-MB-231 cells	Therapy and Imaging	[175]

	W:14; A.R.:3.5								
	L:32; W:11; A.R.:3-4	10	N.D.	892	Methylene blue and Methoxy polyethylene glycol thiol (mPEG-SH)	*In vitro*	CT-26 mouse colon cancer cells	Therapy	[180]
	L:40; W:10	10-13	N.D.	840	PEG and Dox	*In vitro*/*In vivo*	MCF-7 cells/Ehrlich ascites cells bearing Balb/c mice	Therapy	[173]
	L:80; W:20; A.R.:4	14	L:180; W:75; A.R.:2,4	820	PEGylated RVG29	*In vitro*/*In vivo*	N2a cells/N2a cells bearing Balb/c nu/nu mice/ ICR mice/ BALB/c nude mice	Therapy	[176]
	L:38; W:11; A.R.:3.4	18	L:70; W:47;	770	Dox	*In vitro*	HeLa and FibH cells	Therapy	[158]
	A.R.:4.1	35	N.D.	850	APTES/Folic acid/1-tetradecanol and Dox	*In vitro*	KB cells	Therapy	[204]
	L:50; W:10;	15	124	800	HA/RGD and Dox	*In vitro*	SKOV-3 and HOSEpiC cells	Therapy	[174]
	L:38; W:11; A.R.:3.4	18	L:70; W:47;	770	Dox	*In vitro*	HeLa and FibH cells	Therapy	[4]
	L:46; W:13; A.R.:3.6	13	N.D.	800	Sulfonatocalix[4]arene supramolecular switches	Proof-of-concept	N.A.	Therapy	[114]
	L:40; W:15;	18	N.D.	696	5,5-dithiobis (2-nitrobenzoic acid)/Folic acid and Rhodamine B isothiocyanate	*In vitro*	HeLa cells	Imaging	[205]
	A.R.:3.9	6/20/75	N.D.	790/802/806	PEGylated nanorods	Proof-of-concept	N.A.	Imaging	[144]
	L:45; A.R.:3	13	N.D.	720	Hematoporphyrin	*In vitro*	MDA-MB-231 cells	Therapy and Imaging	[206]
	N.D.	30	N.D.	780	Dox	*In vitro*	A549 cells	Therapy and Imaging	[178]
	L:40 W:10 A.R.:3.9	14	N.D.	791	ß-cyclodextrins/adamantine conjugated PEG and lactobionic acid	*In vitro*/*In vivo*	HepG2 cells and BALB/c nude mice	Therapy and Imaging	[181]
Cages	60	12-127	N.D.	750-800	N.A.	Proof-of-concept	N.A.	N.A.	[185]
	47	45	140	650 and 900	Yb-2,4-dimethoxyhematoporphyrin	*In vitro*	HeLa cells	Therapy	[187]

	60	33	126	530	PNIPAM	*In vitro*	HeLa cells	Therapy	[150]
	40	45	129	752	APTES-SMCC-Tat peptide	*In vitro*	MCF-7 cells	Therapy	[189]
	50	10	N.D.	515-820	Yb,4-dimethoxyhematoporphyrin	*In vitro*	*Staphylococcus Aureus*	Therapy	[188]
Stars	N.D.	N.D.	N.D.	900	mPEG-SH/3,30-diethylthiatricarbocyanine iodide and Methylene blue	*In vitro*	BT549 cells	Therapy	[193]
	75	35	140	N.D.	PEG and IR-780 perchlorate	*In vivo*	C57BL/6 mice KPC PDAC, Hi-Myc, Ink4a/Arf−/−, MMTV-PyMT, DDLS mouse models	Imaging	[192]
	55	25	105	850	PVP	*In vitro*	HeLa cells	Imaging	[207]
	60	N.D.	N.D.	795	mPEG and Perflurohexane	*In vitro*/*In vivo*	C6 cells/ C6 tumor-bearing nude mice	Therapy and Imaging	[194]
	50	50-60	N.D.	800	Folic acid-PEG-phospholipid and Dox	*In vitro*/*In vivo*	HeLa and A549 cells/ HeLa cells bearing Balb/c mice	Therapy and Imaging	[195]
	N.D.	10	N.D.	700	PEG	*In vivo*	MDA-MB-231 cells bearing nude mice	Therapy and Imaging	[208]

2.10. References

[1] R.L. Siegel, K.D. Miller, A. Jemal, Cancer statistics, 2019, Ca-Cancer J. Clin. 69(1) (2019) 7-34.

[2] F. Bray, J. Ferlay, I. Soerjomataram, R.L. Siegel, L.A. Torre, A. Jemal, Global cancer statistics 2018: GLOBOCAN estimates of incidence and mortality worldwide for 36 cancers in 185 countries, Ca-Cancer J. Clin. 68(6) (2018) 394-424.

[3] J.M. Noh, W. Park, Y.S. Kim, J.-Y. Kim, H.J. Kim, J. Kim, J.H. Kim, M.S. Yoon, J.H. Choi, W.S. Yoon, Comparison of clinical outcomes of adenocarcinoma and adenosquamous carcinoma in uterine cervical cancer patients receiving surgical resection followed by radiotherapy: a multicenter retrospective study (KROG 13-10), Gynecol. Oncol. 132(3) (2014) 618-623.

[4] A.F. Moreira, D.R. Dias, E.C. Costa, I.J. Correia, Thermo-and pH-responsive nano-in-micro particles for combinatorial drug delivery to cancer cells, Eur. J. Pharm. Sci. 104 (2017) 42-51.

[5] C.F. Rodrigues, T.A. Jacinto, A.F. Moreira, E.C. Costa, S.P. Miguel, I.J. Correia, Functionalization of AuMSS nanorods towards more effective cancer therapies, Nano Res. 12(4) (2019) 719-732.

[6] D. Rosenblum, N. Joshi, W. Tao, J.M. Karp, D. Peer, Progress and challenges towards targeted delivery of cancer therapeutics, Nat. Commun. 9(1) (2018) 1410.

[7] W. Sang, Z. Zhang, Y. Dai, X. Chen, Recent advances in nanomaterial-based synergistic combination cancer immunotherapy, Chem. Soc. Rev. (2019).

[8] C.J. Kearney, D.J. Mooney, Macroscale delivery systems for molecular and cellular payloads, Nat. Mater. 12(11) (2013) 1004.

[9] M.O. Dellacherie, B.R. Seo, D.J. Mooney, Macroscale biomaterials strategies for local immunomodulation, Nat. Rev. Mater. (2019) 1.

[10] J.W. Lee, M.R. Prausnitz, Drug delivery using microneedle patches: not just for skin, Expert Opin. Drug Delivery (2018).

[11] R.J. Pettis, A.J. Harvey, Microneedle delivery: clinical studies and emerging medical applications, Ther. Delivery 3(3) (2012) 357-371.

[12] R.F. Donnelly, T.R.R. Singh, A.D. Woolfson, Microneedle-based drug delivery systems: microfabrication, drug delivery, and safety, Drug delivery 17(4) (2010) 187-207.

[13] Y.-C. Kim, J.-H. Park, M.R. Prausnitz, Microneedles for drug and vaccine delivery, Adv. Drug Delivery Rev. 64(14) (2012) 1547-1568.

[14] M.N. Mohammed, K.B. Yusoh, J.H.B.H. Shariffuddin, Poly (N-vinyl caprolactam) thermoresponsive polymer in novel drug delivery systems: A review, Mater. Express 8(1) (2018) 21-34.

[15] Y. Hao, W. Li, X. Zhou, F. Yang, Z. Qian, Microneedles-based transdermal drug delivery systems: a review, J. Biomed. Nanotechnol. 13(12) (2017) 1581-1597.

[16] R.S. Riley, C.H. June, R. Langer, M.J. Mitchell, Delivery technologies for cancer immunotherapy, Nat. Rev. Drug Discovery (2019) 1.

[17] Y. Ye, J. Yu, D. Wen, A.R. Kahkoska, Z. Gu, Polymeric microneedles for transdermal protein delivery, Adv. Drug Delivery Rev. 127 (2018) 106-118.

[18] G. Mojeiko, M. de Brito, G.C. Salata, L.B. Lopes, Combination of microneedles and microemulsions to increase celecoxib topical delivery for potential application in chemoprevention of breast cancer, Int. J. Pharm. 560 (2019) 365-376.

[19] Y. Zhang, P. Feng, J. Yu, J. Yang, J. Zhao, J. Wang, Q. Shen, Z. Gu, ROS-Responsive Microneedle Patch for Acne Vulgaris Treatment, Adv. Ther. 1(3) (2018).

[20] Y. Hao, H. Li, Y. Cao, Y. Chen, M. Lei, T. Zhang, Y. Xiao, B. Chu, Z. Qian, Uricase and Horseradish Peroxidase Hybrid CaHPO4 Nanoflower Integrated with Transcutaneous Patches for Treatment of Hyperuricemia, J. Biomed. Nanotechnol. 15(5) (2019) 951-965.

[21] G. Cole, A.A. Ali, C.M. McCrudden, J.W. McBride, J. McCaffrey, T. Robson, V.L. Kett, N.J. Dunne, R.F. Donnelly, H.O. McCarthy, DNA vaccination for cervical cancer: Strategic optimisation of RALA mediated gene delivery from a biodegradable microneedle system, Eur. J. Pharm. Biopharm. 127 (2018) 288-297.

[22] H.T.T. Duong, Y. Yin, T. Thambi, T.L. Nguyen, V.G. Phan, M.S. Lee, J.E. Lee, J. Kim, J.H. Jeong, D.S. Lee, Smart vaccine delivery based on microneedle arrays decorated with ultra-pH-responsive copolymers for cancer immunotherapy, Biomaterials 185 (2018) 13-24.

[23] S. Bhatnagar, P. Kumari, S.P. Pattarabhiran, V.V.K. Venuganti, Zein microneedles for localized delivery of chemotherapeutic agents to treat breast cancer: drug loading, release behavior, and skin permeation studies, AAPS PharmSciTech 19(4) (2018) 1818-1826.

[24] Z. Zhou, H. Lin, C. Li, Z. Wu, Recent progress of fully synthetic carbohydrate-based vaccine using TLR agonist as build-in adjuvant, Chin. Chem. Lett. 29(1) (2018) 19-26.

[25] Y. Hao, M. Dong, T. Zhang, J. Peng, Y. Jia, Y. Cao, Z. Qian, Novel approach of using near-Infrared Responsive PEGylated Gold Nanorod Coated Poly (L-lactide) microneedles to enhance

the antitumor efficiency of Docetaxel-Loaded MPEG-PDLLA Micelles for Treating an A431 tumor, ACS Appl. Mater. Interfaces 9(18) (2017) 15317-15327.

[26] Y. Ma, S.E. Boese, Z. Luo, N. Nitin, H.S. Gill, Drug coated microneedles for minimally-invasive treatment of oral carcinomas: development and in vitro evaluation, Biomed. Microdevices 17(2) (2015) 44.

[27] X. Lan, J. She, D.-a. Lin, Y. Xu, X. Li, W.-f. Yang, V.W.Y. Lui, L. Jin, X. Xie, Y.-x. Su, Microneedle-mediated delivery of lipid-coated cisplatin nanoparticles for efficient and safe cancer therapy, ACS Appl. Mater. Interfaces 10(39) (2018) 33060-33069.

[28] M.-C. Chen, Z.-W. Lin, M.-H. Ling, Near-infrared light-activatable microneedle system for treating superficial tumors by combination of chemotherapy and photothermal therapy, ACS Nano 10(1) (2015) 93-101.

[29] S. Bhatnagar, N.G. Bankar, M.V. Kulkarni, V.V.K. Venuganti, Dissolvable microneedle patch containing doxorubicin and docetaxel is effective in 4T1 xenografted breast cancer mouse model, Int. J. Pharm. 556 (2019) 263-275.

[30] O. Jonas, H.M. Landry, J.E. Fuller, J.T. Santini, J. Baselga, R.I. Tepper, M.J. Cima, R. Langer, An implantable microdevice to perform high-throughput in vivo drug sensitivity testing in tumors, Sci. Transl. Med. 7(284) (2015) 284ra57-284ra57.

[31] T. Waghule, G. Singhvi, S.K. Dubey, M.M. Pandey, G. Gupta, M. Singh, K. Dua, Microneedles: a smart approach and increasing potential for transdermal drug delivery system, Biomed. Pharmacother. 109 (2019) 1249-1258.

[32] E. Larrañeta, M.T. McCrudden, A.J. Courtenay, R.F. Donnelly, Microneedles: a new frontier in nanomedicine delivery, Pharm. Res. 33(5) (2016) 1055-1073.

[33] S. Bhatnagar, K. Dave, V.V.K. Venuganti, Microneedles in the clinic, J. Controlled Release 260 (2017) 164-182.

[34] K. Cheung, D.B. Das, Microneedles for drug delivery: trends and progress, Drug delivery 23(7) (2016) 2338-2354.

[35] W. Chen, H. Li, D. Shi, Z. Liu, W. Yuan, Microneedles as a delivery system for gene therapy, Front. Pharmacol. 7 (2016) 137.

[36] A. Ullah, C.M. Kim, G.M. Kim, Porous polymer coatings on metal microneedles for enhanced drug delivery, R. Soc. Open Sci. 5(4) (2018) 171609.

[37] B. Schepens, P.J. Vos, X. Saelens, K. van der Maaden, Vaccination with influenza hemagglutinin-loaded ceramic nanoporous microneedle arrays induces protective immune responses, Eur. J. Pharm. Biopharm. 136 (2019) 259-266.

[38] T.E. Andersen, A.J. Andersen, R.S. Petersen, L.H. Nielsen, S.S. Keller, Drug loaded biodegradable polymer microneedles fabricated by hot embossing, Microelectron. Eng. 195 (2018) 57-61.

[39] K. Ita, Dissolving microneedles for transdermal drug delivery: Advances and challenges, Biomed. Pharmacother. 93 (2017) 1116-1127.

[40] Y. Chen, B.Z. Chen, Q.L. Wang, X. Jin, X.D. Guo, Fabrication of coated polymer microneedles for transdermal drug delivery, J. Controlled Release 265 (2017) 14-21.

[41] K.S. Ahmed, X. Shan, J. Mao, L. Qiu, J. Chen, Derma roller® microneedles-mediated transdermal delivery of doxorubicin and celecoxib co-loaded liposomes for enhancing the anticancer effect, Mater. Sci. Eng. C 99 (2019) 1448-1458.

[42] T. Ilić, S. Savić, B. Batinić, B. Marković, M. Schmidberger, D. Lunter, M. Savić, S. Savić, Combined use of biocompatible nanoemulsions and solid microneedles to improve transport of a model NSAID across the skin: In vitro and in vivo studies, Eur. J. Pharm. Sci. 125 (2018) 110-119.

[43] A. Ahad, A.A. Al-Saleh, A.M. Al-Mohizea, F.I. Al-Jenoobi, M. Raish, A.E.B. Yassin, M.A. Alam, Pharmacodynamic study of eprosartan mesylate-loaded transfersomes Carbopol® gel under Dermaroller® on rats with methyl prednisolone acetate-induced hypertension, Biomed. Pharmacother. 89 (2017) 177-184.

[44] Y. He, C. Hong, J. Li, M.T. Howard, Y. Li, M.E. Turvey, D.S. Uppu, J.R. Martin, K. Zhang, D.J. Irvine, Synthetic Charge-Invertible Polymer for Rapid and Complete Implantation of Layer-by-Layer Microneedle Drug Films for Enhanced Transdermal Vaccination, ACS Nano 12(10) (2018) 10272-10280.

[45] P. Schipper, K. van der Maaden, V. Groeneveld, M. Ruigrok, S. Romeijn, S. Uleman, C. Oomens, G. Kersten, W. Jiskoot, J. Bouwstra, Diphtheria toxoid and N-trimethyl chitosan layer-by-layer coated pH-sensitive microneedles induce potent immune responses upon dermal vaccination in mice, J. Controlled Release 262 (2017) 28-36.

[46] Q.L. Wang, X.P. Zhang, B.Z. Chen, X.D. Guo, Dissolvable layered microneedles with core-shell structures for transdermal drug delivery, Mater. Sci. Eng. C 83 (2018) 143-147.

[47] K. van der Maaden, E. Sekerdag, P. Schipper, G. Kersten, W. Jiskoot, J. Bouwstra, Layer-by-layer assembly of inactivated poliovirus and N-trimethyl chitosan on pH-sensitive microneedles for dermal vaccination, Langmuir 31(31) (2015) 8654-8660.

[48] T.-M. Tuan-Mahmood, M.T. McCrudden, B.M. Torrisi, E. McAlister, M.J. Garland, T.R.R. Singh, R.F. Donnelly, Microneedles for intradermal and transdermal drug delivery, Eur. J. Pharm. Sci. 50(5) (2013) 623-637.

[49] R.F. Donnelly, T.R.R. Singh, M.J. Garland, K. Migalska, R. Majithiya, C.M. McCrudden, P.L. Kole, T.M.T. Mahmood, H.O. McCarthy, A.D. Woolfson, Hydrogel-forming microneedle arrays for enhanced transdermal drug delivery, Adv. Funct. Mater. 22(23) (2012) 4879-4890.

[50] J.G. Hardy, E. Larrañeta, R.F. Donnelly, N. McGoldrick, K. Migalska, M.T. McCrudden, N.J. Irwin, L. Donnelly, C.P. McCoy, Hydrogel-forming microneedle arrays made from light-responsive materials for on-demand transdermal drug delivery, Mol. Pharmaceutics 13(3) (2016) 907-914.

[51] X. Hong, L. Wei, F. Wu, Z. Wu, L. Chen, Z. Liu, W. Yuan, Dissolving and biodegradable microneedle technologies for transdermal sustained delivery of drug and vaccine, Drug Des., Dev. Ther. 7 (2013) 945.

[52] A.S. Rzhevskiy, T.R.R. Singh, R.F. Donnelly, Y.G. Anissimov, Microneedles as the technique of drug delivery enhancement in diverse organs and tissues, J. Controlled Release 270 (2018) 184-202.

[53] J. Banchereau, K. Palucka, Immunotherapy: Cancer vaccines on the move, Nat. Rev. Clin. Oncol. 15(1) (2018) 9-10.

[54] R.S. Riley, C.H. June, R. Langer, M.J. Mitchell, Delivery technologies for cancer immunotherapy, Nat Rev Drug Discov 18(3) (2019) 175-196.

[55] J.H. Kim, J.U. Shin, S.H. Kim, J.Y. Noh, H.R. Kim, J. Lee, H. Chu, K.Y. Jeong, K.H. Park, J.D. Kim, H.K. Kim, D.H. Jeong, T.S. Yong, J.W. Park, K.H. Lee, Successful transdermal allergen delivery and allergen-specific immunotherapy using biodegradable microneedle patches, Biomaterials 150 (2018) 38-48.

[56] Y. Ye, J. Wang, Q. Hu, G.M. Hochu, H. Xin, C. Wang, Z. Gu, Synergistic Transcutaneous Immunotherapy Enhances Antitumor Immune Responses through Delivery of Checkpoint Inhibitors, ACS Nano 10(9) (2016) 8956-63.

[57] J. Arya, M.R. Prausnitz, Microneedle patches for vaccination in developing countries, J. Controlled Release 240 (2016) 135-141.

[58] A. Makkouk, G.J. Weiner, Cancer immunotherapy and breaking immune tolerance: new approaches to an old challenge, Cancer Res. 75(1) (2015) 5-10.

[59] M. Leone, J. Mönkäre, J. Bouwstra, G. Kersten, Dissolving microneedle patches for dermal vaccination, Pharm. Res. 34(11) (2017) 2223-2240.

[60] D.J. Irvine, M.C. Hanson, K. Rakhra, T. Tokatlian, Synthetic nanoparticles for vaccines and immunotherapy, Chem. Rev. 115(19) (2015) 11109-11146.

[61] D. Wang, T. Wang, J. Liu, H. Yu, S. Jiao, B. Feng, F. Zhou, Y. Fu, Q. Yin, P. Zhang, Acid-activatable versatile micelleplexes for PD-L1 blockade-enhanced cancer photodynamic immunotherapy, Nano Lett. 16(9) (2016) 5503-5513.

[62] M. Zaric, O. Lyubomska, O. Touzelet, C. Poux, S. Al-Zahrani, F. Fay, L. Wallace, D. Terhorst, B. Malissen, S. Henri, Skin dendritic cell targeting via microneedle arrays laden with antigen-encapsulated poly-D, L-lactide-co-glycolide nanoparticles induces efficient antitumor and antiviral immune responses, ACS Nano 7(3) (2013) 2042-2055.

[63] N.W. Kim, S.-Y. Kim, J.E. Lee, Y. Yin, J.H. Lee, S.Y. Lim, E.S. Kim, H.T.T. Duong, H.K. Kim, S. Kim, Enhanced Cancer Vaccination by In Situ Nanomicelle-Generating Dissolving Microneedles, ACS Nano 12(10) (2018) 9702-9713.

[64] R.D. Weeratna, S.R. Makinen, M.J. McCluskie, H.L. Davis, TLR agonists as vaccine adjuvants: comparison of CpG ODN and Resiquimod (R-848), Vaccine 23(45) (2005) 5263-5270.

[65] Z.-x. Zhou, L. Sun, Immune effects of R848: evidences that suggest an essential role of TLR7/8-induced, Myd88-and NF-κB-dependent signaling in the antiviral immunity of Japanese flounder (Paralichthys olivaceus), Dev. Comp. Immunol. 49(1) (2015) 113-120.

[66] Y. Ye, J. Wang, Q. Hu, G.M. Hochu, H. Xin, C. Wang, Z. Gu, Synergistic transcutaneous immunotherapy enhances antitumor immune responses through delivery of checkpoint inhibitors, ACS nano 10(9) (2016) 8956-8963.

[67] S. Seton-Rogers, Anticancer drugs: Switching off immune suppression, Nat. Rev. Drug Discovery 16(1) (2016) 16.

[68] M.L.B. Salvadori, P.K.F. da Cunha Bianchi, L.H. Gebrim, R.S. Silva, J.R. Kfoury, Effect of the association of 1-methyl-DL-tryptophan with paclitaxel on the expression of indoleamine 2, 3-dioxygenase in cultured cancer cells from patients with breast cancer, Med. Oncol. 32(11) (2015) 248.

[69] C. Wang, Y. Ye, G.M. Hochu, H. Sadeghifar, Z. Gu, Enhanced cancer immunotherapy by microneedle patch-assisted delivery of anti-PD1 antibody, Nano Lett. 16(4) (2016) 2334-2340.

[70] C. Cui, H. Chen, B. Chen, T. Tan, Genipin cross-linked glucose oxidase and catalase multi-enzyme for gluconic acid synthesis, Appl. Biochem. Biotechnol. 181(2) (2017) 526-535.

[71] A.A. Ali, C.M. McCrudden, J. McCaffrey, J.W. McBride, G. Cole, N.J. Dunne, T. Robson, A. Kissenpfennig, R.F. Donnelly, H.O. McCarthy, DNA vaccination for cervical cancer; a novel technology platform of RALA mediated gene delivery via polymeric microneedles, Nanomedicine 13(3) (2017) 921-932.

[72] J. Pan, W. Ruan, M. Qin, Y. Long, T. Wan, K. Yu, Y. Zhai, C. Wu, Y. Xu, Intradermal delivery of STAT3 siRNA to treat melanoma via dissolving microneedles, Sci. Rep. 8(1) (2018) 1117.

[73] H. Yu, H. Lee, A. Herrmann, R. Buettner, R. Jove, Revisiting STAT3 signalling in cancer: new and unexpected biological functions, Nat. Rev. Cancer 14(11) (2014) 736.

[74] P.C. DeMuth, X. Su, R.E. Samuel, P.T. Hammond, D.J. Irvine, Nano-layered microneedles for transcutaneous delivery of polymer nanoparticles and plasmid DNA, Adv. Mater. 22(43) (2010) 4851-6.

[75] S.A. Tawde, L. Chablani, A. Akalkotkar, M.J. D'Souza, Evaluation of microparticulate ovarian cancer vaccine via transdermal route of delivery, J. Controlled Release 235 (2016) 147-154.

[76] S. Indermun, R. Luttge, Y.E. Choonara, P. Kumar, L.C. Du Toit, G. Modi, V. Pillay, Current advances in the fabrication of microneedles for transdermal delivery, J. Controlled Release 185 (2014) 130-138.

[77] X. Zhao, X. Li, P. Zhang, J. Du, Y. Wang, Tip-loaded fast-dissolving microneedle patches for photodynamic therapy of subcutaneous tumor, J. Controlled Release 286 (2018) 201-209.

[78] C.F. Thorn, C. Oshiro, S. Marsh, T. Hernandez-Boussard, H. McLeod, T.E. Klein, R.B. Altman, Doxorubicin pathways: pharmacodynamics and adverse effects, Pharmacogenet. Genomics 21(7) (2011) 440.

[79] R.S. Herbst, F.R. Khuri, Mode of action of docetaxel–a basis for combination with novel anticancer agents, Cancer Treat. Rev. 29(5) (2003) 407-415.

[80] P. Pei, F. Yang, J. Liu, H. Hu, X. Du, N. Hanagata, S. Zhao, Y. Zhu, Composite-dissolving microneedle patches for chemotherapy and photothermal therapy in superficial tumor treatment, Biomater. Sci. 6(6) (2018) 1414-1423.

[81] C. Shirata, J. Kaneko, Y. Inagaki, T. Kokudo, M. Sato, S. Kiritani, N. Akamatsu, J. Arita, Y. Sakamoto, K. Hasegawa, Near-infrared photothermal/photodynamic therapy with indocyanine

green induces apoptosis of hepatocellular carcinoma cells through oxidative stress, Sci. Rep. 7(1) (2017) 13958.

[82] Y. Hao, Y. Chen, M. Lei, T. Zhang, Y. Cao, J. Peng, L. Chen, Z. Qian, Near-Infrared Responsive PEGylated Gold Nanorod and Doxorubicin Loaded Dissolvable Hyaluronic Acid Microneedles for Human Epidermoid Cancer Therapy, Adv. Ther. 1(2) (2018) 1800008.

[83] A.F. Moreira, C.F. Rodrigues, C.A. Reis, E.C. Costa, P. Ferreira, I.J. Correia, Development of poly-2-ethyl-2-oxazoline coated gold-core silica shell nanorods for cancer chemo-photothermal therapy, Nanomedicine 13(20) (2018) 2611-2627.

[84] L. Dong, Y. Li, Z. Li, N. Xu, P. Liu, H. Du, Y. Zhang, Y. Huang, J. Zhu, G. Ren, Au nanocage-strengthened dissolving microneedles for chemo-photothermal combined therapy of superficial skin tumors, ACS Appl. Mater. Interfaces 10(11) (2018) 9247-9256.

[85] S.M. Davidson, O. Jonas, M.A. Keibler, H.W. Hou, A. Luengo, J.R. Mayers, J. Wyckoff, A.M. Del Rosario, M. Whitman, C.R. Chin, Direct evidence for cancer-cell-autonomous extracellular protein catabolism in pancreatic tumors, Nat. Med. 23(2) (2017) 235.

[86] H.X. Nguyen, B.D. Bozorg, Y. Kim, A. Wieber, G. Birk, D. Lubda, A.K. Banga, Poly (vinyl alcohol) microneedles: Fabrication, characterization, and application for transdermal drug delivery of doxorubicin, Eur. J. Pharm. Biopharm. 129 (2018) 88-103.

[87] A.K. Jain, C.H. Lee, H.S. Gill, 5-Aminolevulinic acid coated microneedles for photodynamic therapy of skin tumors, J. Controlled Release 239 (2016) 72-81.

[88] Y. Ma, S.E. Boese, Z. Luo, N. Nitin, H.S. Gill, Drug coated microneedles for minimally-invasive treatment of oral carcinomas: development and in vitro evaluation, Biomed Microdevices 17(2) (2015) 44.

[89] M.C. Chen, K.W. Wang, D.H. Chen, M.H. Ling, C.Y. Liu, Remotely triggered release of small molecules from LaB6@SiO2-loaded polycaprolactone microneedles, Acta Biomater. 13 (2015) 344-53.

[90] R.F. Donnelly, D.I. Morrow, P.A. McCarron, A.D. Woolfson, A. Morrissey, P. Juzenas, A. Juzeniene, V. Iani, H.O. McCarthy, J. Moan, Microneedle-mediated intradermal delivery of 5-aminolevulinic acid: potential for enhanced topical photodynamic therapy, J. Controlled Release 129(3) (2008) 154-62.

[91] X. Yang, M.X. Yang, B. Pang, M. Vara, Y.N. Xia, Gold Nanomaterials at Work in Biomedicine, Chem. Rev. 115(19) (2015) 10410-10488.

[92] X.H. Huang, P.K. Jain, I.H. El-Sayed, M.A. El-Sayed, Gold nanoparticles: interesting optical properties and recent applications in cancer diagnostic and therapy, Nanomedicine 2(5) (2007) 681-693.

[93] N. Li, P.X. Zhao, D. Astruc, Anisotropic Gold Nanoparticles: Synthesis, Properties, Applications, and Toxicity, Angew. Chem. Int. Edit. 53(7) (2014) 1756-1789.

[94] X. Huang, M.A. El-Sayed, Gold nanoparticles: Optical properties and implementations in cancer diagnosis and photothermal therapy, J. Adv. Res. 1(1) (2010) 13-28.

[95] X.H. Huang, P.K. Jain, I.H. El-Sayed, M.A. El-Sayed, Plasmonic photothermal therapy (PPTT) using gold nanoparticles, Lasers Med. Sci. 23(3) (2008) 217-228.

[96] S.B. Lee, H.W. Lee, T.D. Singh, Y. Li, S.K. Kim, S.J. Cho, S.-W. Lee, S.Y. Jeong, B.-C. Ahn, S. Choi, Visualization of macrophage recruitment to inflammation lesions using highly sensitive and stable radionuclide-embedded gold nanoparticles as a nuclear bio-imaging platform, Theranostics 7(4) (2017) 926.

[97] L. Jing, X. Liang, Z. Deng, S. Feng, X. Li, M. Huang, C. Li, Z. Dai, Prussian blue coated gold nanoparticles for simultaneous photoacoustic/CT bimodal imaging and photothermal ablation of cancer, Biomaterials 35(22) (2014) 5814-5821.

[98] A.K. Rengan, A.B. Bukhari, A. Pradhan, R. Malhotra, R. Banerjee, R. Srivastava, A. De, In vivo analysis of biodegradable liposome gold nanoparticles as efficient agents for photothermal therapy of cancer, Nano Lett. 15(2) (2015) 842-848.

[99] Z. Li, H. Huang, S. Tang, Y. Li, X.-F. Yu, H. Wang, P. Li, Z. Sun, H. Zhang, C. Liu, Small gold nanorods laden macrophages for enhanced tumor coverage in photothermal therapy, Biomaterials 74 (2016) 144-154.

[100] X. Cheng, R. Sun, L. Yin, Z. Chai, H. Shi, M. Gao, Light-Triggered Assembly of Gold Nanoparticles for Photothermal Therapy and Photoacoustic Imaging of Tumors In Vivo, Adv. Mater. 29(6) (2017).

[101] M. Sun, D. Peng, H. Hao, J. Hu, D. Wang, K. Wang, J. Liu, X. Guo, Y. Wei, W. Gao, Thermally Triggered in Situ Assembly of Gold Nanoparticles for Cancer Multimodal Imaging and Photothermal Therapy, ACS Appl. Mater. Interfaces 9(12) (2017) 10453-10460.

[102] J.C. Love, L.A. Estroff, J.K. Kriebel, R.G. Nuzzo, G.M. Whitesides, Self-assembled monolayers of thiolates on metals as a form of nanotechnology, Chem. Rev. 105(4) (2005) 1103-1169.

[103] J.Y. Liu, Q.A. Peng, Protein-gold nanoparticle interactions and their possible impact on biomedical applications, Acta Biomater. 55 (2017) 13-27.

[104] H.H. Deng, F.F. Wang, X.Q. Shi, H.P. Peng, A.L. Liu, X.H. Xia, W. Chen, Water-soluble gold nanoclusters prepared by protein-ligand interaction as fluorescent probe for real-time assay of pyrophosphatase activity, Biosens. Bioelectron. 83 (2016) 1-8.

[105] A. Gupta, D.F. Moyano, A. Parnsubsakul, A. Papadopoulos, L.-S. Wang, R.F. Landis, R. Das, V.M. Rotello, Ultrastable and biofunctionalizable gold nanoparticles, ACS Appl. Mater. Interfaces 8(22) (2016) 14096–14101.

[106] E.C. Dreaden, A.M. Alkilany, X. Huang, C.J. Murphy, M.A. El-Sayed, The golden age: gold nanoparticles for biomedicine, Chem. Soc. Rev. 41(7) (2012) 2740-2779.

[107] Y.-S. Chen, W. Frey, S. Kim, K. Homan, P. Kruizinga, K. Sokolov, S. Emelianov, Enhanced thermal stability of silica-coated gold nanorods for photoacoustic imaging and image-guided therapy, Opt. Express 18(9) (2010) 8867-8878.

[108] G. Jalani, M. Cerruti, Nano graphene oxide-wrapped gold nanostars as ultrasensitive and stable SERS nanoprobes, Nanoscale 7(22) (2015) 9990-9997.

[109] X. Huang, P.K. Jain, I.H. El-Sayed, M.A. El-Sayed, Gold nanoparticles: interesting optical properties and recent applications in cancer diagnostics and therapy, Nanomedicine 2(5) (2007) 681-693.

[110] W.G. Kreyling, A.M. Abdelmonem, Z. Ali, F. Alves, M. Geiser, N. Haberl, R. Hartmann, S. Hirn, D.J. De Aberasturi, K. Kantner, In vivo integrity of polymer-coated gold nanoparticles, Nat. Nanotechnol. 10(7) (2015) 619-623.

[111] P. Del Pino, F. Yang, B. Pelaz, Q. Zhang, K. Kantner, R. Hartmann, N. Martinez de Baroja, M. Gallego, M. Möller, B.B. Manshian, Basic physicochemical properties of polyethylene glycol coated gold nanoparticles that determine their interaction with cells, Angew. Chem., Int. Ed. 55(18) (2016) 5483-5487.

[112] Z. Zhang, C. Liu, J. Bai, C. Wu, Y. Xiao, Y. Li, J. Zheng, R. Yang, W. Tan, Silver nanoparticle gated, mesoporous silica coated gold nanorods (AuNR@ MS@ AgNPs): low premature release and multifunctional cancer theranostic platform, ACS Appl. Mater. Interfaces 7(11) (2015) 6211-6219.

[113] N.S. Abadeer, M.R. Brennan, W.L. Wilson, C.J. Murphy, Distance and plasmon wavelength dependent fluorescence of molecules bound to silica-coated gold nanorods, ACS nano 8(8) (2014) 8392-8406.

[114] H. Li, L.-L. Tan, P. Jia, Q.-L. Li, Y.-L. Sun, J. Zhang, Y.-Q. Ning, J. Yu, Y.-W. Yang, Near-infrared light-responsive supramolecular nanovalve based on mesoporous silica-coated gold nanorods, Chem. Sci. 5(7) (2014) 2804-2808.

[115] M. Colilla, A. Baeza, M. Vallet-Regí, Mesoporous silica nanoparticles for drug delivery and controlled release applications, The Sol-Gel Handbook-Synthesis, Characterization, and Applications: Synthesis, Characterization and Applications, 3-Volume Set (2015) 1309-1344.

[116] V. Mamaeva, C. Sahlgren, M. Lindén, Mesoporous silica nanoparticles in medicine—recent advances, Adv. Drug Delivery Rev. 65(5) (2013) 689-702.

[117] A.F. Moreira, V.M. Gaspar, E.C. Costa, D. de Melo-Diogo, P. Machado, C.M. Paquete, I.J. Correia, Preparation of end-capped pH-sensitive mesoporous silica nanocarriers for on-demand drug delivery, Eur. J. Pharm. Biopharm. 88(3) (2014) 1012-1025.

[118] I.I. Slowing, B.G. Trewyn, S. Giri, V.Y. Lin, Mesoporous silica nanoparticles for drug delivery and biosensing applications, Adv. Funct. Mater. 17(8) (2007) 1225-1236.

[119] J. Lu, M. Liong, J.I. Zink, F. Tamanoi, Mesoporous silica nanoparticles as a delivery system for hydrophobic anticancer drugs, Small 3(8) (2007) 1341-1346.

[120] M. Kanehara, Y. Watanabe, T. Teranishi, Thermally stable silica-coated hydrophobic gold nanoparticles, J. Nanosci. Nanotechnol. 9(1) (2009) 673-675.

[121] J. Chen, R. Zhang, L. Han, B. Tu, D. Zhao, One-pot synthesis of thermally stable gold@ mesoporous silica core-shell nanospheres with catalytic activity, Nano Res. 6(12) (2013) 871-879.

[122] R. Ghosh Chaudhuri, S. Paria, Core/shell nanoparticles: classes, properties, synthesis mechanisms, characterization, and applications, Chem. Rev. 112(4) (2011) 2373-2433.

[123] J.-T. Song, X.-Q. Yang, X.-S. Zhang, D.-M. Yan, Z.-Y. Wang, Y.-D. Zhao, Facile Synthesis of Gold Nanospheres Modified by Positively Charged Mesoporous Silica, Loaded with Near-Infrared Fluorescent Dye, for in Vivo X-ray Computed Tomography and Fluorescence Dual Mode Imaging, ACS Appl. Mater. Interfaces 7(31) (2015) 17287-17297.

[124] S. Liu, M. Han, Synthesis, functionalization, and bioconjugation of monodisperse, Silica-Coated gold nanoparticles: Robust bioprobes, Adv. Funct. Mater. 15(6) (2005) 961-967.

[125] Y. Kobayashi, M.A. Correa-Duarte, L.M. Liz-Marzán, Sol− gel processing of silica-coated gold nanoparticles, Langmuir 17(20) (2001) 6375-6379.

[126] E. Mine, A. Yamada, Y. Kobayashi, M. Konno, L.M. Liz-Marzán, Direct coating of gold nanoparticles with silica by a seeded polymerization technique, J. Colloid Interface Sci. 264(2) (2003) 385-390.

[127] F. Caruso, M. Spasova, V. Salgueiriño-Maceira, L. Liz-Marzán, Multilayer Assemblies of Silica-Encapsulated Gold Nanoparticles on Decomposable Colloid Templates, Adv. Mater. 13(14) (2001) 1090-1094.

[128] I. Pastoriza-Santos, J. Pérez-Juste, L.M. Liz-Marzán, Silica-coating and hydrophobation of CTAB-stabilized gold nanorods, Chem. Mater. 18(10) (2006) 2465-2467.

[129] N. Li, P. Zhao, D. Astruc, Anisotropic gold nanoparticles: synthesis, properties, applications, and toxicity, Angew. Chem., Int. Ed. 53(7) (2014) 1756-1789.

[130] P. Zhao, N. Li, D. Astruc, State of the art in gold nanoparticle synthesis, Coord. Chem. Rev. 257(3) (2013) 638-665.

[131] D.T. Nguyen, D.-J. Kim, K.-S. Kim, Controlled synthesis and biomolecular probe application of gold nanoparticles, Micron 42(3) (2011) 207-227.

[132] S. Ahmed, S. Ikram, Biosynthesis of gold nanoparticles: a green approach, J. Photochem. Photobiol., B 161 (2016) 141-153.

[133] T. Murakami, K. Tsuchida, Recent advances in inorganic nanoparticle-based drug delivery systems, Mini-Rev. Med. Chem. 8(2) (2008) 175-183.

[134] R.C. Ferrier Jr, G. Gines, D. Gasparutto, B. Pépin-Donat, P. Rannou, R.J. Composto, Tuning Optical Properties of Functionalized Gold Nanorods through Controlled Interactions with Organic Semiconductors, J. Phys. Chem. C 119(31) (2015) 17899-17909.

[135] E. Yasun, C. Li, I. Barut, D. Janvier, L. Qiu, C. Cui, W. Tan, BSA modification to reduce CTAB induced nonspecificity and cytotoxicity of aptamer-conjugated gold nanorods, Nanoscale 7(22) (2015) 10240-10248.

[136] J.S. DuChene, W. Niu, J.M. Abendroth, Q. Sun, W. Zhao, F. Huo, W.D. Wei, Halide anions as shape-directing agents for obtaining high-quality anisotropic gold nanostructures, Chem. Mater. 25(8) (2012) 1392-1399.

[137] L. Scarabelli, M. Coronado-Puchau, J.J. Giner-Casares, J. Langer, L.M. Liz-Marzán, Monodisperse gold nanotriangles: size control, large-scale self-assembly, and performance in surface-enhanced Raman scattering, ACS nano 8(6) (2014) 5833-5842.

[138] B. Pelaz, V. Grazu, A. Ibarra, C. Magen, P. del Pino, J.M. de la Fuente, Tailoring the synthesis and heating ability of gold nanoprisms for bioapplications, Langmuir 28(24) (2012) 8965-8970.

[139] F. Tian, F. Bonnier, A. Casey, A.E. Shanahan, H.J. Byrne, Surface enhanced Raman scattering with gold nanoparticles: effect of particle shape, Anal. Methods 6(22) (2014) 9116-9123.

[140] S.E. Lohse, C.J. Murphy, The quest for shape control: a history of gold nanorod synthesis, Chem. Mater 25(8) (2013) 1250-1261.

[141] K. Chandra, K.S. Culver, S.E. Werner, R.C. Lee, T.W. Odom, Manipulating the anisotropic structure of gold nanostars using good's buffers, Chem. Mater 28(18) (2016) 6763-6769.

[142] X. Xia, Y. Xia, Gold nanocages as multifunctional materials for nanomedicine, Front. Phys. 9(3) (2014) 378-384.

[143] Y. Hua, K. Chandra, D.H.M. Dam, G.P. Wiederrecht, T.W. Odom, Shape-dependent nonlinear optical properties of anisotropic gold nanoparticles, J. Phys. Chem. Lett. 6(24) (2015) 4904-4908.

[144] Y.-S. Chen, W. Frey, S. Kim, P. Kruizinga, K. Homan, S. Emelianov, Silica-coated gold nanorods as photoacoustic signal nanoamplifiers, Nano Lett. 11(2) (2011) 348-354.

[145] C. Argyo, V. Weiss, C. Bräuchle, T. Bein, Multifunctional mesoporous silica nanoparticles as a universal platform for drug delivery, Chem. Mater. 26(1) (2013) 435-451.

[146] A.F. Moreira, D.R. Dias, I.J. Correia, Stimuli-responsive mesoporous silica nanoparticles for cancer therapy: A review, Microporous Mesoporous Mater. 236 (2016) 141-157.

[147] S. Sreejith, J. Joseph, K.T. Nguyen, V.M. Murukeshan, S.W. Lye, Y. Zhao, Graphene oxide wrapping of gold–silica core–shell nanohybrids for photoacoustic signal generation and bimodal imaging, ChemNanoMat 1(1) (2015) 39-45.

[148] M. Hembury, C. Chiappini, S. Bertazzo, T.L. Kalber, G.L. Drisko, O. Ogunlade, S. Walker-Samuel, K.S. Krishna, C. Jumeaux, P. Beard, Gold–silica quantum rattles for multimodal imaging and therapy, Proc. Natl. Acad. Sci. 112(7) (2015) 1959-1964.

[149] J. Liu, C. Detrembleur, D. Pauw-Gillet, S. Mornet, C. Jérôme, E. Duguet, Gold Nanorods Coated with Mesoporous Silica Shell as Drug Delivery System for Remote Near Infrared Light-Activated Release and Potential Phototherapy, Small 11(19) (2015) 2323-2332.

[150] J. Yang, D. Shen, L. Zhou, W. Li, X. Li, C. Yao, R. Wang, A.M. El-Toni, F. Zhang, D. Zhao, Spatially confined fabrication of core–shell gold nanocages@ mesoporous silica for near-infrared controlled photothermal drug release, Chem. Mater. 25(15) (2013) 3030-3037.

[151] Y. Chen, H.R. Chen, D.P. Zeng, Y.B. Tian, F. Chen, J.W. Feng, J.L. Shi, Core/Shell Structured Hollow Mesoporous Nanocapsules: A Potential Platform for Simultaneous Cell Imaging and Anticancer Drug Delivery, ACS nano 4(10) (2010) 6001-6013.

[152] G. Terentyuk, E. Panfilova, V. Khanadeev, D. Chumakov, E. Genina, A. Bashkatov, V. Tuchin, A. Bucharskaya, G. Maslyakova, N. Khlebtsov, Gold nanorods with a hematoporphyrin-loaded silica shell for dual-modality photodynamic and photothermal treatment of tumors in vivo, Nano Res. 7(3) (2014) 325-337.

[153] S. Wang, P. Huang, L. Nie, R. Xing, D. Liu, Z. Wang, J. Lin, S. Chen, G. Niu, G. Lu, Single continuous wave laser induced photodynamic/plasmonic photothermal therapy using photosensitizer-functionalized gold nanostars, Adv. Mater. 25(22) (2013) 3055-3061.

[154] X.Y. Xu, W. Ho, X.Q. Zhang, N. Bertrand, O. Farokhzad, Cancer nanomedicine: from targeted delivery to combination therapy, Trends Mol. Med. 21(4) (2015) 223-232.

[155] R.R. Castillo, M. Colilla, M. Vallet-Regi, Advances in mesoporous silica-based nanocarriers for co-delivery and combination therapy against cancer, Expert Opin. Drug Del. 14(2) (2017) 229-243.

[156] W.W. Li, X.Y. Chen, Gold nanoparticles for photoacoustic imaging, Nanomedicine 10(2) (2015) 299-320.

[157] L.E. Cole, R.D. Ross, J.M.R. Tilley, T. Vargo-Gogola, R.K. Roeder, Gold nanoparticles as contrast agents in x-ray imaging and computed tomography, Nanomedicine 10(2) (2015) 321-341.

[158] D.R. Dias, A.F. Moreira, I.J. Correia, The effect of the shape of gold core–mesoporous silica shell nanoparticles on the cellular behavior and tumor spheroid penetration, J. Mater. Chem. B 4(47) (2016) 7630-7640.

[159] K. Hayashi, M. Nakamura, H. Miki, S. Ozaki, M. Abe, T. Matsumoto, K. Ishimura, Gold nanoparticle cluster–plasmon-enhanced fluorescent silica core–shell nanoparticles for X-ray computed tomography–fluorescence dual-mode imaging of tumors, Chem. Commun. 49(46) (2013) 5334-5336.

[160] S. Jain, D. Hirst, J. O'sullivan, Gold nanoparticles as novel agents for cancer therapy, Br. J. Radiol. 85(1010) (2012) 101-113.

[161] J.J. Pasternak, E.E. Williamson, Clinical pharmacology, uses, and adverse reactions of iodinated contrast agents: a primer for the non-radiologist, Mayo Clinic Proceedings, Elsevier, 2012, pp. 390-402.

[162] J. Hainfeld, D. Slatkin, T. Focella, H. Smilowitz, Gold nanoparticles: a new X-ray contrast agent, Br. J. Radiol. 79(939) (2006) 248-253.

[163] Y. Kobayashi, H. Inose, T. Nakagawa, Y. Kubota, K. Gonda, N. Ohuchi, X-ray imaging technique using colloid solution of Au/silica core-shell nanoparticles, J. Nanostruct. Chem. 3(1) (2013) 62.

[164] M.M. van Schooneveld, D.P. Cormode, R. Koole, J.T. van Wijngaarden, C. Calcagno, T. Skajaa, J. Hilhorst, D.C. Hart, Z.A. Fayad, W.J. Mulder, A fluorescent, paramagnetic and PEGylated gold/silica nanoparticle for MRI, CT and fluorescence imaging, Contrast Media Mol. Imaging 5(4) (2010) 231-236.

[165] M.F. Kircher, A. De La Zerda, J.V. Jokerst, C.L. Zavaleta, P.J. Kempen, E. Mittra, K. Pitter, R. Huang, C. Campos, F. Habte, A brain tumor molecular imaging strategy using a new triple-modality MRI-photoacoustic-Raman nanoparticle, Nat. Med. 18(5) (2012) 829-834.

[166] M. Ramasamy, J.-H. Lee, J. Lee, Development of gold nanoparticles coated with silica containing the antibiofilm drug cinnamaldehyde and their effects on pathogenic bacteria, Int. J. Nanomed. 12 (2017) 2813.

[167] E. Hemmer, A. Benayas, F. Légaré, F. Vetrone, Exploiting the biological windows: current perspectives on fluorescent bioprobes emitting above 1000 nm, Nanoscale Horiz. 1(3) (2016) 168-184.

[168] K.-S. Lee, M.A. El-Sayed, Dependence of the enhanced optical scattering efficiency relative to that of absorption for gold metal nanorods on aspect ratio, size, end-cap shape, and medium refractive index, J. Phys. Chem. B 109(43) (2005) 20331-20338.

[169] B. Hu, L.-P. Zhang, X.-W. Chen, J.-H. Wang, Gold nanorod-covered kanamycin-loaded hollow SiO 2 (HSKAu rod) nanocapsules for drug delivery and photothermal therapy on bacteria, Nanoscale 5(1) (2013) 246-252.

[170] W. Liu, Z. Zhu, K. Deng, Z. Li, Y. Zhou, H. Qiu, Y. Gao, S. Che, Z. Tang, Gold nanorod@ chiral mesoporous silica core–shell nanoparticles with unique optical properties, J. Am. Chem. Soc. 135(26) (2013) 9659-9664.

[171] N.-T. Chen, K.-C. Tang, M.-F. Chung, S.-H. Cheng, C.-M. Huang, C.-H. Chu, P.-T. Chou, J.S. Souris, C.-T. Chen, C.-Y. Mou, Enhanced plasmonic resonance energy transfer in

mesoporous silica-encased gold nanorod for two-photon-activated photodynamic therapy, Theranostics 4(8) (2014) 798.

[172] W. Li, X. Chen, Gold nanoparticles for photoacoustic imaging, Nanomedicine 10(2) (2015) 299-320.

[173] A.S. Monem, N. Elbialy, N. Mohamed, Mesoporous silica coated gold nanorods loaded doxorubicin for combined chemo–photothermal therapy, Int. J. Pharm. 470(1) (2014) 1-7.

[174] H. Zhou, H. Xu, X. Li, Y. Lv, T. Ma, S. Guo, Z. Huang, X. Wang, P. Xu, Dual targeting hyaluronic acid-RGD mesoporous silica coated gold nanorods for chemo-photothermal cancer therapy, Mater. Sci. Eng., C 81 (2017) 261-270.

[175] Y. Liu, M. Xu, Q. Chen, G. Guan, W. Hu, X. Zhao, M. Qiao, H. Hu, Y. Liang, H. Zhu, Gold nanorods/mesoporous silica-based nanocomposite as theranostic agents for targeting near-infrared imaging and photothermal therapy induced with laser, Int. J. Nanomed. 10 (2015) 4747.

[176] C. Lee, H.S. Hwang, S. Lee, B. Kim, J.O. Kim, K.T. Oh, E.S. Lee, H.G. Choi, Y.S. Youn, Rabies Virus-Inspired Silica-Coated Gold Nanorods as a Photothermal Therapeutic Platform for Treating Brain Tumors, Adv. Mater. 29(13) (2017).

[177] D. de Melo-Diogo, C. Pais-Silva, D.R. Dias, A.F. Moreira, I.J. Correia, Strategies to improve cancer photothermal therapy mediated by nanomaterials, Adv. Healthcare Mater. 6(10) (2017).

[178] Z. Zhang, L. Wang, J. Wang, X. Jiang, X. Li, Z. Hu, Y. Ji, X. Wu, C. Chen, Mesoporous silica-coated gold nanorods as a light-mediated multifunctional theranostic platform for cancer treatment, Adv. Mater. 24(11) (2012) 1418-1423.

[179] S. Shen, H. Tang, X. Zhang, J. Ren, Z. Pang, D. Wang, H. Gao, Y. Qian, X. Jiang, W. Yang, Targeting mesoporous silica-encapsulated gold nanorods for chemo-photothermal therapy with near-infrared radiation, Biomaterials 34(12) (2013) 3150-3158.

[180] S.-H. Seo, B.-M. Kim, A. Joe, H.-W. Han, X. Chen, Z. Cheng, E.-S. Jang, NIR-light-induced surface-enhanced Raman scattering for detection and photothermal/photodynamic therapy of cancer cells using methylene blue-embedded gold nanorod@ SiO 2 nanocomposites, Biomaterials 35(10) (2014) 3309-3318.

[181] G.F. Luo, W.H. Chen, Q. Lei, W.X. Qiu, Y.X. Liu, Y.J. Cheng, X.Z. Zhang, A Triple-Collaborative Strategy for High-Performance Tumor Therapy by Multifunctional Mesoporous Silica-Coated Gold Nanorods, Adv. Funct. Mater. 26(24) (2016) 4339-4350.

[182] J. Chen, B. Wiley, Z.Y. Li, D. Campbell, F. Saeki, H. Cang, L. Au, J. Lee, X. Li, Y. Xia, Gold nanocages: engineering their structure for biomedical applications, Adv. Mater. 17(18) (2005) 2255-2261.

[183] Z. Wang, Z. Chen, Z. Liu, P. Shi, K. Dong, E. Ju, J. Ren, X. Qu, A multi-stimuli responsive gold nanocage–hyaluronic platform for targeted photothermal and chemotherapy, Biomaterials 35(36) (2014) 9678-9688.

[184] Y. Sun, Y. Xia, Mechanistic study on the replacement reaction between silver nanostructures and chloroauric acid in aqueous medium, J. Am. Chem. Soc. 126(12) (2004) 3892-3901.

[185] B.N. Khlebtsov, V.A. Khanadeev, E.V. Panfilova, O.A. Inozemtseva, A.M. Burov, N.G. Khlebtsov, A simple Mie-type model for silica-coated gold nanocages, J. Quant. Spectrosc. Radiat. Transfer 121 (2013) 23-29.

[186] C.M. Cobley, J. Chen, E.C. Cho, L.V. Wang, Y. Xia, Gold nanostructures: a class of multifunctional materials for biomedical applications, Chem. Soc. Rev. 40(1) (2011) 44-56.

[187] B. Khlebtsov, E. Panfilova, V. Khanadeev, O. Bibikova, G. Terentyuk, A. Ivanov, V. Rumyantseva, I. Shilov, A. Ryabova, V. Loshchenov, Nanocomposites containing silica-coated gold–silver nanocages and Yb–2, 4-Dimethoxyhematoporphyrin: Multifunctional capability of IR-luminescence detection, photosensitization, and photothermolysis, ACS nano 5(9) (2011) 7077-7089.

[188] B.N. Khlebtsov, E.S. Tuchina, V.A. Khanadeev, E.V. Panfilova, P.O. Petrov, V.V. Tuchin, N.G. Khlebtsov, Enhanced photoinactivation of Staphylococcus aureus with nanocomposites containing plasmonic particles and hematoporphyrin, J. Biophotonics 6(4) (2013) 338-351.

[189] F. Hu, Y. Zhang, G. Chen, C. Li, Q. Wang, Double-Walled Au Nanocage/SiO2 Nanorattles: Integrating SERS Imaging, Drug Delivery and Photothermal Therapy, Small 11(8) (2015) 985-993.

[190] P. Pallavicini, E. Cabrini, M. Borzenkov, L. Sironi, G. Chirico, Applications of Gold Nanostars: Nanosensing, Thermal Therapy, Delivery Systems, Gold Nanostars, Springer2015, pp. 43-59.

[191] S. Atta, T.V. Tsoulos, L. Fabris, Shaping Gold Nanostar Electric Fields for Surface-Enhanced Raman Spectroscopy Enhancement via Silica Coating and Selective Etching, J. Phys. Chem. C 120(37) (2016) 20749-20758.

[192] S. Harmsen, R. Huang, M.A. Wall, H. Karabeber, J.M. Samii, M. Spaliviero, J.R. White, S. Monette, R. O'Connor, K.L. Pitter, Surface-enhanced resonance Raman scattering nanostars for high-precision cancer imaging, Sci. Transl. Med. 7(271) (2015) 271ra7-271ra7.

[193] A.M. Fales, H. Yuan, T. Vo-Dinh, Silica-Coated Gold Nanostars for Combined Surface-Enhanced Raman Scattering (SERS) Detection and Singlet-Oxygen Generation: A Potential Nanoplatform for Theranostics, Langmuir 27(19) (2011) 12186-12190.

[194] X. Li, L. Xing, K. Zheng, P. Wei, L. Du, M. Shen, X. Shi, Formation of Gold Nanostar-Coated Hollow Mesoporous Silica for Tumor Multimodality Imaging and Photothermal Therapy, ACS Appl. Mater. Interfaces 9(7) (2017) 5817-5827.

[195] J. An, X.-Q. Yang, K. Cheng, X.-L. Song, L. Zhang, C. Li, X.-S. Zhang, Y. Xuan, Y.-Y. Song, B.-Y. Fang, In vivo CT/Photoacoustic imaging and NIR-Triggered chemo-photothermal combined therapy based on a gold nanostar, mesoporous silica and thermo-sensitive liposomes composited nanoprobe, ACS Appl. Mater. Interfaces (2017).

[196] Q. Zeng, Y. Zhang, W. Ji, W. Ye, Y. Jiang, J. Song, Inhibitation of cellular toxicity of gold nanoparticles by surface encapsulation of silica shell for hepatocarcinoma cell application, ACS Appl. Mater. Interfaces 6(21) (2014) 19327-19335.

[197] A.S. Thakor, R. Luong, R. Paulmurugan, F.I. Lin, P. Kempen, C. Zavaleta, P. Chu, T.F. Massoud, R. Sinclair, S.S. Gambhir, The Fate and Toxicity of Raman-Active Silica-Gold Nanoparticles in Mice, Sci. Transl. Med. 3(79) (2011) 79ra33-79ra33.

[198] B. Gao, J. Xu, L. Shen, H. Chen, H.-j. Yang, A.-h. Li, W.-h. Xiao, Cellular uptake and intra-organ biodistribution of functionalized silica-coated gold nanorods, Mol. Imaging Biol. 18(5) (2016) 667-676.

[199] L.M. Liz-Marzán, M. Giersig, P. Mulvaney, Synthesis of nanosized gold− silica core− shell particles, Langmuir 12(18) (1996) 4329-4335.

[200] E. Mine, A. Yamada, Y. Kobayashi, M. Konno, L.M. Liz-Marzan, Direct coating of gold nanoparticles with silica by a seeded polymerization technique, J Colloid Interface Sci 264(2) (2003) 385-90.

[201] Y. Lu, Y. Yin, Z.-Y. Li, Y. Xia, Synthesis and self-assembly of Au@ SiO2 core− shell colloids, Nano Lett. 2(7) (2002) 785-788.

[202] M. Hu, X. Wang, G.V. Hartland, V. Salgueiriño-Maceira, L.M. Liz-Marzán, Heat dissipation in gold–silica core-shell nanoparticles, Chem. Phys. Lett. 372(5) (2003) 767-772.

[203] J.V. Jokerst, Z. Miao, C. Zavaleta, Z. Cheng, S.S. Gambhir, Affibody-functionalized gold-silica nanoparticles for Raman molecular imaging of the epidermal growth factor receptor, Small 7(5) (2011) 625-33.

[204] J. Liu, C. Detrembleur, M.C. De Pauw-Gillet, S. Mornet, C. Jerome, E. Duguet, Gold Nanorods Coated with Mesoporous Silica Shell as Drug Delivery System for Remote Near Infrared Light-Activated Release and Potential Phototherapy, Small 11(19) (2015) 2323-2332.

[205] Z.Y. Wang, S.F. Zong, J. Yang, J. Li, Y.P. Cui, Dual-mode probe based on mesoporous silica coated gold nanorods for targeting cancer cells, Biosens. Bioelectron. 26(6) (2011) 2883-2889.

[206] T.T. Zhao, H. Wu, S.Q. Yao, Q.H. Xu, G.Q. Xu, Nanocomposites Containing Gold Nanorods and Porphyrin-Doped Mesoporous Silica with Dual Capability of Two-Photon Imaging and Photosensitization, Langmuir 26(18) (2010) 14937-14942.

[207] O. Bibikova, A. Popov, A. Bykov, A. Prilepskii, M. Kinnunen, K. Kordas, V. Bogatyrev, N. Khlebtsov, S. Vainio, V. Tuchin, Optical properties of plasmon-resonant bare and silica-coated nanostars used for cell imaging, J. Biomed. Opt. 20(7) (2015) 076017-076017.

[208] V. Raghavan, C. O'Flatharta, R. Dwyer, A. Breathnach, H. Zafar, P. Dockery, A. Wheatley, I. Keogh, M. Leahy, M. Olivo, Dual plasmonic gold nanostars for photoacoustic imaging and photothermal therapy, Nanomedicine 12(5) (2017) 457-471.

Chapter 3

Research Work 1

Development of poly-2-ethyl-2-oxazoline coated gold-core silica shell nanorods for cancer chemo-photothermal therapy

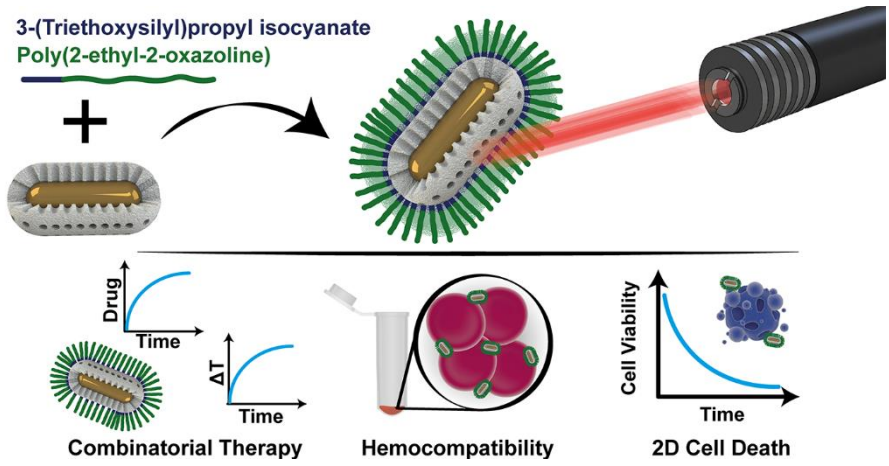

This chapter is based on the publication:

Moreira, A.F., Rodrigues, C. F., Reis, C. A., Costa, E. C., Ferreira, P., & Correia, I. J. (2018). Development of poly-2-ethyl-2-oxazoline coated gold-core silica shell nanorods for cancer chemo-photothermal therapy. Nanomedicine, 13(20), 2611-2627.

3.1. Abstract

Aim: Develop a new PEOZ-based coating for Dox-loaded AuMSS nanorods application in cancer chemo-PTT. **Methods:** PEOZ functionalized AuMSS nanorods were obtained through the chemical grafting on AuMSS of a PEOZ silane derivative. **Results:** The PEOZ chemical grafting on the surface of AuMSS nanorods allowed the neutralization of nanodevices' surface charge, from -30 mV to -15 mV, which improved nanoparticles' biocompatibility, namely by decreasing the blood hemolysis to negligible levels. *In vitro* antitumoral studies revealed that the combined treatment mediated by the PEOZ coated AuMSS nanorods result in a synergistic effect, allowing the complete eradication of cervical cancer cells. **Conclusion:** The application of the PEOZ coating improves the AuMSS nanorods performance as a multifunctional combinatorial therapy for cervical cancer.

Keywords: Combinatorial Therapy, Photothermal Therapy, Drug Delivery, Gold Core Silica Shell Nanorods, Cancer.

3.2. Introduction

Combinatorial therapies are considered one of the most promising approaches to treat cancer [1-4]. The conjugation of two or more therapeutic approaches for cancer has the potential to reduce the adverse side-effects while simultaneously maximizing the molecules tumoricidal activity by surpassing cancer cells resistance mechanisms [1]. One of the most explored combinatorial treatments involves the conjugation of chemotherapy with hyperthermia (*e.g.* PTT) mediated by nanomaterials [5-8]. Hyperthermia explores the application of high temperatures, superior to 39.5ºC, with the aim to induce damage or ultimately the cancer cells death [9, 10]. For that purpose, researchers have been employing nanomaterials that are able to mediate a temperature increase in response to specific stimuli such as magnetic field, ultrasounds and NIR radiation [7, 11, 12]. In this perspective, the utilization of NIR light is fundamental since it has a good tissue penetration and the body components have minimal or no absorption in this region of the electromagnetic spectrum, minimizing the therapy off-target interactions [13-15]. Among the different NIR light responsive nanomaterials, gold nanoparticles have been considered promising candidates for medical applications due to its plasmonic properties. Gold nanoparticles have been used as imaging agents (*i.e.* contrast enhancers for CT or MRI) or PTT agents (*i.e.* promoting the heat generation in response to NIR light) [16-18]. Further, gold nanomaterials are biocompatible, bioinert and present a high flexibility in terms of shape, size, and surface chemistry [19-22]. However, gold nanoparticles are prone to aggregate when in contact with biological fluids and suffer degradation when exposed to certain radiation wavelengths [23, 24]. Moreover, PTT mediated by NIR responsive nanomaterials loses efficiency gradually as the NIR light penetrates deeper into the tissues, thus depending from the tumor location, some tumor cells would receive sub-optimal laser exposure decreasing the therapeutic efficacy [22, 25]. To address these issues, researchers have been performing different surface modifications on gold nanomaterials, comprising polymeric, small molecules and silica coatings [2, 26-28]. Among them, the gold nanomaterials functionalization with a mesoporous silica shell (AuMSS) exhibit a great potential to efficiently achieve the combination between PTT and chemotherapy [29]. The mesoporous silica coating provides a biocompatible and chemically inert shell with a large surface area that can be modified with functional groups that confer to the nanodevice an enhanced colloidal stability, targeting or stimulus responsiveness [30, 31]. More importantly, the inclusion of the mesoporous silica shell stabilizes and protects the gold-core from degradation when exposed to NIR radiation and further improves the particle capacity to encapsulate and deliver bioactive molecules, specifically to cancer cells [26, 31-34].

In this work, it is reported for the first time the functionalization of AuMSS nanorods with PEOZ for the combinatorial therapy of cancer. PEOZ is a non-ionic, biocompatible and biodegradable polymer, highly soluble in water and displays a good temperature stability [35, 36]. Further, PEOZ reduces the unspecific interactions with serum proteins (*e.g.* albumin), opsonins and

complement system mediators. This steric protection provided by the PEOZ decreases the formation of the protein corona on the particles surface, reducing their recognition by the reticuloendothelial system and consequently increasing the nanoparticles blood circulation time [37]. An increased blood circulation time is of paramount importance for the nanoparticles reach the tumor region, extravasate through the defective vasculature and exert the desired therapeutic effect [38, 39]. The AuMSS post-synthesis modification was achieved by using 3-(triethoxysilyl)propyl isocyanate (TESPIC) to create a silane derivative of PEOZ (TPEOZ), thus allowing its condensation on the particle surface. The results revealed that the PEOZ grafting increased the AuMSS nanorods stability and biocompatibility. Further, the AuMSSs showed to be capable to simultaneous act as a drug delivery system and PTT agent leading to an improved therapeutic effect towards cervical cancer cells.

3.3. Materials and Methods

3.3.1. Materials

Hydrogen tetrachloroaurate (III) hydrate ($HAuCl_4$) was purchased from Alfa Aesar (Karlsruhe, Germany). TEOS was bought from Acros Organics (Geel, Belgium). Hexadecyltrimethylammonium bromide (CTAB) and tetrahydrofuran (THF) were obtained from Tokyo Chemical Industry (Tokyo, Japan). Hydrochloric acid (HCl) was acquired from Panreac (Barcelona, Spain). Methanol was gotten from VWR International (Carnaxide, Portugal). L-ascorbic acid (AA), silver nitrate ($AgNO_3$), Dulbecco's Modified Eagle medium-high glucose (DMEM-HG), Fluorescein-5-isothiocyanate (FITC), resazurin, phosphate-buffered saline (PBS) solution, ethanol, formaldehyde, paraformaldehyde, sodium borohydride ($NaBH_4$), TESPIC and trypsin were purchased from Sigma–Aldrich (Sintra, Portugal). HeLa cells (ATCC® CCL-2™) were acquired from ATCC (Middlesex, UK). Hoechst 33342® and wheat germ agglutinin conjugate Alexa 594® (WGA-Alexa Fluor® 594) were bought from Invitrogen (Carlsbad, CA). Dox was obtained from Carbosynth (Berkshire, UK). Fetal bovine serum was acquired to Biochrom AG (Berlin, Germany). Cell imaging plates were acquired from Ibidi GmbH (Munich, Germany). Cell culture t-flasks were obtained from Orange Scientific (Braine-l'Alleud, Belgium). PEOZ (Mw: 5,000 $g.mol^{-1}$) was acquired from Polysciences, Inc. (Bergstrasse, Germany).

3.3.2. Synthesis of AuMSS nanorods

Au-MSS rods were synthesized through a procedure that comprised three main steps [40, 41]. Initially, a seed solution was prepared by adding under stirring, 0.60 mL of $NaBH_4$ (0.01 M) to an aqueous solution containing 5 mL of CTAB (0.20 M) and 5.00 mL of $HAuCl_4$ (0.0005 M). Subsequently, the grow solution was prepared by adding, under stirring, 210 µL of AA (0.08 M) to an aqueous solution containing 15 mL of CTAB (0.20 M), 30 µL of $AgNO_3$ (0.10 M) and 300 µL of $HAuCl_4$ (0.05 M). Lastly, to produce the AuNRs, the seed solution was added to the growth solution and left at 30ºC for 16 h. The synthesis of the MSS was carried out by adapting the

method described by Gorelikov and colleagues [41]. Initially, AuNRs were centrifuged to remove the excess of CTAB and resuspended in ultrapure water. Subsequently, CTAB (0.01 M) was added and left under stirring overnight. Afterward, NaOH (0.10 M) was added to the solution and mixed for 30 min. Then, 30 µL of a TEOS (20% v/v) solution in methanol were added to the sample. This step was repeated three times with 30 min intervals and the solution was left under stirring for 24 h. The final solution was centrifuged at 12,000 g for 20 min and washed several times with ultrapure water to recover the AuMSS nanorods. Then, the removal of the CTAB surfactant template from nanoparticles was performed by adapting a solvent based approach, already described by Moreira and co-workers [34].

3.3.3. AuMSS nanorods' functionalization with PEOZ

PEOZ-silane derivative was produced through a hydrogen-transfer nucleophilic addition reaction between the hydroxyl groups of PEOZ and isocyanate groups of TESPIC [42]. Before the reaction, 500 mg of PEOZ were dried at 50°C in a vacuum oven for 18 h. Then, the dried PEOZ was dissolved in 60 mL of dry THF under a nitrogen atmosphere by vigorous stirring at 60°C for 6 h. Afterward, 100 µL of TESPIC were added to the reaction mixture and stirred for further 24 h. Subsequently, the THF was removed by rotary evaporation and the TESPIC modified PEOZ (TPEOZ) polymer was further purified by performing dialysis in ultrapure water.

The TPEOZ linking to the AuMSS nanorods was promoted by adapting a method from He and colleagues [42]. Briefly, 50 mg of AuMSS were dispersed in 30 mL of an ethanol solution (33% v/v) at pH 4. Afterward, 50 mg of TPEOZ were also dissolved in 30 mL of an ethanol solution (33% v/v) at pH 4 and added dropwise to the particles' solution under magnetic agitation (1,000 rpm). After 24 h, the modified nanoparticles were recovered by centrifugation (12,000 g for 15 min) and washed with ultrapure water. To remove the unreacted polymer chains, the TPEOZ modified AuMSSs (AuMSS_TPEOZ) were dialysate (molecular weight cut-off 10,000 Da) for 24 h in ultrapure water.

3.3.4. Drug loading

The Dox loading on AuMSS or AuMSS_TPEOZ nanoparticles was accomplished through the impregnation of the particles in a Dox solution [26]. Briefly, AuMSS or AuMSS_TPEOZ were resuspended in 5 mL of methanol containing Dox (40 $\mu g.mL^{-1}$). The solution was then sonicated for 15 min and stirred for 48 h at room temperature. Afterward, the drug-loaded nanoparticles (AuMSS/Dox and AuMSS_TPEOZ/Dox) were recovered by centrifugation at 18,000 g, for 30 min and freeze-dried. The supernatant was stored to determine the amount of drug loaded within nanocarriers. The Dox content in the nanoparticles was calculated by measuring the supernatant absorbance at 485 nm, using a UV-vis Spectrophotometer (Thermo Scientific Evolution™ 201 Bio UV-Vis Spectrophotometer, Thermo Fisher Scientific Inc., USA), and a

calibration curve (Abs = 16.715C - 0.0005; r^2 = 0.9971). The encapsulation efficiency (E.E.) of AuMSS or AuMSS_TPEOZ was calculated through the equation (3.1):

$$E.E.(\%) = \frac{(Initial\ drug\ weight - Drug\ weight\ in\ supernatant)}{Initial\ drug\ weight} \times 100 \quad \text{Eq. (3.1)}$$

3.3.5. *In vitro* drug release

The characterization of the drug release profile of the nanocarriers was performed according to a method previously described in the literature [43]. Briefly, the AuMSS or AuMSS_TPEOZ were resuspended in PBS and inserted in a Float-A-Lyzer dialysis bag with a molecular cut-off of 1,000 Da. The dialysis was performed at 37ºC, under magnetic stirring in 10 mL of PBS solution, at pH 5.6 or 7.4. At different time points, 1 mL of samples was collected, and the same volume of fresh PBS was added to the dialysis medium, in order to maintain the PBS volume constant during the experiment. The Dox content was measured by the above-described UV-vis method.

3.3.6. Evaluation of the AuMSS nanorods' PTT capacity

The evaluation of the *in vitro* PTT capacity of AuMSS or AuMSS_TPEOZ was performed as previously reported in the literature [44, 45]. Briefly, AuMSS or AuMSS_TPEOZ at 200 $\mu g.mL^{-1}$ in PBS were irradiated with a NIR laser (808 nm, 1.7 $W.cm^{-2}$). The temperature variation of the solution was measured at different time points (from 1 up to 10 min) by using a thermocouple sensor with an accuracy of 0.1ºC. A control group without the particles was also irradiated and the temperature variation was monitored.

3.3.7. Characterization of the AuMSS nanorods' physicochemical properties

The nanoparticles morphology was analyzed by Transmission Electron Microscopy (TEM – Hitachi-HT7700, Japan). The nanoparticles samples were placed on formvar-coated copper grids and allowed to dry at room temperature, then the images were acquired at an accelerating voltage of 100 kV. After image acquisition, the nanoparticles gold core length and width, silica shell thickness and total size were measured by using a specific software (ImageJ 2.0.0, NIH Image, USA). The success of AuMSS nanorods synthesis and NIR absorption capacity was evaluated by acquiring the UV-vis spectra in an UV-vis Spectrophotometer (Thermo Scientific Evolution™ 201 Bio UV-vis Spectrophotometer, Thermo Fisher Scientific Inc., USA) at 300 $nm.min^{-1}$ scanning rate, with a wavelength range from 200 to 1,100 nm. The AuMSS nanorods purification efficacy was assessed by acquiring the Fourier Transformed Infrared Spectroscopy (FTIR) spectra in a Nicolet iS10 spectrometer, with a 4 cm^{-1} spectral resolution from 600 to 4,000 nm (Thermo Scientific Inc., Massachusetts, USA). Further, FTIR and Thermogravimetric Analysis (TGA) were performed to evaluate the particles surface

modification with TPEOZ derivative. Briefly, TGA analysis were carried out in a TGA equipment SDT Q500 (Thermal Analysis (TA) Instruments, Delaware, USA) and the samples were heated from room temperature to 600ºC at a heating rate of 10ºC.min^{-1} under nitrogen purge with a flow rate of 100 mL.min^{-1}. The measurement of AuMSS and AuMSS_TPEOZ zeta potential was performed by using a Zetasizer Nano ZS equipment (Malvern Instruments, Worcestershire, UK).

3.3.8. Biocompatibility assays

The biocompatibility of AuMSS and AuMSS_TPEOZ was assessed by incubating the nanomaterials with HeLa cells. Then, a resazurin-based assay was performed to evaluate cells viability in the presence of nanomaterials [34]. Briefly, HeLa cells were seeded into a 96-well flat bottom culture plates at a density of 10,000 cells per well. During 24 h, cells were cultured at 37°C in a humid atmosphere containing 5% CO_2. After this period, the cells were incubated with different concentrations of AuMSSs or AuMSS_TPEOZ, ranging from 25 to 200 μg.mL^{-1}. After 24, 48 and 72 h of exposure, the culture medium was replaced and cells were incubated with 10% (v/v) of resazurin (1 mg.mL^{-1}), at 37ºC and 5% CO_2, during 4 h. The produced resorufin was then quantified with a spectrofluorometer (Spectramax Gemini XS, Molecular Devices LLC, USA) at an excitation/emission wavelength of λ_{ex}=560 nm and λ_{em}=590 nm. The effect of nanoparticles in HeLa cells was also monitored by acquiring optical microscopy images in an Olympus CX41 inverted optical microscope equipped with an Olympus SP-500 UZ digital camera. Cells incubated with absolute (100% v/v) ethanol were used as positive control (K^+) and cells without being exposed to MSNs samples were used as negative controls (K^-).

3.3.9. Cells' migration ability

In order to evaluate the influence of nanoparticles in the HeLa cells migration ability, the *in vitro* wound closure assay was performed [2]. Briefly, HeLa cells were seeded on 12-well flat bottom culture plates at a density of 100,000 cells per well, with 2 mL of medium. Cells were maintained in culture (37°C, in a humidified atmosphere with 5% CO_2), until cell confluence was reached. After that, the medium was removed, and a gap was created by using the micropipette tip. Then, cells were incubated with AuMSS or AuMSS_TPEOZ nanoparticles (50, 100 or 200 μg.mL^{-1}) up to 72 h, whereas cells non-treated with nanoparticles were used as the control group. At predetermined time points, images were captured by using an Olympus CX41 inverted optical microscope equipped with an Olympus SP-500 UZ digital camera and the cell migration distance was measured using ImageJ software (Image J 2.0.0, NIH Image, USA).

3.3.10. Hemolysis assay

Hemolysis experiments were performed according to previous reports [46, 47]. EDTA stabilized blood samples were freshly obtained from adult mice. Initially, the whole blood samples were centrifuged at 500g, for 5 min, at 4°C to recover the red blood cells (RBCs). Then, the RBCs were washed three times with NaCl solution (150 mM). Afterward, the RBCs were diluted in

PBS, distributed by the test tubes and centrifuged. Subsequently, 1 mL of AuMSS or AuMSS_TPEOZ solutions in PBS at different concentrations (50, 100 and 200 μg.mL^{-1}) were added to the RBC suspension. Moreover, positive (K^+) and negative (K^-) control samples were prepared by adding 1 mL of Triton-X 100 and PBS, respectively. Then, the samples were incubated at room temperature for 4 and 24 h. The samples were slightly shaken once for every 30 min to resuspend the RBCs and particles. After the incubation period, the samples were centrifuged at 500 g for 5 min, at 4ºC and 100 μL of supernatants were transferred to a 96-well plate to measure the hemoglobin absorbance at 570 nm. RBCs hemolysis percentage RBCs was calculated using the equation 3.2:

$$Hemolysis\ (\%) = \frac{Sample\ Abs - Negative\ Control\ Abs}{Positive\ Control\ Abs - Negative\ Control\ Abs} \quad \text{Eq.(3.2)}$$

3.3.11. AuMSS nanorods' cellular uptake

The AuMSS uptake by HeLa cells was assessed by fluorescence spectroscopy, by adapting a method previously described in the literature [48]. Briefly, HeLa cells were seeded at a density of 10,000 cells per well in 96-well flat bottom culture plates. During 24 h, cells were cultured at 37ºC in a humid atmosphere containing 5% CO_2. After this period, cells were washed with Krebs Ringer buffer and incubated with free Dox (3 μM), AuMSS/Dox or AuMSS_TPEOZ/Dox at a concentration of 100 μg.mL^{-1}. After 4 h of incubation exposure, cells were washed with ice-cold Krebs Ringer buffer and lysed with 1% Triton X-100 in Krebs Ringer buffer, for 30 min, at 37°C. Then, the Dox fluorescence was quantified with a spectrofluorometer (Spectramax Gemini XS, Molecular Devices LLC, USA) at an excitation/emission wavelength of λ_{ex} =480 nm and λ_{em}=570 nm. Cells only incubated with Krebs Ringer buffer were used as a negative control.

To further confirm the uptake results, Confocal Laser Scanning Microscopy (CLSM) was performed to confirm the nanoparticles internalization by HeLa cells [49]. To accomplish that, 20,000 HeLa cells were seeded on μ-Slide 8 well Ibidi imaging plates (Ibidi GmbH, Germany), and incubated at 37ºC in 5% CO_2 humidified atmosphere. After 24 h, cells were exposed to uncoated or coated FITC tagged or Dox-loaded AuMSS at a concentration of 100 μg.mL^{-1}, during 4 h. After incubation, cells were washed with PBS, fixed with paraformaldehyde 4% (w/v), for 15 min, and rinsed again with PBS. Then, cells were treated with WGA-Alexa Fluor® 594 for cell cytoplasm staining and the cell nucleus was labeled with Hoechst 33342®. Imaging experiments were performed in multi-track mode on a confocal microscope (Zeiss LSM 710, Carl Zeiss, Germany), where consecutive z-stacks were acquired. 3D reconstructions and image analysis were performed in Zeiss Zen 2010 software.

3.3.12. AuMSS nanorods' *in vitro* cytotoxic activity

The AuMSSs cytotoxic effect was evaluated by the resazurin assay [50]. Briefly, 10,000 HeLa cells were seeded in 96-well plates containing DMEM-HG culture medium. After 24 h of culture,

free Dox or different particle formulations AuMSS or AuMSS_TPEOZ (with or without Dox) were added to HeLa cells. After 6 h, the cells were irradiated with a laser (808 nm, 1.7 $W.cm^{-2}$ for 5 min). After 24 h of incubation, the cells viability was assessed by using the resazurin assay. Cells incubated with ethanol (99.9% v/v) were used as positive control (K^+) whereas cells without being exposed to microparticle samples were used as negative controls (K^-).

3.3.13. Statistical analysis

All data are presented as the mean±standard deviation (s.d.). One-way analysis of variance (ANOVA) with the Student–Newman–Keuls post-test was used to compare the results obtained for the different groups. A p-value lower than 0.05 (*$p<0.05$) was considered statistically significant. Statistical analysis was performed using GraphPad Prism v.6.0 software (Trial version, GraphPadSoftware, CA, USA).

3.4. Results

3.4.1. AuMSS nanorods' physicochemical characterization

The AuMSS successful production and particle size was evaluated through TEM. The AuMSS nanorods displayed a homogeneous distribution and are organized in a single gold-core coated with a uniform silica shell (Figure 3.1 A and B). Furthermore, the gold core presented a mean length and width of 49±7 and 14±2 nm, respectively, that corresponds to an A.R. of 3.5 (Figure 3.1 A and C). Moreover, the Au-MSS nanorods presented a mean mesoporous silica shell thickness of 23±2 nm resulting in particles with a total length and width of 84±10 and 56±5 nm (Figure 3.1 D). Furthermore, the TEM images of AuMSS_TPEOZ nanorods do not show any significant variations on the particle overall size (Figure 3.1 A). However, the surface charge measurements show a neutralization of the particles' zeta potential from -30 mV to -15 mV after the surface functionalization with TPEOZ (Figure 3.1 E).

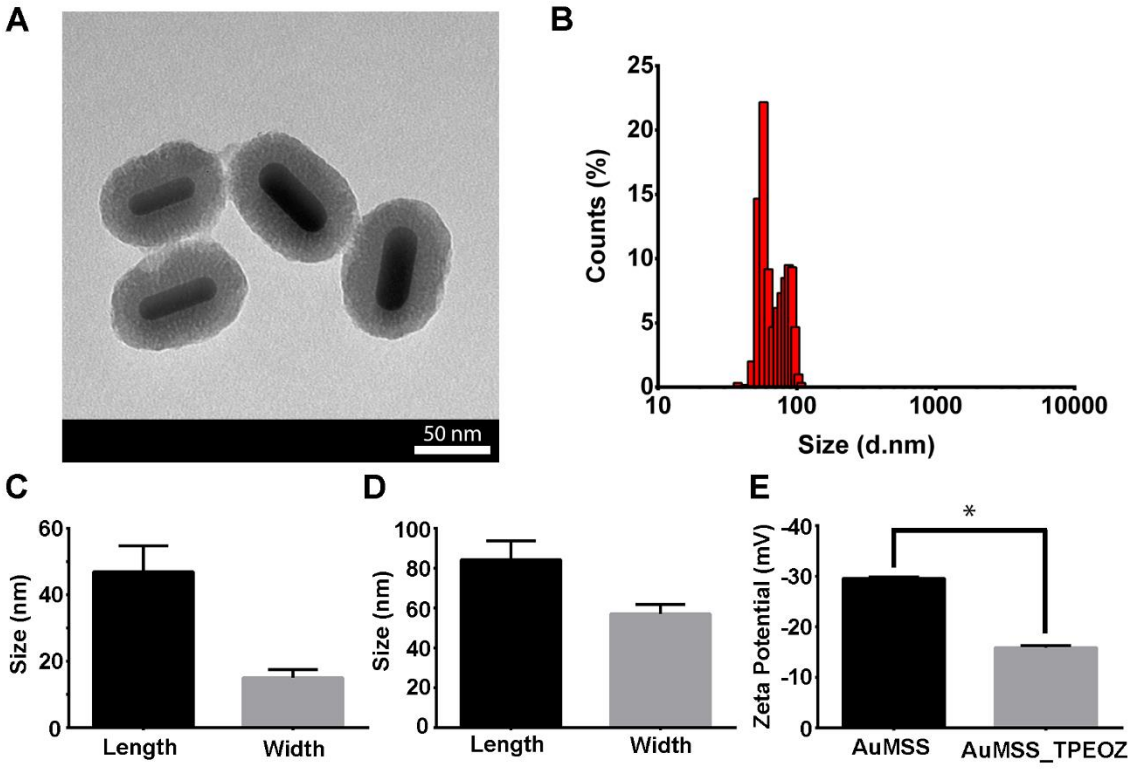

Figure 3.1 - Size and surface charge analysis of AuMSS and AuMSS_TPEOZ. (A) TEM image of AuMSS_TPEOZ nanorods. (B) AuMSS size distribution (length and width included), n=300. Size analysis of the gold-core (C) and AuMSS (D), n=300. (E) Surface charge analysis of AuMSS and AuMSS_TPEOZ. Data are presented as mean±s.d., *p<0.05, n=3.

The AuMSS nanorods modification with the TPEOZ was further confirmed by FTIR (Figure 3.2 A). The AuMSS spectra show the characteristic peaks of the mesoporous silica shell, in the 1,100 to 750 cm^{-1} region, that corresponds to Si-O-Si, Si-O and Si-OH vibrations [34]. In the AuMSS_TPEOZ spectra the PEOZ characteristic peaks are observed at 1,650 cm^{-1} (assigned to the vibration of the amide bond) and at the 2,900 cm^{-1} region corresponding to the C-H stretch of PEOZ [51]. Moreover, the successful grafting of the silane-modified PEOZ on the surface of nanorods was also confirmed by the increase of the ratio between the Si-O-Si peak at 1,045 cm^{-1} and Si-OH peak at 950 cm^{-1}. Additionally, the Au-MSS nanorods polymeric content was determined by performing TGA (Figure 3.2 B). The TGA curve show a 30% weight loss for the AuMSS_TPEOZ nanorods whereas the AuMSS presented a minimal weight variation with the temperature increase up to 600ºC.

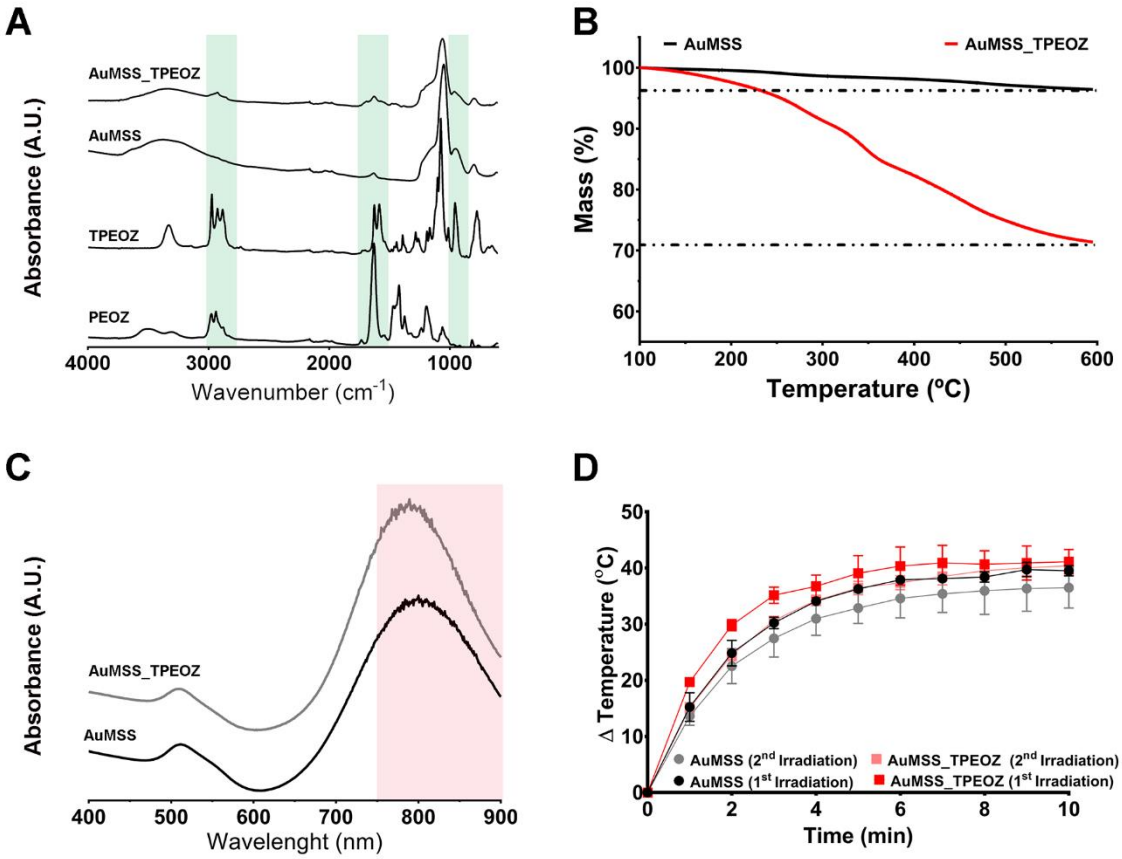

Figure 3.2 - Physicochemical characterization of AuMSS derivatives. (A) FTIR spectra of PEOZ, TPEOZ, AuMSS, and AuMSS_TPEOZ. (B) TGA analysis of AuMSS and AuMSS_TPEOZ nanorods. (C) UV-vis spectra of AuMSS and AuMSS_TPEOZ nanorods. (D) Temperature variation curve when AuMSS or AuMSS_TPEOZ were irradiated with NIR light (808 nm, 1.7 $W.cm^{-2}$, 10 min). Data are presented as mean±s.d., n=3.

The UV spectra of both AuMSS and AuMSS_TPEOZ (Figure 3.2 C) show the characteristic peaks of gold nanorods at 500 nm and close to 800 nm. Afterward, the PTT ability of AuMSS and AuMSS_TPEOZ, at a concentration of 200 $\mu g.mL^{-1}$, was evaluated by measuring the temperature variations upon irradiation with an 808 nm NIR light for 1 up to 10 min (Figure 3.2 D). Both formulations presented a similar behavior, with a pronounced temperature increase (ΔT of 35-40ºC) until 5 min of irradiation that stabilized until the end of the experiment (Figure 3.2 D). Further, no significant changes in the nanorods PTT ability were observed after a second irradiation session.

3.4.2. Analysis of the AuMSS nanorods' drug loading and release profile

The AuMSS_TPEOZ potential application in the encapsulation of bioactive molecules was investigated using Dox (Figure 3.3 A). The obtained results show that AuMSS nanorods can encapsulate 17 µg of Dox per particle mg, whereas the AuMSS_TPEOZ appear to present a slightly higher Dox encapsulation with 18 µg of Dox per particle mg. These values translate to

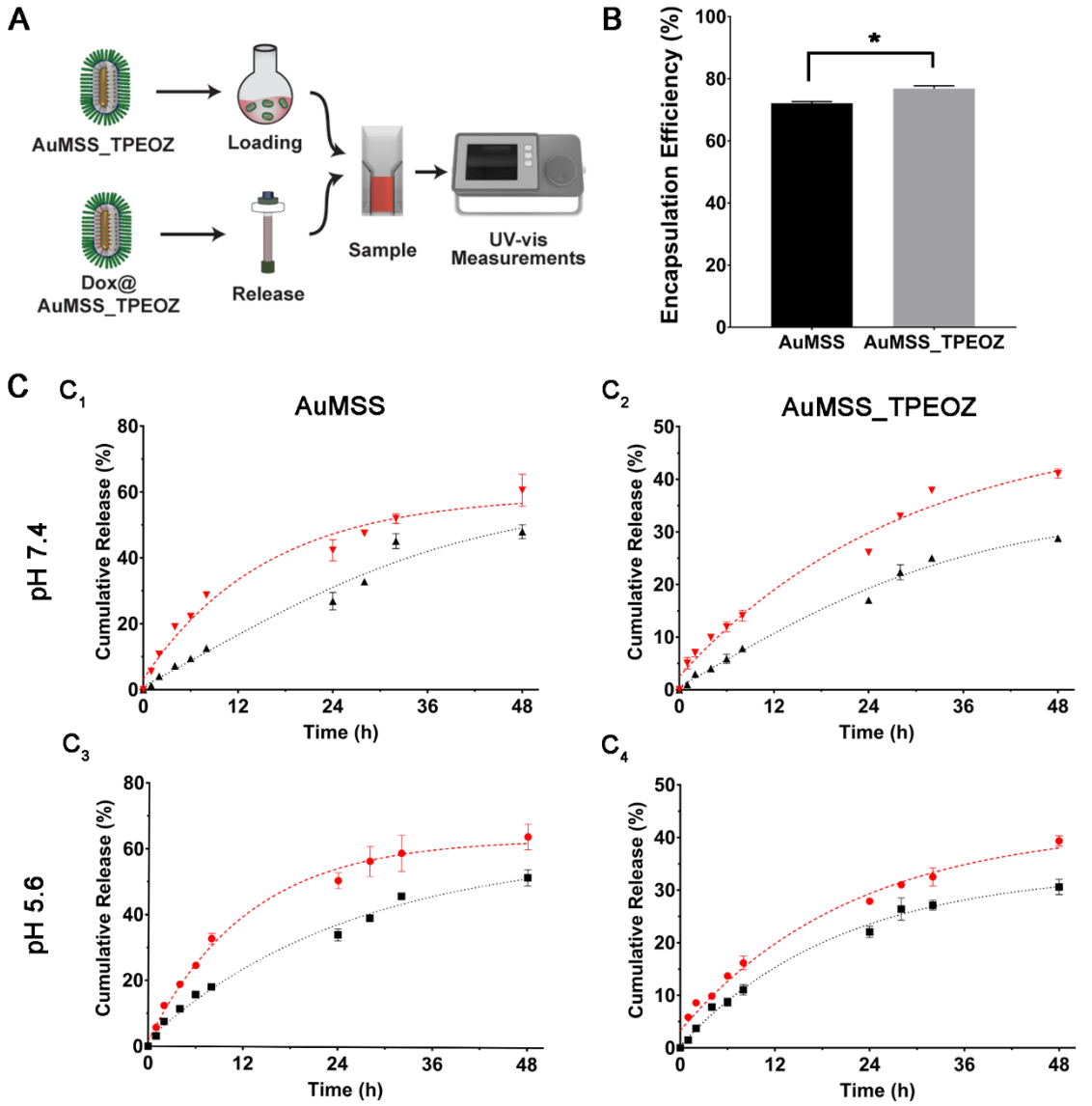

Figure 3.3 - Characterization of Dox E.E. and release profile. (A) Schematics of the drug loading and release methodology. (B) Dox E.E. on AuMSS and AuMSS_TPEOZ nanorods. AuMSS (C1 and C3) and AuMSS_TPEOZ (C2 and C4) Dox cumulative release at pH 5.6 and 7.4, with (red line) or without (black line) NIR laser irradiation. Data are presented as mean±s.d., n=3. Student's t-test was used to compare the results obtained in (B), *p<0.05.

encapsulation efficiencies of 72% for AuMSS and 76% for AuMSS_TPEOZ nanorods (Figure 3.3 B). After the Dox loading, the release profile of the AuMSS/Dox and AuMSS_TPEOZ/Dox was characterized at two pH values, 5.6 (to simulate the tumor microenvironment) and 7.4 (to simulate physiological conditions) with or without NIR laser irradiation [52-55]. The obtained results (Figure 3.3 C) show that the total amount of Dox released is not significantly affected by the pH variation. However, the particles incubated in acidic pH present a faster drug release in the initial hours. The AuMSS nanorods released 35% of the drug when incubated 24 h at pH 5.6, whereas only 26% of the drug was released during the same period at pH 7.4. Further, the inclusion of the PEOZ polymer shell resulted in a slower and controlled drug release, 50% of

drug released for AuMSS and 30% for AuMSS_TPEOZ nanorods. Moreover, the NIR laser irradiation for 5 min increased the drug release from the nanorods, around of 65% of drug was released from AuMSS and 40% for AuMSS_TPEOZ (Figure 3.3 C).

3.4.3. Characterization of the AuMSS nanorods' biocompatibility

Before assessing the biological performance of AuMSS and AuMSS_TPEOZ nanorods, the biocompatibility of both materials was evaluated using HeLa cells. The results revealed that HeLa cells treated with AuMSS or AuMSS_TPEOZ nanorods up to 200 $\mu g.mL^{-1}$ present a cell viability close to 100% (Figure 3.4 A and B). Further, no alterations in cell morphology were observed in the optical microscopy images (Figure 3.4 C).

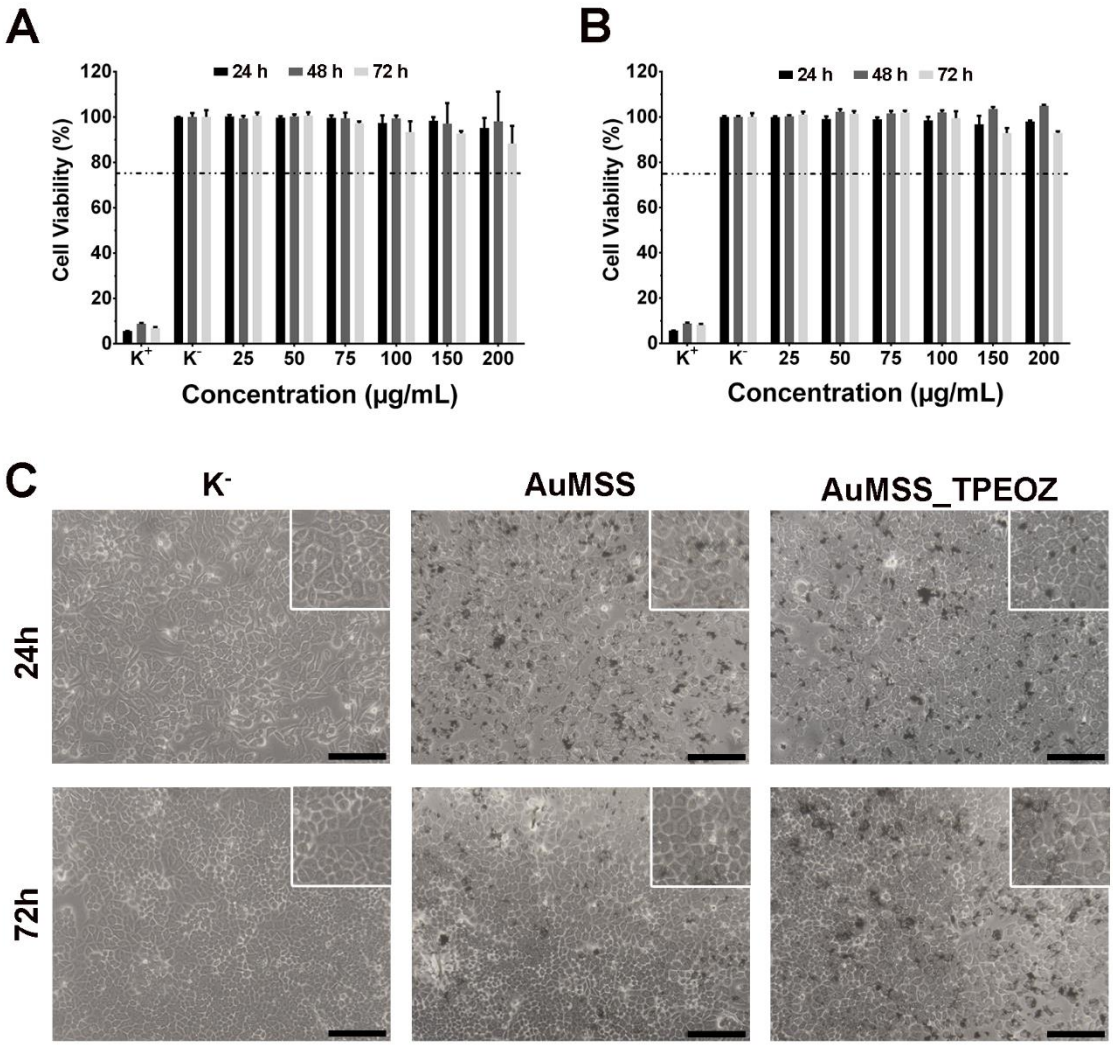

Figure 3.4 - Evaluation of the AuMSS derivatives biocompatibility in HeLa cells at 24, 48 and 72 h. Biocompatibility analysis for AuMSS (A) and AuMSS_TPEOZ (B) nanorods. Optical microscopy images of cells incubated with AuMSS or AuMSS_TPEOZ nanorods (C), insert shows a 1.6x ampliation of the images. Scale bars corresponds to 200 µm. Positive control (K^+): cells treated with ethanol; Negative control (K^-): cells without nanoparticles incubation. Data are presented as mean±s.d., n=5.

To further characterize the biocompatibility of AuMSS derivatives, the nanoparticles effect on the HeLa cells migration was also evaluated (Figure 3.5 A, 3.5 B). As can be observed, the migration behavior of HeLa cells incubated with AuMSS or AuMSS_TPEOZ was similar to that of the control group, *i.e.* non-treated cells. In fact, all the test groups presented the cell gap almost closed after 72 h of incubation even at a nanoparticle concentration of 200 $\mu g.mL^{-1}$. Moreover, the possible influence of the PEOZ inclusion on the AuMSS biocompatibility was also evaluated by studying the nanorods hemocompatibility (Figure 3.5 C and D). For that purpose, the erythrocytes lysis was quantified upon incubation with AuMSS or AuMSS_TPEOZ at concentrations up to 200 $\mu g.mL^{-1}$.

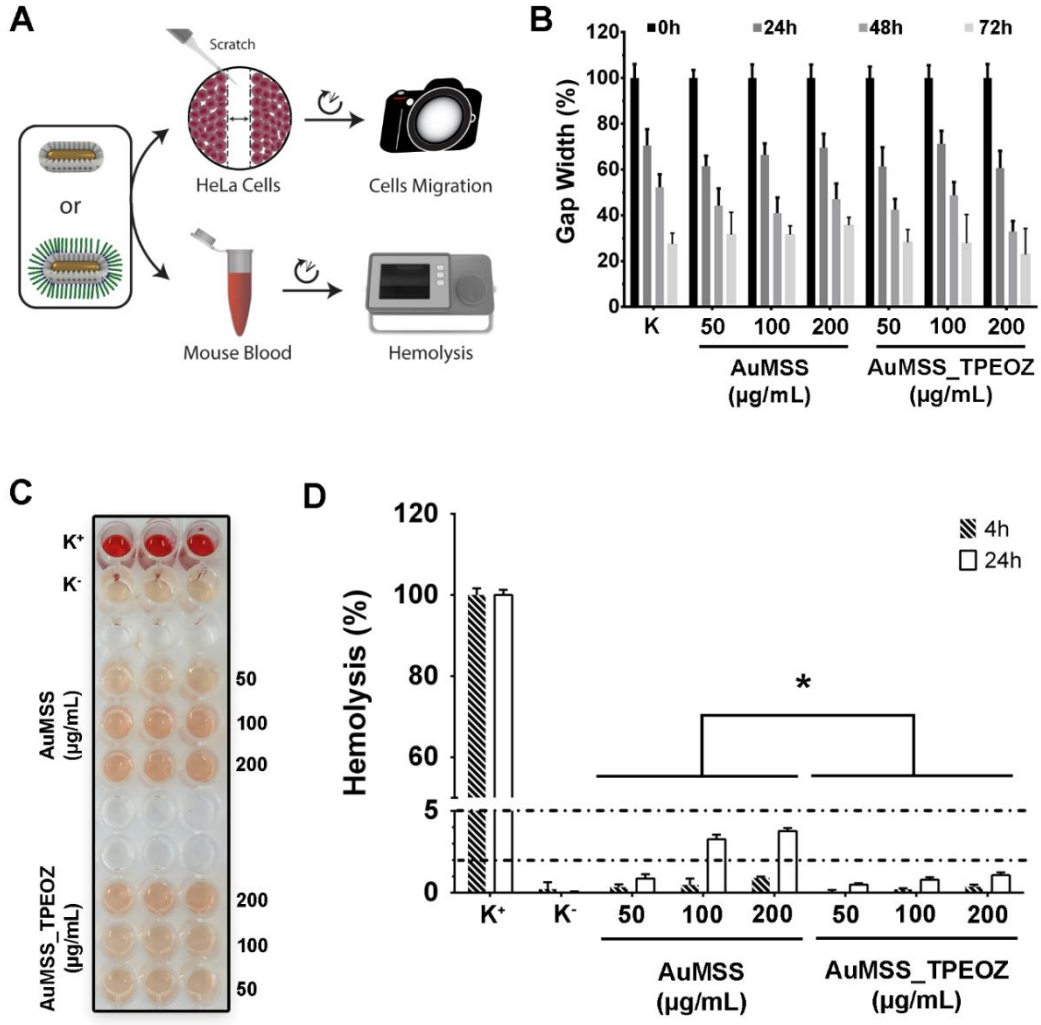

Figure 3.5 - Analysis of the AuMSS derivatives effect on the HeLa cells migration behavior and its hemocompatibility. (A) Schematics of the cells migration evaluation and hemocompatibility methodology. (B) Analysis of the AuMSS and AuMSS_TPEOZ nanorods effect on the HeLa cells migration behavior at 0, 24, 48 and 72 h of incubation; cells non-exposed to nanoparticles (K). (C) Optical image of the blood supernatants recovered after AuMSS and AuMSS_TPEOZ nanorods incubation for 24 h; Triton-X 100 was used as positive control for RBCs lysis (K^+) and PBS as negative control (K-). (D) Analysis of the RBCs lysis upon incubation with different concentrations of AuMSS or AuMSS_TPEOZ nanorods. Data are presented as mean±s.d., *$p<0.05$, n=5.

The obtained results show that AuMSS nanorods at 100 and 200 $\mu g.mL^{-1}$ are slightly hemolytic since 4% of hemoglobin was released after 24 h of incubation. On the other side, the PEOZ grafting on the particle surface improved the hemocompatibility of AuMSS, being registered less than 1% of hemolysis even at the concentration of 200 $\mu g.mL^{-1}$. This data is in accordance with the guidelines established by international agencies (ISO/TR 7406) regarding the critically safe hemolytic ratio.

3.4.4. AuMSS nanorods' uptake by Hela cells

After assessing the biocompatibility of the AuMSS derivatives, the nanorods cellular uptake by HeLa cancer cells was evaluated by CLSM and fluorescence spectroscopy (Figure 3.6 B). The AuMSS derivatives tracking was achieved by FITC staining. In Figure 3.6 A, it is possible to observe the presence of both AuMSS or AuMSS_TPEOZ nanorods (identified with the white arrows) in the interior of the HeLa cells. Further, after confirming that the nanorods were internalized by the HeLa cells, their drug delivery capacity was studied by assessing the Dox delivery to HeLa cells. With that in mind, free Dox, Dox@AuMSS, and Dox@AuMSS_TPEOZ were incubated 4 h with HeLa cells and then the Dox fluorescence was measured (Figure 3.6 C). The fluorescence spectroscopy studies revealed that the AuMSS derivatives, when compared to the free Dox administration, can improve Dox internalization by HeLa cells, 150% and 220% for Dox@AuMSS and Dox@AuMSS_TPEOZ nanorods, respectively. Moreover, CLSM images also corroborated this efficient Dox delivery by AuMSS derivatives.

3.4.5. Evaluation of the therapeutic effect mediated by AuMSS derivatives

After confirming the nanoparticles biocompatibility, the AuMSS derivatives anticancer potential as well as the capacity to combine both PTT and chemotherapy was assessed on HeLa cancer cells (Figure 3.7). For this purpose, HeLa cells were incubated for 48 h with AuMSS or AuMSS_TPEOZ formulations with or without being subjected to NIR laser irradiation for 5 min. In Figure 3.7 B it is possible to perceive that the different AuMSS formulations led to a decrease in the cell viability which was proportional to the tested concentrations. In fact, the combined administration of Dox and PTT mediated by both AuMSS and AuMSS_TPEOZ nanorods resulted in an improved therapeutic effect, more than 95% of cellular death even when a concentration of 100 $\mu g.mL^{-1}$ was used. On the other side, the stand-alone modalities presented a cell death close to 70% for PTT and 80% for Dox delivery at a particle concentration of 200 $\mu g.mL^{-1}$. Further, no significant differences were observed between the groups treated with uncoated or PEOZ coated AuMSS.

3.5. Discussion

The AuMSS with a rod-like shape were synthesized by using a seed-mediated growth method previously described in the literature [40, 41]. The synthesis procedure is comprised of 3 individual steps, *i.e.* the formation of the seed particles, the growth of the gold nanorod and finally the formation of the mesoporous silica shell using CTAB as a soft template to generate the pores.

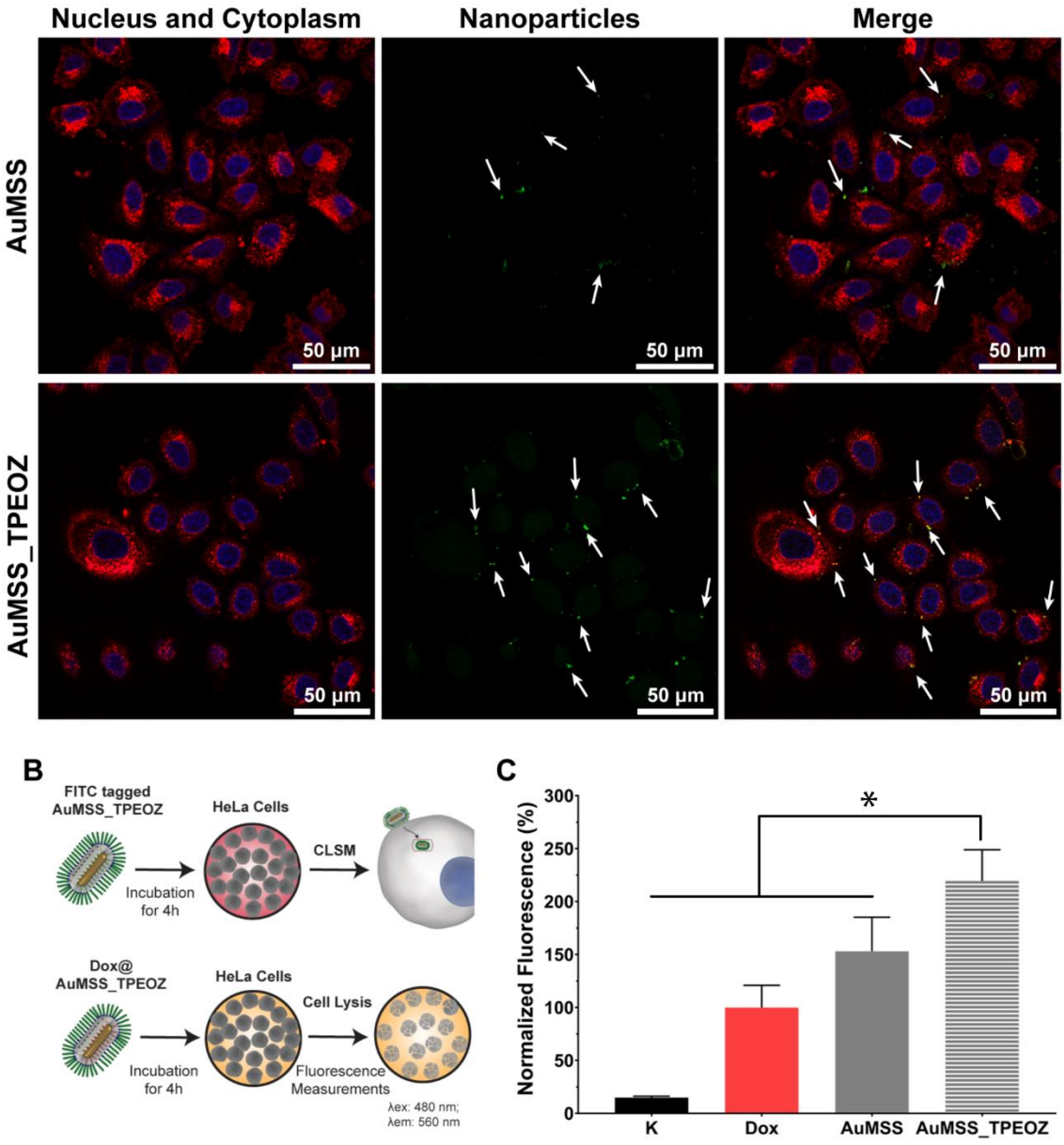

Figure 3.6 - Analysis of AuMSS derivatives uptake by HeLa cells after 4 h of incubation. (A) CLSM images of FITC stained AuMSS derivatives uptake after 4 h of incubation with HeLa cells, the white arrows are pointing to internalized nanoparticles (Hoechst 33342®: λ_{ex}= 405 nm and λ_{em}= 410-480 nm; WGA-Alexa Fluor® 594 λ_{ex}= 561 nm and λ_{em}=600-720 nm). (B) Schematics of AuMSS derivatives uptake experiments. (C) Fluorescence spectroscopy analysis of Dox-loaded AuMSS derivatives uptake by HeLa cells, fluorescence was normalized towards the free Dox-treated group. Data are presented as mean±s.d., *p<0.05, n=5.

Then, the CTAB was removed by a solvent based approach and the silane-modified PEOZ was grafted on the particle surface. The gold core size is critically important for the efficient NIR laser conversion to heat, in fact, A.R. between 3 and 4 have been reported has optimal to absorb the NIR light [56, 57]. On the other side, the AuMSS overall size (<200 nm) still allows them to exploit the enhanced permeability and retention effect and therefore accumulate passively in the tumor tissue [58]. The AuMSS surface charge neutralization after the functionalization with TPEOZ indicate the successful grafting polymer on the particle surface, since the recorded differences can be attributed to the loss of the surface silanol and to the neutral charge of PEOZ. As described in the literature, the nanoparticles pharmacokinetic profile, blood circulation time and biocompatibility are highly influenced by their surface charge [59, 60]. In fact, a neutral surface charge (±10mV) is until now considered the ideal for nanoparticles circulation [58]. The AuMSS modification was further confirmed by FTIR and TGA analysis. The weight losses observed for AuMSS_TPEOZ correspond to the pyrolysis of the polymer chains chemically grafted on the particle surface, whereas the AuMSS remain intact being only verified weight losses attributed to the evaporation of water in the interior of the particle mesopores or the loss of the functional hydroxyl groups [61, 62]. This successful incorporation of PEOZ on the particle surface is of paramount importance since it can reduce the nanoparticle unspecific interactions, increase the nanoparticles blood circulation time and consequently the tumor accumulation [37]. The AuMSS_TPEOZ potential for being applied in cancer PTT and chemotherapy was also evaluated.

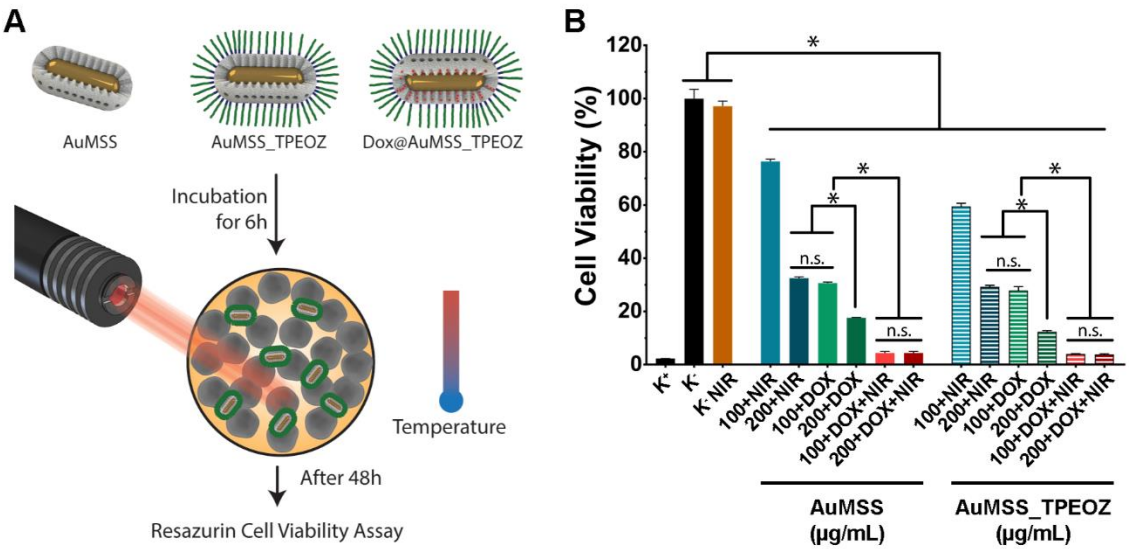

Figure 3.7- Cytotoxic activity of AuMSS derivatives in HeLa cells. (A) Schematics of AuMSS derivatives cytotoxicity experiments. (B) Analysis of the AuMSS derivatives toxicity towards HeLa cells at 48 h, with or without NIR laser irradiation for 5 min. Positive control (K^+): cells treated with ethanol; Negative control (K^-): cells without nanoparticles incubation. Data are presented as mean±s.d, *$p<0.05$ n= 5, n.s. non-significant.

The AuMSS derivatives UV-vis spectra present the two different peaks attributed to the transverse and longitudinal plasmon resonance characteristic from gold nanorods. Further, the peaks at 500 nm and 800 nm are in accordance with the gold core A.R. [21, 56, 57, 63, 64]. These results also demonstrated that the inclusion of the PEOZ coating does not impact on the UV-vis absorption of the AuMSS. Additionally, the high-intensity peak observed in the 800 nm region (*i.e.* NIR region of the spectra) supports the particles applicability for NIR-mediated PTT [14, 15]. In accordance to this, the temperature increases of 35-40ºC mediated by the AuMSS upon NIR laser irradiation can lead to the cancer cells death through diverse mechanisms such as protein denaturation and disruption of the cellular membrane [45, 65]. The AuMSS derivatives good photothermic stability can be explained by the silica coating that stabilizes and protects the gold cores from premature degradation, thus allowing these nanomaterials to support multiple irradiation cycles without sacrificing their heat conversion capacity. The drug encapsulation studies revealed an increased Dox E.E. for AuMSS_TPEOZ nanorods indicating an additional entrapment of the drug molecules between the polymer chains and silica surface. Similarly, the inclusion of the PEOZ polymer shell resulted in a slower and controlled drug release, which can be justified by the additional polymer barrier that the Dox molecules need to surpass in order to be released into the media. Nevertheless, both formulations presented a release profile divided into two phases characteristic of mesoporous silica nanoparticles, an initial burst liberation followed by a sustained drug diffusion during the time of the experiment [26]. On the other side, the NIR laser irradiation also prompted the drug release due to the increase of the media temperature and consequently higher drug solubility.

The PEOZ impact on the AuMSS biosafety was evaluated by assessing the nanoparticles biocompatibility, effect on the cells' migration behaviour and hemocompatibility. In agreement with several reports available in the literature for AuMSS based nanosystems, both nanorods formulations showed an excellent biocompatibility within the tested concentration range (25–200 $\mu g.mL^{-1}$) and did not elicit any significative impact on cells motility [26, 66, 67]. On the other side, when incubated with RBCs it was observed a protective effect of the AuMSS_TPEOZ nanorods surface charge neutralization, thus improving the nanoparticles hemocompatibility [47, 68-70]. The cells membrane is the last barrier that the nanoparticles have to overcome to deliver their payload to cancer cells. The cell internalization studies indicate that the neutralization of the particle surface charge (*i.e.* from -30 mV to -15 mV after the PEOZ grafting) can favor the nanoparticle interaction with the cellular membrane enhancing the cellular uptake [58]. Such behavior will allow the drug delivery in the interior of the cell thus avoiding the drug premature degradation in the extracellular medium. Finally, the AuMSS derivatives anticancer potential as well as their capacity to combine both PTT and chemotherapy was assessed on HeLa cancer cells. The obtained results indicate that the combinatorial therapy allows a more effective treatment, almost eradicating all the cancer cells, even using half of the concentration of the stand-alone PTT or chemo-based treatments. These data are in accordance with other reports available in the literature, where the increase

in temperature in combination with the drug delivery led to an improved cytotoxic capacity of the nanoparticles [63, 71]. Such fact is attributed to the combined action of the high temperatures that promote the cell death by inducing the proteins denaturation, the disruption of the cellular membrane and cells sensitization to the Dox action, a DNA intercalating drug that leads to cell apoptosis [34, 45]. Altogether, our findings suggest that PEOZ coating improves the AuMSS nanorods biological performance as a multifunctional combinatorial therapy for cervical cancer.

3.6. Conclusion

The AuMSS nanorods are multifunctional nanomaterials that have the potential for combining in one single system the chemotherapeutic and NIR-mediated PTT activities as well as bioimaging. However, in cancer therapy related applications, the blood circulation time is a deciding factor for the nanoparticles' extravasation through the defective vasculature, accumulation in the tumor tissue and ultimately for the therapeutic outcome. With that in mind, herein, PEOZ was used for the first time to improve the performance of AuMSS/Dox nanorods. The obtained results reveal that the functionalization of AuMSS nanorods increases the nanoparticles stability and biocompatibility, namely by decreasing the blood hemolysis to safe and negligible levels. Such results can be attributed to the neutralization of the AuMSS nanorods surface charge, which also led to an improved Dox uptake on HeLa cervical cancer cells. Otherwise, the *in vitro* antitumoral studies revealed that the combined treatment (*i.e.* NIR induced PTT and chemotherapy) mediated by the AuMSS_PEOZ/Dox nanorods showed a synergistic effect when compared to the chemotherapy or PTT treatment alone, allowing the complete eradication of cervical cancer cells. In fact, the present findings encourage the application of this simple multifunctional nanomaterial for exploring new drug-PTT combinations and to bridge the gap between pre-clinical research and clinical use. In the future, the realization of *in vivo* assays is pivotal to confirm the versatility and the enhanced therapeutic effect of this combinatorial therapeutic approach for cancer.

3.7. References

[1] B. Al-Lazikani, U. Banerji, P. Workman, Combinatorial drug therapy for cancer in the post-genomic era, Nat. Biotechnol., 30 (2012) 679-692.

[2] A.F. Moreira, D.R. Dias, E.C. Costa, I.J. Correia, Thermo- and pH-responsive nano-in-micro particles for combinatorial drug delivery to cancer cells, Eur. J. Pharm. Sci., 104 (2017) 42-51.

[3] X.Y. Xu, W. Ho, X.Q. Zhang, N. Bertrand, O. Farokhzad, Cancer nanomedicine: from targeted delivery to combination therapy, Trends Mol. Med., 21 (2015) 223-232.

[4] V.M. Gaspar, A.F. Moreira, E.C. Costa, J.A. Queiroz, F. Sousa, C. Pichon, I.J. Correi, Gas-generating TPGS-PLGA microspheres loaded with nanoparticles (NIMPS) for co-delivery of minicircle DNA and anti-tumoral drugs, Colloids Surf., B, 134 (2015) 287-294.

[5] X.Y. Wang, J.S. Zhang, Y.T. Wang, C.P. Wang, J.R. Xiao, Q. Zhang, Y.Y. Cheng, Multi-responsive photothermal-chemotherapy with drug-loaded melanin-like nanoparticles for synergetic tumor ablation, Biomaterials, 81 (2016) 114-124.

[6] R.C. Lv, P.P. Yang, F. He, S.L. Gai, G.X. Yang, Y.L. Dai, Z.Y. Hou, J. Lin, An imaging-guided platform for synergistic photodynamic/photothermal/chemo-therapy with pH/temperature-responsive drug release, Biomaterials, 63 (2015) 115-127.

[7] X.L. Tu, L.N. Wang, Y.H. Cao, Y.F. Ma, H. Shen, M.X. Zhang, Z.J. Zhang, Efficient cancer ablation by combined photothermal and enhanced chemo-therapy based on carbon nanoparticles/doxorubicin@SiO2 nanocomposites, Carbon, 97 (2016) 35-44.

[8] S. Shen, H.Y. Tang, X.T. Zhang, J.F. Ren, Z.Q. Pang, D.G. Wang, H.L. Gao, Y. Qian, X.G. Jiang, W.L. Yang, Targeting mesoporous silica-encapsulated gold nanorods for chemo-photothermal therapy with near-infrared radiation, Biomaterials, 34 (2013) 3150-3158.

[9] C.L.K. Pang, Hyperthermia in Oncology, CRC Press, Boca Raton, Florida2015.

[10] K.F. Chu, D.E. Dupuy, Thermal ablation of tumours: biological mechanisms and advances in therapy, Nat. Rev. Cancer, 14 (2014) 199-208.

[11] T. Boissenot, A. Bordat, B. Larrat, M. Varna, H. Chacun, A. Paci, V. Poinsignon, E. Fattal, N. Tsapis, Ultrasound-induced mild hyperthermia improves the anticancer efficacy of both Taxol(R) and paclitaxel-loaded nanocapsules, J. Controlled Release, 264 (2017) 219-227.

[12] X. Yao, X. Niu, K. Ma, P. Huang, J. Grothe, S. Kaskel, Y. Zhu, Graphene Quantum Dots-Capped Magnetic Mesoporous Silica Nanoparticles as a Multifunctional Platform for Controlled Drug Delivery, Magnetic Hyperthermia, and Photothermal Therapy, Small, 13 (2017).

[13] S. Stolik, J.A. Delgado, A. Perez, L. Anasagasti, Measurement of the penetration depths of red and near infrared light in human "ex vivo" tissues, J. Photochem. Photobiol., B, 57 (2000) 90-93.

[14] D. de Melo-Diogo, C. Pais-Silva, D.R. Dias, A.F. Moreira, I.J. Correia, Strategies to Improve Cancer Photothermal Therapy Mediated by Nanomaterials, Adv. Healthcare Mater., 6 (2017).

[15] J. Eichler, J. Knof, H. Lenz, Measurements on the depth of penetration of light (0.35--1.0 microgram) in tissue, Radiat. Environ. Biophys., 14 (1977) 239-242.

[16] X. Cheng, R. Sun, L. Yin, Z. Chai, H. Shi, M. Gao, Light-Triggered Assembly of Gold Nanoparticles for Photothermal Therapy and Photoacoustic Imaging of Tumors *In vivo*, Adv. Mater., 29 (2017).

[17] C. Wang, C. Xu, L. Xu, C. Sun, D. Yang, J. Xu, F. He, S. Gai, P. Yang, A novel core-shell structured upconversion nanorod as multimodal bioimaging and photothermal ablation agent for cancer theranostics, J. Mater. Chem. B, (2018).

[18] L. Mocan, C. Matea, F.A. Tabaran, O. Mosteanu, T. Pop, C. Puia, L. Agoston-Coldea, G. Zaharie, T. Mocan, A.D. Buzoianu, Selective ex vivo photothermal nano-therapy of solid liver tumors mediated by albumin conjugated gold nanoparticles, Biomaterials, 119 (2017) 33-42.

[19] X.H. Huang, P.K. Jain, I.H. El-Sayed, M.A. El-Sayed, Gold nanoparticles: interesting optical properties and recent applications in cancer diagnostic and therapy, Nanomedicine, 2 (2007) 681-693.

[20] N. Li, P.X. Zhao, D. Astruc, Anisotropic Gold Nanoparticles: Synthesis, Properties, Applications, and Toxicity, Angew. Chem. Int. Edit., 53 (2014) 1756-1789.

[21] X. Huang, M.A. El-Sayed, Gold nanoparticles: Optical properties and implementations in cancer diagnosis and photothermal therapy, J. Adv. Res., 1 (2010) 13-28.

[22] X.H. Huang, P.K. Jain, I.H. El-Sayed, M.A. El-Sayed, Plasmonic photothermal therapy (PPTT) using gold nanoparticles, Lasers Med. Sci., 23 (2008) 217-228.

[23] J.C. Love, L.A. Estroff, J.K. Kriebel, R.G. Nuzzo, G.M. Whitesides, Self-assembled monolayers of thiolates on metals as a form of nanotechnology, Chem. Rev., 105 (2005) 1103-1169.

[24] Y.-S. Chen, W. Frey, S. Kim, K. Homan, P. Kruizinga, K. Sokolov, S. Emelianov, Enhanced thermal stability of silica-coated gold nanorods for photoacoustic imaging and image-guided therapy, Opt. Express, 18 (2010) 8867-8878.

[25] B. Jang, Y.S. Kim, Y. Choi, Effects of gold nanorod concentration on the depth-related temperature increase during hyperthermic ablation, Small, 7 (2011) 265-270.

[26] D.R. Dias, A.F. Moreira, I.J. Correia, The effect of the shape of gold core-mesoporous silica shell nanoparticles on the cellular behavior and tumor spheroid penetration, J. Mater. Chem. B, 4 (2016) 7630-7640.

[27] N.S. Abadeer, M.R. Brennan, W.L. Wilson, C.J. Murphy, Distance and plasmon wavelength dependent fluorescence of molecules bound to silica-coated gold nanorods, ACS nano, 8 (2014) 8392-8406.

[28] H. Li, L.-L. Tan, P. Jia, Q.-L. Li, Y.-L. Sun, J. Zhang, Y.-Q. Ning, J. Yu, Y.-W. Yang, Near-infrared light-responsive supramolecular nanovalve based on mesoporous silica-coated gold nanorods, Chem. Sci., 5 (2014) 2804-2808.

[29] A.F. Moreira, C.F. Rodrigues, C.A. Reis, E.C. Costa, I.J. Correia, Gold-core silica shell nanoparticles application in imaging and therapy: A review, Microporous Mesoporous Mater., 270 (2018) 168-179.

[30] M. Colilla, A. Baeza, M. Vallet-Regí, Mesoporous silica nanoparticles for drug delivery and controlled release applications, The Sol-Gel Handbook-Synthesis, Characterization, and Applications: Synthesis, Characterization and Applications, 3-Volume Set, (2015) 1309-1344.

[31] V. Mamaeva, C. Sahlgren, M. Lindén, Mesoporous silica nanoparticles in medicine—recent advances, Adv. Drug Delivery Rev., 65 (2013) 689-702.

[32] I.I. Slowing, B.G. Trewyn, S. Giri, V.Y. Lin, Mesoporous silica nanoparticles for drug delivery and biosensing applications, Adv. Funct. Mater., 17 (2007) 1225-1236.

[33] J. Lu, M. Liong, J.I. Zink, F. Tamanoi, Mesoporous silica nanoparticles as a delivery system for hydrophobic anticancer drugs, Small, 3 (2007) 1341-1346.

[34] A.F. Moreira, V.M. Gaspar, E.C. Costa, D. de Melo-Diogo, P. Machado, C.M. Paquete, I.J. Correia, Preparation of end-capped pH-sensitive mesoporous silica nanocarriers for on-demand drug delivery, Eur. J. Pharm. Biopharm., 88 (2014) 1012-1025.

[35] R. Konradi, B. Pidhatika, A. Muhlebach, M. Textort, Poly-2-methyl-2-oxazoline: A peptide-like polymer for protein-repellent surfaces, Langmuir, 24 (2008) 613-616.

[36] A. Mero, G. Pasut, L.D. Via, M.W.M. Fijten, U.S. Schubert, R. Hoogenboom, F.M. Veronese, Synthesis and characterization of poly(2-ethyl 2-oxazoline)-conjugates with proteins and drugs: Suitable alternatives to PEG-conjugates?, J. Controlled Release, 125 (2008) 87-95.

[37] O. Koshkina, D. Westmeier, T. Lang, C. Bantz, A. Hahlbrock, C. Wurth, U. Resch-Genger, U. Braun, R. Thiermann, C. Weise, M. Eravci, B. Mohr, H. Schlaad, R.H. Stauber, D. Docter, A. Bertin, M. Maskos, Tuning the Surface of Nanoparticles: Impact of Poly(2-ethyl-2-oxazoline) on Protein Adsorption in Serum and Cellular Uptake, Macromol. Biosci., 16 (2016) 1287-1300.

[38] H.L. Ou, T.J. Cheng, Y.M. Zhang, J.J. Liu, Y.X. Ding, J.R. Zhen, W.Z. Shen, Y.J. Xu, W.Z. Yang, P. Niu, J.F. Liu, Y.L. An, Y. Liu, L.Q. Shi, Surface-adaptive zwitterionic nanoparticles for prolonged blood circulation time and enhanced cellular uptake in tumor cells, Acta Biomater., 65 (2018) 339-348.

[39] J.W. Nichols, Y.H. Bae, Odyssey of a cancer nanoparticle: From injection site to site of action, Nano Today, 7 (2012) 606-618.

[40] B. Nikoobakht, M.A. El-Sayed, Preparation and Growth Mechanism of Gold Nanorods (NRs) Using Seed-Mediated Growth Method, Chem. Mater., 15 (2003) 1957-1962.

[41] I. Gorelikov, N. Matsuura, Single-Step Coating of Mesoporous Silica on Cetyltrimethyl Ammonium Bromide-Capped Nanoparticles, Nano Lett., 8 (2008) 369-373.

[42] Y.J. Li, B. Yan, Photophysical Properties of a Novel Organic-Inorganic Hybrid Material: Eu(III)-beta-Diketone Complex Covalently Bonded to SiO2/ZnO Composite Matrix, Photochem. Photobiol., 86 (2010) 1008-1015.

[43] D. de Melo-Diogo, V.M. Gaspar, E.C. Costa, A.F. Moreira, D. Oppolzer, E. Gallardo, I.J. Correia, Combinatorial delivery of Crizotinib–Palbociclib–Sildenafil using TPGS-PLA micelles for improved cancer treatment, Eur. J. Pharm. Biopharm., 88 (2014) 718-729.

[44] Y. Liu, M. Xu, Q. Chen, G. Guan, W. Hu, X. Zhao, M. Qiao, H. Hu, Y. Liang, H. Zhu, Gold nanorods/mesoporous silica-based nanocomposite as theranostic agents for targeting near-infrared imaging and photothermal therapy induced with laser, Int. J. Nanomed., 10 (2015) 4747-4761.

[45] D. de Melo-Diogo, C. Pais-Silva, E.C. Costa, R.O. Louro, I.J. Correia, D-alpha-tocopheryl polyethylene glycol 1000 succinate functionalized nanographene oxide for cancer therapy, Nanomedicine (Lond), 12 (2017) 443-456.

[46] V.M. Gaspar, E.C. Costa, J.A. Queiroz, C. Pichon, F. Sousa, I.J. Correia, Folate-Targeted Multifunctional Amino Acid-Chitosan Nanoparticles for Improved Cancer Therapy, Pharm. Res., 32 (2015) 562-577.

[47] A. Yildirim, E. Ozgur, M. Bayindir, Impact of mesoporous silica nanoparticle surface functionality on hemolytic activity, thrombogenicity and non-specific protein adsorption, J. Mater. Chem. B, 1 (2013) 1909-1920.

[48] A. Bernd, M. Ott, H. Ishikawa, H. Schroten, C. Schwerk, G. Fricker, Characterization of efflux transport proteins of the human choroid plexus papilloma cell line HIBCPP, a functional *in vitro* model of the blood-cerebrospinal fluid barrier, Pharm. Res., 32 (2015) 2973-2982.

[49] E.C. Costa, A.F. Moreira, D. de Melo-Diogo, I.J. Correia, Clear T immersion optical clearing method for intact 3D spheroids imaging through confocal laser scanning microscopy, Opt. Laser Technol., 106 (2018) 94-99.

[50] S.P. Miguel, M.P. Ribeiro, H. Brancal, P. Coutinho, I.J. Correia, Thermoresponsive chitosan–agarose hydrogel for skin regeneration, Carbohydr. Polym., 111 (2014) 366-373.

[51] A. Colombo, F. Gherardi, S. Goidanich, J.K. Delaney, E.R. de la Rie, M.C. Ubaldi, L. Toniolo, R. Simonutti, Highly transparent poly(2-ethyl-2-oxazoline)-TiO2 nanocomposite coatings for the conservation of matte painted artworks, RSC Adv., 5 (2015) 84879-84888.

[52] E.C. Costa, A.F. Moreira, D. de Melo-Diogo, V.M. Gaspar, M.P. Carvalho, I.J. Correia, 3D tumor spheroids: an overview on the tools and techniques used for their analysis, Biotechnol. Adv., 34 (2016) 1427-1441.

[53] Y.C. Bai, Y.C. Hsia, Y.T. Lin, K.H. Chen, F.I. Chou, C.M. Yang, Y.J. Chuang, Effect of Tumor Microenvironment on Selective Uptake of Boric Acid in HepG2 Human Hepatoma Cells, Anticancer Res., 37 (2017) 6347-6353.

[54] N. Dixit, K. Vaibhav, R.S. Pandey, U.K. Jain, O.P. Katare, A. Katyal, J. Madan, Improved cisplatin delivery in cervical cancer cells by utilizing folate-grafted non-aggregated gelatin nanoparticles, Biomed. Pharmacother., 69 (2015) 1-10.

[55] Q. Zhang, C. Shen, N. Zhao, F.J. Xu, Redox-Responsive and Drug-Embedded Silica Nanoparticles with Unique Self-Destruction Features for Efficient Gene/Drug Codelivery, Adv. Funct. Mater., 27 (2017) 1606229.

[56] S.W. Wang, W. Xi, F.H. Cai, X.Y. Zhao, Z.P. Xu, J. Qian, S.L. He, Three-Photon Luminescence of Gold Nanorods and Its Applications for High Contrast Tissue and Deep *In vivo* Brain Imaging, Theranostics, 5 (2015) 251-266.

[57] G.F. Luo, W.H. Chen, Q. Lei, W.X. Qiu, Y.X. Liu, Y.J. Cheng, X.Z. Zhang, A Triple-Collaborative Strategy for High-Performance Tumor Therapy by Multifunctional Mesoporous Silica-Coated Gold Nanorods, Adv. Funct. Mater., 26 (2016) 4339-4350.

[58] A.F. Moreira, D.R. Dias, I.J. Correia, Stimuli-responsive mesoporous silica nanoparticles for cancer therapy: A review, Microporous Mesoporous Mater., 236 (2016) 141-157.

[59] C.B. He, Y.P. Hu, L.C. Yin, C. Tang, C.H. Yin, Effects of particle size and surface charge on cellular uptake and biodistribution of polymeric nanoparticles, Biomaterials, 31 (2010) 3657-3666.

[60] I. Slowing, B.G. Trewyn, V.S.Y. Lin, Effect of surface functionalization of MCM-41-type mesoporous silica nanoparticleson the endocytosis by human cancer cells, J. Am. Chem. Soc., 128 (2006) 14792-14793.

[61] J. Kobler, K. Moller, T. Bein, Colloidal suspensions of functionalized mesoporous silica nanoparticles, ACS nano, 2 (2008) 791-799.

[62] J.M. Kim, S.M. Chang, S.M. Kong, K.S. Kim, J. Kim, W.S. Kim, Control of hydroxyl group content in silica particle synthesized by the sol-precipitation process, Ceram. Int., 35 (2009) 1015-1019.

[63] T. Zhang, Z. Ding, H. Lin, L. Cui, C. Yang, X. Li, H. Niu, N. An, R. Tong, F. Qu, pH-Sensitive Gold Nanorods with a Mesoporous Silica Shell for Drug Release and Photothermal Therapy, Eur. J. Inorg. Chem., 2015 (2015) 2277-2284.

[64] A.M. Alkilany, P.K. Nagaria, C.R. Hexel, T.J. Shaw, C.J. Murphy, M.D. Wyatt, Cellular Uptake and Cytotoxicity of Gold Nanorods: Molecular Origin of Cytotoxicity and Surface Effects, Small, 5 (2009) 701-708.

[65] A.L. Oei, L.E. Vriend, J. Crezee, N.A. Franken, P.M. Krawczyk, Effects of hyperthermia on DNA repair pathways: one treatment to inhibit them all, Radiat. Oncol., 10 (2015) 165.

[66] A.S. Thakor, R. Luong, R. Paulmurugan, F.I. Lin, P. Kempen, C. Zavaleta, P. Chu, T.F. Massoud, R. Sinclair, S.S. Gambhir, The Fate and Toxicity of Raman-Active Silica-Gold Nanoparticles in Mice, Sci. Transl. Med., 3 (2011) 79ra33-79ra33.

[67] X.G. Hu, X.H. Gao, Multilayer coating of gold nanorods for combined stability and biocompatibility, Phys Chem Chem Phys, 13 (2011) 10028-10035.

[68] T.X. Viegas, M.D. Bentley, J.M. Harris, Z.F. Fang, K. Yoon, B. Dizman, R. Weimer, A. Mero, G. Pasut, F.M. Veronese, Polyoxazoline: Chemistry, Properties, and Applications in Drug Delivery, Bioconjugate Chem., 22 (2011) 976-986.

[69] Q.J. He, J.M. Zhang, J.L. Shi, Z.Y. Zhu, L.X. Zhang, W.B. Bu, L.M. Guo, Y. Chen, The effect of PEGylation of mesoporous silica nanoparticles on nonspecific binding of serum proteins and cellular responses, Biomaterials, 31 (2010) 1085-1092.

[70] P. Khullar, V. Singh, A. Mahal, P.N. Dave, S. Thakur, G. Kaur, J. Singh, S.S. Kamboj, M.S. Bakshi, Bovine Serum Albumin Bioconjugated Gold Nanoparticles: Synthesis, Hemolysis, and Cytotoxicity toward Cancer Cell Lines, J. Phys. Chem. C, 116 (2012) 8834-8843.

[71] Z. Zha, S. Zhang, Z. Deng, Y. Li, C. Li, Z. Dai, Enzyme-responsive copper sulphide nanoparticles for combined photoacoustic imaging, tumor-selective chemotherapy and photothermal therapy, Chem. Commun., 49 (2013) 3455-3457.

Chapter 4

Research Work 2

Thermo- and pH- responsive Nano-in-Micro particles for combinatorial drug delivery to cancer cells

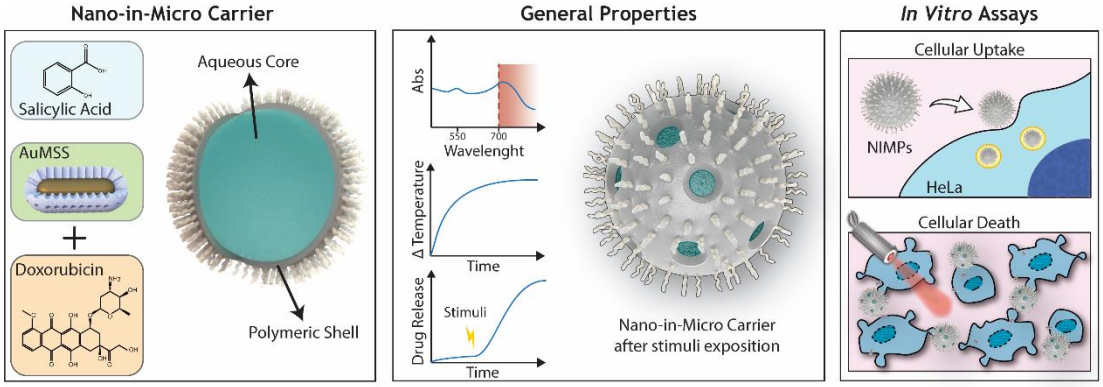

This chapter is based on the publication:

Moreira, A.F., Dias, D. R., Costa, E. C., & Correia, I. J. (2017). Thermo-and pH-responsive nano-in-micro particles for combinatorial drug delivery to cancer cells. European Journal of Pharmaceutical Sciences, 104, 42-51.

4.1. Abstract

Drug combinatorial therapy has been gaining the scientific community attention as a suitable approach to increase treatments efficacy and promote cancer eradication. In this study, a new pH- and thermo- responsive carrier was developed by combining Dox-loaded AuMSS nanorods with SA loaded PLGA based microparticles (NIMPS). The obtained results showed that the drugs and nanorods release could be triggered by the NIR laser irradiation or by the exposition to an acidic environment. The *in vitro* 2D cell studies showed that the NIMPS are biocompatible and easily uptaken by HeLa cells. In addition, 3D cell culture models revealed that the NIMPS administration, combined with the NIR laser irradiation, was capable of reducing the size of the HeLa spheroids up to 48%. Overall, the attained data support the application of the nano-in-micro spheres as a dual stimuli responsive drug carrier system for the local administration of combined therapies to cervical cancer cells.

4.2. Introduction

In the United States, cervical cancer arises as the most common type of cancer affecting women [1]. The currently available treatments such as surgical removal, radiotherapy, and chemotherapy have several drawbacks associated that lead to negative health, gynecologic and obstetric outcomes [2]. Particularly, in chemotherapy, the non-specific biodistribution of the therapeutic molecules originates severe side-effects that limit the maximum dose and the number of treatments that can be administered to each patient [3]. Additionally, the cancer cells can develop multidrug resistance mechanisms, such as the overexpression of drug efflux proteins, that avoid drug accumulation inside the tumor cells and impairs the treatment efficacy [4, 5].

Drug combinatorial administration has been gaining the scientific community attention as a suitable approach for promoting cancer eradication. This therapeutic modality intends to overcome the cancer cells multidrug resistance by attacking these cells at different levels and on different disease hallmarks [6]. However, the use of multiple drugs at the same time can be challenging since unexpected drug-drug interactions can occur [7]. Moreover, the simultaneous use of different drugs can affect the pharmacokinetic profile or even potentiate the side effects of each other. To surpass such limitation, different drug delivery systems have been developed during the past years [8]. These drug carriers are able to increase the drug solubility, decrease the drugs unspecific interactions and protect them from premature degradation while promoting their accumulation at the target site [9]. A particularly valuable strategy that has been employed, comprises the development of nano-in-micro drug delivery carriers [10, 11]. These systems allow the simultaneous loading of two different drugs by using the nanoparticle and the microparticle as two different reservoirs. Therefore, different therapeutic molecules can be encapsulated within the carrier structure and their release rate can be engineered for occurring simultaneously or in a specific order. The capacity to control the therapeutic molecules release rates is fundamental for the development of more precise and personalized therapies [12-14]. Stimuli-responsive carriers can promote the cargo release in response to different extracellular or intracellular signals [15]. Redox potential variation, ionic strength, enzymatic degradation, light, temperature, and pH are some of the stimuli that can be exploited for creating dynamic drug delivery systems that sense and react to their surrounding environment [16, 17].

Herein, pH and temperature responsive nano-in-micro spheres were produced to allow the localized delivery of multiple drugs to cancer cells combined with real-time imaging. The microspheres were produced by using PVA, PLGA and D-α-tocopherol polyethylene glycol succinate (TPGS) polymers. Then AuMSS/Dox rod-like nanoparticles and SA were encapsulated in PLGA microparticles. In addition, a gas generating agent (*i.e.* $NaHCO_3$) was also incorporated within the microparticles for conferring them a pH-responsive character. On the other side, the incorporation of AuMSSs besides conferring a second drug reservoir, imprints a NIR responsivity

and also work as x-ray imaging and CT contrast agents, allowing real-time monitoring of carrier distribution within the tumor and therapeutic outcome [18, 19].

4.3. Materials and Methods

4.3.1. Materials

$HAuCl_4$ was purchased from Alfa Aesar (Germany). TEOS and dimethyl sulfoxide (DMSO) were acquired from Acros Organics (Belgium). CTAB and SA were obtained from Tokyo Chemical Industry (Japan). HCl was bought from Panreac (Spain). Methanol was purchased from VWR International (Portugal). AA, silver nitrate ($AgNO_3$), Dulbecco's Modified Eagle Medium: nutrient mixture F-12 (DMEM-F12), DMEM-HG, resazurin, PBS, ethanol, dichloromethane (DCM), PVA (MW: 31,000 $g.mol^{-1}$), PLGA (75:25, MW: 76,000 $g.mol^{-1}$), TPGS (MW: 1,000 $g.mol^{-1}$), formaldehyde, sodium borohydride ($NaBH_4$) and trypsin were acquired from Sigma–Aldrich (Portugal). FibH cells were obtained from Promocell (Germany) and human cervical cancer (HeLa) cells (ATCC® CCL-2™) were acquired from ATCC (United Kingdom). Hoechst 33342® and WGA-Alexa Fluor® 594 were bought from Invitrogen (USA). Dox was obtained from Carbosynth (United Kingdom). Cell imaging plates were purchased from Ibidi (Germany). Cell culture t-flasks were obtained from Orange Scientific (Belgium).

4.3.2. Synthesis of AuMSS nanorods

The nanorods were synthesized using a procedure adapted from literature that comprised three main steps [20, 21]. Initially, a seed solution was prepared through the addition of 0.60 mL of $NaBH_4$ (0.01 M) under magnetic stirring to an aqueous solution containing 5 mL of CTAB (0.2 M) and 5 mL of $HAuCl_4$ (0.0005 M). The seed solution was then left undisturbed for 6 h at 30°C. Subsequently, the growth solution was prepared by adding 0.21 mL of AA (0.0788 M) to an aqueous solution containing 15 mL of CTAB (0.2 M), 0.03 mL of $AgNO_3$ (0.1 M) and 0.3 mL of $HAuCl_4$ (0.05 M). Following, the seed solution (0.04 mL) was added to the growth solution, stirred for 5 min and then left at 30ºC for 16 h, in order to originate the gold nanorod core.

The synthesis of the mesoporous silica shell was carried out by adapting the method previously described in the literature [20]. Initially, the previously produced gold nanorods were centrifuged (12,000 g, for 20 min at 25°C) to remove the excess of CTAB and resuspended in 10 mL of ultrapure water. Subsequently, 0.7 mL of CTAB (0.01 M) were added and left under stirring overnight. After, 0.07 mL of NaOH (0.1 M) were added to the solution and mixed for 30 min. Then, 0.03 mL of a solution of TEOS (20% v/v) in methanol were injected to the previous solution. This step was repeated three times, with 30 min intervals, and the solution was left under stirring for 24 h. The assembled particles were centrifuged at 12,000 g for 20 min at 25°C, and washed several times with ultrapure water.

The surfactant (CTAB) was removed from rods AuMSSs by adapting the solvent based approach already described in the literature [13]. Briefly, the nanoparticles were resuspended in an acidic solution (HCl 7.5% v/v in ethanol) followed by several washing steps with ethanol (99.9% v/v) to eliminate CTAB residues. The final product was then recovered by centrifugation (18,000 g for 15 min at 25°C) and freeze-dried to collect the final powder.

4.3.3. Physicochemical characterization of the AuMSS nanorods

TEM was used to characterize the nanoparticles morphology. Initially, nanoparticles samples were placed on formvar-coated copper grids and allowed to dry at 25°C. Then, the TEM images were acquired at an accelerating voltage of 100 kV using a TEM microscope (HT7700, Hitachi, Japan). Afterward, the nanoparticles total size, silica shell thickness, and gold core size were measured by using a specific software (Image J 2.0.0, NIH Image, USA). The UV-vis spectra of nanoparticles were acquired in an UV-vis spectrophotometer (Evolution™ 201 Bio, Thermo Scientific Inc., USA) at 300 $nm.min^{-1}$ scanning rate, with a wavelength range from 200 to 1,100 nm.

4.3.4. AuMSS nanorods' loading capacity

The Dox loading in AuMSS was accomplished by adapting a method already described in the literature [22]. Briefly, rods AuMSS were resuspended in PBS (5 mL, pH 7.2) containing Dox (10% w/w) and sonicated for 15 min. Then, the rods AuMSSs were left under magnetic agitation for 48 h at 25°C, in dark conditions. Subsequently, the Dox-loaded AuMSSs (AuMSS/Dox) were recovered by centrifugation at 18,000 g for 30 min and then freeze-dried, the obtained supernatant was stored for drug loading quantification.

The Dox content on the nanoparticles was calculated by measuring the supernatant absorbance at 485 nm, in a UV-vis Spectrophotometer (Evolution™ 201 Bio, Thermo Fisher Scientific Inc., USA) and using a calibration curve (Abs = 1.4169 C + 0.0083; R^2 = 0.999). The AuMSS E.E. was calculated through equation (4.1):

$$\text{E.E. (\%)} = \frac{\text{(Initial drug weight – Drug weight in supernatant)}}{\text{Initial drug weight}} \times 1 \quad \text{Eq.(4.1)}$$

4.3.5. Production of nano-in-micro spheres

PLGA microparticles were synthesized by using a water-in-oil-in-water (W/O/W) double emulsion, solvent-diffusion-evaporation approach method adapted from [23]. Initially, AuMSSs/Dox (160 µg), $NaHCO_3$ (2.5 mg) and SA (300 µg) were added to 1 mL of aqueous PVA (10 $mg.mL^{-1}$) solution and then stirred at 600 rpm for 15 min. Afterward, 2 mL of PLGA (5 $mg.mL^{-1}$ in DCM) were added and the primary emulsification was carried out by using an ultrasonicator (5510E-DTH, Branson Ultrasonics, USA) for 30 min, at 25°C. Subsequently, 6 mL of aqueous TPGS (0.3 $mg.mL^{-1}$) were added to the primary emulsification and homogenized at

11,000 rpm for 30 min in an ice bath using an ultraturrax equipped with a 10G dispersing tip (X10/25, Ystral®, Germany) to form the W/O/W double emulsion. Subsequently, to evaporate the DCM and promote the particle solidification the double emulsification was transferred into ultrapure water and stirred overnight at 25°C. The PLGA microparticles were then recovered by centrifugation at 400g for 30 min at 25°C. The SA loaded microspheres, AuMSS/Dox-loaded microspheres and dual loaded microspheres were named as Micro/SA, Micro/AuMSS/Dox, and NIMPS, respectively. The supernatant was recovered for drug loading quantification purposes and the SA content was determined by measuring the supernatant absorbance at 297 nm with an UV–vis spectrophotometer (Evolution™ 201 Bio, Thermo Scientific Inc., USA). Subsequently, the particles were washed 3 times with ultrapure water and then resuspended in 20 mL of ultrapure water and freeze-dried.

The surface morphology of the prepared PLGA microparticles was characterized by scanning electron microscopy (SEM), using Hitachi S-3400N scanning electron microscope. Size and zeta potential analysis of microparticles was performed by dynamic light scattering (DLS) using a Zetasizer equipment (Nano ZS, Malvern Instruments, UK). X-ray diffraction (XRD) patterns were also obtained using an X-ray diffractometer (Geiger Flex D-max III/c, Rigaku Americas Corporation, USA) to determine the presence of $NaHCO_3$ in synthesized microparticles. The Dox loading in AuMSS was accomplished

4.3.6. Characterization of the PTT capacity

The *in vitro* PTT capacity of nano-in-micro carriers was performed as previously reported in the literature [24]. Briefly, Blank or NIMPS at a concentration of 400 $\mu g.mL^{-1}$ were irradiated with a NIR laser light (808 nm, 1.7 $W.cm^{-2}$). The temperature increase of the solution was measured at different time points (from 1 up to 10 min) by using a thermocouple sensor with an accuracy of 0.1ºC. A control group without the particles was also irradiated and temperature variation was evaluated.

4.3.7. *In vitro* drug release

The analysis of the thermo- and pH-responsive release profile of NIMPS was performed accordingly a method previously described in the literature [25]. The SA release studies were performed at 37ºC using a dialysis bag (1 mL) with a molecular weight cut-off of 1,000 Da under magnetic stirring in PBS, at different pH (5.6 and 7.4) and with or without NIR laser irradiation. To avoid solubility issues or drug precipitation, sink conditions were assured throughout the assay. At predetermined time intervals, 1 mL samples were collected and analyzed at 297 nm by using an UV–vis spectrophotometer (Evolution™ 201 Bio, Thermo Scientific Inc., USA).

4.3.8. Biocompatibility assays

NIMPS biocompatibility was evaluated through a resazurin-based assay [26]. Briefly, the FibH or HeLa cells were seeded into a 96-well flat bottom culture plates with DMEM-F12 and

DMEM-HG media, respectively, at a density of 10,000 cells/well. Subsequently, cells were cultured for 24 h, at 37ºC in an incubator with a humidified atmosphere containing 5% CO_2. Then, the culture medium was removed, and the cells were incubated with different concentrations of NIMPS, ranging from 50 to 1,000 μg.mL^{-1}. After 24, 48 and 72 h of exposure, the medium was replaced and cells were incubated with 10% (v/v) of resazurin (1 mg.mL^{-1}), at 37ºC and 5% CO_2, during 4 h. The produced resorufin, present in culture medium, was then quantified by using a microwell plate reader (Spectramax Gemini XS, Molecular Devices LLC, USA) at an excitation/emission wavelength of λ_{ex}=560 nm and λ_{em}=590 nm. Cells incubated with ethanol (99.9% v/v) were used as positive control (K^+) and cells without being exposed to microparticle samples were used as negative controls (K^-).

4.3.9. 2D cellular uptake analysis

The NIMPS uptake by HeLa cells was studied by CLSM. Briefly, 20,000 HeLa cells were seeded on μ-Slide 8 well Ibidi imaging plates (Ibidi GmbH, Germany), and incubated at 37ºC in 5% CO_2 humidified atmosphere. After 24 h, cells were exposed to NIMPS at a concentration of 200 μg.mL^{-1}, during 1 or 4 h. After incubation, cells were washed with PBS, fixed with paraformaldehyde 4%, for 15 min and rinsed again with PBS. Then, cells were treated with WGA-Alexa Fluor® 594 for cell cytoplasm staining and the cell nucleus was labeled with Hoechst 33342®. Imaging experiments were performed multi-track mode on a confocal microscope (Zeiss LSM 710, Carl Zeiss, Germany), where consecutive z-stacks were acquired. 3D reconstructions and image analysis were performed in Zeiss Zen 2010 software.

4.3.10. Analysis of the NIMPS' 2D cytotoxic effect

The NIMPS cytotoxic effect was evaluated by the MTT assay [27]. Briefly, 10,000 HeLa cells were seeded in 96 well plates containing DMEM-HG culture medium and left to grow for 24 h. After, different microparticle formulations, at a concentration of 200 μg.mL^{-1} or 400 μg.mL^{-1}, were incubated for 24 and 48 h. At each time point, the medium in each well was replaced and 50 μL of MTT solution (5 mg.mL^{-1}) were added to each well. After 4 h of incubation, the solution was removed and 200 μL of DMSO were added to dissolve the resulting crystals. The reduction of MTT to its insoluble formazan product was quantified by measuring the sample absorbance at 570 nm using a microwell plate reader (Sunrise-Basic™, TECAN, Switzerland). Cells incubated with ethanol (99.9% v/v) were used as positive control (K^+) and cells without being exposed to microparticle samples were used as negative controls (K^-).

4.3.11. Characterization of the NIMPS' uptake and cytotoxicity on 3D tumor spheroids

3D tumor spheroids of HeLa cells were assembled accordingly to a method described elsewhere [22]. Briefly, hydrogel micromolds were produced by casting 2% (w/v) liquid agarose in a negative scaffold with an array of 81-wells. After, HeLa cells were seeded at a density of

1,000,000 cells per agarose micromold. Subsequently, 3D multicellular tumor spheroids were grown at 37°C with DMEM-HG medium, in a humidified atmosphere with 5% CO_2, until they reach a mean diameter ranging from 700 to 800 µm.

To evaluate the microspheres uptake and Dox distribution within the spheroids, the spheroids were incubated with NIMPS at a concentration of 400 $\mu g.mL^{-1}$, with or without NIR laser irradiation. After 24 h, the spheroids were washed with PBS and CLSM images were acquired with a confocal microscope (Zeiss LSM 710, Carl Zeiss, Germany). Successive z-stacks were acquired, and the 3D reconstruction of confocal images and analysis was performed in the Zeiss Zen 2010 software. The cytotoxic effect of the NIMPS on 3D tumor spheroids was evaluated by measuring the spheroids area variation and cells viability. In brief, the 3D tumor spheroids were incubated with micro/AuMSS/Dox or NIMPS at a concentration of 400 $\mu g.mL^{-1}$ (with or without NIR laser irradiation) and spheroids size and organization was monitored during 6 days by using Olympus CX41 inverted optical microscope equipped with an Olympus SP-500 UZ digital camera. The variation of the spheroids area was analyzed by using specific software (Image J 2.0.0, NIH Image, USA). The spheroids' cell viability was measured at 48 h by using a resazurin-based assay. Briefly, after the spheroids' incubation with the microspheres, the medium was replaced with fresh medium containing resazurin (1% v/v) and then the spheroids were incubated for 24 h in the dark. 3D spheroids cell viability was then determined by following the resazurin protocol described above.

4.3.12. Statistical Analysis

All data are presented as the mean±standard deviation (s.d.). ANOVA with the Student–Newman–Keuls post-test was used to compare different groups. A p value lower than 0.05 was considered statistically significant. Statistical analysis was performed using GraphPad Prism v.6.0 software (GraphPad Software, USA).

4.4. Results and discussion

4.4.1. NIMPS physicochemical characterization

Thermo- and pH- responsive PLGA microspheres were produced by the W/O/W solvent diffusion-evaporation method. Initially, the first water phase comprised of the gas-generating agent ($NaHCO_3$) and by the PVA surfactant, were mixed with the oil phase containing PLGA dissolved in DCM. Primary emulsification was promoted by the action of ultrasound waves which generated well-defined PLGA droplets by disrupting the oil-water interface. The resulting microcarriers were subsequently mixed with the second water phase containing TPGS. TPGS was used as an alternative to the commonly used PVA polymer due to the TPGS capacity to inhibit P-glycoprotein (a drug efflux pump often overexpressed by cancer cells) and increase the nanocarriers uptake [28-31]. Following the establishment of the W/O/W double emulsion

the organic solvent was diffused by mixing and evaporated under reduced pressure which led to the formation of spherical PLGA microspheres coated with TPGS. The NIMPS characterization by TEM and DLS (Figure 4.1) showed that the encapsulation of the AuMSSs and SA resulted in microspheres with a larger size, 2.5 µm, whereas the Blank microspheres presented a size of 1.6 µm (Figure 4.1 C). The loading of the drug and nanoparticles within the microspheres did not induce any significant variation in the particle surface charge, maintaining a -20 mV surface charge value. The obtained results are in agreement with previous studies reported in the literature, where the nanoparticle loading also induced an increase of the microspheres size [28].

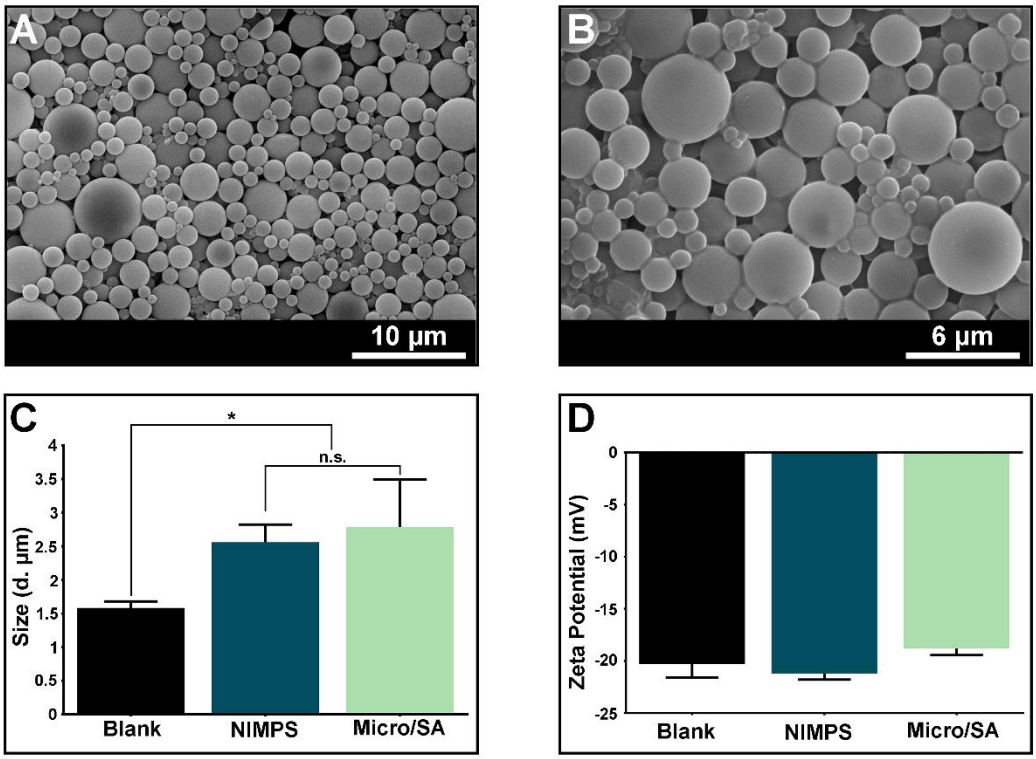

Figure 4.1 - Characterization of NIMPS size, charge and morphology. SEM images of PLGA microspheres without AuMSSs (Blank) (A) and NIMPS (B) microcarriers. Size (C) and charge (D) analysis of Blank, NIMPS, and micro/SA. Data are presented as mean±s.d., *$p<0.05$, n= 3.

Following the successful formulation of NIMPS, the presence of the gas-generating agent ($NaHCO_3$) in the carriers was analyzed by X-ray diffraction. As demonstrated in Figure 4.2 A, the characteristic peaks of the $NaHCO_3$ crystalline structure are present in microsphere formulations, at 2Θ 30° and 35°, and absent on the microspheres produced without $NaHCO_3$. Such indicates that during the microspheres assembly process, the bicarbonate salt is efficiently encapsulated and it imprints to the particle a pH-responsive behavior. The broad XRD peak centered at 2Θ ≈ 19.5° is assigned to the amorphous PLGA microspheres (Figure 4.2 A). Furthermore, the presence of Si and Au elements in the elemental analysis of the NIMPS sample (Figure 4.2 B) indicate the successful loading of AuMSSs on the microspheres. The UV-vis spectra

of NIMPS was also acquired to confirm the successful packing of AuMSSs on microspheres. Gold nanorods UV-vis spectra usually display two characteristic absorption peaks due to transverse plasmon resonance and longitudinal plasmon resonance [32]. Herein, the produced NIMPS displayed two absorption peaks due to the transverse plasmon resonance, in the 500 nm region, and another originated by the longitudinal plasmon resonance, within the 770 nm region. Such results are consistent with those previously attained for other gold nanorods coated with silica shell, that were previously presented in the literature [22, 33-35]. Afterward, the NIMPS capacity to convert NIR light into heat was evaluated. For this purpose, Blank and NIMPS microspheres were exposed to 808 nm NIR light for 1 up to 10 min and the temperature changes were recorded (Figure 4.2 D). The Blank microspheres, at a concentration of 400 $\mu g.mL^{-1}$, did not elicit any significant changes in the medium temperature upon exposure to NIR light. Such data is in agreement with the UV-vis spectrum previously obtained for microspheres since these particles have no absorption in the NIR region. On the other side, the NIMPS, at a concentration of 400 $\mu g.mL^{-1}$, caused a temperature increase of almost 8ºC, after a 10 min NIR laser irradiation. This temperature variation, that occurs in response to NIR laser irradiation, can be explored to trigger the drug release from the NIMPS and consequently improve their therapeutic effect [36, 37].

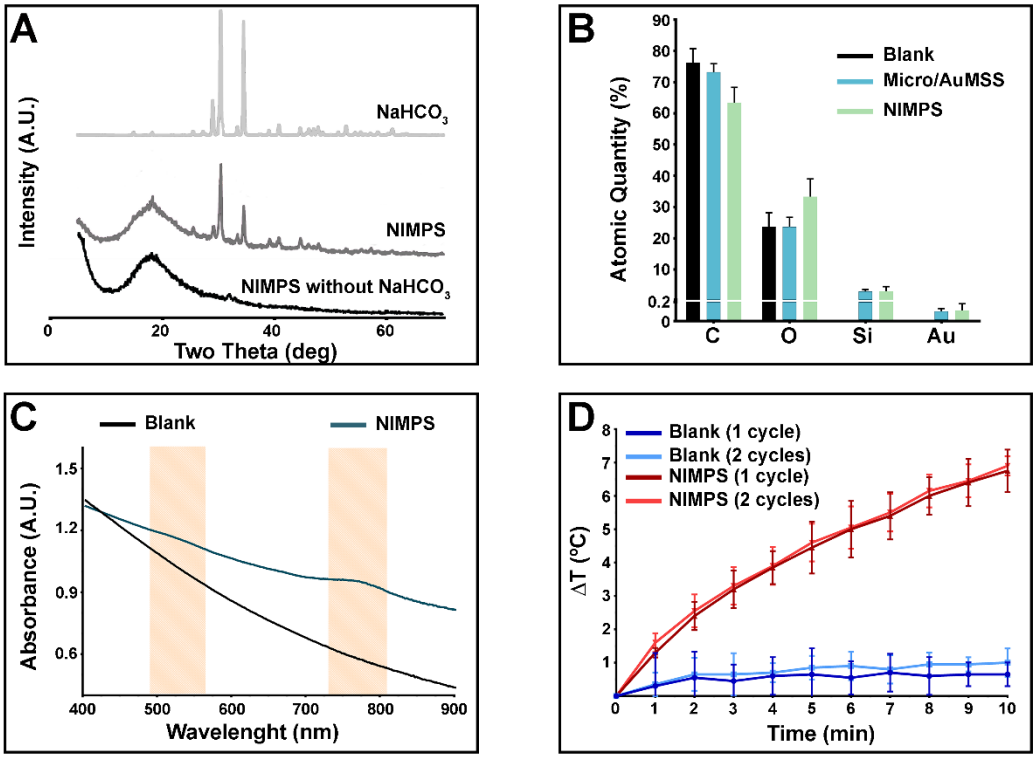

Figure 4.2 - Physicochemical characterization of NIMPS microspheres. XRD spectrum of NIMPS without $NaHCO_3$, NIMPS, and $NaHCO_3$ (A). Elemental analysis of Blank and NIMPS microspheres (B). UV-vis spectrum of Blank and NIMPS microspheres (C). Temperature variation curves after 1 or 2 cycles of NIR laser irradiation of Blank and NIMPS microspheres (D). Data are presented as mean±s.d., *p<0.05, n= 3.

Moreover, it is important to notice that the NIMPS microspheres showed a good photothermic stability since no variations in the heating profile were observed, after one or two irradiation sessions. Such result shows that the NIMPS can support multiple NIR laser irradiation sessions without suffering a premature degradation and consequently decrease their heat conversion capacity [38].

4.4.2. NIMPS drug loading and release profile

The NIMPS potential to encapsulate anti-tumoral drugs was evaluated by including SA in the first aqueous phase used in the assembly process. The results presented in Figure 4.3 B demonstrate that the SA E.E. was higher than 60%, *i.e.*, about 180 µg of SA were encapsulated in each mg of NIMPS. On the other side, the AuMSSs/Dox E.E. was 75% that corresponds to 125 µg of nanoparticles per mg of NIMPS. The AuMSSs were previously loaded with Dox and presented a 52% E.E., which corresponds to 52 µg Dox per mg of AuMSSs. These results demonstrate the NIMPS capacity to simultaneously encapsulate chemotherapeutic drugs as well as nanoparticles in order to a combinatorial drug therapy be achieved.

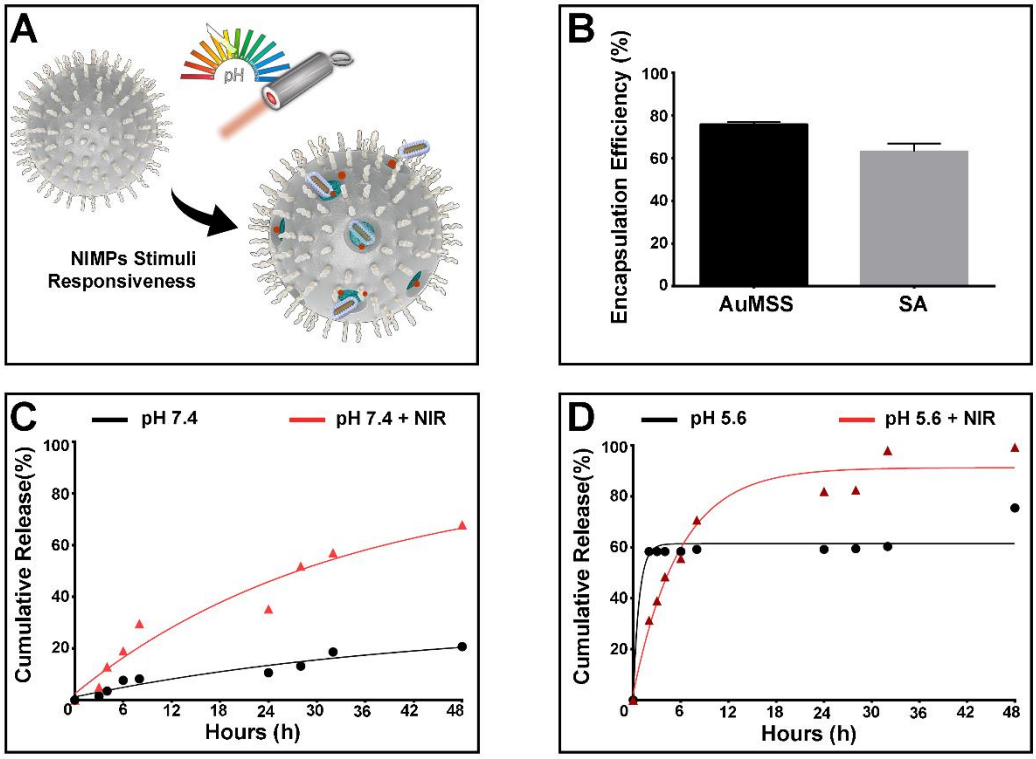

Figure 4.3 - Characterization of NIMPS SA and AuMSSs E.E. and drug release profile. Schematics of NIMPS responsiveness to pH and NIR laser irradiation (A). SA and AuMSSs E.E. on NIMPS microspheres (B). SA release profile at pH 7.4 (C) and 5.6 (D) in the presence or absence of NIR laser irradiation. Data are presented as mean±s.d., *p<0.05, n= 3.

After confirming the NIMPS ability to encapsulate both drugs and nanoparticles, their responsiveness to acidic environments and temperature variation was investigated. The stimuli-dependent release profile was promoted via a pH- or thermal- triggered disruption of particles core/shell structure (Figure 4.3 A). Such responsive character displayed by NIMPS is governed by the AuMSSs heat generation in response to NIR laser irradiation or through the generation of CO_2 bubbles in response to the acidic environment by the sodium bicarbonate ($NaHCO_3 + HCl \rightarrow NaCl + H_2CO_3$; $H_2CO_3 \rightarrow CO_2(g) + H_2O$) [30]. Eventually, the temperature increase disrupts the particle shell or the produced CO2 bubbles, that diffuse through the particle shell, originate pores that stimulate a rapid release of the anti-tumoral drugs.

Drug release assays were performed both in physiological and acidic conditions (*i.e.* pH 7.4 and 5.6) in the absence or under NIR irradiation (Figure 4.3 C and D). As the results demonstrate, the immersion of NIMPS in acidic medium results in a rapid and extensive SA release (Figure 4.3 C and D). In fact, the particles that were exposed to pH=5.6 exhibit a 3-fold higher drug release, when compared to their equivalents immersed in physiological conditions (pH=7.4) (Figure 4.3 C). A higher drug release was also noticed when NIMPS were irradiated with the NIR laser light, both at pH 7.4 and 5.6 (Figure 4.3 C and D). Moreover, it is important to emphasize that at physiological pH the microcarriers have a negligible burst release since only 20% of the loaded drug is released after 48 h (Figure 4.3 C). Such capacity to retain the anti-tumoral drug in the core of the particle is crucial to reduce off-target cytotoxic effects upon their administration *in vivo* [39, 40]. Additionally, SEM analysis was also used to complement the characterization of microsphere structural stability in environments with different pH or under NIR laser irradiation (Figure 4.4). The attained results showed that the NIMPS exposed to acidic medium display various holes in their shell due to the effervescent reaction promoted by $NaHCO_3$ and acid (Figure 4.4 A and B). Particles destruction is also confirmed by the significant amount of free polymer noticed in the SEM images (Figure 4.4 A and B). Moreover, it was also possible to observe that Blank microspheres were capable of preserving their structural and morphological integrity upon NIR laser irradiation, contrasting with the NIMPS that under NIR laser irradiation were destroyed (Figure 4.4 D). Such findings confirm the stimuli-responsive profile of NIMPS and also its potential to perform a controlled drug release at the target tumor site.

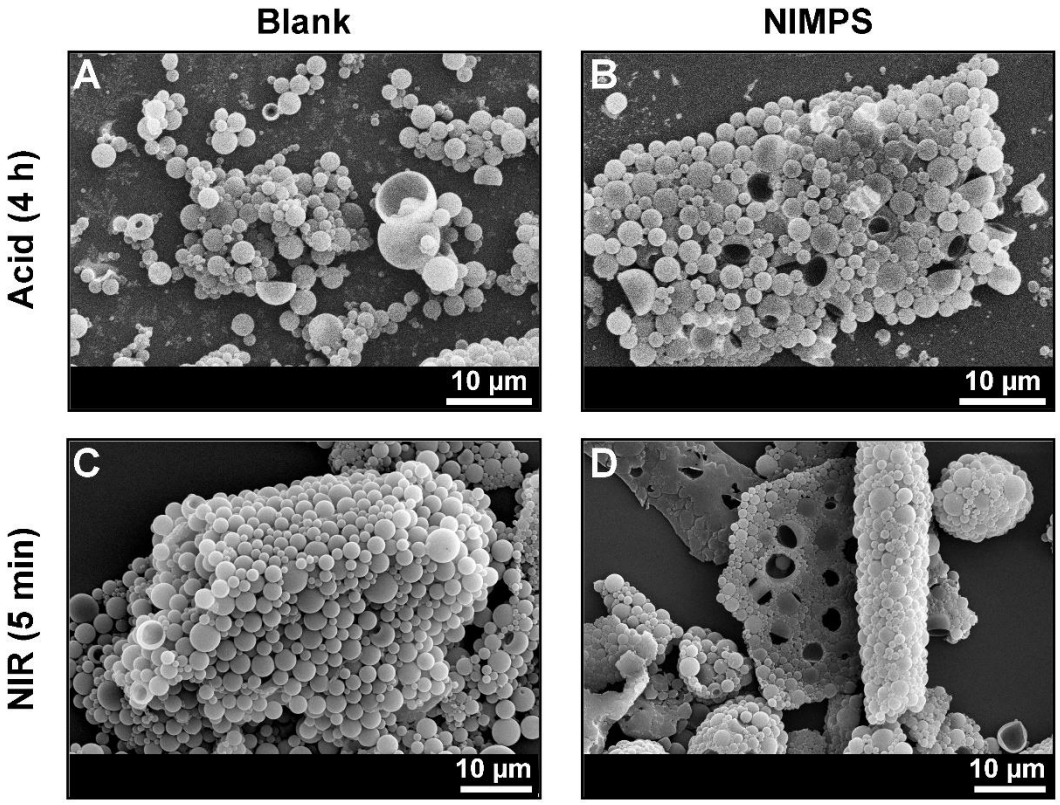

Figure 4. 4 - Characterization of Blank and NIMPS microspheres morphology by SEM analysis. Microspheres structural and morphology integrity after 4 hours in an acidic environment (A and B) or after NIR laser irradiation for 5 min (C and D).

4.4.3. NIMPS biocompatibility and cellular uptake

The characterization of NIMPS biocompatibility was performed by using FibH (Figure 4.5 A) and HeLa (Figure 4.5 B) cells. The obtained results show that the cells remained metabolically active up to 72 h of incubation with NIMPS. Further, such data is in agreement with previous studies available in the literature, where PVA-PLGA-PVA or PVA-PLGA-TPGS microspheres were used [28, 41]. Subsequently, the cellular internalization of these microspheres by HeLa cells was also evaluated. The microspheres tracking was achieved by taking advantage of the Dox autofluorescence. The results (Figure 4.6) showed that after only 1 h of incubation, Dox fluorescence was noticed within the interior of the HeLa cells. Moreover, at 4 h of incubation time, the Dox amount inside the cells increased, being even possible to observe various microspheres on the cytoplasm of these cancer cells. Altogether, this data demonstrates that NIMPS are capable of being internalized by HeLa cells as well as deliver its content in their intracellular space in order to exert the desired therapeutic effect, thus avoiding the drug premature degradation in the extracellular medium. Further, these results also confirm the previous reports available in literature where the TPGS inclusion was able to significantly enhance the cellular uptake of the drug carriers [28, 42].

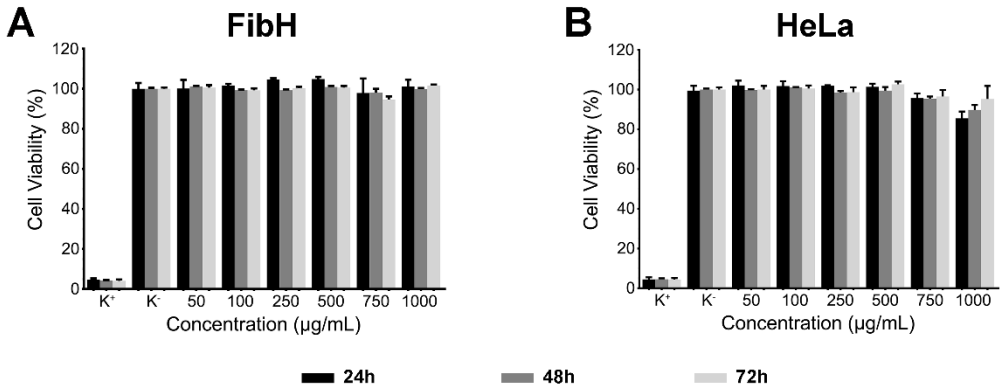

Figure 4.5 - Evaluation of the cytotoxic profile of NIMPS for 24, 48 and 72 h on FibH (A) and HeLa (B) cells. Positive control (K+): cells treated with ethanol. (K-): non-treated cells. Data are presented as mean±s.d., *ρ<0.05, n= 5.

Moreover, the cellular uptake of microspheres with this size has been already reported in the literature [23]. In fact, Ke and coworkers explored the cellular uptake routes of PLGA-PVA microspheres and showed that these carriers are internalized through an energy-dependent process, like macropinocytosis [23]. From a therapeutic point of view, the microspheres capacity to deliver its content in cell cytoplasm is critical for improving the therapeutic outcome and also avoid drug premature degradation [43].

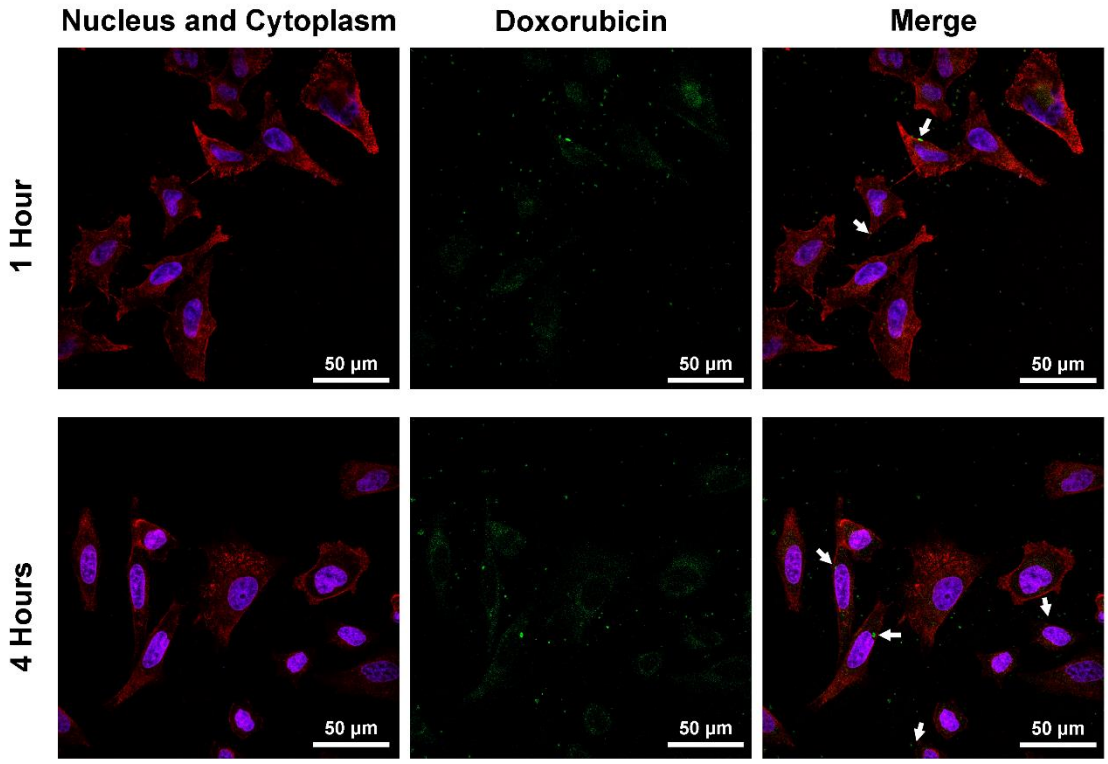

Figure 4.6 - CLSM images of NIMPS uptake by HeLa cells after 1 and 4 h. Blue channel: Hoechst 33342® stained nucleus; Red channel: WGA-Alexa Fluor® 594 for cell cytoplasm staining, green channel: Dox. The white arrows are pointing to the internalized particles.

4.4.4. Evaluation of the NIMPS cytotoxicity

The therapeutic potential of NIMPS towards HeLa cancer cells was assessed by an MTT assay. For that purpose, HeLa cells were incubated with different microspheres formulations, with concentrations ranging from 200 or 400 μg.mL^{-1} and with or without being irradiated with NIR laser light. In Figure 4.7 it is possible to perceive that the different AuMSS formulations led to a decrease in the cell viability which was proportional to the tested concentrations and to the incubation period. Furthermore, after 24 h, the cells incubated with the NIMPS (at a concentration of 400 μg.mL^{-1}) without being irradiated presented a cellular viability superior to 90%. However, when the same group was irradiated with NIR laser light the cellular viability decreased to values lower than 70%. Such difference in the particle cytotoxic activity can be justified by the NIMPS heat generation capacity under NIR laser irradiation, which promotes a faster drug release and can also sensitize cells to drug action. After 48 h of incubation (Figure 4.7 B), the NIR irradiation effect on the microspheres cytotoxic ability is more pronounced. The NIMPS exposed to NIR light induced a decrease in cellular viability to about 35%, whereas the non-irradiated group presented a cellular viability of 80%. These results are in accordance with other reports available in the literature, where the increase in temperature and consequent higher drug release led to an improved cytotoxic capacity [35, 44]. Additionally, the obtained data show that the drug combinatorial therapy can lead to an improved therapeutic outcome since the microspheres loaded only with SA or AuMSS/Dox presented higher cellular viabilities (90 and 60%, respectively) than the NIMPS counterparts (inferior to 35%). Therefore, the gathered data supports the NIMPS application as a simple and cost-effective carrier to promote a pH- and temperature- responsive localized administration of drug combinations to cancer cells.

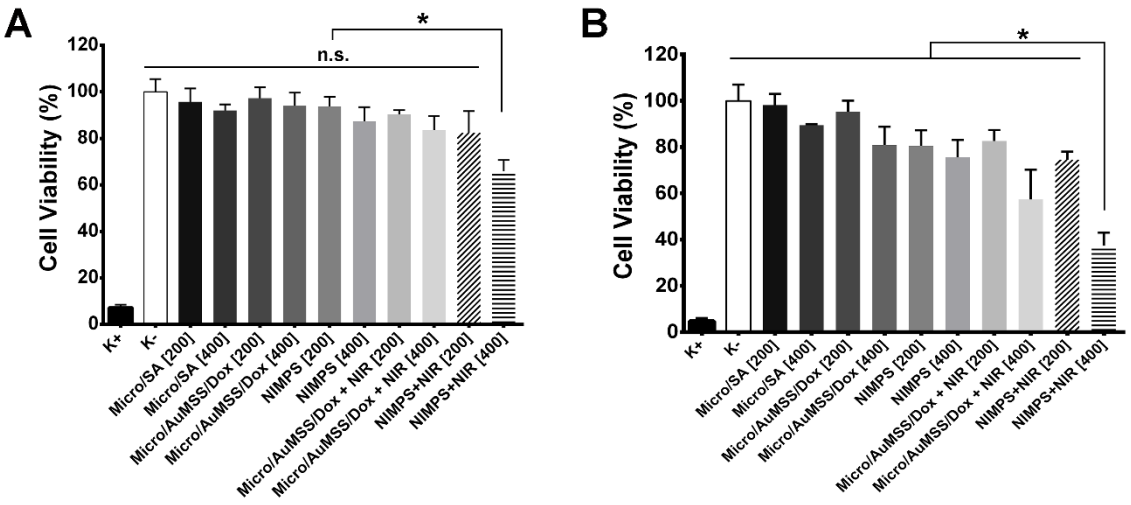

Figure 4.7 - Characterization of the cytotoxic activity of microspheres on HeLa cells at 24 (A) and 48 h (B). Positive control (K^+): cells treated with ethanol. Negative control (K^-): non-treated cells. Data are presented as mean±s.d., *$p<0.05$, n= 5.

4.4.5. NIMPS' uptake and cytotoxicity on 3D tumor spheroids

HeLa 3D spheroids were assembled by using agarose based micro-molded scaffolds. The 3D cellular organization of the spheroids mimics, *in vitro*, the features of poorly vascularized tumors (*e.g.* necrotic core, physical barriers, solid structure, pH, and waste product gradients), which render them properties their use as platforms for testing new drug delivery system or drugs [45]. The NIMPS uptake and distribution in HeLa spheroids was monitored by using CLSM (Figure 4.8). In Figure 4.8, it is possible to observe that the group treated with NIMPS exposed to NIR laser irradiation presented a more uniform Dox distribution through the surface of the spheroid (Figure 4.8 A and B) and a higher mean fluorescence intensity resulting from the increased accumulation of Dox within the 3D cell culture models (Figure 4.8 C). Altogether, this data supports the use of NIR laser irradiation to trigger the drug release in order to improve its distribution within 3D spheroids, and, subsequently, lead to an enhanced therapeutic efficacy *in vivo*.

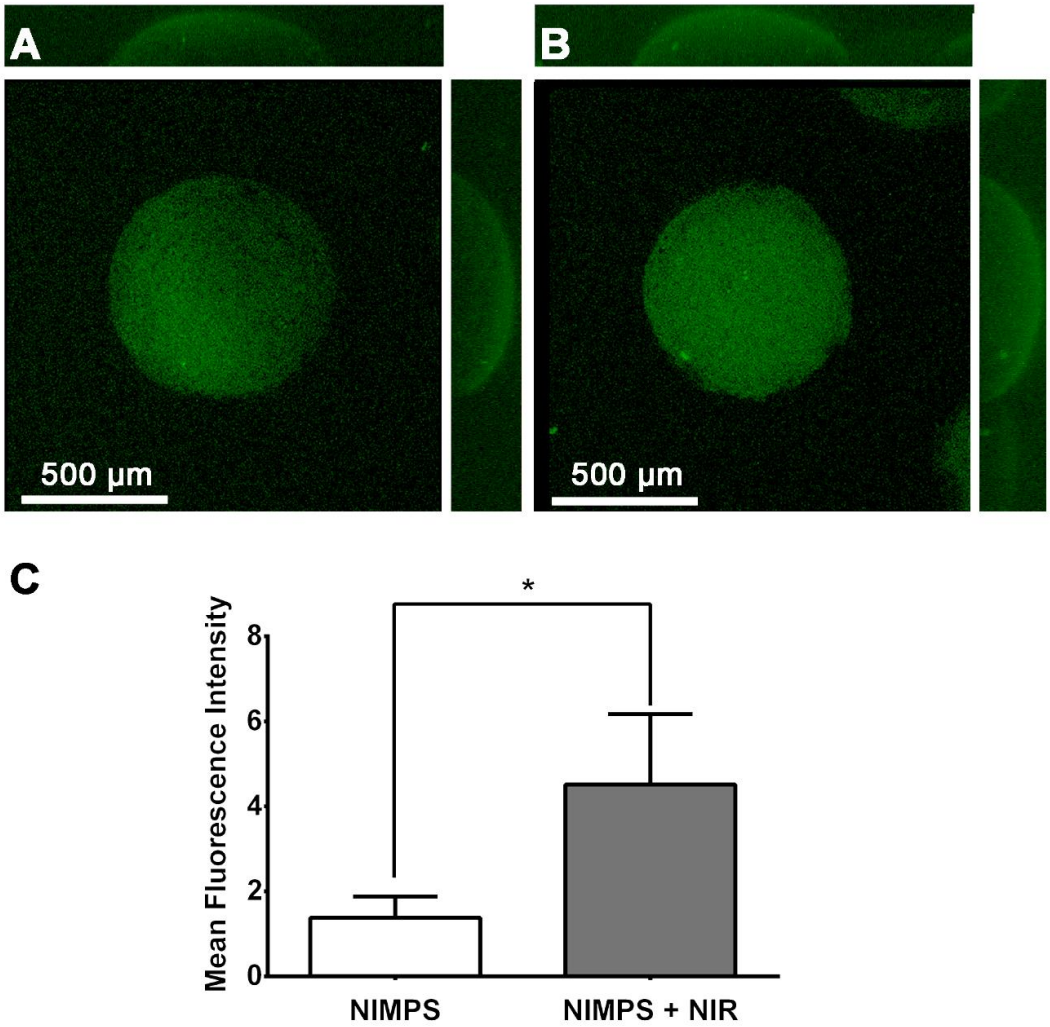

Figure 4.8 - Evaluation of the 3D tumor penetration capacity of NIMPS. Representative 3D CLSM images reconstruction and orthogonal sections of the NIMPS treated spheroids, without (A) and with (B) NIR laser irradiation, after 24 h of incubation. Analysis of the Dox mean fluorescence intensity in HeLa spheroids (C). Data are presented as mean±s.d., *$p<0.05$, n= 5.

The NIMPS capacity to promote the tumor cells death and spheroids disassembly were also investigated, by monitoring the variation of the spheroids area along time through optical microscopy (Figure 4.9 A and B). From the analysis of the optical microscopy images, it is possible to verify that the surfaces of the HeLa spheroids exposed to the microspheres were slightly disorganized. Further, with the increase of incubation time, the spheroids presented smaller sizes and their margins started to become disintegrated (Figure 4.9 A). Additionally, the spheroids area at 144 h suffered a significant decrease for those groups irradiated with the NIR laser, 49% and 52% area reduction for micro/AuMSS/Dox and NIMPS, respectively.

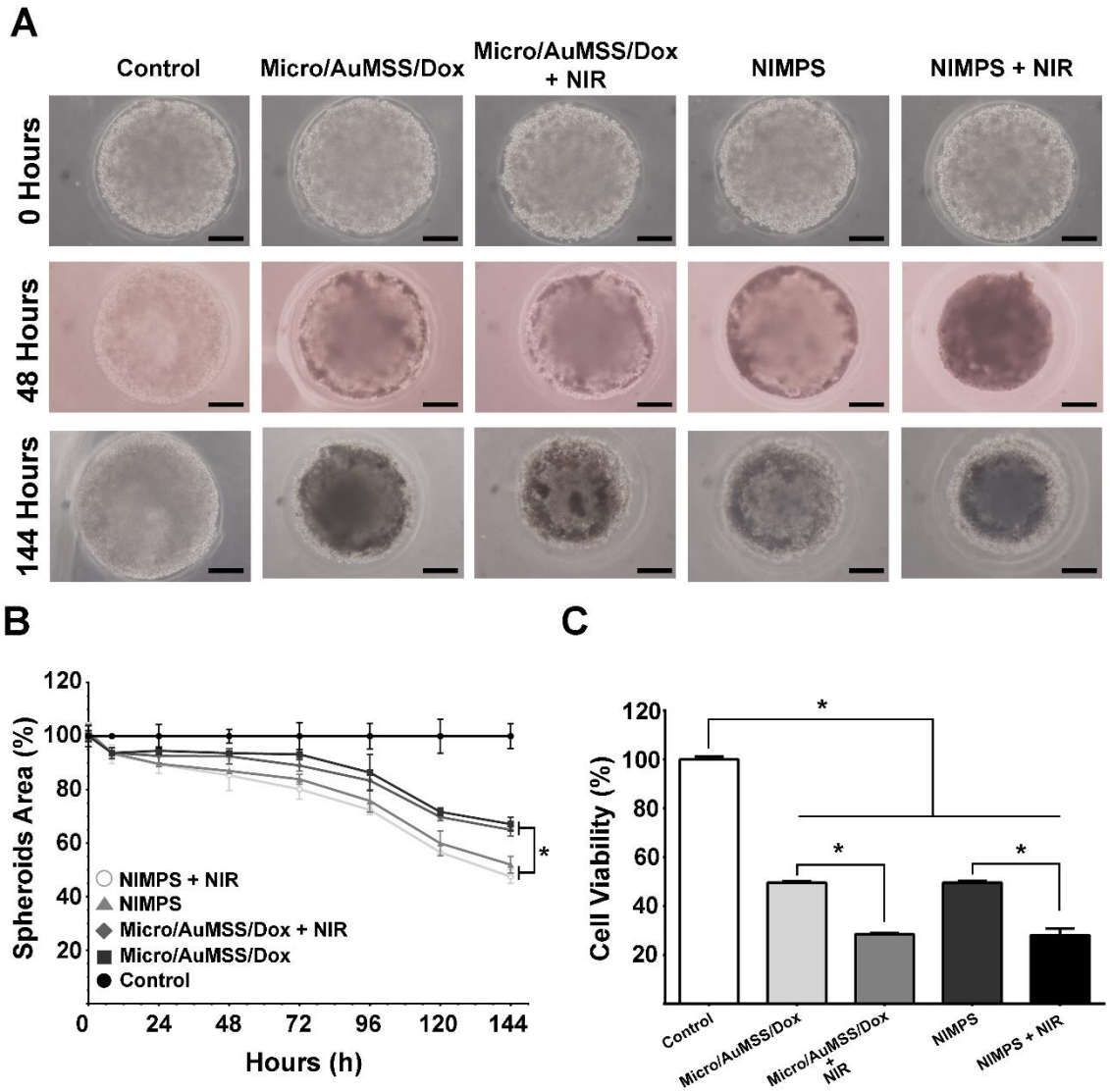

Figure 4.9 - Evaluation of the NIMPS cytotoxicity in 3D HeLa spheroids. Optical microscopy images of spheroids incubated with micro/AuMSS/Dox or NIMPS in the presence or absence of NIR laser irradiation at 0, 48 and 120 h (A). Analysis of the variation of the 3D HeLa spheroids area after microspheres incubation up to 144 h (B). Characterization of the cytotoxic activity of microspheres on 3D HeLa spheroids at 48 h (B). Control: non-treated spheroids. Data are presented as mean±s.d., *$p<0.05$, n= 5.

In contrast, the non-irradiated spheroids only presented an 30% area reduction. Such results demonstrate that the NIR laser irradiation can potentiate the microspheres effect by promoting a faster drug release, that leads to an increased cytotoxicity. Furthermore, the administration of the microspheres to HeLa spheroids resulted in lower cell viabilities, when compared to the control group (≈25% for NIR laser irradiated groups whereas the non-irradiated group presented a cellular viability of ≈50% (Figure 4.9 C)). Moreover, no significant variations in the cell viability were observed between the groups treated in the presence or absence of SA. Such result can be justified by the spheroids organization in cell layers (*i.e.* proliferating, senescent and necrotic cell regions), which makes the antiproliferative action of SA effective, mainly, on the outer cell layer of the spheroids (proliferating region) [45]. Therefore, in the future, the incorporation of more potent anticancer drugs within the microspheres should be considered to further improve the NIMPS anti-tumoral capacity. Furthermore, from a therapeutic point of view, the drugs combination can be a crucial factor since cancer treatment may be improved by attacking the cancer cells at different levels (*i.e.* by acting on different cellular pathways) to originate a synergistic anti-tumoral effect capable of eradicating the tumor without eliciting side effects [46, 47]. Moreover, the presence of AuMSSs or even the gas generation in response to acidic environments found in tumors, can also allow the NIMPS application for real-time *in vivo* imaging (*e.g.* MRI and ultrasounds). These important properties will be crucial for the application of these carriers in clinical environments [18, 19, 48].

4.5. Conclusion

Herein, a pH- and thermo- responsive microspheres containing AuMSS/Dox and SA were produced to allow the localized administration of drug combinations to cancer cells. This straightforward approach allowed the production of a carrier that is capable of encapsulating both drugs and nanoparticles as well as release them in a spatiotemporally controlled mode in response to acidic environments or to NIR irradiation. Furthermore, NIMPS display a biocompatible profile and are capable of being internalized by the HeLa cancer cells. Moreover, the administration of NIMPS to 3D HeLa cell culture models combined with the NIR laser irradiation improved the Dox distribution on the surface of the spheroids and enhanced their cytotoxicity capacity. It is also important to emphasize that to the best of our knowledge, this was the first time that AuMSS were loaded into microspheres for promoting a dual stimuli-responsive and combinatorial drug delivery. In fact, considering the drawbacks associated with standalone cancer treatments, such as those based on single drug administration, the present findings encourage the application of this simple and multifunctional hybrid system for exploring new drug-drug combinations and to bridge the gap between pre-clinical research and clinical use. In the future, the realization of *in vivo* assays is pivotal to confirm the versatility and the enhanced therapeutic effect of this stimuli-responsive drug delivery system.

4.6. References

[1] R.L. Siegel, K.D. Miller, A. Jemal, Cancer statistics, 2015, Ca-Cancer J. Clin., 65 (2015) 5-29.

[2] J.M. Noh, W. Park, Y.S. Kim, J.-Y. Kim, H.J. Kim, J. Kim, J.H. Kim, M.S. Yoon, J.H. Choi, W.S. Yoon, J.-Y. Kim, S.J. Huh, Comparison of clinical outcomes of adenocarcinoma and adenosquamous carcinoma in uterine cervical cancer patients receiving surgical resection followed by radiotherapy: A multicenter retrospective study (KROG 13-10), Gynecol. Oncol., 132 (2014) 618-623.

[3] X.-J. Liang, C. Chen, Y. Zhao, P.C. Wang, Circumventing Tumor Resistance to Chemotherapy by Nanotechnology, in: J. Zhou (Ed.) Multi-Drug Resistance in Cancer, Humana Press, Totowa, NJ, 2010, pp. 467-488.

[4] M.M. Gottesman, T. Fojo, S.E. Bates, Multidrug resistance in cancer: role of ATP-dependent transporters, Nat Rev Cancer, 2 (2002) 48-58.

[5] D. Hanahan, Robert A. Weinberg, Hallmarks of Cancer: The Next Generation, Cell, 144 (2011) 646-674.

[6] B. Al-Lazikani, U. Banerji, P. Workman, Combinatorial drug therapy for cancer in the post-genomic era, Nat. Biotechnol., 30 (2012) 679-692.

[7] D. de Melo-Diogo, V.M. Gaspar, E.C. Costa, A.F. Moreira, D. Oppolzer, E. Gallardo, I.J. Correia, Combinatorial delivery of Crizotinib–Palbociclib–Sildenafil using TPGS-PLA micelles for improved cancer treatment, Eur. J. Pharm. Biopharm., 88 (2014) 718-729.

[8] P. Parhi, C. Mohanty, S.K. Sahoo, Nanotechnology-based combinational drug delivery: an emerging approach for cancer therapy, Drug Discovery Today, 17 (2012) 1044-1052.

[9] P. Couvreur, Nanoparticles in drug delivery: Past, present and future, Adv. Drug Delivery Rev., 65 (2013) 21-23.

[10] R.S. Kaye, T.S. Purewal, H.O. Alpar, Simultaneously manufactured nano-in-micro (SIMANIM) particles for dry-powder modified-release delivery of antibodies, J. Pharm. Sci., 98 (2009) 4055-4068.

[11] A.S. Silva, M.T. Tavares, A. Aguiar-Ricardo, Sustainable strategies for nano-in-micro particle engineering for pulmonary delivery, J. Nanopart. Res., 16 (2014) 2602.

[12] V.M. Gaspar, C. Gonçalves, D. de Melo-Diogo, E.C. Costa, J.A. Queiroz, C. Pichon, F. Sousa, I.J. Correia, Poly(2-ethyl-2-oxazoline)–PLA-g–PEI amphiphilic triblock micelles for co-delivery of minicircle DNA and chemotherapeutics, J. Controlled Release, 189 (2014) 90-104.

[13] A.F. Moreira, V.M. Gaspar, E.C. Costa, D. de Melo-Diogo, P. Machado, C.M. Paquete, I.J. Correia, Preparation of end-capped pH-sensitive mesoporous silica nanocarriers for on-demand drug delivery, Eur. J. Pharm. Biopharm., 88 (2014) 1012-1025.

[14] R.B. Restani, P.I. Morgado, M.P. Ribeiro, I.J. Correia, A. Aguiar-Ricardo, V.D.B. Bonifácio, Biocompatible Polyurea Dendrimers with pH-Dependent Fluorescence, Angew. Chem., Int. Ed., 51 (2012) 5162-5165.

[15] R. Lehner, X. Wang, M. Wolf, P. Hunziker, Designing switchable nanosystems for medical application, J. Controlled Release, 161 (2012) 307-316.

[16] S. Mura, J. Nicolas, P. Couvreur, Stimuli-responsive nanocarriers for drug delivery, Nat Mater, 12 (2013) 991-1003.

[17] A.F. Moreira, D.R. Dias, I.J. Correia, Stimuli-responsive mesoporous silica nanoparticles for cancer therapy: A review, Microporous Mesoporous Mater., 236 (2016) 141-157.

[18] L.E. Cole, R.D. Ross, J.M.R. Tilley, T. Vargo-Gogola, R.K. Roeder, Gold nanoparticles as contrast agents in x-ray imaging and computed tomography, Nanomedicine, 10 (2015) 321-341.

[19] J.-T. Song, X.-Q. Yang, X.-S. Zhang, D.-M. Yan, Z.-Y. Wang, Y.-D. Zhao, Facile Synthesis of Gold Nanospheres Modified by Positively Charged Mesoporous Silica, Loaded with Near-Infrared Fluorescent Dye, for *in vivo* X-ray Computed Tomography and Fluorescence Dual Mode Imaging, ACS Appl. Mater. Interfaces, 7 (2015) 17287-17297.

[20] I. Gorelikov, N. Matsuura, Single-Step Coating of Mesoporous Silica on Cetyltrimethyl Ammonium Bromide-Capped Nanoparticles, Nano Lett., 8 (2008) 369-373.

[21] B. Nikoobakht, M.A. El-Sayed, Preparation and Growth Mechanism of Gold Nanorods (NRs) Using Seed-Mediated Growth Method, Chem. Mater., 15 (2003) 1957-1962.

[22] D.R. Dias, A.F. Moreira, I.J. Correia, The effect of the shape of gold core-mesoporous silica shell nanoparticles on the cellular behavior and tumor spheroid penetration, J. Mater. Chem. B, 4 (2016) 7630-7640.

[23] C.-J. Ke, W.-L. Chiang, Z.-X. Liao, H.-L. Chen, P.-S. Lai, J.-S. Sun, H.-W. Sung, Real-time visualization of pH-responsive PLGA hollow particles containing a gas-generating agent targeted for acidic organelles for overcoming multi-drug resistance, Biomaterials, 34 (2013) 1-10.

[24] Y. Liu, M. Xu, Q. Chen, G. Guan, W. Hu, X. Zhao, M. Qiao, H. Hu, Y. Liang, H. Zhu, D. Chen, Gold nanorods/mesoporous silica-based nanocomposite as theranostic agents for targeting near-infrared imaging and photothermal therapy induced with laser, Int. J. Nanomed., 10 (2015) 4747-4761.

[25] J.G. Marques, V.M. Gaspar, D. Markl, E.C. Costa, E. Gallardo, I.J. Correia, Co-delivery of Sildenafil (Viagra®) and Crizotinib for Synergistic and Improved Anti-tumoral Therapy, Pharm. Res., 31 (2014) 2516-2528.

[26] V.M. Gaspar, E.C. Costa, J.A. Queiroz, C. Pichon, F. Sousa, I.J. Correia, Folate-Targeted Multifunctional Amino Acid-Chitosan Nanoparticles for Improved Cancer Therapy, Pharmaceutical research, 32 (2015) 562-577.

[27] S.P. Miguel, M.P. Ribeiro, H. Brancal, P. Coutinho, I.J. Correia, Thermoresponsive chitosan–agarose hydrogel for skin regeneration, Carbohydr. Polym., 111 (2014) 366-373.

[28] V.M. Gaspar, A.F. Moreira, E.C. Costa, J.A. Queiroz, F. Sousa, C. Pichon, I.J. Correia, Gas-generating TPGS-PLGA microspheres loaded with nanoparticles (NIMPS) for co-delivery of minicircle DNA and anti-tumoral drugs, Colloids Surf., B, 134 (2015) 287-294.

[29] R.V. Kutty, S.L. Chia, M.I. Setyawati, M.S. Muthu, S.-S. Feng, D.T. Leong, *In vivo* and ex vivo proofs of concept that cetuximab conjugated vitamin E TPGS micelles increases efficacy of delivered docetaxel against triple negative breast cancer, Biomaterials, 63 (2015) 58-69.

[30] R.V. Kutty, S.-S. Feng, Cetuximab conjugated vitamin E TPGS micelles for targeted delivery of docetaxel for treatment of triple negative breast cancers, Biomaterials, 34 (2013) 10160-10171.

[31] G.-R. Tan, S.-S. Feng, D.T. Leong, The reduction of anti-cancer drug antagonism by the spatial protection of drugs with PLA–TPGS nanoparticles, Biomaterials, 35 (2014) 3044-3051.

[32] X. Huang, P.K. Jain, I.H. El-Sayed, M.A. El-Sayed, Plasmonic photothermal therapy (PPTT) using gold nanoparticles, Lasers Med. Sci., 23 (2007) 217.

[33] A.M. Alkilany, P.K. Nagaria, C.R. Hexel, T.J. Shaw, C.J. Murphy, M.D. Wyatt, Cellular Uptake and Cytotoxicity of Gold Nanorods: Molecular Origin of Cytotoxicity and Surface Effects, Small, 5 (2009) 701-708.

[34] X. Huang, M.A. El-Sayed, Gold nanoparticles: Optical properties and implementations in cancer diagnosis and photothermal therapy, J. Adv. Res., 1 (2010) 13-28.

[35] T. Zhang, Z. Ding, H. Lin, L. Cui, C. Yang, X. Li, H. Niu, N. An, R. Tong, F. Qu, pH-Sensitive Gold Nanorods with a Mesoporous Silica Shell for Drug Release and Photothermal Therapy, Eur. J. Inorg. Chem., 2015 (2015) 2277-2284.

[36] D. Jaque, L. Martinez Maestro, B. del Rosal, P. Haro-Gonzalez, A. Benayas, J.L. Plaza, E. Martin Rodriguez, J. Garcia Sole, Nanoparticles for photothermal therapies, Nanoscale, 6 (2014) 9494-9530.

[37] Y. Zhang, Z. Hou, Y. Ge, K. Deng, B. Liu, X. Li, Q. Li, Z. Cheng, P.a. Ma, C. Li, J. Lin, DNA-Hybrid-Gated Photothermal Mesoporous Silica Nanoparticles for NIR-Responsive and Aptamer-Targeted Drug Delivery, ACS Appl. Mater. Interfaces, 7 (2015) 20696-20706.

[38] Y.-S. Chen, W. Frey, S. Kim, K. Homan, P. Kruizinga, K. Sokolov, S. Emelianov, Enhanced thermal stability of silica-coated gold nanorods for photoacoustic imaging and image-guided therapy, Opt. Express, 18 (2010) 8867-8878.

[39] H.-J. Li, J.-Z. Du, X.-J. Du, C.-F. Xu, C.-Y. Sun, H.-X. Wang, Z.-T. Cao, X.-Z. Yang, Y.-H. Zhu, S. Nie, J. Wang, Stimuli-responsive clustered nanoparticles for improved tumor penetration and therapeutic efficacy, Proc. Natl. Acad. Sci., 113 (2016) 4164-4169.

[40] S.R. MacEwan, D.J. Callahan, A. Chilkoti, Stimulus-responsive macromolecules and nanoparticles for cancer drug delivery, Nanomedicine, 5 (2010) 793-806.

[41] C.-J. Ke, T.-Y. Su, H.-L. Chen, H.-L. Liu, W.-L. Chiang, P.-C. Chu, Y. Xia, H.-W. Sung, Smart Multifunctional Hollow Microspheres for the Quick Release of Drugs in Intracellular Lysosomal Compartments, Angew. Chem., 123 (2011) 8236-8239.

[42] S.A. Kulkarni, S.-S. Feng, Effects of Particle Size and Surface Modification on Cellular Uptake and Biodistribution of Polymeric Nanoparticles for Drug Delivery, Pharm. Res., 30 (2013) 2512-2522.

[43] T. Sun, Y.S. Zhang, B. Pang, D.C. Hyun, M. Yang, Y. Xia, Engineered Nanoparticles for Drug Delivery in Cancer Therapy, Angew. Chem., Int. Ed., 53 (2014) 12320-12364.

[44] Z. Zha, S. Zhang, Z. Deng, Y. Li, C. Li, Z. Dai, Enzyme-responsive copper sulphide nanoparticles for combined photoacoustic imaging, tumor-selective chemotherapy and photothermal therapy, Chem. Commun., 49 (2013) 3455-3457.

[45] E.C. Costa, A.F. Moreira, D. de Melo-Diogo, V.M. Gaspar, M.P. Carvalho, I.J. Correia, 3D tumor spheroids: an overview on the tools and techniques used for their analysis, Biotechnol. Adv., 34 (2016) 1427-1441.

[46] Q. Hu, W. Sun, C. Wang, Z. Gu, Recent advances of cocktail chemotherapy by combination drug delivery systems, Adv. Drug Delivery Rev., 98 (2016) 19-34.

[47] J.A. Kemp, M.S. Shim, C.Y. Heo, Y.J. Kwon, "Combo" nanomedicine: Co-delivery of multi-modal therapeutics for efficient, targeted, and safe cancer therapy, Adv. Drug Delivery Rev., 98 (2016) 3-18.

[48] K.H. Min, H.S. Min, H.J. Lee, D.J. Park, J.Y. Yhee, K. Kim, I.C. Kwon, S.Y. Jeong, O.F. Silvestre, X. Chen, Y.-S. Hwang, E.-C. Kim, S.C. Lee, pH-Controlled Gas-Generating Mineralized Nanoparticles: A Theranostic Agent for Ultrasound Imaging and Therapy of Cancers, ACS nano, 9 (2015) 134-145.

Chapter 5

Research Work 3

Microneedles mediated chemotherapy and photothermal therapy for the treatment of cancer

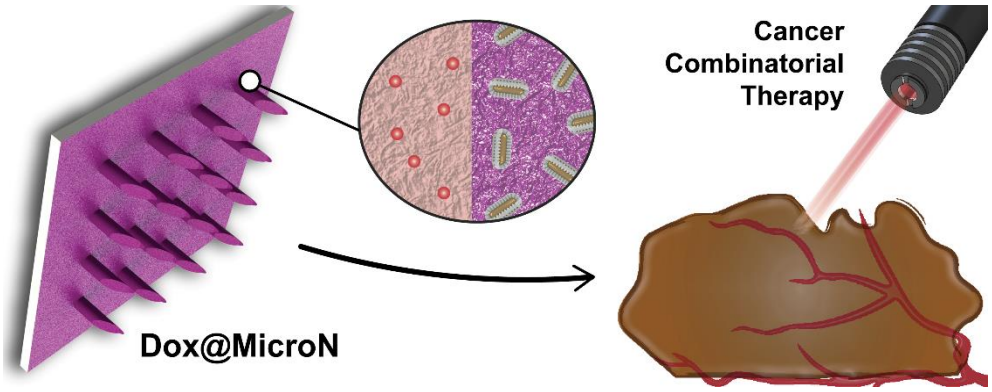

This chapter is based on the publication:

Moreira, A.F., Rodrigues, C. F., Jacinto, T. A., Miguel, S. P., Costa, E. C., & Correia, I. J. (2019). Poly (vinyl alcohol)/Chitosan Layer-by-Layer Microneedles for Cancer Chemo-Photothermal Therapy. International Journal of Pharmaceutics, *in press*, 10.1016/j.ijpharm.2019.118907.

5.1. Abstract

Combination of PTT and chemo therapeutic approaches display a high potential to increase the cancer treatments efficacy or even to promote its eradication. In this study, a new layered PVP microneedle system loaded with Dox and AuMSS nanorods (Dox@MicroN) aimed to be used for the combinatorial therapy of cancer was developed through the alternated electrospraying of chitosan and poly (vinyl alcohol). Then their structural functional features were evaluated, and the data obtained show that both the Dox and AuMSS can be efficiently incorporated into the microneedle's layers. Further, the Dox@MicroN structures were able to penetrate the tumor-mimicking agarose gel and release the Dox in a pH- and thermo-controlled fashion. Furthermore, the Dox@MicroN patches capacity to simultaneously mediate the chemo and PTT effects rendered a superior cytotoxic capacity against the cervical cancer cells. Overall, the Dox@MicroN patches demonstrated to be a simple macroscale delivery device that can be used to mediate the local administration of new drug-PTT combinations, avoiding all the issues related with the systemic administration of anti-cancer therapeutics.

Keywords: Microneedles, layer-by-layer, gold-core silica shell nanorods, combinatorial therapy, cancer.

5.2. Introduction

Cancer is one of the leading causes of death worldwide and its incidence has been increasing in the last decades [1]. In the clinic, the standard treatments for cancer include surgery, chemotherapy, and radiotherapy [2, 3]. However, these therapeutic approaches frequently present a limited efficacy and have associated serious side effects [2, 3]. Further, the intravenous administration of anticancer therapeutics has several drawbacks such as poor solubility, extensive accumulation in major organs, rapid clearance from blood circulation, and limited bioavailability that hinders their therapeutic effectiveness [4, 5]. Therefore, researchers have been exploring new approaches to improve the anticancer efficacy of the currently available therapies [6, 7]. In fact, the conjugation of different therapeutic approaches for cancer has the potential to reduce the adverse side-effects while simultaneously maximizing the molecules tumoricidal activity by surpassing cancer cells resistance mechanisms [6-8]. In this field, the conjugation of hyperthermia (*e.g.* PTT) with chemotherapy regiments arises as one of the most explored combinatorial treatments [9-11].

With this in mind, researchers have been exploring the development of new nanomaterials that are able to mediate a temperature increase in response to specific stimuli (*e.g.* magnetic field, ultrasounds, and NIR radiation) and simultaneously deliver chemotherapeutic agents to cancer cells [12-14]. Among the different approaches, AuMSS nanoparticles are promising candidates for medical applications since they combine in a single platform the PTT ability of gold nanoparticles and drug delivery potential of mesoporous silica [9, 15, 16]. Gold nanoparticles surface plasmon resonance oscillation renders to them a strong absorption in the NIR region, where the body components have minimal or no absorption, minimizing the off-target interactions of the PTT [17-19]. On the other side, the mesoporous silica coating provides a biocompatible and chemically inert shell with a large surface area that can be modified with functional groups in order to confer to the nanodevice an enhanced colloidal stability, targeting or stimulus responsiveness [5, 20, 21]. More importantly, the inclusion of the mesoporous silica shell stabilizes and protects the gold-core from degradation when exposed to NIR radiation and further improves the particle capacity to encapsulate and deliver bioactive molecules, specifically to cancer cells [21-24].

Nevertheless, the systemic therapeutic approaches to cancer (*e.g.* nanomedicines and drugs) are still too complex to be adequately applied in the clinic and present undesired interactions at nontarget sites [25, 26]. To overcome these issues, macroscale delivery devices (*e.g.* microneedle systems and hydrogels) that can be placed at the tumor region and engineered to locally control the delivery of the therapeutic agents, such as drugs and nanoparticles, started to receive a great attention in the past years [25, 27]. In this work, a layered PVP microneedle system loaded with Dox and AuMSS nanorods aimed for the combinatorial therapy of cancer was developed through the alternated electrospraying of Ch

and PVA. PVP is a water soluble and biocompatible polymer approved by the Food and Drugs Administration (FDA) and widely used in the pharmaceutical industry as a coating agent, polymeric membrane, and material for controlled drug release [28, 29]. This material was used as the structural agent of the microneedles due to its mechanical strength, which can endure the forces involved in its insertion on the tumor tissue [30, 31]. Further, the PVP water solubility guarantees the microneedles dissolution and biodegradation [30, 32]. Ch is a cationic polysaccharide that have been greatly explored for drug delivery applications due to its unique characteristics such as biodegradability, biocompatibility, high drug-carrying capacities, and pH sensitivity [33-36]. Otherwise, the PVA is a water soluble and nontoxic anionic polymer that form films with high strength and resistance to acid and alkali media [37, 38]. Additionally, the Ch and PVA polyelectrolyte pairs are compatible with the fabrication of films using the electrospraying method [37, 39]. Therefore, two different and electrostatically stabilized layers were created on the surface of PVP microneedles to contain the therapeutic agents and allow a superior control over the therapeutic effect [40-42].

5.3. Materials and Methods

5.3.1. Materials

$HAuCl_4$ was purchased from Alfa Aesar (Karlsruhe, Germany). TEOS was bought to Acros Organics (Geel, Belgium). CTAB was obtained from Tokyo Chemical Industry Europe (Zwijndrecht, Belgium). HCl was acquired from Panreac (Barcelona, Spain). Methanol was obtained from VWR International (Carnaxide, Portugal). Glacial acetic acid was gathered from LabChem (New York, United States of America). DMEM-HG, DMEM-F12, AA, resazurin, sodium borohydride ($NaBH_4$) PBS solution, ethanol, trypsin, PDMS, PVA (Mw: 31,000 $g.mol^{-1}$), PVP (Mw:360,000 $g.mol^{-1}$), and Ch (Mw: 50,000-190,000 Da) were purchased from Sigma-Aldrich (Sintra, Portugal).WGA-Alexa Fluor® 594 was purchased from Invitrogen (Carlsbad, CA). HeLa cells (ATCC® CCL-2™) were acquired from ATCC (Middlesex, UK). FibH cells were obtained from Promocell (Heidelberg, Germany). Cell culture t-flasks were gotten from Orange Scientific (Braine-l'Alleud, Belgium). Cell imaging plates were acquired from Ibidi GmbH (Munich, Germany).

5.3.2. Synthesis of the AuMSS nanorods

AuMSS nanorods were synthesized through a two-steps procedure as previously described in [7, 43]. Initially, small spherical gold nuclei (seeds) were prepared by adding under stirring, 600 µL of $NaBH_4$ (0.01 M) to an aqueous solution of CTAB (100 mM) and $HAuCl_4$ (0.25 mM). Subsequently, a grow solution was prepared by injecting 210 µL of AA (0.08 M) to an aqueous solution containing 15 mL of CTAB (200 mM), 30 µL of $AgNO_3$ (100 mM) and 300 µL of $HAuCl_4$ (50 mM) under stirring. Lastly, to produce the gold nanorods, the seed solution was added to the growth solution and aged for 16 h at 30ºC.

To produce the mesoporous silica coating, the gold nanorods were centrifuged to remove the excess of CTAB and resuspended in ultrapure water. Subsequently, CTAB (100 mM) was added and the solution was left under stirring overnight. Afterward, NaOH (100 mM) was added to the solution and homogenized for 30 min. Then, three injections of 30 µL of TEOS (20% v/v in methanol) were performed with 30 min intervals and after the final injection, the solution was left under stirring for 24 h. The final solution was centrifuged at 12,000 g for 20 min and washed several times with ultrapure water to recover the AuMSS nanorods. Then, the removal of the CTAB surfactant template from nanoparticles was performed by adapting a solvent based approach, already described by Reis and co-workers [44].

5.3.3. Production of the microneedles patches

The PVP microneedles with a bevel-like tip were produced using the micromoulding technique as described previously in the literature [45]. Briefly, a PVP solution (20% w/v) was poured into a PDMS mold (4x4 array design) and allowed to settle in the needle pores under vacuum for 2 h. Then, the PVP solution was air-dried and gently peeled. After, the Ch and PVA films with a LbL organization were produced by using the electrospraying method [37, 46, 47]. For that purpose, the Ch (1% w/v in acetic acid) and PVA (12% w/v in double distilled water) were sequentially electrosprayed onto the surface of the PVP microneedles using a conventional electrospinning apparatus, comprised of high voltage source (Spellman SL40*10, 0–40 kV) (obtained from Spellman, Corporate Headquarters USA) a precision syringe pump (KDS-100) (acquired from Sigma-Aldrich, Sintra, Portugal), a plastic syringe with a stainless-steel needle (21 Gauge), and an aluminium disk connected to a copper collector. The Ch solution was electrosprayed at a constant flow rate of 0.5 $mL.h^{-1}$, using a working distance of 8-10 cm and an applied voltage of 30 kV. Subsequently, the PVA layer was produced in similar conditions, constant flow rate of 0.2 $mL.h^{-1}$, using a working distance of 10-12 cm and an applied voltage of 32 kV, rendering the PVP_Ch_PVA microneedles.

In order to produce the drug (PVP_Ch/Dox_PVA) or nanoparticles (MicroN) loaded microneedles, before the electrospraying process, the Dox was incorporated on the Ch solution at a final concentration of 100 $\mu g.mL^{-1}$, whereas the AuMSS nanorods were mixed with the PVA solution at a final concentration of 1 $mg.mL^{-1}$. The microneedles containing both Dox and AuMSS nanorods are designated as Dox@MicroN.

5.3.4. Characterization of the MicroN's physicochemical properties

The morphology of the MicroN patches was characterized by SEM. For that purpose, the samples were mounted on aluminum stubs with Araldite glue and sputter-coated with gold using a Quorum Q150R ES sputter coater (Quorum Technologies Ltd, Laughton, East Sussex, England). SEM images were acquired at different magnifications, using an acceleration voltage of 20 kV,

in a Hitachi S-3400N Scanning Electron Microscope (Hitachi, Tokyo, Japan). After that, microneedles dimensions were measured using a software (Image J 2.0.0, NIH Image, USA). The MicroN composition was confirmed by acquiring the FTIR spectra on a Nicolet iS10 spectrometer, with a 4 cm^{-1} spectral resolution from 600 to 4000 nm (Thermo Scientific Inc., Massachusetts, USA). The MicroN NIR absorption capacity was evaluated through the acquisition of the particles' UV-vis spectra an UV-vis spectrophotometer (Thermo Scientific Evolution™ 201 Bio UV-vis Spectrophotometer, Thermo Fisher Scientific Inc., USA) at a 300 $nm.min^{-1}$ scanning rate, with a wavelength range from 200 to 1100 nm.

5.3.5. *In vitro* PTT measurements

The MicroN PTT capacity was evaluated as previously described in the literature [7]. Thus, MicroN samples with 4 mm of diameter and a control group (PBS media) were irradiated with a NIR laser light (808 nm, 1.7 $W.cm^{-2}$). The temperature variation of the solution was measured at different time points (from 1 up to 10 min) by using a thermocouple sensor with an accuracy of 0.1ºC.

5.3.6. Evaluation of the MicroN drug and nanoparticle loading

In order to evaluate the drug and nanoparticle loading, the MicroN was subjected to total degradation through immersion in PBS at pH 5.6 [48]. Then, the supernatant was recovered by centrifugation at 8,000g for 10 min.

The Dox concentration (CDox) on the supernatant was determined by using a microwell plate reader (Spectramax Gemini XS, MolecularDevices LLC, USA) at an excitation/emission wavelength of 470/595 nm and using a calibration curve (Flu = 28.694 CDox + 269.04; R^2 =0.984). In turn, the AuMSS concentrations (CAuMSS) were quantified by measuring the supernatant absorbance at 780 nm in an UV-vis spectrophotometer (Thermo Scientific Evolution 201 Bio UV-vis Spectrophotometer, Thermo Fisher Scientific Inc., USA), and using a calibration curve (ABS = 0.0188 CAuMSS - 0.0539; R^2 =0.997).

5.3.7. Characterization of the MicroN drug release profile

The characterization of the drug release profile of the MicroN patches was performed according to a method previously described in the literature [49]. Briefly, the MicroN patches were resuspended in PBS and inserted in a Float-A-Lyzer dialysis bag with a molecular weight cut-off of 1,000 Da. The dialysis was performed at 37ºC, under magnetic stirring in 10 mL of PBS solution, at pH 5.6 or 7.4. At different time points, 1 mL of samples was collected, and the same volume of fresh PBS was added to the dialysis medium, in order to maintain the PBS volume constant during the experiment. The Dox content was measured by the above-described fluorescent method.

5.3.8. Biocompatibility assays

The MicroN patches biocompatibility was evaluated through a resazurin-based assay, as previously described in [19]. Briefly, FibH and HeLa cells were seeded into 96-well flat bottom culture plates at a density of 10,000 cells per well with 200 µL of culture media (DMEM-F12 or DMEM-HG medium, respectively). During approximately 24 h, cells were cultured at 37ºC in a humid atmosphere containing 5% CO_2. Afterwards, the cells were cultured with the MicroN samples with 4 mm of diameter for 24 or 48 h. Then, the medium was replaced, and the cells were incubated with 10%(v/v) of resazurin (1 $mg.mL^{-1}$), at 37ºC and 5% CO_2 during 4 h.

The resorufin produced by the cells was quantified by using a microwell plate reader (Spectramax Gemini XS, MolecularDevices LLC, USA) at an excitation/emission wavelength of 560/590 nm. Cells cultured in the absence of nanoparticles were used as negative control (K^-), whereas cells incubated with ethanol (99.9%) were used as positive control (K^+).

5.3.9. MicroN *in vitro* penetration studies

The MicroN patch penetration capacity was evaluated *in vitro* using tissue-mimicking agarose gels [50, 51]. For that purpose, agarose was ressuspended in double distilled water (6% w/v), heated up to 90ºC, and casted on µ-Slide 8 well Ibidi imaging plates. Then, the Dox@MicroN patches were inserted on the tissue-mimicking agarose gels and the drug release (*i.e.* diffusion to the agarose gel) was followed overtime by CLSM. For allowing the visualization of the Dox@MicroN layered structure, the PVA-AuMSS layer was stained with WGA-594. Successive z-stacks were acquired in a confocal microscope (Zeiss LSM 710, Carl Zeiss, Germany) and the images 3D reconstruction was performed in the Zeiss Zen 2010 software.

5.3.10. Evaluation of the MicroN cytotoxic effect

The MicroN patch cytotoxic effect was evaluated through the resazurin assay [7]. Briefly, 10,000 HeLa cells were seeded in 96-well plates containing DMEM-HG culture medium. After 24 h of culture, free Dox (14.168 µM) or different MicroN formulations were added to HeLa cells. After 6 h, the cells were irradiated with a laser (808 nm, 1.7 $W.cm^{-2}$ for 5 min) and incubated for 24 h. Then, the cells viability was assessed by using the resazurin assay, cells incubated with ethanol (99.9% v/v) were used as positive control (K^+), whereas cells without being exposed to the patch were used as negative controls (K^-).

5.3.11. Statistical analysis

All data are presented as mean±standard deviation (s.d.). ANOVA with the Student–Newman–Keuls post-test was used for multiple groups comparison. A p-value lower than 0.05 ($p< 0.05$) was considered statistically significant. Statistical analysis was performed using GraphPad Prism v.6.0 software (Trial version, GraphPadSoftware, CA, USA).

5.4. Results and discussion

5.4.1. MicroN's physicochemical characterization

Recently, macroscale delivery systems have started to be reexplored for cancer therapy, as tools to avoid the complexity and side-effects of the systemic administration of anticancer therapeutics (*e.g.* drugs and nanoparticles) [52-54]. In this field, the microneedles-based systems can locally mediate the release of therapeutics and increase its penetration [55, 56]. In this study, an electrospray technique was used to produce a layered microneedle system loaded with Dox and AuMSS nanorods for the chemo-PTT of cancer. The rigid PVP microneedle backbone was produced using a PDMS mold consisting in a 16 (4 by 4) microneedles array (Figure 5.1 A). Then, the PVP microneedles were coated with two different layers composed by Ch and PVA using the electrospraying method (Figure 5.1 A). The resulting MicroN patch presented microneedles with a bevel-like structure with 425 µm, 1420 µm, and 1740 µm of width, height, and tip-to-tip distance, respectively (Figure 5.1 B and C). Further, the PVA layer also contained AuMSS nanorods with a total length and width of 84±10 and 56±5 nm (gold core with A.R. of 3.5, mean length and width of 49±7 and 14±2 nm) (Figure 5.2A). The gold core size is paramount for the nanoparticles capacity to mediate the NIR light conversion to heat, in fact, A.R. between 3 and 4 have been reported as optimal to absorb the NIR light and produce a PTT effect [15]. The MicroN FTIR spectra (Figure 5.2B) clearly shows the characteristic peak of PVP at 1645 cm^{-1} which is assigned to the stretching vibration of the C=O bond [57]. Further, it is possible to observe the Ch C-O-C asymmetric stretching at 1160 cm^{-1} and the C-O stretching vibrations of the pyranose ring at 1060-1026 cm^{-1} as well as the PVA C-H stretching at the 2911 cm^{-1} [34, 58]. Additionally, the AuMSS incorporation in the PVA layer is confirmed by the presence of the mesoporous silica shell' characteristic peaks in the 1100 to 750 cm^{-1} region, that corresponds to Si-O-Si, Si-O and Si-OH vibrations [3, 5]. Additionally, the UV-vis spectra of AuMSS and MicroN show the characteristic peaks of gold nanorods at 500 nm and 770 nm, which correspond to the gold nanorod transversal and longitudinal surface plasmon resonance, respectively. The presence of these two different peaks in the UV-vis absorbance spectrum is in agreement with the data reported in the literature for other AuMSS nanorods with a similar A.R. [3, 7, 24]. Thus, the FTIR and UV spectra (Figure 5.2 B and C) confirmed the successful incorporation of the AuMSS nanorods on the MicroN patches. Further, the strong absorption band in the 700-900 nm range (region of the spectra where the biologic constituents present a low absorption) support the MicroN patches' application as PTT agents.

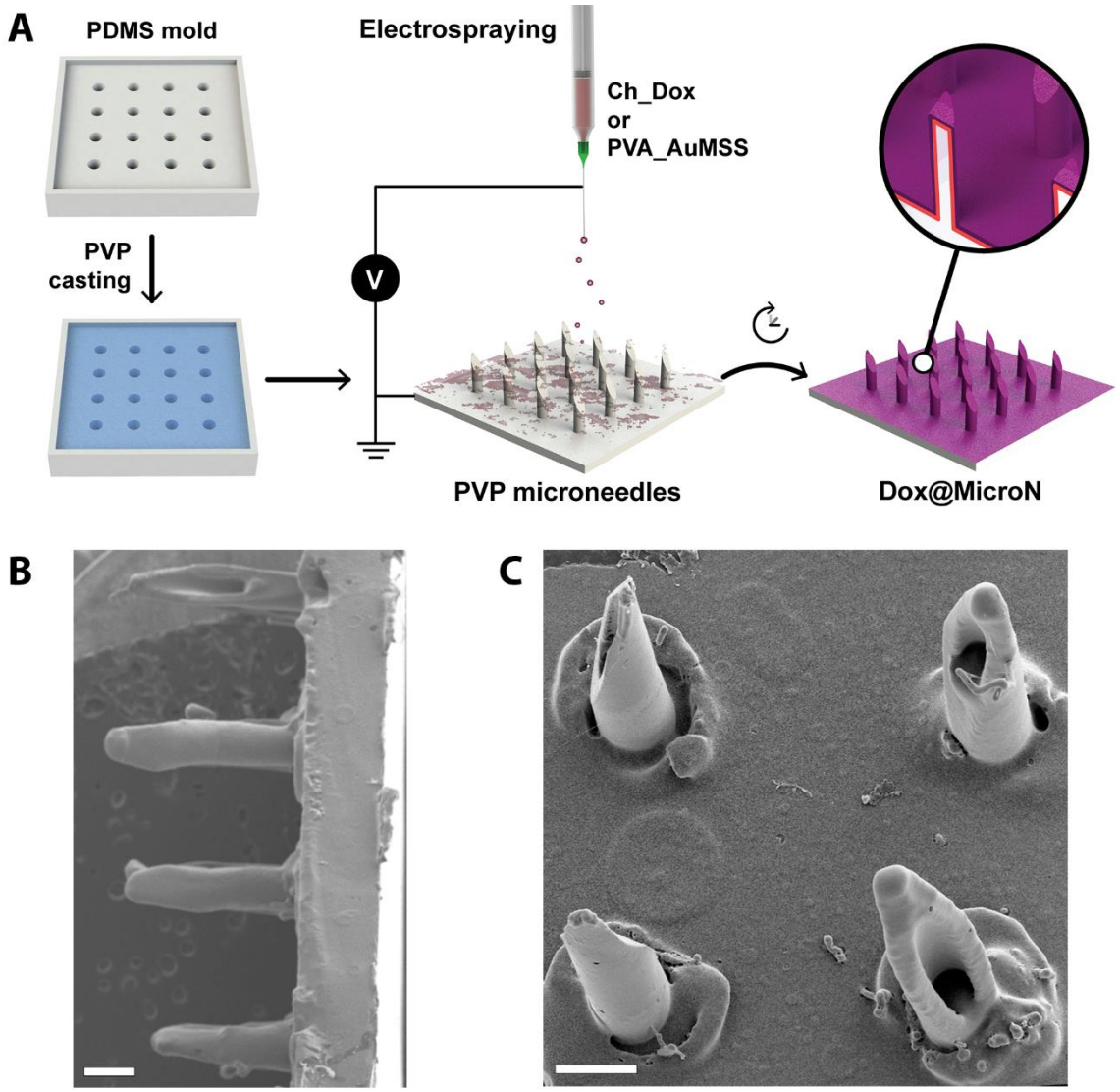

Figure 5.1 - Morphological analysis of the MicroN patches. (A) Schematics of the Dox@MicroN production process. SEM images of the Dox@Micron patches, (B) side-view and (C) top-view. The scale bars correspond to 500 µm.

Afterward, the MicroN PTT capacity was evaluated by monitoring the temperature changes upon irradiation with an 808 nm NIR light for 1 up to 10 min (Figure 5.2 D). The obtained results show that the MicroN patches mediate a sharp temperature increase during the first 5 min of irradiation (ΔT of 15ºC) that stabilizes until the end of the experiment. Such PTT capacity is in accordance with previous reports in the literature, where AuMSS nanorods could mediate an increase in the temperature mainly in the first 5 min of irradiation. Further, this PTT effect indicate that the MicroN patches may sensitize the cancer cells to the chemotherapy action or even induce its death by mediating the proteins denaturation and disruption of the cellular membrane [59, 60].

5.4.2. MicroN's drug loading and release profile

The PVP_Ch_PVA microneedles potential to act as a macroscale drug delivery platform was evaluated by investigating its capacity to encapsulate chemotherapeutic drugs (Dox) and nanomedicines (AuMSS). Upon the microneedles' total degradation, the Dox loading was determined by measuring the supernatant fluorescence (λ_{ex}=470 nm and λ_{em}=595 nm), whereas the amount of AuMSS nanorods in the PVA layer was quantified by measuring the absorbance at 780 nm (Figure 5.3 A). The obtained results show that the Dox@MicroN patches contain 0.155 $\mu g.mm^{-2}$ of Dox and 3.285 $\mu g.mm^{-2}$ of AuMSS nanorods (encapsulation efficiencies of 64.052% and 86.642%). After confirming the Dox loading, the MicroN patches' drug release profile was characterized at two pH values, 5.6 (to simulate the tumor microenvironment and lysosomal compartments) and 7.4 (to simulate physiological conditions) with or without NIR laser irradiation. The obtained results (Figure 5.3 B) show that the Dox release occurs in a pH dependent manner, *i.e.* at pH 7.4 reached the 12% whereas this value increase to 56% at pH 5.6. These differences in the Dox drug release are attributed to the protonation of the Ch' NH_2 groups at acidic pH, that leads to the polymeric matrix swelling facilitating the drug diffusion [36].

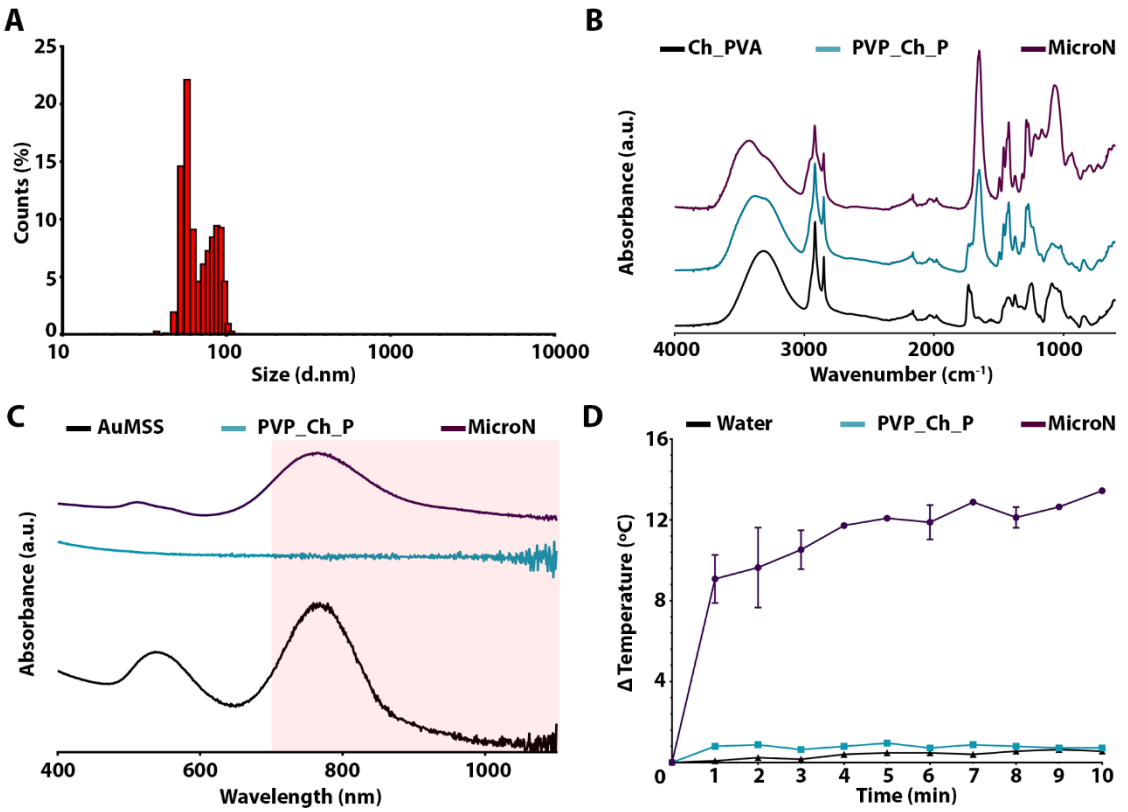

Figure 5.2 - Physicochemical characterization of the MicroN patches. (A) AuMSS nanorods size distribution (length and width included), n=300. (B) FTIR spectra of Ch_PVA, PVP_Ch_PVA microneedles, and MicroN patches. (C) UV-vis spectra of AuMSS, PVP_Ch_PVA microneedles, and MicroN patches. (D) *In vitro* PTT effect of the MicroN patches upon NIR light irradiation (808 nm, 1.7 $W.cm^{-2}$, 10 min). Data are presented as mean±s.d., n= 3.

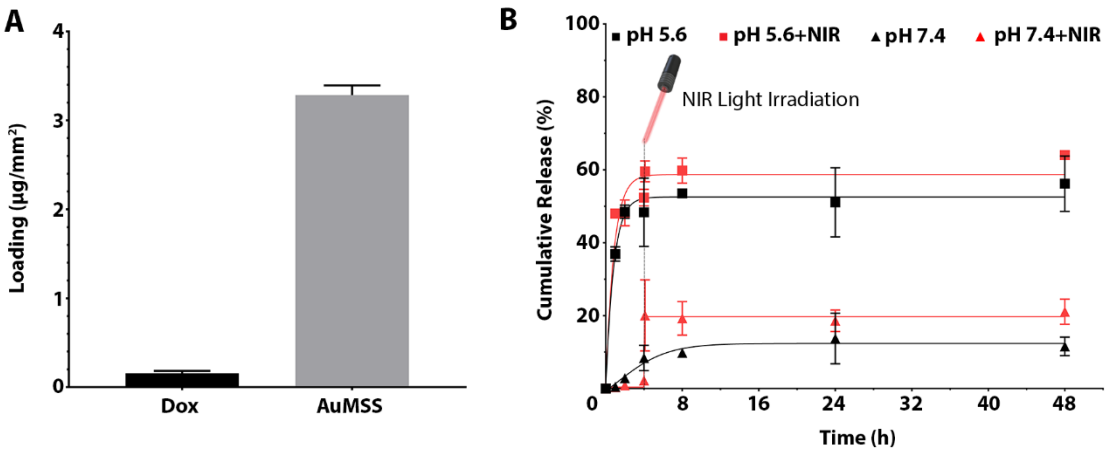

Figure 5.3 - Characterization of the MicroN drug loading and release profile. (A) Analysis of the Dox and AuMSS loading efficiency. (B) Dox cumulative release from Dox@MicroN patches at pH 5.6 (squares) or 7.4 (triangles). Black lines - Dox release in the absence of NIR light irradiation; Red lines – Dox release with samples NIR light irradiation after 4 h of incubation. Data are presented as mean±s.d., n=3.

Additionally, after 4 h of incubation, the Dox@MicroN irradiation with a NIR laser for 5 min and consequent heat generation further increased the amount of Dox released, reaching the 20.05% at pH 7.4 and the 59.55% at pH 5.6. Such behavior may be justified by the increase in the media temperature upon the MicroN patches irradiation and consequent improvement of the polymers' and drugs' solubility. Therefore, these results demonstrate that the MicroN patches can promote an on demand sustained and controlled release of chemotherapeutics upon insertion into the target site. Moreover, agarose penetration and diffusion tests were performed to demonstrate the Dox@MicroN drug delivery capacity (Figure 5.4 A). The model agarose gel was prepared to mimic the viscoelastic properties of tumor tissues [50, 51]. In fact, Manickam and colleagues demonstrated that the mechanical properties of breast and prostate tumors could be reproduced by agarose constructs using a concentration of 6-8% (w/v) [51]. Additionally, the agarose gel provides a homogeneous and transparent medium compatible with confocal microscopy imaging and therefore allows the monitoring of the Dox@MicroN patches penetration and drug delivery [50]. The obtained results clearly demonstrate the layered organization of the Dox@MicroN patches with an inner green layer (Ch layer containing Dox) and an outer red layer PVA-AuMSS layer stained with WGA-Alexa Fluor® 594) (Figure 5.4 B). Further, these results also show that the microneedles can endure the mechanical forces during its handling and insertion in the tumor-mimicking agarose gel (Figure 5.4 and 5.5).

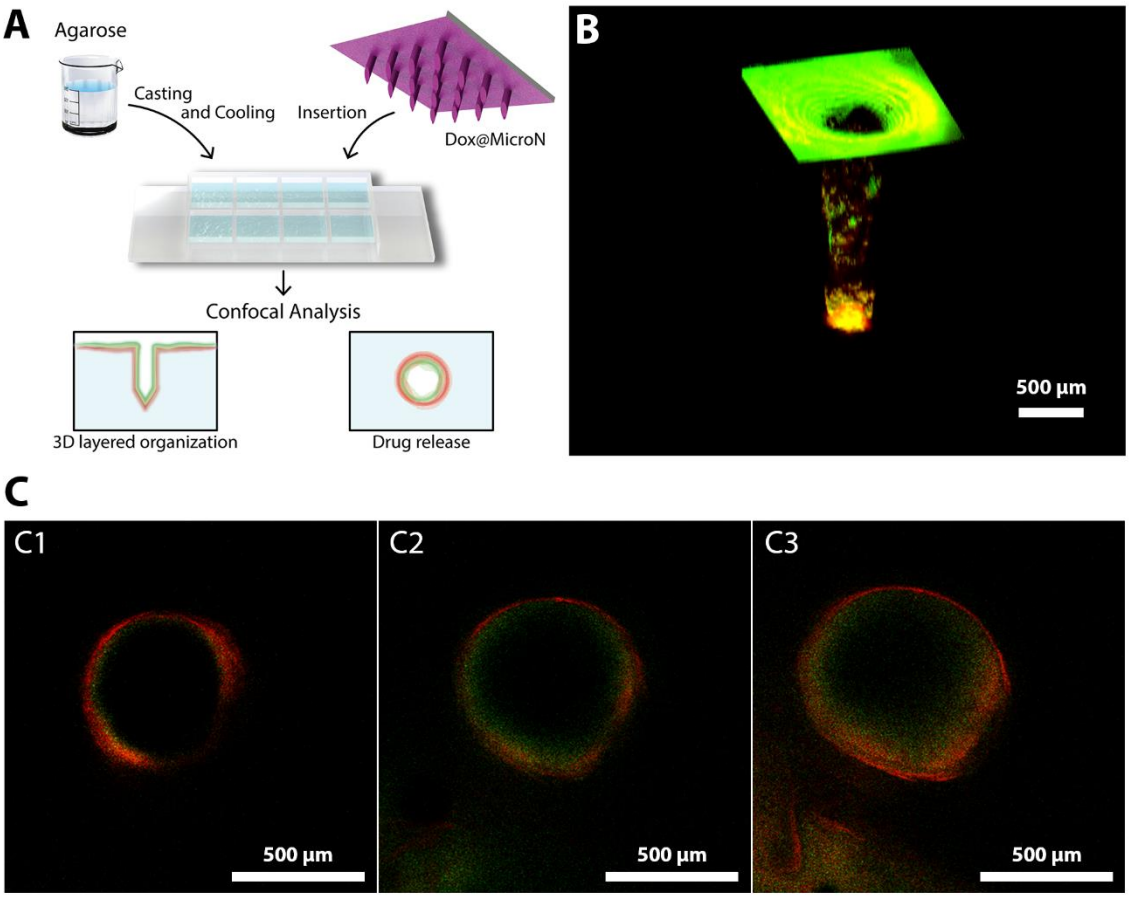

Figure 5.4 - *In vitro* characterization of the Dox@MicroN patches' tissue insertion ability. (A) Schematics of the Dox@MicroN agarose penetration studies. The casting of an agarose (6% w/v) solution originates a tissue mimicking construct with the mechanical and viscoelastic properties of a tumor tissue. (B) 3D reconstruction of the Dox@MicroN microneedle inserted on the agarose construct, Green channel: Dox and Red channel: WGA-Alexa Fluor® 594 stained PVA layer. (C) Cross-section images of the Dox and WGA-Alexa Fluor® 594 release to the agarose construct at 10 (C1), 20 (C2), and 30 (C3) min after the Dox@MicroN patch insertion.

On the other side, in the Figure 5.4 C, it is clearly noticed that the hydrogel area stained at green and red increases with the incubation time (10, 20, and 30 min), indicating the molecules diffusion from the Dox@MicroN patches to the agarose polymeric matrix. These data support the Dox@MicroN patches application for the local delivery of the therapeutic agents, controlling its pharmacokinetics and allowing them to reach deeper regions of the tumor tissue.

5.4.3. Evaluation of the MicroN's cytocompatibility

The MicroN patches biocompatibility was analyzed through the resazurin assay in both FibH and HeLa cells, which represent healthy and cancerous cells, respectively. For that purpose, MicroN samples with 4 mm of diameter were incubated in contact with the cells for 24, 48, and 72h. The obtained results (Figure 5.6) demonstrate that the PVP and PVP_Ch_PVA microneedles do not induce any cytotoxic effect on both cell lines over the 3 days of the study, cell viabilities were superior to 70%.

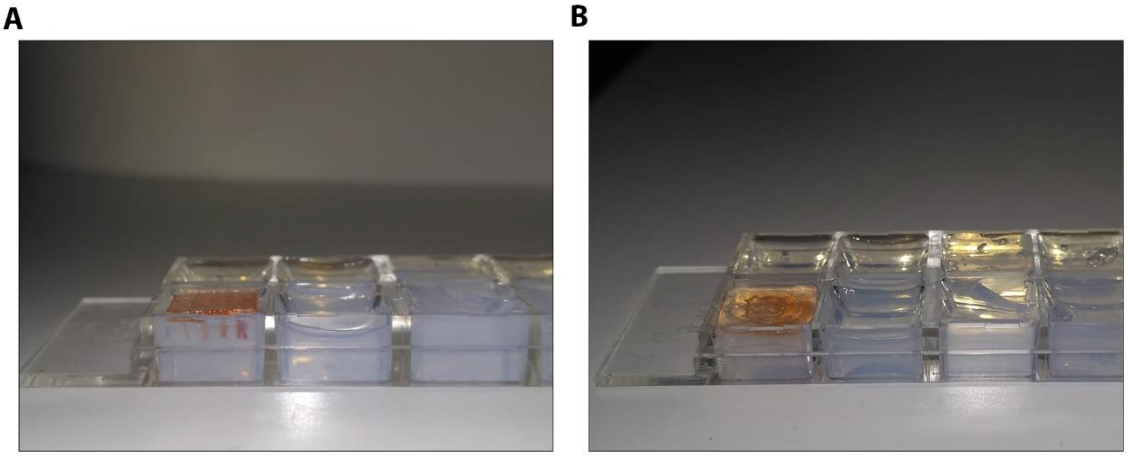

Figure 5.5 - Macroscopic images of the Dox@MicroN patches penetration in agarose gels at 0 min (A) and 30 min (B) of incubation.

Additionally, the incorporation of the AuMSS nanorods did not compromise the microneedles biocompatibility. Furthermore, no alterations on the normal cell morphology were observed in the optical images of the cells cultured in contact the MicroN samples (Figure 5.7). These findings clearly demonstrate the cytocompatibility of the MicroN patches, which is fundamental for the aimed biomedical application. Additionally, the MicroN cytocompatibility is in agreement with previous reports available in the literature for Ch/PVA-based macrostructures and AuMSS based nanosystems [7, 24, 34, 37]. In fact, the PVP, Ch, and PVA are described as biocompatible and FDA-approved polymers for biomedical applications and the AuMSS nanorods are reported as biocompatible in concentrations ranging 25-200 $\mu g.mL^{-1}$.

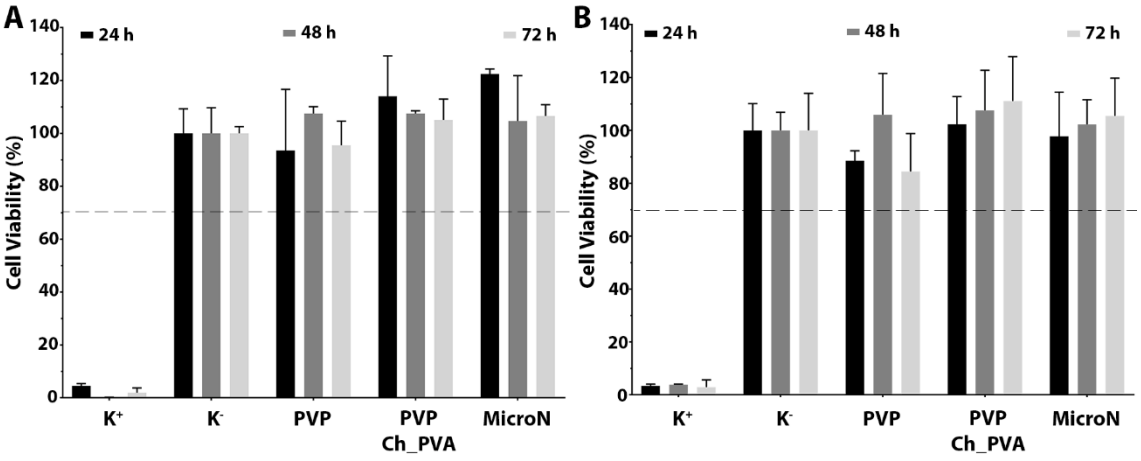

Figure 5.6 - Evaluation of the MicroN patches biocompatibility in FibH (A) and HeLa (B) at 24, 48, and 72 h. Positive control (K^+): cells treated with ethanol; Negative control (K^-): cells without microneedles incubation. Data are presented as mean±s.d., n=5.

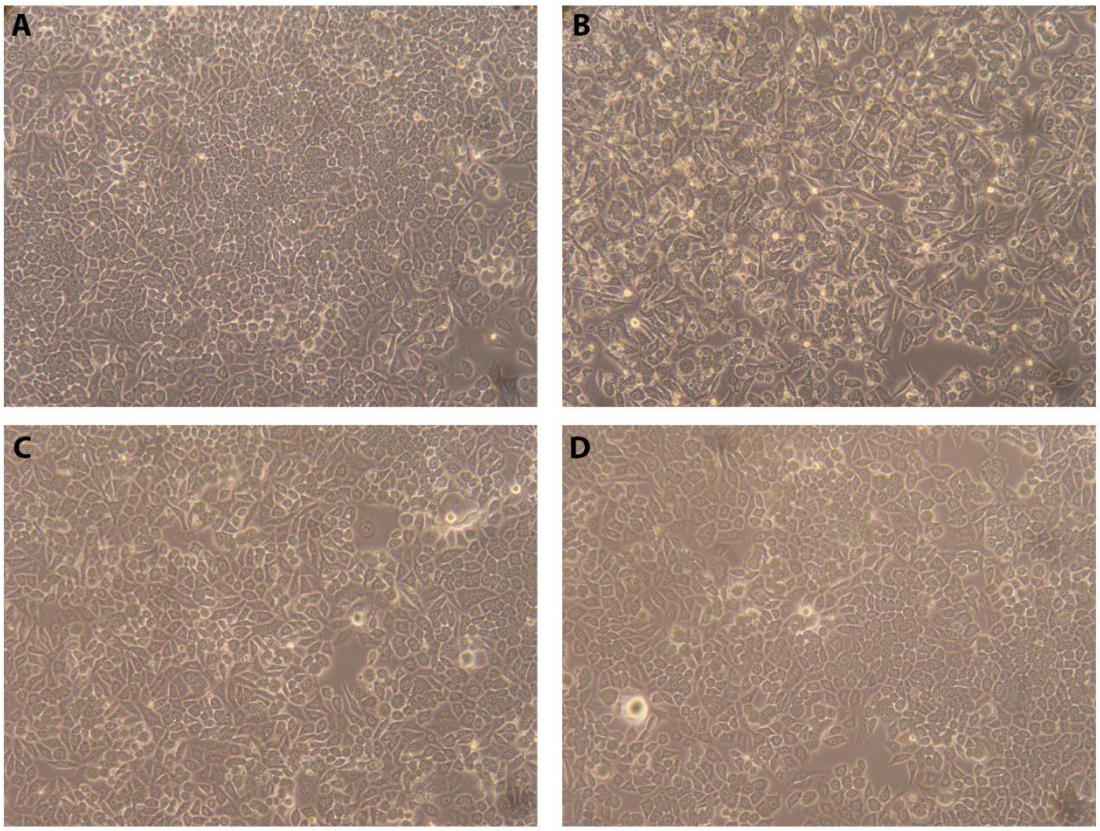

Figure 5.7 - Optical microscopy images at 10x magnification of HeLa cells incubated for 72 h with Control (A), PVP microneedles (B), PVP_Ch_PVA microneedles (C) and MicroN (D).

5.4.4. *In vitro* evaluation of the MicroN therapeutic potential

After assessing the MicroN biocompatibility, the microneedles capacity to combine both the PTT- and chemo- therapies was evaluated towards the HeLa cancer cells. To accomplish that, HeLa cells were incubated for 48 h with MicroN patches with or without being subjected to NIR laser irradiation (Figure 5.8 A). In the Figure 5.8 B, it is possible to observe that the administration of free Dox could reduce the HeLa cells' viability to 3.74%, whereas the stand-alone therapies mediated by the microneedles, *i.e.* PVP_Ch/Dox_PVA and MicroN groups, only reduced the cells' viability to 46.87% and 73.44%, respectively. On the other side, the combined application of the Dox and NIR laser irradiation by the Dox@MicroN patches resulted in a great reduction of the cells' viability to 3.8%. Moreover, it is important to notice that the HeLa cells irradiated with the NIR light (K^- NIR group) did not present any alteration on the cells' viability. Such is in agreement with the literature that reports a minimal or inexistent interaction between the biological components and the NIR light [9, 15]. Therefore, the enhanced cytotoxicity towards the HeLa cancer cells by the chemo-PTT combination mediated by the Dox@MicroN patches can be attributed the local increase in the temperature upon the materials' irradiation, which increases the Dox release as well as sensitizes the cells for the Dox action. Moreover, despite the Dox@MicroN present a similar cytotoxic effect to the bolus administration of the Dox, it would be more benefic in biomedical applications, due to the

decreased interactions with healthy cells and improved pharmacokinetics that contribute for a sustained therapeutic effect. In fact, the Dox@MicroN patches capacity to promote an on-demand release of the chemotherapeutics in response to the environment pH or NIR light irradiation would allow the maintenance of its therapeutic effect during extended periods of time, increasing the antitumoral efficacy while simultaneously avoiding its interaction with healthy tissues.

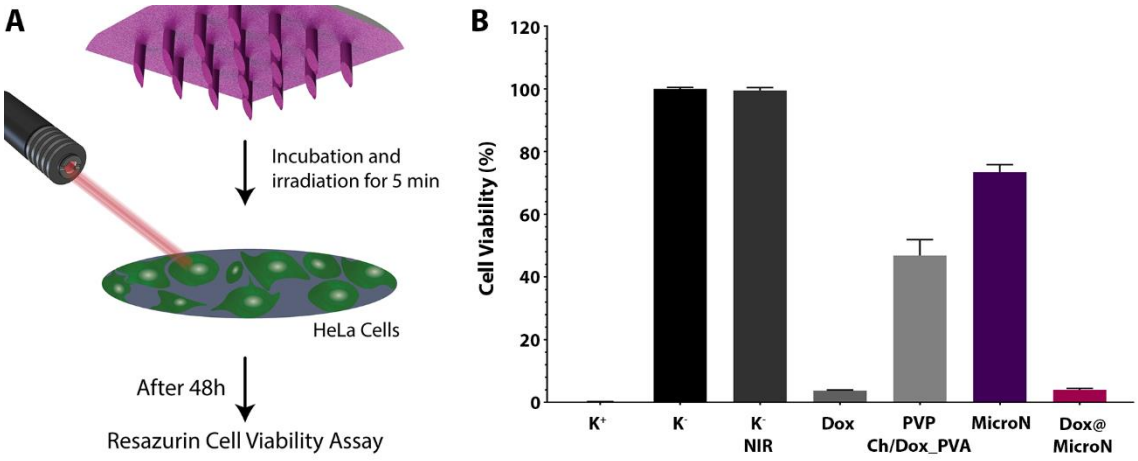

Figure 5.8 - Cytotoxic activity of Dox@MicroN patches on HeLa cells. (A) Schematics of the Dox@MicroN cytotoxicity experiments. (B) Analysis of the microneedles patches toxicity towards HeLa cells at 48 h, with or without NIR laser irradiation. The MicroN and Dox@MicroN groups were irradiated for 5 min with NIR light (808 nm and 1.7 $W.cm^{-2}$). Positive control (K^+): cells treated with ethanol; Negative control (K^-): cells without nanoparticles incubation. Data are presented as mean±s.d..

5.5. Conclusion

In the present study, a layered PVP microneedle system loaded with Dox and AuMSS nanorods for the combinatorial therapy of cancer was reported for the first time. For that purpose, the PVP microneedles were coated using a straightforward approach based on the alternated electrosprayed deposition of the Dox loaded Ch and AuMSS nanorods containing PVA solutions through the electrospraying technique. The *in vitro* results demonstrated that the Dox@MicroN structures can efficiently penetrate the tumor-mimicking agarose gel and release the Dox in a pH- and thermo-controlled fashion. Furthermore, the Dox@MicroN patches capacity to simultaneously mediate the chemo- and PTT-therapies rendered in a superior cytotoxic effect against the cervical cancer cells. In fact, the present findings encourage the application of this simple macroscale delivery device for the local administration of new drug-PTT combinations, avoiding all the issues related with the complex systemic administration of anti-cancer therapeutics. In the future, the fine-tuning of the Dox@MicroN patches (thickness and number of layers), as well as the encapsulation of drug combinations, should be pursued to further optimize the therapeutic effect for *in vivo* assays.

5.6. References

[1] F. Bray, J. Ferlay, I. Soerjomataram, R.L. Siegel, L.A. Torre, A. Jemal, Global cancer statistics 2018: GLOBOCAN estimates of incidence and mortality worldwide for 36 cancers in 185 countries, Ca-Cancer J. Clin., 68 (2018) 394-424.

[2] J.M. Noh, W. Park, Y.S. Kim, J.-Y. Kim, H.J. Kim, J. Kim, J.H. Kim, M.S. Yoon, J.H. Choi, W.S. Yoon, Comparison of clinical outcomes of adenocarcinoma and adenosquamous carcinoma in uterine cervical cancer patients receiving surgical resection followed by radiotherapy: a multicenter retrospective study (KROG 13-10), Gynecol. Oncol., 132 (2014) 618-623.

[3] A.F. Moreira, D.R. Dias, E.C. Costa, I.J. Correia, Thermo-and pH-responsive nano-in-micro particles for combinatorial drug delivery to cancer cells, Eur. J. Pharm. Sci., 104 (2017) 42-51.

[4] X.-J. Liang, C. Chen, Y. Zhao, P.C. Wang, Circumventing tumor resistance to chemotherapy by nanotechnology, Multi-Drug Resistance in Cancer, Springer2010, pp. 467-488.

[5] A.F. Moreira, V.M. Gaspar, E.C. Costa, D. de Melo-Diogo, P. Machado, C.M. Paquete, I.J. Correia, Preparation of end-capped pH-sensitive mesoporous silica nanocarriers for on-demand drug delivery, Eur. J. Pharm. Biopharm., 88 (2014) 1012-1025.

[6] B. Al-Lazikani, U. Banerji, P. Workman, Combinatorial drug therapy for cancer in the post-genomic era, Nat. Biotechnol., 30 (2012) 679.

[7] A.F. Moreira, C.F. Rodrigues, C.A. Reis, E.C. Costa, P. Ferreira, I.J. Correia, Development of poly-2-ethyl-2-oxazoline coated gold-core silica shell nanorods for cancer chemo-photothermal therapy, Nanomedicine, 13 (2018) 2611-2627.

[8] V.M. Gaspar, A.F. Moreira, E.C. Costa, J.A. Queiroz, F. Sousa, C. Pichon, I.J. Correia, Gas-generating TPGS-PLGA microspheres loaded with nanoparticles (NIMPS) for co-delivery of minicircle DNA and anti-tumoral drugs, Colloids Surf., B, 134 (2015) 287-294.

[9] A.F. Moreira, C.F. Rodrigues, C.A. Reis, E.C. Costa, I.J. Correia, Gold-core silica shell nanoparticles application in imaging and therapy: A review, Microporous Mesoporous Mater., 270 (2018) 168-179.

[10] J. Nam, S. Son, L.J. Ochyl, R. Kuai, A. Schwendeman, J.J. Moon, Chemo-photothermal therapy combination elicits anti-tumor immunity against advanced metastatic cancer, Nature communications, 9 (2018) 1074.

[11] H. Ye, K. Wang, M. Wang, R. Liu, H. Song, N. Li, Q. Lu, W. Zhang, Y. Du, W. Yang, Bioinspired nanoplatelets for chemo-photothermal therapy of breast cancer metastasis inhibition, Biomaterials, (2019).

[12] T. Boissenot, A. Bordat, B. Larrat, M. Varna, H. Chacun, A. Paci, V. Poinsignon, E. Fattal, N. Tsapis, Ultrasound-induced mild hyperthermia improves the anticancer efficacy of both Taxol(R) and paclitaxel-loaded nanocapsules, J. Controlled Release, 264 (2017) 219-227.

[13] X. Yao, X. Niu, K. Ma, P. Huang, J. Grothe, S. Kaskel, Y. Zhu, Graphene Quantum Dots-Capped Magnetic Mesoporous Silica Nanoparticles as a Multifunctional Platform for Controlled Drug Delivery, Magnetic Hyperthermia, and Photothermal Therapy, Small, 13 (2017).

[14] X.L. Tu, L.N. Wang, Y.H. Cao, Y.F. Ma, H. Shen, M.X. Zhang, Z.J. Zhang, Efficient cancer ablation by combined photothermal and enhanced chemo-therapy based on carbon nanoparticles/doxorubicin@SiO2 nanocomposites, Carbon, 97 (2016) 35-44.

[15] C.F. Rodrigues, T.A. Jacinto, A.F. Moreira, E.C. Costa, S.P. Miguel, I.J. Correia, Functionalization of AuMSS nanorods towards more effective cancer therapies, Nano Res., 12 (2019) 719-732.

[16] D. de Melo-Diogo, C. Pais-Silva, D.R. Dias, A.F. Moreira, I.J. Correia, Strategies to improve cancer photothermal therapy mediated by nanomaterials, Adv. Healthcare Mater., 6 (2017) 1700073.

[17] J. Eichler, J. Knof, H. Lenz, Measurements on the depth of penetration of light (0.35–1.0 μm) in tissue, Radiation and environmental biophysics, 14 (1977) 239-242.

[18] S. Stolik, J. Delgado, A. Perez, L. Anasagasti, Measurement of the penetration depths of red and near infrared light in human “ex vivo” tissues, Journal of Photochemistry and Photobiology B: Biology, 57 (2000) 90-93.

[19] C.F. Rodrigues, C.A. Reis, A.F. Moreira, P. Ferreira, I.J. Correia, Optimization of gold core-mesoporous silica shell functionalization with TPGS and PEI for cancer therapy, Microporous Mesoporous Mater., 285 (2019) 1-12.

[20] M. Colilla, A. Baeza, M. Vallet-Regí, Mesoporous silica nanoparticles for drug delivery and controlled release applications, The Sol-Gel Handbook-Synthesis, Characterization, and Applications: Synthesis, Characterization and Applications, 3-Volume Set, (2015) 1309-1344.

[21] V. Mamaeva, C. Sahlgren, M. Lindén, Mesoporous silica nanoparticles in medicine—recent advances, Adv. Drug Delivery Rev., 65 (2013) 689-702.

[22] I.I. Slowing, B.G. Trewyn, S. Giri, V.Y. Lin, Mesoporous silica nanoparticles for drug delivery and biosensing applications, Adv. Funct. Mater., 17 (2007) 1225-1236.

[23] J. Lu, M. Liong, J.I. Zink, F. Tamanoi, Mesoporous silica nanoparticles as a delivery system for hydrophobic anticancer drugs, Small, 3 (2007) 1341-1346.

[24] D.R. Dias, A.F. Moreira, I.J. Correia, The effect of the shape of gold core-mesoporous silica shell nanoparticles on the cellular behavior and tumor spheroid penetration, J. Mater. Chem. B, 4 (2016) 7630-7640.

[25] S. Talebian, J. Foroughi, S.J. Wade, K.L. Vine, A. Dolatshahi-Pirouz, M. Mehrali, J. Conde, G.G. Wallace, Biopolymers for antitumor implantable drug delivery systems: recent advances and future outlook, Adv. Mater., 30 (2018) 1706665.

[26] N. Oliva, J.o. Conde, K. Wang, N. Artzi, Designing hydrogels for on-demand therapy, Accounts of chemical research, 50 (2017) 669-679.

[27] P. Huang, H. Song, Y. Zhang, J. Liu, J. Zhang, W. Wang, J. Liu, C. Li, D. Kong, Bridging the gap between macroscale drug delivery systems and nanomedicines: a nanoparticle-assembled thermosensitive hydrogel for peritumoral chemotherapy, ACS Appl. Mater. Interfaces, 8 (2016) 29323-29333.

[28] S.A. Papadimitriou, P. Barmpalexis, E. Karavas, D.N. Bikiaris, Optimizing the ability of PVP/PEG mixtures to be used as appropriate carriers for the preparation of drug solid dispersions by melt mixing technique using artificial neural networks: I, Eur. J. Pharm. Biopharm., 82 (2012) 175-186.

[29] X. Liu, Y. Xu, Z. Wu, H. Chen, Poly (N-vinylpyrrolidone)-modified surfaces for biomedical applications, Macromol. Biosci., 13 (2013) 147-154.

[30] S.P. Sullivan, N. Murthy, M.R. Prausnitz, Minimally invasive protein delivery with rapidly dissolving polymer microneedles, Adv. Mater., 20 (2008) 933-938.

[31] L.Y. Chu, M.R. Prausnitz, Separable arrowhead microneedles, J. Controlled Release, 149 (2011) 242-249.

[32] K.A. Moga, L.R. Bickford, R.D. Geil, S.S. Dunn, A.A. Pandya, Y. Wang, J.H. Fain, C.F. Archuleta, A.T. O'Neill, J.M. DeSimone, Rapidly–dissolvable microneedle patches via a highly scalable and reproducible soft lithography approach, Adv. Mater., 25 (2013) 5060-5066.

[33] S.P. Miguel, A.F. Moreira, I.J. Correia, Chitosan based-asymmetric membranes for wound healing: A review, International journal of biological macromolecules, (2019).

[34] B.P. Antunes, A.F. Moreira, V. Gaspar, I. Correia, Chitosan/arginine–chitosan polymer blends for assembly of nanofibrous membranes for wound regeneration, Carbohydr. Polym., 130 (2015) 104-112.

[35] H. Hamedi, S. Moradi, S.M. Hudson, A.E. Tonelli, Chitosan based hydrogels and their applications for drug delivery in wound dressings: A review, Carbohydr. Polym., (2018).

[36] P.I. Soares, A.I. Sousa, J.C. Silva, I.M. Ferreira, C.M. Novo, J.P. Borges, Chitosan-based nanoparticles as drug delivery systems for doxorubicin: Optimization and modelling, Carbohydr. Polym., 147 (2016) 304-312.

[37] Y. Liu, S. Wang, W. Lan, Fabrication of antibacterial chitosan-PVA blended film using electrospray technique for food packaging applications, International journal of biological macromolecules, 107 (2018) 848-854.

[38] S. Jiang, S. Liu, W. Feng, PVA hydrogel properties for biomedical application, Journal of the mechanical behavior of biomedical materials, 4 (2011) 1228-1233.

[39] C. Luo, T. Okubo, M. Nangrejo, M. Edirisinghe, Preparation of polymeric nanoparticles by novel electrospray nanoprecipitation, Polymer International, 64 (2015) 183-187.

[40] Y. Al Thaher, S. Latanza, S. Perni, P. Prokopovich, Role of poly-beta-amino-esters hydrolysis and electrostatic attraction in gentamicin release from layer-by-layer coatings, J. Colloid Interface Sci., 526 (2018) 35-42.

[41] M. Keeney, X. Jiang, M. Yamane, M. Lee, S. Goodman, F. Yang, Nanocoating for biomolecule delivery using layer-by-layer self-assembly, J. Mater. Chem. B, 3 (2015) 8757-8770.

[42] W. Cui, J. Li, G. Decher, Self-Assembled Smart Nanocarriers for Targeted Drug Delivery, Adv. Mater., 28 (2016) 1302-1311.

[43] I. Gorelikov, N. Matsuura, Single-step coating of mesoporous silica on cetyltrimethyl ammonium bromide-capped nanoparticles, Nano Lett., 8 (2008) 369-373.

[44] C.A. Reis, C.F. Rodrigues, A.F. Moreira, T.A. Jacinto, P. Ferreira, I.J. Correia, Development of gold-core silica shell nanospheres coated with poly-2-ethyl-oxazoline and beta-cyclodextrin aimed for cancer therapy, Mater Sci Eng C Mater Biol Appl, 98 (2019) 960-968.

[45] L.K. Vora, R.F. Donnelly, E. Larraneta, P. Gonzalez-Vazquez, R.R.S. Thakur, P.R. Vavia, Novel bilayer dissolving microneedle arrays with concentrated PLGA nano-microparticles for targeted intradermal delivery: Proof of concept, J Control Release, 265 (2017) 93-101.

[46] D.R. Figueira, S.P. Miguel, K.D. de Sa, I.J. Correia, Production and characterization of polycaprolactone- hyaluronic acid/chitosan- zein electrospun bilayer nanofibrous membrane for tissue regeneration, Int J Biol Macromol, 93 (2016) 1100-1110.

[47] R.M.D. Soares, N.M. Siqueira, M.P. Prabhakaram, S. Ramakrishna, Electrospinning and electrospray of bio-based and natural polymers for biomaterials development, Mater Sci Eng C Mater Biol Appl, 92 (2018) 969-982.

[48] S.P. Miguel, D. Simoes, A.F. Moreira, R.S. Sequeira, I.J. Correia, Production and characterization of electrospun silk fibroin based asymmetric membranes for wound dressing applications, Int J Biol Macromol, 121 (2019) 524-535.

[49] D. de Melo-Diogo, V.M. Gaspar, E.C. Costa, A.F. Moreira, D. Oppolzer, E. Gallardo, I.J. Correia, Combinatorial delivery of Crizotinib-Palbociclib-Sildenafil using TPGS-PLA micelles for improved cancer treatment, Eur J Pharm Biopharm, 88 (2014) 718-729.

[50] D. Zhang, D.B. Das, C.D. Rielly, Microneedle assisted micro-particle delivery from gene guns: experiments using skin-mimicking agarose gel, J Pharm Sci, 103 (2014) 613-627.

[51] K. Manickam, R.R. Machireddy, S. Seshadri, Characterization of biomechanical properties of agar based tissue mimicking phantoms for ultrasound stiffness imaging techniques, J Mech Behav Biomed Mater, 35 (2014) 132-143.

[52] S.N. Thomas, Triple threat to colorectal cancer, Sci. Transl. Med., 8 (2016) 352ec132-352ec132.

[53] G. Mojeiko, M. de Brito, G.C. Salata, L.B. Lopes, Combination of microneedles and microemulsions to increase celecoxib topical delivery for potential application in chemoprevention of breast cancer, Int. J. Pharm., 560 (2019) 365-376.

[54] X. Lan, J. She, D.-a. Lin, Y. Xu, X. Li, W.-f. Yang, V.W.Y. Lui, L. Jin, X. Xie, Y.-x. Su, Microneedle-mediated delivery of lipid-coated cisplatin nanoparticles for efficient and safe cancer therapy, ACS Appl. Mater. Interfaces, 10 (2018) 33060-33069.

[55] S. Bhatnagar, N.G. Bankar, M.V. Kulkarni, V.V.K. Venuganti, Dissolvable microneedle patch containing doxorubicin and docetaxel is effective in 4T1 xenografted breast cancer mouse model, Int. J. Pharm., 556 (2019) 263-275.

[56] Y. Hao, Y. Chen, M. Lei, T. Zhang, Y. Cao, J. Peng, L. Chen, Z. Qian, Near-Infrared Responsive PEGylated Gold Nanorod and Doxorubicin Loaded Dissolvable Hyaluronic Acid Microneedles for Human Epidermoid Cancer Therapy, Advanced Therapeutics, 1 (2018) 1800008.

[57] S. Selvam, M. Sundrarajan, Functionalization of cotton fabric with PVP/ZnO nanoparticles for improved reactive dyeability and antibacterial activity, Carbohydr. Polym., 87 (2012) 1419-1424.

[58] H.S. Mansur, C.M. Sadahira, A.N. Souza, A.A. Mansur, FTIR spectroscopy characterization of poly (vinyl alcohol) hydrogel with different hydrolysis degree and chemically crosslinked with glutaraldehyde, Mater. Sci. Eng., C, 28 (2008) 539-548.

[59] A.L. Oei, L.E. Vriend, J. Crezee, N.A. Franken, P.M. Krawczyk, Effects of hyperthermia on DNA repair pathways: one treatment to inhibit them all, Radiat. Oncol., 10 (2015) 165.

[60] D. de Melo-Diogo, C. Pais-Silva, E.C. Costa, R.O. Louro, I.J. Correia, D-alpha-tocopheryl polyethylene glycol 1000 succinate functionalized nanographene oxide for cancer therapy, Nanomedicine (Lond), 12 (2017) 443-456.

Chapter 6

Concluding Remarks and Future Trends

Concluding Remarks and Future Trends

Despite all the efforts performed so far, cancer remains as one of the most impactful health disorders worldwide. Such condition is justified by the cancer's complexity and heterogeneity as well as by the widely known limitations of the conventional treatments (chemotherapy and radiotherapy). In this way, researchers have been exploring combinatorial therapeutic approaches, such as the simultaneous administration of photothermal and chemotherapy regimens, to overcome the cancer cells' resistance mechanisms and maximize the antitumoral effect. Among the different nanomedicines that can mediate the photothermal effect and drug delivery to cancer cells, the AuMSS nanoparticles have been demonstrating a tremendous potential in pre-clinical studies.

However, data recently obtained indicates that the nanomedicines present a reduced accumulation in human tumors, with less than 0.7% of the administered dose successfully reaching the tumor site. Such fact prompted a paradigm shift in cancer targeted therapies, with researchers taking a step back and starting to re-explore the use of macroscale delivery systems (*e.g.* microneedles and hydrogels) to promote a controlled and localized delivery of therapeutics to tumor tissue. Particularly, the microneedle systems have been explored in cancer therapy to activate anticancer immune responses from the host (antigens, genetic material, and immune adjuvants) or to deliver agents with anticancer activity (drugs and nanoparticles). Thus, the local application of microneedle systems has the potential to increase the distribution and dose of therapeutic agents that accumulate in the deepest regions of the tumor region while simultaneously reducing their interaction with adjacent healthy tissues.

The present doctoral plan aimed to develop an LbL microneedle system to mediate the simultaneous delivery of AuMSS nanorods and chemotherapeutic agents. Such was pursued by i) exploring a production method of AuMSS nanorods with imaging and therapy properties; ii) optimizing a nano-in-micro system that can incorporate these nanoplatforms and allow to control the release rate in response to variations in pH and temperature; and iii) developing a microneedle system that can improve the therapeutics penetration in the tumor and promote the local and combined administration of AuMSS nanorods PTT agents and chemotherapeutic drugs.

In the first study performed in this doctoral thesis, AuMSS nanorods were functionalized for the first time with PEOZ, an alternative to the commonly used PEG for improving nanoparticles' stability. The AuMSS nanorods' functionalization increased the stability and biocompatibility of the nanoparticles, namely by decreasing the blood hemolysis to safe and negligible levels. Further, the neutralization of the AuMSS nanorods' surface charge also contributed to an improved Dox uptake in HeLa cervical cancer cells. Otherwise, the combined treatment (*i.e.*

NIR induced PTT and chemotherapy) mediated by the AuMSS_PEOZ/Dox nanorods showed a synergistic effect when compared to the chemotherapy or PTT treatment alone, allowing the complete eradication of cervical cancer cells.

In the second experimental study, pH- and thermoresponsive microspheres containing AuMSS nanorods, Dox, and SA were produced to allow the localized administration of nanomedicines and drug combinations to cancer cells. The produced nano-in-micro particles displayed dual-stimuli responsive drug delivery, a biocompatible profile and were effectively internalized by the HeLa cancer cells. Moreover, the microspheres administration to 3D HeLa cell culture models combined with the NIR laser irradiation improved the drugs' distribution on the surface of the spheroids and enhanced their cytotoxicity capacity.

Nevertheless, the intra-tumoral administration of liquid drug/nanoparticle formulations has been associated to increased storage costs, demands trained personal to administer, and induces an increase in the interstitial pressure that facilitates the therapeutics leakage to the adjacent healthy tissues.

In the last practical work, a layered PVP microneedle system loaded with Dox and AuMSS nanorods for the combinatorial therapy of cancer was reported for the first time. The electrospraying technique was used to introduce layers of Dox loaded Ch and AuMSS nanorods enriched PVA. The *in vitro* results demonstrated that the produced microneedle patches can efficiently penetrate the tumor-mimicking agarose gel and release the Dox in a pH- and thermo-controlled fashion. Furthermore, the Dox@MicroN patches' capacity to simultaneously mediate the chemo- and PTT effects rendered a superior cytotoxic effect against the cervical cancer cells. Such results encourage the application of this simple macroscale delivery device for the local administration of new drug-PTT combinations, which can potentially avoid all the issues related to the complex systemic administration of anti-cancer therapeutics. Further, comparing to the intra-tumoral administration of therapeutics using the conventional needles, the microneedles provide a better spatial and temporal control over the therapeutics release to the tumor tissue, which can improve the therapeutic effectiveness and limit the drug leakage to the adjacent healthy tissues.

Overall, the results obtained in this doctoral thesis support the applicability of microneedle-based drug delivery devices in cancer therapy and highlight the synergic therapeutic effect that can be obtained by combining different therapeutic approaches in one single system.

In the future, the following topics will be essential to accelerate the translation of microneedle-based anticancer therapies from the bench to the bedside:

1. *Optimization of microneedles structure*

The combination of microneedles with LbL production techniques can be a highly promising and straightforward approach to allow the production of complex and hierarchically organized structures that support cancer combinatorial therapy. Moreover, the optimization of the microneedles structure such as the number of layers, thickness, and layer sequence will be essential to maximize the therapeutic efficacy. Such will allow the tailoring of the therapeutic agents' release sequence, dose, and timing for the combination of different therapeutic strategies.

2. *Optimization of microneedles application methods*

The reproducibility of the microneedles therapeutic effect will be closely linked to the success of its application on the targeted location. In that way, the development of simple administration methods that guarantee the complete insertion of the microneedle tips and spare the utilization of complex apparatus will be of paramount importance for the anticancer efficacy and the dissemination of this technology.

3. *In vivo validation of Microneedles*

The microneedles biosafety, major organs biocompatibility, and biodegradation constitute a barrier for their clinical translation. In this regard, the utilization of FDA approved materials in the microneedles assembly will be essential to guarantee the systems' safety. Further, the evaluation of the microneedles' *in vivo* behavior and the biodistribution of the therapeutic agents, such as drugs and nanomedicines, is still poorly investigated. Moreover, comprehensive studies of the combination indexes are crucial to determine the best therapeutic combinations and to optimize the therapeutic doses that must be encapsulated and administered. In this way, validating such materials *in vitro* and *in vivo* can be of great interest for fully disclosing the therapeutic potential of the microneedle-based devices.